Dynamic computational models of cell-extracellular matrix and cell-cell interactions

Doctoral thesis

DYNAMIC COMPUTATIONAL MODELS OF CELL-EXTRACELLULAR MATRIX AND CELL-CELL INTERACTIONS

Zeynep Karagöz

2023

Cover İpek Aydın, 2023
Production Karagöz 2023 || Proefschriften.nl
ISBN 978-94-6469-633-2

DYNAMIC COMPUTATIONAL MODELS OF CELL-EXTRACELLULAR MATRIX AND CELL-CELL INTERACTIONS

Dissertation

To obtain the degree of Doctor at Maastricht University,
on the authority of the Rector Magnificus, Prof. dr. Pamela Habibović,
in accordance with the decision of the Board of Deans,
to be defended in public
on Tuesday 9 January 2024, at 16:00 hours

by

Zeynep Karagöz
Born on October 2, 1992 in İzmir, Turkey

Supervisors
Dr. Aurélie Carlier
Prof. dr. Martijn van Griensven

Assessment Committee
Prof. dr. Tim Welting (Chair)
Dr. Marian Breuer
Prof. dr. Liesbet Geris (University of Liège and Katholieke Universiteit Leuven, Belgium)
Dr. Sandra Loerakker (Eindhoven University of Technology, the Netherlands)

Paranymphs
Dr. Sangita Swapnasrita
Hamidreza Jafarinia

To all the women in the world,
who fight for their existence in all walks of life.

Contents

1

General Introduction

The main goal of regenerative medicine is to replace or repair impaired tissues and organs. The field of tissue engineering advanced over the years, within regenerative medicine, aiming to develop cell culture and (bio)material systems with similar characteristics to the native tissues. All tissues of multicellular organisms consist of cells (of different types) that reside in a non-cellular microenvironment which is called the extracellular matrix (ECM). The essence of the multicellularity is the continuous communication of single cells with neighboring cells and the ECM. The proteins responsible for both cell-cell and cell-extracellular environment interactions are shown to be highly conserved in evolutionary analyses among vertebrates and invertebrates (Hynes & Zhao, 2000). This evolutionary conservation credits the fundamental role of intercellular communication and adhesion in sustaining the organismal well-being. This is also why the development of (bio)materials with similar characteristics to the native tissues is successful in improving *in vitro* tissue regeneration (Akhmanova *et al*., 2015; Dankers *et al*., 2011; Galván-Chacón *et al*., 2022; Malheiro *et al*., 2022; Tassinari *et al*., 2023).

Although the exact composition is tissue-specific, the ECM essentially contains fibrous proteins, polysaccharides and water (Frantz *et al*., 2010). Cells adhere to the ECM via adaptor proteins called integrins (Figure 1.1). This cell-ECM adhesion provides both mechanical and biochemical cues for the cells, in order to physically support them, drive their growth, differentiation and migration (Miller *et al*., 2020). ECM proteins are continuously produced and degraded by the cells depending on the dynamic interactions between cells and the ECM, ensuring tissue homeostasis (Frantz *et al*., 2010). In case of tissue damage, for instance, cells receive signals from the ECM and from neighboring (damaged) cells, directing them to start producing more ECM components and/or proliferate in order to repair the damage. This is a delicate process, so that the malfunctioning of it can be pathological. Uncontrolled and excessive production of ECM results in fibrosis, or permanent scarring in the tissue (Wynn & Ramalingam, 2012). Fibrosis is a currently a major challenge in regenerative medicine, since there are no therapies available to reverse or halt the formation of fibrotic lesions once started (Fernández-Colino *et al*., 2019).

Cell-cell communication is mediated mainly by the cadherin protein family (Figure 1.1). Cadherins, with four subfamilies, allow the cells in a tissue to selectively adhere to one another. This cell-cell adhesion maintains the tissue integrity and allows the cells to communicate via biochemical signals resulting in a multitude of cellular behavior (Yap & Kovacs, 2003). Similar to cell-ECM interactions, malfunction of cell-cell adhesion can also result in pathol-

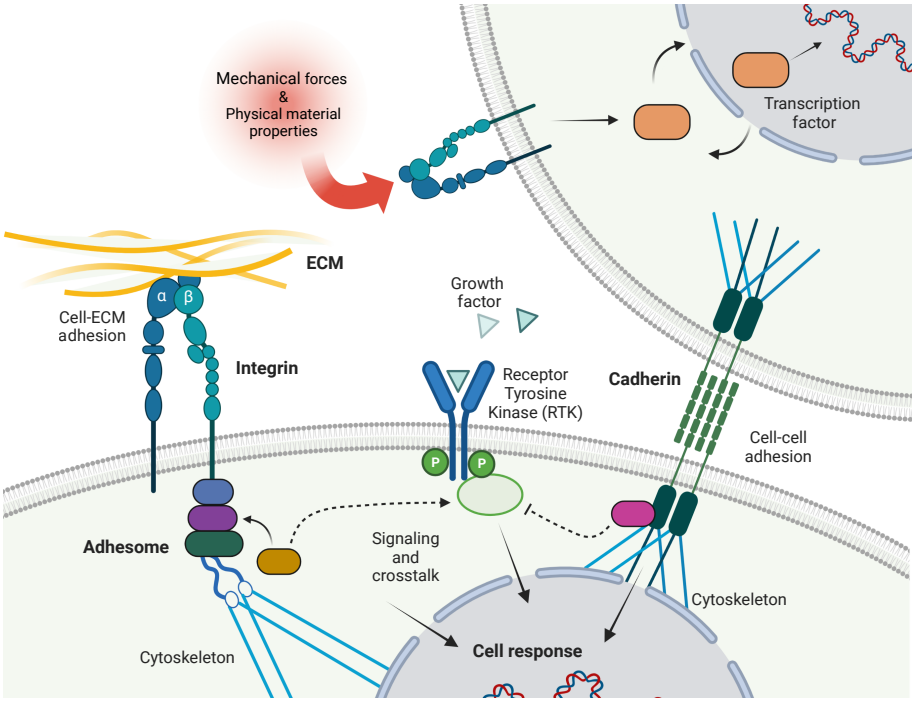

Figure 1.1: An overview of the cell-cell and cell-ECM interactions. Integrins maintain the cell-ECM communication by relaying the extracellular biochemical and mechanical signals to the cell via the adaptor proteins in the adhesome. Cadherins facilitate the cell-cell adhesion and therefore support the tissue integrity. They also participate in intra-cellular signaling by engaging in crosstalk with other cell surface receptors (e.g., growth factor receptors and integrins). All these extracellular information is processed by the cell and cell behavior is adjusted in response to the extracellular input.

ogy, such as tumor growth, infiltration and metastasis (Hajra & Fearon, 2002). Since the integrin and cadherin pathways have shown to interact at multiple levels (Barcelona-Estaje *et al*., 2021; Mui *et al*., 2016) control over cell-cell interactions via cadherins is as important as the control over cell-ECM interactions for advancing the regenerative medicine applications (Barcelona-Estaje *et al*., 2021; Passanha, 2021).

To this end, a detailed understanding of the fundamental processes of the cell-cell and the cell-ECM interfaces is necessary. Given the variability in proteins and cellular processes involved, an interdisciplinary approach is indispensable for this type of research. Tissue engineers and material scientists working hand in hand with molecular and cellular biologists are creating diverse advanced materials and tissue culture systems. Yet there are still many open questions which are not easily addressed by experimental methods. What are the optimal mechanical, chemical and biological conditions for inducing (stem) cell differentiation to different fates? How do the cells of the same origin behave differently under different *in vitro* conditions? How to optimize tissue grafting for each patient? Why some implants are rejected by some patients and not others? Computational (*in silico*) modeling of biological data is a powerful tool to address these open questions. Computational tools have not only been used for product and process design in tissue engineering but they have also helped to resolve complex interactions within biological systems (Geris, 2013).

For example, in the past, *in silico* models have been used to explain the behavior of cells and tissues under healthy, diseased and healing conditions. Oers *et al*., 2014 model proposed a mechanical explanation on the formation of blood vessel-like structures in endothelial cell cultures. Blood vessel formation (angiogenesis) has also been explored specifically in bone fracture healing by Carlier *et al*., 2012, highlighting the importance of the cellular signaling in cell decision-making and bone formation. Later, Borgiani *et al*., 2021 used their computational model to explain the clinically observed diverse outcome of bone morphogenetic protein 2 treatment in critical sized bone defects. Similarly, Perier-Metz *et al*., 2020 focused on the treatment of large bone defects, but focused on exploring the effect of the scaffold structure on the treatment success. At a smaller scale, the model of Adler *et al*., 2020 provided an explanation to the limited time window in which escaping fibrosis is possible during wound healing upon injury.

In this thesis, we suggest that a computational approach is very useful in expanding our fundamental knowledge on cell decision-making affected specif-

ically by cell-cell and cell-ECM interactions, with the long-term aim to improve current regenerative medicine strategies. The thesis is composed of one review and four research articles, each focusing on a different aspect of cell-cell or cell-ECM communication.

In **Chapter 2**, we introduce the integrin protein family and their central role in cell-ECM interactions while giving an up to date summary of the published computational models of integrin function. The chapter divides the integrin function (and the computational models of integrin function) into three spatial categories, namely, the function outside the cell, on the cell membrane and in the cytosol. This categorization allows us to explain the distinct strategies applied for modeling the integrin function at different length and time scales. Altogether, *in silico* models of integrin function, provide mathematical explanations to the interactions between integrins and their ligands, integrins and other cell membrane receptors and integrins among themselves. We further explain current challenges in advancing the computational modeling efforts as well as the challenges in the experimental methods studying integrins. We identify one of the biggest obstacles in the field as the difficulty in obtaining integrin sub-type and integrin ligand specific information by both experimental and computational methods. We conclude by providing suggestions to overcome biological and computational challenges to advance our understanding of cell-ECM interactions via integrins.

In **Chapter 3**, we take on one of the challenges stated in **Chapter 2**, and develop a computational model of integrin activity, accounting for integrin ligand binding competition. We model two ECM proteins both of which have the ability to bind the integrin sub-type in the model. Integrin activation, ligand binding and clustering are explicitly modeled using ordinary differential equations (ODEs). Mass action reaction kinetics are used in this molecular scale model (Figure 1.2). Reaction rates and initial concentrations of integrins and their ligands have been obtained from previously published studies. After simulating experimentally observed ligand concentrations compositions, we conclude that the ligand with a higher binding affinity occupies more integrins at the steady state. We close the chapter by interpreting the results from a regenerative medicine perspective.

Chapter 4 focuses on a process that was largely simplified in **Chapter 3**, the integrin clustering and adhesion formation. We take a novel approach to combine biochemical and mechanical interactions at the initial stages of adhesion formation. ODEs are used to model integrin clustering, binding to adaptor proteins and to cytoskeleton in a force-dependent manner. We assume

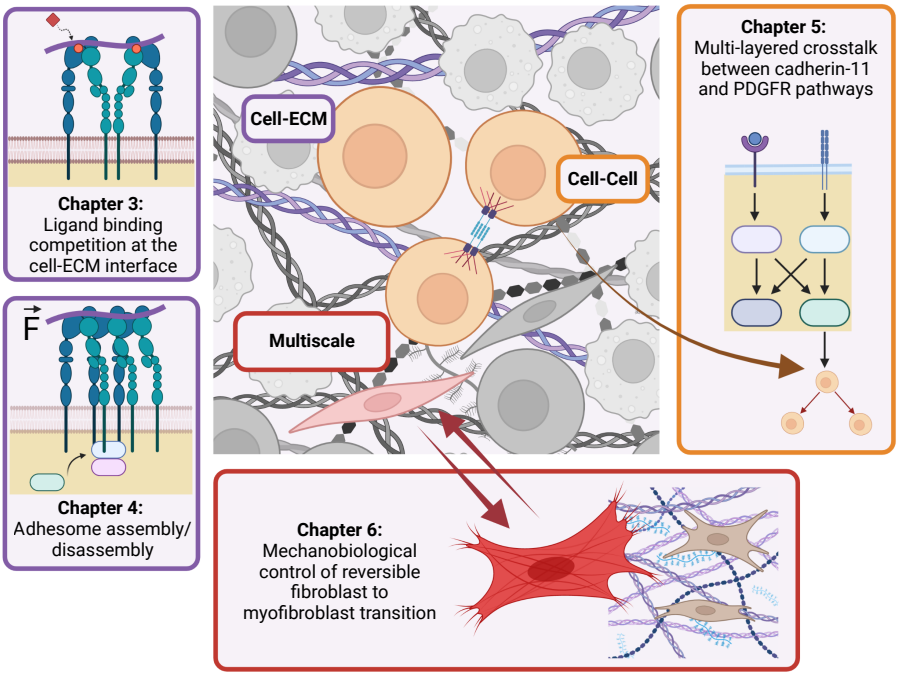

Figure 1.2: An overview of the four research projects concerning computational modeling of the cell-cell and cell-ECM interactions as described in this thesis.

mass action kinetics for the biochemical reactions and a Hookean spring system to calculate the forces on different proteins in this molecular scale model (Figure 1.2). With this combined biochemical-mechanical model of dynamic adhesion assembly, we are able to predict the fraction of nascent adhesions that have a potential to become mature focal adhesions under different substrate stiffnesses.

In **Chapter 5**, we focus on cell-cell interactions via cadherins. We use a computational model to represent the experimentally proven interactions between cadherin-11 and two plateled-derived growth factor receptors (PDGFRs) and we inspect whether the crosstalk also exists downstream of the signaling initiated by the two receptor families. Using ODEs we build a standardized qualitative dynamical system of the reaction networks of cadherin-11 and PDGFRs and we compare the effect of cadherin-11 on cell proliferation in different crosstalk setups. This model is able to predict cellular level outcomes using molecular level information (Figure 1.2). We conclude that the receptor level crosstalk (i.e., the physical binding between cadherin-11 and the two PDGFRs) is not sufficient to establish a cadherin-11 mediated control over cell proliferation. We suggest there needs to be another level of crosstalk between downstream signaling proteins of the two receptor families for cadherin-11 to affect cell proliferation.

Finally in **Chapter 6**, we scale up to the tissue level (Figure 1.2) and we model the reversible fibroblast to myofibroblast transition (FMT); which has been experimentally shown to be initiated by ECM tension. This model couples two powerful modeling techniques, namely an agent based model for cellular and subcellular biochemical reactions and a finite element model to capture the mechanical properties of the ECM. With this coupled approach we are able to show the continuous and dynamic interactions between the ECM and the cells that initiate the FMT. We propose that by mechanosensitive production of new ECM, mechanical properties of the tissue changes over time which then reverses the FMT process.

References

Adler, M., Mayo, A., Zhou, X., Franklin, R. A., Meizlish, M. L., Medzhitov, R., Kallenberger, S. M., & Alon, U. (2020). Principles of Cell Circuits for Tissue Repair and Fibrosis. *iScience*, *23*(2). https://doi.org/10.1016/j.isci.2020.100841

Akhmanova, M., Osidak, E., Domogatsky, S., Rodin, S., & Domogatskaya, A. (2015). Physical, Spatial, and Molecular Aspects of Extracellular Matrix of In Vivo Niches and Artificial Scaffolds Relevant to Stem Cells Research. *Stem Cells International*, *2015*, 167025. https://doi.org/10.1155/2015/167025

Barcelona-Estaje, E., Dalby, M. J., Cantini, M., & Salmeron-Sanchez, M. (2021). You Talking to Me? Cadherin and Integrin Crosstalk in Biomaterial Design. *Advanced Healthcare Materials*, *10*(6), 2002048. https://doi.org/10.1002/adhm.202002048

Borgiani, E., Duda, G. N., Willie, B. M., & Checa, S. (2021). Bone morphogenetic protein 2-induced cellular chemotaxis drives tissue patterning during critical-sized bone defect healing: An in silico study. *Biomechanics and Modeling in Mechanobiology*, *20*(4), 1627–1644. https://doi.org/10.1007/s10237-021-01466-0

Carlier, A., Geris, L., Bentley, K., Carmeliet, G., Carmeliet, P., & Oosterwyck, H. V. (2012). MOSAIC: A Multiscale Model of Osteogenesis and Sprouting Angiogenesis with Lateral Inhibition of Endothelial Cells. *PLOS Computational Biology*, *8*(10), e1002724. https://doi.org/10.1371/journal.pcbi.1002724

Dankers, P. Y. W., Boomker, J. M., Huizinga-van der Vlag, A., Wisse, E., Appel, W. P. J., Smedts, F. M. M., Harmsen, M. C., Bosman, A. W., Meijer, W., & van Luyn, M. J. A. (2011). Bioengineering of living renal membranes consisting of hierarchical, bioactive supramolecular meshes and human tubular cells. *Biomaterials*, *32*(3), 723–733. https://doi.org/10.1016/j.biomaterials.2010.09.020

Fernández-Colino, A., Iop, L., Ventura Ferreira, M. S., & Mela, P. (2019). Fibrosis in tissue engineering and regenerative medicine: Treat or trigger? *Advanced Drug Delivery Reviews*, *146*, 17–36. https://doi.org/10.1016/j.addr.2019.07.007

Frantz, C., Stewart, K. M., & Weaver, V. M. (2010). The extracellular matrix at a glance. *Journal of Cell Science*, *123*(24), 4195–4200. https://doi.org/10.1242/jcs.023820

Galván-Chacón, V. P., Zampouka, A., Hesse, B., Bohner, M., Habibovic, P., & Barata, D. (2022). Bone-on-a-Chip: A Microscale 3D Biomimetic Model to Study Bone Regeneration. *Advanced Engineering Materials*, *24*(7), 2101467. https://doi.org/10.1002/adem.202101467

Geris, L. (Ed.). (2013). *Computational Modeling in Tissue Engineering* (Vol. 10). Springer. https://doi.org/10.1007/978-3-642-32563-2

Hajra, K. M., & Fearon, E. R. (2002). Cadherin and catenin alterations in human cancer. *Genes, Chromosomes and Cancer*, *34*(3), 255–268. https://doi.org/10.1002/gcc.10083

Hynes, R. O., & Zhao, Q. (2000). The Evolution of Cell Adhesion. *Journal of Cell Biology*, *150*(2), F89–F96. https://doi.org/10.1083/JCB.150.2.F89

Malheiro, A., Seijas-Gamardo, A., Harichandan, A., Mota, C., Wieringa, P., & Moroni, L. (2022). Development of an In Vitro Biomimetic Peripheral Neurovascular Platform. *ACS Applied Materials & Interfaces*, *14*(28), 31567–31585. https://doi.org/10.1021/acsami.2c03861

Miller, A. E., Hu, P., & Barker, T. H. (2020). Feeling Things Out: Bidirectional Signaling of the Cell–ECM Interface, Implications in the Mechanobiology of Cell Spreading, Migration, Proliferation, and Differentiation. *Advanced Healthcare Materials*, *9*(8), 1901445. https://doi.org/10.1002/ADHM.201901445

Mui, K. L., Chen, C. S., & Assoian, R. K. (2016). The mechanical regulation of integrin–cadherin crosstalk organizes cells, signaling and forces. *Journal of Cell Science*, *129*(6), 1093–1100. https://doi.org/10.1242/jcs.183699

Oers, R. F. M. v., Rens, E. G., LaValley, D. J., Reinhart-King, C. A., & Merks, R. M. H. (2014). Mechanical Cell-Matrix Feedback Explains Pairwise and Collective Endothelial Cell Behavior In Vitro. *PLOS Computational Biology*, *10*(8), e1003774. https://doi.org/10.1371/journal.pcbi.1003774

Passanha, F. R. (2021). *Advancing regenerative medicine by generating knowledge about the nature of cadherins in human mesenchymal stem cells*. Maastricht University.

Perier-Metz, C., Duda, G. N., & Checa, S. (2020). Mechano-Biological Computer Model of Scaffold-Supported Bone Regeneration: Effect of Bone Graft and Scaffold Structure on Large Bone Defect Tissue Patterning. *Frontiers in Bioengineering and Biotechnology*, *8*.

Tassinari, R., Olivi, E., Cavallini, C., Taglioli, V., Zannini, C., Marcuzzi, M., Fedchenko, O., & Ventura, C. (2023). Mechanobiology: A landscape for reinterpreting stem cell

heterogeneity and regenerative potential in diseased tissues. *iScience*, *26*(1). https://doi.org/10.1016/j.isci.2022.105875

Wynn, T. A., & Ramalingam, T. R. (2012). Mechanisms of fibrosis: Therapeutic translation for fibrotic disease. *Nature Medicine*, *18*(7), 1028–1040. https://doi.org/10.1038/nm.2807

Yap, A. S., & Kovacs, E. M. (2003). Direct cadherin-activated cell signaling. *The Journal of Cell Biology*, *160*(1), 11–16. https://doi.org/10.1083/jcb.200208156

2

Towards Understanding the Messengers of Extracellular Space: Computational Models of Outside-In Integrin Reaction Networks

This chapter has been **published** as: Karagöz, Z., Rijns, L., Dankers, P. Y. W., van Griensven, M., & Carlier, A. (2021). Towards understanding the messengers of extracellular space: Computational models of outside-in integrin reaction networks. *Computational and Structural Biotechnology Journal*, *19*, 303–314. https://doi.org/10.1016/J.CSBJ.2020.12.025.

Abstract

The interactions between cells and their extracellular matrix (ECM) are critically important for homeostatic control of cell growth, proliferation, differentiation and apoptosis. Transmembrane integrin molecules facilitate the communication between ECM and the cell. Since the characterization of integrins in the late 1980s, there has been great advancement in understanding the function of integrins at different subcellular levels. However, the versatility in molecular pathways integrins are involved in, the high diversity in their interaction partners both outside and inside the cell as well as on the cell membrane and the short lifetime of events happening at the cell–ECM interface make it difficult to elucidate all the details regarding integrin function experimentally. To overcome the experimental challenges and advance the understanding of integrin biology, computational modeling tools have been used extensively. In this review, we summarize the computational models of integrin signaling while we explain the function of integrins at three main subcellular levels (outside the cell, cell membrane, cytosol). We also discuss how these computational modeling efforts can be helpful in other disciplines such as biomaterial design. As such, this review is a didactic modeling summary for biomaterial researchers interested in complementing their experimental work with computational tools or for seasoned computational scientists that would like to advance current *in silico* integrin models.

2.1 Introduction

The evolution of cell adhesion, both to other cells and to surfaces, has been a critical step in the emergence of multicellular organisms on earth (Hynes & Zhao, 2000). Today, we know that cells of all multicellular metazoans, reside in a mesh of fibrous proteins, referred to as the extracellular matrix (ECM) (Hynes, 2004). Adhesion to the ECM is required for the homeostatic control of cell growth, proliferation, differentiation and apoptosis (Miller *et al*., 2020). Furthermore, interaction between cells of the same tissue/organ is facilitated by the ECM, resulting in biochemical and biophysical information exchange (Sun *et al*., 2016). When the natural cell–ECM interaction is perturbed, because cells cannot adhere or the ECM properties have drastically changed, morbid or cancerous phenotypes are observed at the cell/tissue/organ level (Butcher *et al*., 2009; Cox & Erler, 2011; Handorf *et al*., 2015). The ECM therefore, not only functions as a structural support for a group of cells in a tissue, but it actively communicates with the cells to ensure homeostasis.

Experimental research on the subcellular structures that form the link between cells and their matrix started in the early 1970s (Hynes, 2004). After nearly 20 years, a family of heterodimeric proteins, called integrins, were characterized as cell-surface receptors for ECM proteins that mediate the communication of cells and their ECM in animals (Hynes, 1987) (Figure 2.1). Each integrin molecule consists of non-covalently associated α and β subunits. To date, 24 unique integrins have been found in mammals, which are combinations of 18 different α and eight different β subunits (Barczyk *et al*., 2009; Hynes, 2002) (Figure 2.2. Each integrin molecule is able to recognize and bind to a defined set of ECM ligands via its ectodomain (Humphries *et al*., 2006; Hynes, 2002) and to cytosolic ligands via its cytoplasmic tails (Hynes, 2002). This way, integrins create physical anchor points between the extracellular space and the cytoplasm (Figure 2.1.1, blue).

There are different ways in which integrins orchestrate the communication between the cells and their extracellular environment. Multiple integrins of the same or different type, when bound to their ligands, can cluster together (Figure 2.1.2a, green) and initiate the formation of a multi-protein complex at the cell–ECM interface called a "focal adhesion" (FA) (Eyckmans *et al*., 2011). The cytoplasmic side of the FAs contain many different molecules and protein kinases, such as focal adhesion kinase (FAK), proto-oncogene tyrosine-protein kinase Src and small GTPase Ras, to start and maintain several signaling cascades (Eyckmans *et al*., 2011). It is also known that integrins can facilitate and/or enhance signaling via other cell-surface receptors (such as

syndecans or receptor tyrosine kinases) by establishing a " crosstalk" with them (Eliceiri, 2001; Mahabeleshwar *et al.*, 2007)(Figure 2.1.2b, green). In addition, on the cytosolic side, FAs harbor numerous other proteins such as talin and vinculin. Via these proteins, FAs are bound to the actin cytoskeleton and can affect the cell shape and motility (Critchley & Gingras, 2008; Eyckmans *et al.*, 2011) (Figure 2.1.3b, yellow).

Having such key functions in the cell–ECM communication and initiating cellular responses to signals from the ECM, integrins have been a common target in the biomaterial and tissue engineering fields. Biomaterials designed for regenerative medicine and in specific tissue engineering applications are aimed to direct specific cellular behavior (e.g., regeneration) by designing instructive biomaterials with or without the addition of growth factors (Almouemen *et al.*, 2019; Karimi *et al.*, 2018; Werner *et al.*, 2020). Materials inspired by tissue-specific geometric, chemical and physical properties of the ECM have been successfully used to guide the cells to a desired behavior (Werner *et al.*, 2020). Recently, materials decorated with bioactive molecules have been produced to actively communicate with cells (Karimi *et al.*, 2018). These promising strategies require thorough understanding of integrin function, as it is the key mediator of ECM–cell interactions.

Since the characterization of integrins in the late 1980s, there has been great advancement in understanding the function of integrins at different levels. However, the versatility in molecular pathways integrins are involved in, the high diversity in their interaction partners both outside and inside the cell as well as on the cell membrane and the short lifetime of events happening at the cell–ECM interface make it difficult to elucidate all the details regarding integrin function experimentally (Bidone, Skeeters, *et al.*, 2019; Cheng *et al.*, 2017; Huttenlocher & Horwitz, 2011; Hynes, 2004).

To overcome the experimental difficulties and to integrate knowledge on integrin function at different cellular levels that come from different *in vitro* methods, *in silico* efforts have come into play. Computational modeling of biological data is a powerful tool and helps to resolve complex interactions within biological systems. A computational (or *in silico*) model is a mathematical simplification of the actual system. It aims at replicating the behavior of the system it represents, allowing to perform simulations and test novel hypothesis *in silico* (Brodland, 2015; Scholma *et al.*, 2014).

The level of detail and precision of a computational model, as well as the amount of data needed to build one, depend on the research question and

the mathematical method (Scholma *et al.*, 2014). The most detailed mathematical description of a biological system is by ordinary or partial differential equations (ODEs/PDEs). This type of model provides information on the changes in the amount of each component in the model over time. Although they are precise in the information they provide, these models are parameter-intensive, meaning that one needs the initial amounts of each species observed in the model, as well as the time-dependent relationship between them (e.g., reaction rates) to build the model. These type of models may get very complicated very quickly because every species in the system must be represented by one equation (Scholma *et al.*, 2014). Logic-based Boolean models are at the other side of the spectrum in terms of precision and data intensity. They are not based on precise measurements of biological molecules, but they work in an ON/OFF manner, based on observations such as "when molecule A is present in the system, B gets activated". The simplicity in construction makes these type of models suitable for representation of large biological networks such as signaling cascades (Scholma *et al.*, 2014). The criteria for deciding on a type of model are therefore 1) the amount and the characteristics of the data at hand and 2) the specific purposes of modeling. There can be multiple ways to model a biological process, and all of them can be correct at the same time (Voit *et al.*, 2008).

Our molecule of interest in this review, integrin, has also been studied *in silico* since it is at the heart of the cell–ECM communication, yet difficult to study experimentally. As integrin function can be divided into three main spatial categories—1) extracellular space (Figure 2.1 – blue), 2) cell membrane (Figure 2.1 – green) and 3) cytosol (Figure 2.1 – yellow)—the computational models of integrin function can also be grouped into the same three main categories. In the following sections, we explain the function of integrin at these three spatial categories following an outside-in perspective and summarize the computational models that belong to each category (Table 2.1).

A review of computational models that centralizes around the molecular reaction networks of integrins does not exist to our knowledge. We aim at filling this gap and providing the scientific community with a guideline that can be used in two ways: first, as a roadmap on how the integrin function can be modeled computationally using different methods, and second, as a starting point for new computational models as we also state possible extensions to existing models and open questions in the field. We do not include in this review the computational models of processes related to integrin function (e.g., mechanosensing and cell motility) that do not explicitly explain the role of integrins. Comprehensive reviews of computational models of

1. Outside	2. Membrane		3. Cytosol	
Cell-ECM adhesion	Integrin clustering	Receptor crosstalk	Signaling	Cytoskeletel remodeling
Blucher *et al.*, 2014	Jamali *et al.*, 2013	Bazzazi *et al.*, 2018	Cirit *et al.*, 2010	Macdonald *et al.*, 2008
Hudson *et al.*, 2017	Yu *et al.*, 2017	Bauer *et al.*, 2010		Escribano *et al.*, 2014
Bidone, Skeeters, *et al.*, 2019	Cheng *et al.*, 2020			

Table 2.1: *In silico* models describing integrin function at different sub-cellular levels that are reviewed in the text. Models are listed under the sub-cellular space category they address.

mechanosensing (B. Chen *et al.*, 2015) and cell shape and motility (Holmes & Edelstein-Keshet, 2012) can be found elsewhere.

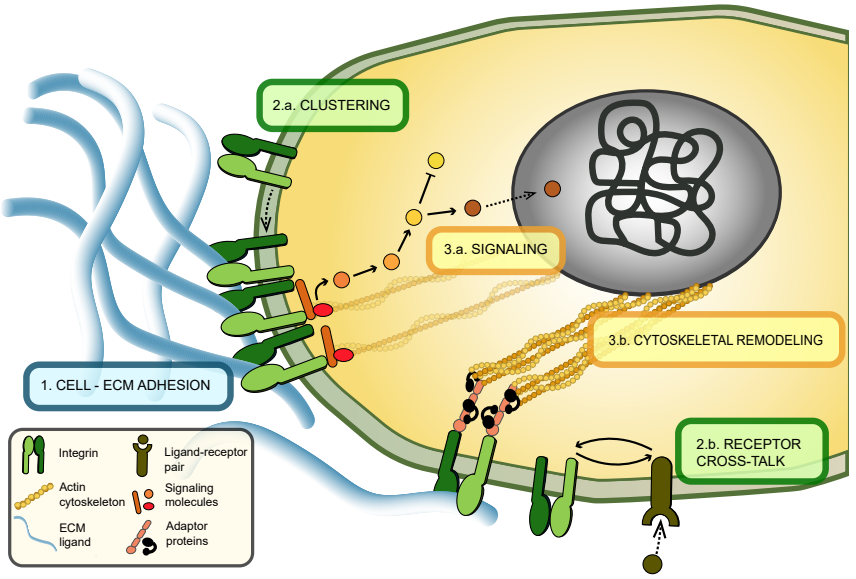

Figure 2.1: Integrins are transmembrane proteins that function at multiple cellular levels. Outside the cells (1, blue), ectodomains of integrins selectively bind to extracellular ligands. On the cell membrane (2, green), multiple integrin molecules are recruited to the focal adhesion site and physically cluster together (2.a) and/or integrins interact with other cell surface receptors to enhance their activity, resulting in signaling crosstalk. (2.b). In the cytosol (3, yellow), integrins initiate signaling cascades (3.a) and are connected to the actin cytoskeleton via adaptor proteins and can initiate cytoskeletal remodeling (3.b).

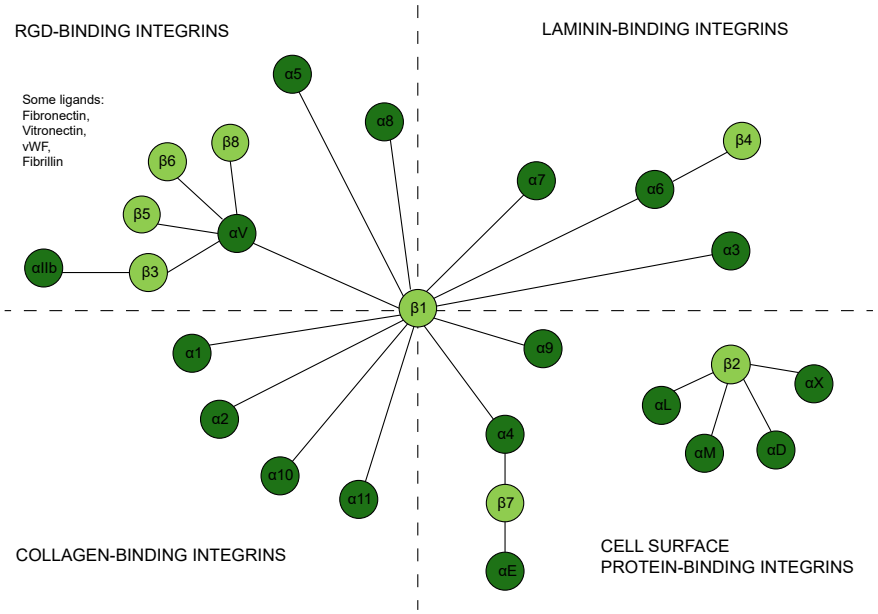

Figure 2.2: A schematic overview of the 24 unique types of integrins, that are composed of 18 different α (dark green) and eight different β subunits (light green). Integrins are grouped into four classes according to their ligand-binding properties. Adapted from (Hudson *et al.*, 2017).

2.2 Extracellular Matrix Proteins Binding to Integrins

In its simplest form, ligand binding at the interface between the α and β subunits of integrins requires that there are integrins present on the portion of the cell membrane that is exposed to the ECM and that those integrins are in their active form. Such a system has the following reactions:

$$\mathrm{S} \xleftrightarrow{k_D^+/k_D^-} \mathrm{I} \tag{2.1}$$

$$\mathrm{L} + \mathrm{I} \xleftrightarrow{k_L^+/k_L^-} \mathrm{LI} \tag{2.2}$$

Where S is the inactive integrin concentration that and becomes active with the rate k_D^+. I is the active integrin concentration at the reaction site that can bind to ligands, L, with the reaction rate k_L^+ to form the ligand–integrin complex, LI. The reverse reactions have the rates k_D^- and k_L^-, respectively.

The rate of change in concentration of each species in this simple system can be expressed as ODEs in the following form:

$$\frac{d[I]}{dt} = k_D^+[S] - k_L^+[L][I] + k_L^-[LI] - k_D^-[S] \tag{2.3}$$

$$\frac{d[L]}{dt} = -k_L^+[L][I] + k_L^-[LI] \tag{2.4}$$

$$\frac{d[S]}{dt} = -k_D^+[S] + k_D^-[I] \tag{2.5}$$

By numerically solving these ODEs, some important questions can be answered, such as "What is the equilibrium concentration of each species?", "How fast does the system reach the equilibrium?" and "How do the equilibrium concentrations depend on the binding parameter values?" To numerically solve a system like this, one needs to plug in the initial concentrations of each species and rate constants in the equations. The system of equations can be converted to computer code and then numerically solved

for convenience. Tellurium (Choi *et al.*, 2018) and bioCRNpyler (Poole *et al.*, 2022) in Python offer ODE based modeling of biological systems for the users who are experienced and/or interested in coding. In platforms like VCell (https://vcell.org/) and Morpheus (Starruß *et al.*, 2014), however, a user does not have to actively code but can still analyze differential equation systems (Vasilevich *et al.*, 2017).

Blucher *et al.*, 2014 use a similar ODE system to the equations 2.3-2.5 to model integrin–ligand binding kinetics. They use rate constants that are consistent with values measured for multiple types of integrins by atomic force microscopy (Lee *et al.*, 2007), and estimate the initial values for the concentration of each species. In this sense, this model can provide only theoretical information on the reaction kinetics. They solve the equations in MATLAB by both deterministic and stochastic simulations. When averaged, the results of 100 stochastic simulations matched the deterministic simulations. Moreover, they reveal that the system is most dynamic during the first quarter of the simulation time and then reaches a steady state for each model species (Blucher *et al.*, 2014).

Each of the 24 different integrin molecules goes through the processes of activation, ligand binding and clustering at different rates. In their model, Blucher *et al.*, 2014 do not take into account the different integrin and ligand types. They rather provide a general overview of the dynamics of ligand binding to integrins. Although it is still interesting to mathematically explain the interactions at the cell–ECM interface, adding the complexity of different integrin–ligand pairs to such an ODE system would provide more biologically relevant estimations. This of course requires knowledge of different reaction rates for different integrin–ligand pairs, which is not present for all (see discussion for more details).

Besides being dependent on the types of interacting molecules, integrin–ligand binding is a dynamic process and is greatly affected by the changes in ECM. Proteomics studies demonstrated that ECM composition dynamically changes in response to acute stress of injury (Hudson *et al.*, 2017; Massey *et al.*, 2017). The effect of changes in the ECM ligand concentration on the integrin binding kinetics can be quantified using an ODE model similar to equations 2.3-2.5, when the ligand and integrin concentrations are known experimentally. Hudson et al. addressed this question using a combined *in vivo–in silico* approach, including a mouse model to induce fibrosis in the liver with CCl4 exposure and a complementary *in silico* model. Using liquid chromatography with mass spectrometry (LC-MS/MS) quantification, an increase in the

amount of multiple types of collagen, fibrillary proteins, glycoproteins and proteoglycans in case of chronic CCl4-induced liver fibrosis was reported. Next, an ODE model to quantify the changes in integrin–ligand binding and integrin clustering upon changes in the ECM composition was used. The ODE model is similar to the simple example above except that Hudson *et al.*, 2017 account for clustering among integrin molecules as well and assume all the integrins are active by the time the simulation starts. This is a valid simplification because this model is focused more on the integrin–ligand binding kinetics and accounts for different binding rates of different integrin–ligand pairs, which increases the number of equations to be solved.

The dynamics of integrin type $\alpha 1\beta 1$-collagens type I–IV and integrin type $\alpha V\beta 3$-fibronectin and von Willebrand factor are investigated separately by Hudson *et al.*, 2017. For all integrin–ligand pairs in this study, when the ligand amount increases — as in case of fibrosis in the tissue — the steady-state value of ligand-bound integrins is higher and is reached faster than in healthy tissue conditions (Figure 2.3.A). When expanded to account for further behavioral effects of integrin signaling on the cell, which will be discussed in the following sections, this model could provide valuable information on the timing of events for different integrin types at the cell–ECM interface.

Although individual integrin-ligand pairs can be modeled and simulated mutually exclusively, as by Hudson *et al.*, 2017, multiple different integrin types are found simultaneously at the cell–ECM interface. The reasons for this coexistence of different types of integrins at the adhesion sites have been widely discussed. Different nanoscale properties of integrin subtypes point to different roles for them. $\beta 1$ integrins, for instance, are found basally active on the cell membrane whereas $\beta 3$ integrins rapidly transform between active–inactive states (Li *et al.*, 2017). Similarly, $\beta 1$ integrins have higher affinity for fibronectin than $\beta 3$ integrins do (Bidone, Skeeters, *et al.*, 2019). Explaining the contribution of the different integrin properties, such as activation and ligand-binding affinity, to the adhesion formation is a challenge *in vitro* as well as *in silico*.

Using a highly coarse-grained model, Bidone, Skeeters, *et al.*, 2019 demonstrated that the simultaneous presence of $\beta 1$ and $\beta 3$ integrins at the nascent adhesion sites can in fact contribute to different aspect of the physics of cellular adhesion. The model space is a quasi-2D surface on which single-point integrins can get activated/deactivated, bind to ligands and interact with each other to form clusters. Integrins that have high affinity for a ligand and that are also more stable in their active state — such as $\beta 1$ — are responsible

for strong individual adhesion to extracellular ligands. Conversely, integrins with lower affinity for a ligand — such as $\beta 3$ — have stronger affinity for other integrin molecules, resulting in focal adhesions where many integrins cluster but their binding to the ECM ligands is less consistent than for $\beta 1$ integrins (Bidone, Skeeters, *et al.*, 2019). Their work therefore suggests that integrin–ligand binding and integrin clustering are competing processes and that the nanoscale properties of integrins determine the dominant process (Figure 2.3.B).

The computational models mentioned here either considered integrins as equally active and ready-to-bind to ligands (Hudson *et al.*, 2017) or as molecules with a defined rate of activation (Bidone, Skeeters, *et al.*, 2019; Blucher *et al.*, 2014). This was because these models were focused more on the chemical reactions that occur during or following the integrin-ligand binding, therefore a more detailed representation of the integrin activation was not necessary. However, there is a significant amount of computational modeling efforts around the actual mechanisms of integrin activation. These efforts mainly include molecular dynamics simulations, and although out of the scope of this review, we refer the readers to (Bidone, Polley, *et al.*, 2019) and (W. Chen *et al.*, 2011) for two of such molecular dynamics simulations.

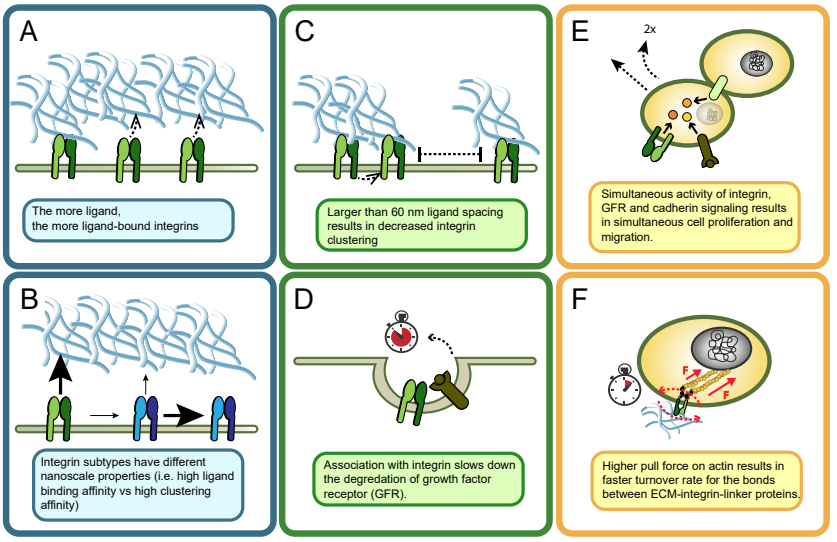

Figure 2.3: Graphical illustration of the main findings from computational models about integrin function at the three sub-cellular levels.

2.3 Integrin Function on the Cell Membrane

The second spatial level of integrin action is on the cell membrane where integrins have two main function with long range effects: 1) clustering among each other and 2) crosstalk with other cell membrane receptors. Clustering of ligand–bound integrins happens with the help of polyvalent extracellular ligands and/or cytoplasmic linker proteins and is prominent in the maturation of focal adhesions (van der Flier & Sonnenberg, 2001). The crosstalk between integrins and other cell membrane receptors is important in establishing and maintaining intercellular signaling cascades that have further impact on cell behavior (Eliceiri, 2001). As such, it is interesting to explore the mathematics behind the molecular biology of integrin activity on the cell membrane.

2.3.1 Integrin Clustering

Experimental observations suggest the joint effect of substrate stiffness and spatial organization of ECM ligands to be prominent in the formation of cellular adhesions. Substrate rigidity regulates the dynamics of cell adhesion by modulating the mechanical force to promote conformational changes in integrin and ligand molecules (J. Huang *et al.*, 2012; Ye *et al.*, 2015). Therefore, rigidity influences the reactions between integrin and their ligands, which were discussed in the previous section. The spatial organization of integrin ligands, however, is observed to affect the continuance of the cellular adhesion which is related to clustering of ligand–bound integrins on the cell membrane. On substrates where the ligand spacing is larger than 70 nm, the focal adhesions stay immature (because integrins cannot cluster) whereas ligand spacing smaller than 70 nm promotes maturation of focal adhesions (Arnold *et al.*, 2004; Ye *et al.*, 2015).

The underlying mechanochemical mechanism of integrin clustering in response to ligand spacing has been studied by Yu *et al.*, 2017 using Monte Carlo simulations. Their model space was a 6×6 μm^2 square patch of cell membrane with 100–1000 integrins that are free to diffuse to the non-occupied, nearest-neighbor location. The model does not account for different types of integrins but rather simulates the integrin function in a generalized way. At each step of the simulation, integrins follow a set of rules based on a system that is similar to the one introduced before (reactions 2.1-2.2), except that integrin clustering (reaction 2.6) is added to the reaction system and the ODEs are rearranged accordingly.

$$\mathrm{LI} + \mathrm{LI} \xleftrightarrow{k_C^+/k_C^-} \mathrm{C} \tag{2.6}$$

According to reaction 2.6, ligand-bound integrins can form clusters (C) with the nearest ligand-bound integrin (LI) at rate $k_C{}^+$, and similarly, clusters can dissociate at rate $k_C{}^-$. The Monte Carlo method introduces stochasticity to the system at the beginning of each simulation by randomly sampling the integrin molecules on the membrane that will undergo reactions 2.1–2.6 and therefore setting the initial conditions for the ODE system. Stochasticity is inherently present in biological systems since many cellular reactions depend on the random motion of molecules (Johnston, 2012), so it is important to account for the randomness. The integrins that are not contributing to the ODEs are free to diffuse on the membrane to the next nearest neighbor with a constant rate. This way, the integrins are shuffled at each simulation step and their spatial distribution changes (Yu *et al.*, 2017).

In another interesting *in silico* experiment, Yu et al. set ligands at fixed positions in the model space, but with different spacing between them (20, 40, 60, 80 and 100 nm). At the end of the *in silico* experiments with ligand spacing 20 to 60 nm, 60% of total integrins in the model space are found in the clustered form. With ligand spacing exceeding 60 nm, a sharp decrease in the amount of clustering is observed (Figure 2.3.C). At 80 nm ligand spacing or greater, only about 10% of integrins are clustered. (Yu *et al.*, 2017) The reason behind this observation is that when ligand spacing is larger than a threshold of 60 nm, there are less ligands available (L in reaction 2.2) in the designated experiment space for the active integrins (I in reactions 2.1 & 2.2) to bind while diffusing through the cell membrane, therefore reducing the possibility of integrin clustering (C in reaction 2.6). Consequently, these *in silico* results provide a mechanochemical mechanism of the experimental observations that ligand spacing is crucial in adhesion maturation (Arnold *et al.*, 2004; Ye *et al.*, 2015; Yu *et al.*, 2017).

Another *in silico* model has achieved a similar result. In their agent-based model (ABM), Jamali *et al.*, 2013 conclude that ligand spacing has a key role in initiating integrin clustering. More specifically, in an ABM, each element in the system is called an agent and agents interact with each other following particular rules of interaction (i.e., biochemical reactions). Different from ODE-based models, to account for the heterogeneous and stochastic nature of

biochemical systems, ABM models assign a certain probability when assessing each interaction between the agents, rather than assigning a particular rate for each reaction (Jamali *et al.*, 2013). The assigned probabilities of events are calculated based on the observed properties of agents. For example, the agents move to a new location within the model space with a probability that correlates with the actual diffusion coefficient of the molecule each agent represents (Jamali *et al.*, 2013).

The ABM model of integrin clustering also shows that increased affinity between integrin subunits promotes clustering especially when ECM ligand concentration is low (Jamali *et al.*, 2013). However, both of the models report for a standardized integrin–ligand pair and do not comment on the effects of different reaction rates when considering different integrin–ligand pairs. Yet both models could be made integrin- and ligand-type specific, when the binding energies required for a specific integrin–ligand and integrin–integrin pair would be known.

An interesting remark by Yu *et al.*, 2017 is that integrin clustering might not only be orchestrated from the ECM side but also from cytosolic side. This is based on the experimental findings of integrin activation being accompanied by talin binding to the β subunit of integrins. Talin is a protein forming the link between integrins and the cytoskeleton and it has also been shown to aid integrin clustering via its head domain (Bouaouina *et al.*, 2012; Critchley & Gingras, 2008; Yu *et al.*, 2017). Therefore, it is exciting to hypothesize that integrin clustering on the membrane is tightly controlled by the ligand organization on the ECM side, but also affected by the events happening in the cytosol, although further research is needed here.

After observing that integrin clustering is mediated by ECM properties and cytosolic factors, an anticipated question is about the role of these integrin clusters in the process of mechanotransduction. A recent spatial Monte Carlo model by Cheng *et al.*, 2020 suggests that large integrin clusters on the cell membrane are spots for focal adhesion kinase (FAK) phosphorylation. As the substrate stiffness affects the size of the clusters, it directly translates into the level of FAK phosphorylation, hence downstream signaling. They validate their model findings with *in vitro* experiments and show that stiffer substrates result in larger integrin clusters and more phosphorylated FAK is found in cytosol (Cheng *et al.*, 2020). This model provides an explanation for how different cell types respond to different ECM stiffness and proposes different roles for different integrin types, in accordance with Bidone et al. model from 2019 (Cheng *et al.*, 2020).

2.3.2 Crosstalk Between Integrins and Other Membrane Receptors

Being on the cell membrane, integrins are known to cooperate with other cell membrane receptors to serve their crucial role in regulating biological events, like cell migration and proliferation. Transforming growth factor beta (TGF-β) receptor, platelet-derived growth factor (PDGF) receptor, vascular endothelial growth factor (VEGF) receptor, bone morphogenic protein 2 (BMP-2) receptor are, for example, known partners of integrins (Eliceiri, 2001; Porter & Hogg, 1998).

Experimental observations indicate the stabilization of VEGF receptor activity upon interaction with integrin $\alpha v\beta 3$ during angiogenesis. It is also known that a protein kinase, Src, is a mediator between the two receptors (Mahabeleshwar *et al.*, 2007). Yet the exact mechanism of action of this cooperation could not be revealed by *in vitro* methods. A kinetic rule-based ODE model by Bazzazi et al. investigated the mechanisms behind this crosstalk. The *in silico* model of Bazzazi *et al.*, 2018 consists of four species: integrin $\alpha v\beta 3$ as a single entity, VEGF receptor, VEGF and Src kinase. Integrin and VEGF receptor are assumed to be pre-associated with each other in an inactive state in order to avoid the complication of modeling the physical proximity of the molecules. The following set of rules defines the biological actions in the model: 1) VEGF binding to VEGF receptor, 2) VEGF receptor activation by autophosphorylation, 3) internalization and degradation of VEGF-bound VEGF receptor, 4) activation of Src, 5) integrin activation by phosphorylation by Src, and 6) active integrin–active VEGF receptor association at a second site. They obtain the parameter values by fitting the model to a consistent set of experimental studies and further perform a sensitivity analysis to identify the most sensitive parameters and thereby the most essential step in the reaction set (Bazzazi *et al.*, 2018).

From the global sensitivity analysis, the rate of internalization and degradation of the VEGF receptor is approximately 400-fold lower when it is associated to the active integrin than when they are not associated. In other words, the underlying mechanism of stabilization of VEGF receptor activity by integrin is via slowing the degradation process of the VEGF receptor ((Bazzazi *et al.*, 2018), Figure 2.3.D). This model cannot be generalized to every integrin and associated receptor, but it is one of the few attempts in explaining the mechanism behind crosstalk between integrins and other receptors in angiogenesis and is therefore of great value. Another *in silico* model deals with receptor crosstalk but is focused on the interactive effects of the two receptors

in downstream signaling, rather than the receptor-integrin kinetics (Bauer *et al.*, 2010). Therefore, it will be discussed in the appropriate section below.

2.4 Integrin Function in the Cytosol

The third level of integrin function is in the cytosol, where external cues are translated into biochemical signals. Integrin adhesomes, complexes harboring multiple proteins, assemble at the cytoplasmic tails of integrins as the adhesions mature. The composition of the integrin adhesome is cell type specific, however, with an attempt to identify a consensus set, 60 proteins have been found to be crucial in the integrin adhesomes (Horton *et al.*, 2015; Horton *et al.*, 2016). Components of integrin adhesome are responsible for transmitting the signals received from integrins to other parts in the cell, eventually affecting cellular decision-making. There is extensive literature on the molecular biology of signaling pathways where integrins are involved as well as their effect on cell behavior (Bouaouina *et al.*, 2012; Harburger & Calderwood, 2009). Here, we focus on *in silico* methods that quantitatively explore the action mechanism of cellular events in response to integrin function.

2.4.1 Signaling Activities

Active and ligand-bound integrins, via the multiprotein complexes at their cytoplasmic tails, are known to activate focal adhesion kinase (FAK) and start a signaling cascade that affects cellular behavior, such as motility or proliferation. Players of the growth factor receptor and integrin cascades interact by inhibiting/activating one another in feedback loops. The details of these signaling cascades are out of the scope of this review and can be found in other dedicated reviews (Bouaouina *et al.*, 2012; Harburger & Calderwood, 2009; Miller *et al.*, 2020). In the next paragraphs, we review the *in silico* models of integrin signaling and crosstalk.

The association of integrins and growth factor receptors in angiogenesis was mentioned earlier as we explored integrin-VEGF receptor (VEGFR) association that stabilizes VEGFR activity by slowing the receptor degradation (Bazzazi *et al.*, 2018). Growth factor binding to growth factor receptors (GFR) promotes proliferation and cell survival mostly via the mitogen-activated protein kinase (MAPK) signaling pathway. However, growth factor–initiated signaling is not enough for the cell to proliferate. It is also known that cell-to-cell

communication via cadherins is another factor that ensures proper cell proliferation in presence of growth factors in angiogenesis (Zanetti *et al*., 2002). These findings suggest crosstalk between the signaling pathways of three cell membrane receptors, namely integrin, VEGFR and cadherin.

Bauer et al. explore the interplay between downstream signaling to VEGFR, cadherin and integrin during angiogenesis, with a stochastic Boolean network model. In Boolean networks, molecular species show a binary behavior, i.e., they are either ON or OFF. It is a practical way of modeling when the quantitative kinetic data of particular biochemical reactions is not enough to support an ODE type of model. If the concentration of a molecular species in the model at any time point is above a certain threshold, the species is ON, while the concentrations below the threshold translates into OFF behavior. A "probability of happening" function is added for each molecular interaction in the Bauer et al. model, to account for the noise or randomness in signaling cascades.

To test the dependence and additive effects of VEGFR– and integrin-induced signaling while also taking into account the cell-to-cell communication through cadherin signaling, they set the initial states of molecular species to randomly chosen binary sets (ON/OFF) and report the output states that correspond to the following cell level phenotypes: proliferating, quiescent, migratory and apoptotic. As expected, in the absence of VEGFR or integrin signaling activity, apoptosis is induced. When VEGFR and integrin signaling are both active, they observe one signaling molecule, namely Rac, is of particular importance. In their model, active Rac enables the cells to migrate whereas inactive Rac results in quiescent cells. When they allow cell-to-cell contact together with active VEGFR and integrin signaling and Rac activity, proliferation is observed while cells migrate (Figure 2.3.E). While this is contrary to the general assumption of proliferation and migration events being temporally exclusive of each other (Gao *et al*., 2005; Giese *et al*., 1996; Hatzikirou *et al*., 2012), there is evidence of both events happening simultaneously in cancer cells (Corcoran & Del Maestro, 2003). Wound healing is another process, that requires both cell motility and proliferation, and the predictions from the Bauer et al. model might be helpful in that area of biology (Grada *et al*., 2017).

Another *in silico* model explores the effect of Rac and related signaling on protrusion velocity at the leading edge of motile cells (Cirit et al., 2010). It is an ODE-based model with stochastic simulations that reports the protrusion velocity in a dimensionless manner. This model incorporates the modulation

of Rac signaling by nascent adhesions via paxillin, which is one of the proteins in the complex that interacts with integrin cytosolic tails. The Cirit et al. model also confirms the positive correlation between Rac activity and cell protrusion in case of nascent adhesion between the cell and the ECM.

In addition to modeling the cellular response to integrin-related signaling, the dynamic assembly-disassembly of the integrin adhesome is another area in biology that can benefit from computational methods. Exploring the composition of the adhesomes at the time of assembly and disassembly via proteomics analyses revealed that integrin presence is stable throughout the assembly-disassembly (30 minutes). However, adaptor proteins between integrins and actin cytoskeleton leave the assembly in about 15 minutes and with different kinetics (Horton *et al.*, 2015). The distinct binding-unbinding kinetics of adhesome proteins have been studied experimentally using techniques like fluorescence recovery after photobleaching (FRAP) (Berkovich *et al.*, 2011; Lavelin *et al.*, 2013). Computational modeling can help to interpret these experimental findings by simulating various hypotheses on the assembly and disassembly of the integrin adhesome, complementing the previous work on functional network identification of the integrin adhesome (Horton *et al.*, 2015; Horton *et al.*, 2016; O'Brien *et al.*, 2019; Zaidel-Bar *et al.*, 2007).

2.4.2 Cytoskeletal Remodeling

Integrin and downstream signaling activities directly affect cell motility as summarized above. Yet, the physical connection of integrins to the actin cytoskeleton (Figure 2.1) is crucial for the cell to actively change its shape to accommodate motility. During protrusion, the actin cytoskeleton actively changes shape and length. Actin-linked integrins are subjected to myosin-mediated forces while still being linked to the ECM proteins on their ectodomains. At this point, when integrins are already bound to their ligands and to the actin cytoskeleton, understanding the effect of push and pull forces on integrins is as important as understanding the effect of ECM properties on the cell shape and migration. For this reason, most of the computational efforts on modeling of the cytoskeletal remodeling and cell shape changes focuses on the mechanics of the process, and some of these efforts have been nicely reviewed (Holmes & Edelstein-Keshet, 2012). Here, we mention two *in silico* models that are at the molecular level and focus more on the biochemical reaction dynamics. Importantly, both of these *in silico* models do not treat integrins as individual entities but either as a complex always bound to its

ligand (Macdonald *et al.*, 2008) or as an inseparable part of a bigger adhesion complex (Escribano *et al.*, 2014).

The ODE-based model by Macdonald et al. considers the binding-unbinding events between three main species: actin filaments, integrin receptor bound to a ligand on the ECM and a linker complex that theoretically contains all the proteins linking the integrins to the actin cytoskeleton. All three species can combine to form complexes of 2 or 3 among them. The effect of the force exerted on the linkages between the integrin–linker complex and actin is modeled in two ways: 1) negatively by increasing the dissociation rate constants of all possible complexes 2) positively by reinforcing the bond between the species in the actin–linker–integrin complex. This opposing effect of force on linkages creates a biphasic scenario when steady-state levels of each species are observed at changing levels of force (10^{-12} to 10^{-10} N). Lower levels of force exerted on actin/integrin linkages results in a higher number of actin–linker–integrin complexes than when under high force levels. A force of 10^{-10} N causes the breakage of linkages, while a force of 10^{-12} N strengthens the linkages (Macdonald *et al.*, 2008) (Figure 2.3.F).

A rather more sophisticated model of actin remodeling is described by Escribano *et al.*, 2014 They modelled the ECM with a discrete number of ligands on it, the adhesion complex that is representative of the integrin and the linker proteins in the cytosol, the actin filaments with changing length and the myosin motor proteins of which the number affects the amount of the pull force. At high levels of pull force (i.e., high number of myosin proteins on the actin filaments), this *in silico* model proposes an increased velocity for the actin filaments (Escribano *et al.*, 2014). This is in accordance with the previous model of Macdonald *et al.*, 2008, as increased velocity requires increased turnover rate for the bonds between adhesion molecules and the ECM.

As force measurements at the cellular level are better established to date than measurements at the single molecular level (that are required to measure rates of integrin clustering, for example), these type of models have a bigger pool of experimental data for validation (see also discussion section). Findings of both models described here have been validated experimentally (Chan & Odde, 2008; Schwarz & Gardel, 2012).

2.5 Conclusion and Outlook

As understood from the many different methods mentioned here, there is no single truth when it comes to computational modeling of integrin function. There are multiple ways to model integrin function, each with their advantages and disadvantages, and often determined by the particular research question. In fact, this is valid for all attempts to computational modeling of biological systems. The level of complexity and nonlinearity in biological systems make it necessary to reduce the system to its essential components (and thus to simplify), while the ever growing possibilities in mathematical and computational methods create new avenues of exploration.

The computational models that address integrin function up to date, capture —to some extend— the nature of events at the cell-ECM interface, albeit focusing on particular processes at distinct scales. *In silico* models of the binding between integrins and their ECM ligands provides an understanding of the binding kinetics and reflect how the kinetics can change with changing ECM conditions (Hudson *et al.*, 2017). These models, usually expressed as ODEs, fall short on spatial aspects of ligand binding as they do not factor in the spatial variations. Models of integrin clustering, provide an explanation for the experimental observations that ligand spacing is a limiting step in the process of integrin clustering (Jamali *et al.*, 2013; Yu *et al.*, 2017). Yet the model geometry is always a rather simplified "square" or "round" area. The majority of computational studies on integrins have captured integrins in general, without specifying the particular subtypes.

Simplifications have also been made about the interaction partners of integrins. Models of integrin–ligand binding assume integrin binding to one ligand at a time whereas in reality one integrin has affinity for binding to multiple ligands in the ECM, resulting in ligand binding competition. On the cytosolic side, large signaling pathways have been simplified to Boolean network models that account for key molecules such as Rac (Bauer *et al.*, 2010) whose activity can explain certain phenotypes. Yet, these types of models lack the numerical details ODE type of models can provide, and in particular, the kinetic rates of the underlying processes. Altogether, *in silico* models of integrin function, provide mathematical explanations to the interactions between integrins and their ligands, integrins and other cell membrane receptors and integrins among themselves.

In this review, we highlighted the *in silico* models that focus on the chemical reaction dynamics of integrin-related cellular events. However, as integrins

are "physical anchor" points between the ECM and the cytoskeleton, they are central to mechanosensitive cellular processes. These include the cellular responses to external mechanical cues like increased proliferation and motility on stiff substrates (Handorf *et al*., 2015). In order to explain the roles of integrins in mechanotransduction, computational models have been developed from a more mechanical point of view as well. For example, Chan and Odde, 2008, introduced the "molecular clutch" model of focal adhesions and explained the biphasic behavior of filopodia in response to mechanical stiffness of the environment (Chan & Odde, 2008). Molecular clutch model represents the engagement between the ECM and the actin cytoskeleton, which resists actin retrograde flow powered by myosins. On stiff substrate, low traction force results in high retrograde flow thus increased protrusion. On the contrary, on soft substrate, high traction force reduces the actin retrograde flow and the protrusion rate of the filpodia (Chan & Odde, 2008; Cheng *et al*., 2017). This molecular clutch behavior has been adapted by many others and further developed. Ligand-bound integrin molecules (i.e., clutches) have been usually modeled as springs and as a part of a bigger architectural complex in these purely mechanical models. Using the molecular clutch principle, Oria et al. have explained the link between adhesion formation and rigidity-dependent ligand spacing sensing of the cells (Oria *et al*., 2017). We refer the reader to (Elosegui-Artola *et al*., 2018) for a nice overview of the molecular clutch hypothesis.

To further the field of integrin biology, a crucial next step, in our opinion, is to combine the computational models that focus on chemical reaction networks with mechanical models. An example of such initiative is the work of Shuaib et al. where they introduced the concept of a hybrid mechanical-agent-based model for bone tissue mechanotransduction. The agent-based model predicts the cytosolic production of ECM proteins, influenced amongst others by the mechanical and compositional inputs of the ECM. These compositional changes of the ECM alter the properties of the mechanical model, which in turn affects the input parameters for the agent-based model (Shuaib *et al*., 2019). Such hybrid models are promising, yet can be challenging due to their multiscale nature. The next paragraphs detail the next steps for modeling the function of integrins computationally, both from a biological perspective as a technical point of view including the challenges of multiscale and multiphysics modeling.

2.5.1 Overcoming Biological Challenges

Modeling the behavior of different types of integrins is one area that is open for exploration. Only four of the models mentioned here (namely; (Bazzazi *et al.*, 2018; Bidone, Skeeters, *et al.*, 2019; Cheng *et al.*, 2020; Hudson *et al.*, 2017)) account for the integrin subtype-specific ligand binding or clustering properties. However, a deeper understanding of differences between integrin subtypes will be helpful in understanding their distinct roles at the cell-ECM interface and therefore cell type-specific integrin expression (Barczyk *et al.*, 2009). Related to this, the competition of multiple ligands with affinity for binding to the same integrin type (Figure 2.2) represents an important model extension as it allows to understand the reasons of various ECM compositions per tissue and to reverse engineer synthetic matrices (see also below) (Gjorevski *et al.*, 2016). Another area of exploration that is biologically relevant is the crosstalk between other cell surface receptors and integrins. For example, it is known that integrins play a central role in activation of TGF-β in ECM, but the interactions between the TGF-β receptors (an RTK) and integrins have not been fully understood (Margadant & Sonnenberg, 2010; Worthington *et al.*, 2011). Another example of integrin crosstalk is with syndecan receptors. Syndecans are transmembrane proteins which often serve as coreceptors, for example by recruiting ligands for other receptors (Couchman, 2003). Especially crosstalk between syndecan-4 and integrins is shown to enhance interactions between the ECM and cytoskeleton (Elfenbein & Simons, 2013). Computational modeling could help unravel the underlying mechanism of action in this crosstalk.

In terms of extending the biological scope of the models, one major challenge in modeling integrin subtypes is in obtaining accurate quantitative measures (i.e., the parameters for the model) on each subtype. It is generally difficult to isolate and quantify transmembrane proteins intact and in desired conformations and integrins are not an exception (Y. Chen *et al.*, 2009; Hynes, 2004). Therefore, for ODE models that require absolute concentration of inactive and/or active integrins on the cell membrane (e.g., Equations 2.3-2.5), the limiting step is obtaining these dynamic quantitative measures. To tackle this challenge, experimental scientists apply indirect ways of measuring the density of integrins on the cell membrane. For instance a good example is by Elosegui-Artola et al. 2014, where they measure the fluorescence intensity of cells when they are bound to rhodamine-labeled fibronectin via integrins on the cell surface. The fluorescence level is then converted into concentration, using the level of emitted fluorescence by known concentra-

tions of fibronectin for their experiment. Another challenge, especially on the way to increase the specificity of the computational models in terms of integrin–ligand pairs, is measuring integrin–ligand binding/unbinding rates. This usually requires sophisticated techniques like surface plasmon resonance (SPR) ((Elosegui-Artola *et al.*, 2014; Kim *et al.*, 2005; Yan *et al.*, 2001) or single molecule dynamic force spectroscopy (Taubenberger *et al.*, 2007). These techniques are not available to all molecular biology labs and require operational expertise as well as very technical equipment. There is an evident need of collaboration between computational and experimental scientists to unravel the unknowns of integrin function.

We propose for the case of computational models of integrin function, experimental biomaterial design is a field where the complementary model–experiment cycle can be established and maintained. In particular, by using modular, synthetic materials, the influence of distinct microenvironment components (e.g., mechanical information, (fractions) of ligand types and ligand concentration) on integrin binding can be assessed individually (Gjorevski *et al.*, 2014). Also, these precisely-defined, tunable materials allow for the measuring of binding strength of specific integrin–ligand pairs by SPR, since the ligands could be isolated and exactly controlled in concentration. Synthetic supramolecular assemblies have great promise for this, because their monomeric building blocks could be functionalized with bioactive cues to easily introduce function using a modular approach (Dankers *et al.*, 2011; Mollet *et al.*, 2014). Noteworthy, the type of supramolecular base material that is used to present the integrin-binding supramolecular additives (i.e., RGD or cyclic (c)RGD conjugated to the corresponding supramolecular motif) affects cell adhesion properties; a bisurea (BU)-based material presents the additives more effectively over a ureido-pyrimidinone (UPy)-system (van Gaal *et al.*, 2019). Also the ligand concentration influences integrin-binding properties, as an increasing concentration of accessible cRGD leads to more FA formation with a decreased size. Furthermore, ligand type effects integrin targeting, since different ligands contain different binding affinities for certain integrin dimers (Kato & Mrksich, 2004); it was shown that substrates containing the higher affinity ligand cRGD led to a two times higher cell attachment rate and had twice the number of FAs than the cells cultured on substrates with its linear equivalent. Another example of modular, integrin-targeting materials is synthetic peptide amphiphiles (PAs) as pioneered by the research group of Stupp. Here they for example employed bioactive PAs bearing the fibronectin-derived RGDS-motif as scaffold for stem cell delivery (Webber *et al.*, 2010). Next to this, Mardilovich et al. designed PAs decorated with fibronectin-derived

integrin-binding motifs GRGDS and its synergistic PHSRN sequence in a spatially controlled manner that matched the natural distance found in fibronectin (Mardilovich *et al*., 2006). They observed similar cell behavior for the synthetic PAs as for the natural fibronectin, and even stronger FA formation and reorganization of the cytoskeleton was found for the PAs. This highlights the importance of using integrin-binding materials with matching spatial organization to its natural counterpart for effective integrin binding. On this note, another class of supramolecular biomaterials in which the spatial organization of integrin-binding motifs can be controlled precisely is DNA origami, owing to its robustness and programmability (Seeman, 2010). To illustrate, Huang et al. designed and synthesized a multi-ligand functionalized, nanoscale particle containing spatially controlled integrin $\alpha V\beta 6$-binding motif (A20FMDV2), and epidermal growth factor (EGF), a protein that binds the epidermal growth factor receptor (EGFR) which is a tyrosine kinase that cooperates closely with integrins (D. Huang *et al*., 2019). They showed that a ligand spacing of 60 nm and the presence of 3 peptides, so 3 integrins, led to maximum cell attachment. Altogether, these examples illustrate the suitability of tunable, modular biomaterials to isolate and judge the effects of distinct microenvironment elements (e.g., ligand concentration and type as well as spatial organization of ligands) on integrin-binding.

In summary, to push forward the field of integrin biology, we invite the field of biomaterial design and *in silico* modeling to come together and think about relevant biological questions and hypotheses to unravel in an iterative loop of simulation and experimental validation (Voit *et al*., 2008). On one hand, *in silico* models could help in predicting the performance of biomaterials which are suitable in steering a desired cellular outcome. In this way, not the full library of materials is required to be synthesized and assessed, but only a relevant range, thereby minimizing research time, effort and costs. While on the other hand, it is the experimental side that could complement *in silico* integrin models, by both providing input values (e.g., binding rates between ligand–integrin receptor) for the computational integrin models and by serving as validation for the model outcomes. In this way, the experimental and computational worlds on integrins should come to a closed cycle that complete one another.

2.5.2 Overcoming Computational Challenges

Finally, we turn to our perspective towards what lies ahead for the computational field. In particular, there are three areas where we stand to make

significant progress. Firstly, to fully understand and help unravel the biology of integrin function, it is essential, in our opinion, to computationally integrate all three layers of action spatially and temporally. In the current computational models, we obtain separate snapshots of events happening at the three distinct spatial layers. However, to be able to simulate and predict all the mechanical interactions and chemical reactions happening, starting with the binding of integrins to the ECM ligands up to the cell's behavioral reaction (e.g., proliferation, differentiation, apoptosis etc.), we will need computational models that combine the mechanochemical integrin actions at the three spatial levels. Modeling the biochemical processes and the mechanical responses of the cytoskeleton as well as the complex mechanochemical feedbacks that emerge from integrin signaling is challenging due to, amongst others, the following technical challenges:

1. The biochemical reactions occurring downstream of the integrin receptors are fundamentally stochastic in nature (e.g., small copy numbers), resulting in local gradients and heterogeneities. Although various algorithms exist for stochastic simulations (Simoni *et al.*, 2019; Székely & Burrage, 2014), they become computationally intractable for large chemical reaction networks with many species;

2. Eukaryotic cells consist of three main kinds of cytoskeletal filaments: microfilaments (actin, 7 nm diameter), microtubules (tubulin, 25 nm diameter) and intermediate filaments (various proteins, 12 nm diameter). Ideally, one would like to represent the exact filamentary network, meaning that all three types of individual fibrils must be discretized at sufficient resolution to resolve the biochemical reactions with the cytoskeleton as well as calculate an accurate mechanical force field (which in turn results in remodeling of the cytoskeletal network);

3. The interesting mechanical and biochemical phenomena take place at the nanometer scale whereas the emergent behavior occurs at the micrometer scale. As such, there is a need to scale-up the simulations in a computational efficient way while retaining the required spatial resolution;

4. Integrin–ligand binding occurs within seconds whereas adhesion maturation requires minutes. Downstream events in the cytosol, from signaling and actin cytoskeleton reorganization to cellular differentiation, can take hours to days to weeks. Similarly to the spatial scale, systems with

> reactions that operate at very different time scales require advanced numerical methods since otherwise every single fast reaction would need to be simulated, requiring a huge computational effort (B. Chen *et al.*, 2015).

Much progress has been made, including optimized numerical algorithms to efficiently solve sparse reaction-diffusion networks (Cao *et al.*, 2004; Gibson & Bruck, 2000), software packages to simulate active cytoskeleton network dynamics (Popov *et al.*, 2016) and advanced hybrid and multiscale techniques to couple various spatial and temporal scales (Herajy *et al.*, 2017; Smith & Yates, 2018). The idea behind the hybrid and multiscale techniques is to partition the system into different spatial or temporal scales and then apply different simulation methods that better fit the scales (e.g., stochastic at the intracellular level, deterministic reaction-diffusion at the tissue level). However, as the partitioning and linking (after the simulation step) introduces errors, it is necessary to develop advanced methods that allow linking different scales in an accurate manner.

Secondly, we are in the age of parallel computing with advanced (parallelized) numerical methods to fully leverage this power. Parallelized calculations can be done on a multicore desktop computer, on high-performance clusters or using cloud computing services. The new hardware developments, including advanced graphical processing units (GPUs) are rapidly increasing the computational power. At the same time, many software plugins are becoming available for Matlab (Klingbeil *et al.*, 2011), Python (Choi *et al.*, 2018), etc. to exploit the power of graphical processing units (GPUs), greatly reducing the computational time.

Thirdly, due to the nature of computational studies — written in a computer-readable coding language — it is possible to easily extend existing *in silico* models or to combine elements of different models to create a new model with larger spatial and temporal scope. However as in experimental studies, for a computational model to be revisited and potentially extended by other scientists than the original authors, the model should be reproducible. There exist many exciting initiatives such as model software repositories (e.g., VCell DB [https://vcell.org/], BioModels [https://ebi.ac.uk/biomodels/], CellML repository [https://cellml.org/]) and collaborations between publishers and the Center for Reproducible Biomedical Modeling [https://reproduciblebiomodels.org/] to check, increase and maintain reproducibility at the peer–review stage in publication process (Papin *et al.*, 2020).

All in all, we believe such practices will help the computational biology field to become more accessible and that through *in silico-in vitro* collaboration we will gain a great amount of fundamental knowledge on integrin biology.

References

Almouemen, N., Kelly, H. M., & O'Leary, C. (2019). Tissue Engineering: Understanding the Role of Biomaterials and Biophysical Forces on Cell Functionality Through Computational and Structural Biotechnology Analytical Methods. *Computational and Structural Biotechnology Journal*, *17*, 591–598. https://doi.org/10.1016/j.csbj.2019.04.008

Arnold, M., Cavalcanti-Adam, E. A., Glass, R., Blümmel, J., Eck, W., Kantlehner, M., Kessler, H., & Spatz, J. P. (2004). Activation of Integrin Function by Nanopatterned Adhesive Interfaces. *ChemPhysChem*, *5*(3), 383–388. https://doi.org/10.1002/cphc.200301014

Barczyk, M., Carracedo, S., & Gullberg, D. (2009). Integrins. *Cell and Tissue Research*, *339*(1), 269. https://doi.org/10.1007/s00441-009-0834-6

Bauer, A. L., Jackson, T. L., Jiang, Y., & Rohlf, T. (2010). Receptor cross-talk in angiogenesis: Mapping environmental cues to cell phenotype using a stochastic, Boolean signaling network model. *Journal of Theoretical Biology*, *264*(3), 838–846. https://doi.org/10.1016/j.jtbi.2010.03.025

Bazzazi, H., Zhang, Y., Jafarnejad, M., & Popel, A. S. (2018). Computational modeling of synergistic interaction between V3 integrin and VEGFR2 in endothelial cells: Implications for the mechanism of action of angiogenesis-modulating integrin-binding peptides. *Journal of Theoretical Biology*, *455*, 212–221. https://doi.org/10.1016/j.jtbi.2018.06.029

Berkovich, R., Wolfenson, H., Eisenberg, S., Ehrlich, M., Weiss, M., Klafter, J., Henis, Y. I., & Urbakh, M. (2011). Accurate Quantification of Diffusion and Binding Kinetics of Non-integral Membrane Proteins by FRAP. *Traffic*, *12*(11), 1648–1657. https://doi.org/10.1111/j.1600-0854.2011.01264.x

Bidone, T. C., Polley, A., Jin, J., Driscoll, T., Iwamoto, D. V., Calderwood, D. A., Schwartz, M. A., & Voth, G. A. (2019). Coarse-Grained Simulation of Full-Length Integrin Activation. *Biophysical Journal*, *116*(6), 1000–1010. https://doi.org/10.1016/j.bpj.2019.02.011

Bidone, T. C., Skeeters, A. V., Oakes, P. W., & Voth, G. A. (2019). Multiscale model of integrin adhesion assembly. *PLOS Computational Biology*, *15*(6), e1007077. https://doi.org/10.1371/JOURNAL.PCBI.1007077

Blucher, A., Salas, M., Williams, N., & Callender, H. (2014). Mathematical modeling of integrin dynamics in initial formation of focal adhesions. *Involve, a Journal of Mathematics*, *7*(4), 509–527. https://doi.org/10.2140/involve.2014.7.509

Bouaouina, M., Harburger, D. S., & Calderwood, D. A. (2012). Talin and Signaling Through Integrins. In M. Shimaoka (Ed.), *Integrin and Cell Adhesion Molecules: Methods and Protocols* (pp. 325–347). Humana Press. https://doi.org/10.1007/978-1-61779-166-6_20

Brodland, G. W. (2015). How computational models can help unlock biological systems. *Seminars in Cell & Developmental Biology*, *47-48*, 62–73. https://doi.org/10.1016/j.semcdb.2015.07.001

Butcher, D. T., Alliston, T., & Weaver, V. M. (2009). A tense situation: Forcing tumour progression. *Nature Reviews Cancer*, *9*(2), 108–122. https://doi.org/10.1038/nrc2544

Cao, Y., Li, H., & Petzold, L. (2004). Efficient formulation of the stochastic simulation algorithm for chemically reacting systems. *The Journal of Chemical Physics*, *121*(9), 4059–4067. https://doi.org/10.1063/1.1778376

Chan, C. E., & Odde, D. J. (2008). Traction dynamics of filopodia on compliant substrates. *Science (New York, N.Y.)*, *322*(5908), 1687–1691. https://doi.org/10.1126/SCIENCE.1163595

Chen, B., Ji, B., & Gao, H. (2015). Modeling Active Mechanosensing in Cell-Matrix Interactions. *Annual Review of Biophysics*, *44*(1), 1–32. https://doi.org/10.1146/annurev-biophys-051013-023102

Chen, W., Lou, J., Hsin, J., Schulten, K., Harvey, S. C., & Zhu, C. (2011). Molecular Dynamics Simulations of Forced Unbending of Integrin

αVβ3. *PLOS Computational Biology*, *7*(2), e1001086. https://doi.org/10.1371/journal.pcbi.1001086

Chen, Y., Munteanu, A. C., Huang, Y.-F., Phillips, J., Zhu, Z., Mavros, M., & Tan, W. (2009). Mapping Receptor Density on Live Cells by Using Fluorescence Correlation Spectroscopy. *Chemistry – A European Journal*, *15*(21), 5327–5336. https://doi.org/10.1002/chem.200802305

Cheng, B., Lin, M., Huang, G., Li, Y., Ji, B., Genin, G. M., Deshpande, V. S., Lu, T. J., & Xu, F. (2017). Cellular mechanosensing of the biophysical microenvironment: A review of mathematical models of biophysical regulation of cell responses. *Physics of Life Reviews*, *22-23*, 88–119. https://doi.org/10.1016/j.plrev.2017.06.016

Cheng, B., Wan, W., Huang, G., Li, Y., Genin, G. M., Mofrad, M. R. K., Lu, T. J., Xu, F., & Lin, M. (2020). Nanoscale integrin cluster dynamics controls cellular mechanosensing via FAKY397 phosphorylation. *Science Advances*, *6*(10). https://doi.org/10.1126/SCIADV.AAX1909

Choi, K., Medley, J. K., König, M., Stocking, K., Smith, L., Gu, S., & Sauro, H. M. (2018). Tellurium: An extensible python-based modeling environment for systems and synthetic biology. *BioSystems*, *171*, 74–79. https://doi.org/10.1016/j.biosystems.2018.07.006

Cirit, M., Krajcovic, M., Choi, C. K., Welf, E. S., Horwitz, A. F., & Haugh, J. M. (2010). Stochastic Model of Integrin-Mediated Signaling and Adhesion Dynamics at the Leading Edges of Migrating Cells. *PLOS Computational Biology*, *6*(2), e1000688. https://doi.org/10.1371/JOURNAL.PCBI.1000688

Corcoran, A., & Del Maestro, R. F. (2003). Testing the “go or grow” hypothesis in human medulloblastoma cell lines in two and three dimensions. *53*(1), 174–185.

Couchman, J. R. (2003). Syndecans: Proteoglycan regulators of cell-surface microdomains? *Nature Reviews Molecular Cell Biology*, *4*(12), 926–938. https://doi.org/10.1038/nrm1257

Cox, T. R., & Erler, J. T. (2011). Remodeling and homeostasis of the extracellular matrix: Implications for fibrotic diseases and cancer. *Disease Models & Mechanisms*, *4*(2), 165–178. https://doi.org/10.1242/dmm.004077

Critchley, D. R., & Gingras, A. R. (2008). Talin at a glance. *Journal of Cell Science*, *121*(9), 1345–1347. https://doi.org/10.1242/jcs.018085

Dankers, P. Y. W., Boomker, J. M., Huizinga-van der Vlag, A., Wisse, E., Appel, W. P. J., Smedts, F. M. M., Harmsen, M. C., Bosman, A. W., Meijer, W., & van Luyn, M. J. A. (2011). Bioengineering of living renal membranes consisting of hierarchical, bioactive supramolecular meshes and human tubular cells. *Biomaterials*, *32*(3), 723–733. https://doi.org/10.1016/j.biomaterials.2010.09.020

Elfenbein, A., & Simons, M. (2013). Syndecan-4 signaling at a glance. *Journal of Cell Science*, *126*(17), 3799–3804. https://doi.org/10.1242/jcs.124636

Eliceiri, B. P. (2001). Integrin and Growth Factor Receptor Crosstalk. *Circulation Research*, *89*(12), 1104–1110. https://doi.org/10.1161/hh2401.101084

Elosegui-Artola, A., Bazellières, E., Allen, M. D., Andreu, I., Oria, R., Sunyer, R., Gomm, J. J., Marshall, J. F., Jones, J. L., Trepat, X., & Roca-Cusachs, P. (2014). Rigidity sensing and adaptation through regulation of integrin types. *Nature materials*, *13*(6), 631. https://doi.org/10.1038/NMAT3960

Elosegui-Artola, A., Trepat, X., & Roca-Cusachs, P. (2018). Control of Mechanotransduction by Molecular Clutch Dynamics. *Trends in Cell Biology*, *28*(5), 356–367. https://doi.org/10.1016/J.TCB.2018.01.008

Escribano, J., Sánchez, M. T., & García-Aznar, J. M. (2014). A discrete approach for modeling cell–matrix adhesions. *Computational Particle Mechanics*, *1*(2), 117–130. https://doi.org/10.1007/s40571-014-0006-7

Eyckmans, J., Boudou, T., Yu, X., & Chen, C. S. (2011). A Hitchhiker's Guide to Mechanobiology. *Developmental Cell*, *21*(1), 35–47. https://doi.org/10.1016/j.devcel.2011.06.015

Gao, C.-F., Xie, Q., Su, Y.-L., Koeman, J., Khoo, S. K., Gustafson, M., Knudsen, B. S., Hay, R., Shinomiya, N., & Woude, G. F. V. (2005). Proliferation and invasion: Plasticity in tumor cells. *Proceedings of the National Academy of Sciences*, *102*(30), 10528–10533. https://doi.org/10.1073/pnas.0504367102

Gibson, M. A., & Bruck, J. (2000). Efficient Exact Stochastic Simulation of Chemical Systems with Many Species and Many Channels.

The Journal of Physical Chemistry A, *104*(9), 1876–1889. https://doi.org/10.1021/jp993732q

Giese, A., Loo, M. A., Tran, N., Haskett, D., Coons, S. W., & Berens, M. E. (1996). Dichotomy of astrocytoma migration and proliferation. *International Journal of Cancer*, *67*(2), 275–282. https://doi.org/10.1002/(SICI)1097-0215(19960717)67:2⟨275::AID-IJC20⟩3.0.CO;2-9

Gjorevski, N., Sachs, N., Manfrin, A., Giger, S., Bragina, M. E., Ordóñez-Morán, P., Clevers, H., & Lutolf, M. P. (2016). Designer matrices for intestinal stem cell and organoid culture. *Nature*, *539*(7630), 560–564. https://doi.org/10.1038/nature20168

Gjorevski, N., Ranga, A., & Lutolf, M. P. (2014). Bioengineering approaches to guide stem cell-based organogenesis. *Development*, *141*(9), 1794–1804. https://doi.org/10.1242/dev.101048

Grada, A., Otero-Vinas, M., Prieto-Castrillo, F., Obagi, Z., & Falanga, V. (2017). Research Techniques Made Simple: Analysis of Collective Cell Migration Using the Wound Healing Assay. *Journal of Investigative Dermatology*, *137*(2), e11–e16. https://doi.org/10.1016/j.jid.2016.11.020

Handorf, A. M., Zhou, Y., Halanski, M. A., & Li, W. J. (2015). Tissue stiffness dictates development, homeostasis, and disease progression. *Organogenesis*, *11*(1), 1–15. https://doi.org/10.1080/15476278.2015.1019687

Harburger, D. S., & Calderwood, D. A. (2009). Integrin signalling at a glance. *Journal of Cell Science*, *122*(2), 159–163. https://doi.org/10.1242/jcs.018093

Hatzikirou, H., Basanta, D., Simon, M., Schaller, K., & Deutsch, A. (2012). 'Go or Grow': The key to the emergence of invasion in tumour progression? *Mathematical Medicine and Biology: A Journal of the IMA*, *29*(1), 49–65. https://doi.org/10.1093/imammb/dqq011

Herajy, M., Liu, F., Rohr, C., & Heiner, M. (2017). Snoopy's hybrid simulator: A tool to construct and simulate hybrid biological models. *BMC Systems Biology*, *11*(1), 71. https://doi.org/10.1186/s12918-017-0449-6

Holmes, W. R., & Edelstein-Keshet, L. (2012). A Comparison of Computational Models for Eukaryotic Cell Shape and Motility. *PLOS Computational Biology*, *8*(12), e1002793. https://doi.org/10.1371/journal.pcbi.1002793

Horton, E. R., Byron, A., Askari, J. A., Ng, D. H. J., Millon-Frémillon, A., Robertson, J., Koper, E. J., Paul, N. R., Warwood, S., Knight, D., Humphries, J. D., & Humphries, M. J. (2015). Definition of a consensus integrin adhesome and its dynamics during adhesion complex assembly and disassembly. *Nature Cell Biology 2015 17:12*, *17*(12), 1577–1587. https://doi.org/10.1038/ncb3257

Horton, E. R., Humphries, J. D., James, J., Jones, M. C., Askari, J. A., & Humphries, M. J. (2016). The integrin adhesome network at a glance. *Journal of Cell Science*, *129*(22), 4159–4163. https://doi.org/10.1242/jcs.192054

Huang, D., Patel, K., Perez-Garrido, S., Marshall, J. F., & Palma, M. (2019). DNA Origami Nanoarrays for Multivalent Investigations of Cancer Cell Spreading with Nanoscale Spatial Resolution and Single-Molecule Control. *ACS Nano*, *13*(1), 728–736. https://doi.org/10.1021/acsnano.8b08010

Huang, J., Peng, X., Xiong, C., & Fang, J. (2012). Influence of substrate rigidity on primary nucleation of cell adhesion: A thermal fluctuation model. *Journal of Colloid and Interface Science*, *366*(1), 200–208. https://doi.org/10.1016/j.jcis.2011.09.046

Hudson, V. S., Dolin, C. E., Poole, L. G., Massey, V. L., Wilkey, D., Beier, J. I., Merchant, M. L., Frieboes, H. B., & Arteel, G. E. (2017). Modeling the Kinetics of Integrin Receptor Binding to Hepatic Extracellular Matrix Proteins. *Scientific Reports*, *7*(1), 1–13. https://doi.org/10.1038/s41598-017-12691-y

Humphries, J. D., Byron, A., & Humphries, M. J. (2006). Integrin ligands at a glance. *Journal of Cell Science*, *119*(19), 3901–3903. https://doi.org/10.1242/jcs.03098

Huttenlocher, A., & Horwitz, A. R. (2011). Integrins in Cell Migration. *Cold Spring Harbor Perspectives in Biology*, *3*(9), a005074. https://doi.org/10.1101/cshperspect.a005074

Hynes, R. O. (1987). Integrins: A family of cell surface receptors. *Cell*, *48*(4), 549–554. https://doi.org/10.1016/0092-8674(87)90233-9

Hynes, R. O. (2002). Integrins: Bidirectional, Allosteric Signaling Machines. *Cell*, *110*(6), 673–687. https://doi.org/10.1016/S0092-8674(02)00971-6

Hynes, R. O. (2004). The emergence of integrins: A personal and historical perspective.

Matrix Biology, *23*(6), 333–340.
https://doi.org/10.1016/j.matbio.2004.08.001
Hynes, R. O., & Zhao, Q. (2000). The Evolution of Cell Adhesion.
Journal of Cell Biology, *150*(2), F89–F96.
https://doi.org/10.1083/JCB.150.2.F89
Jamali, Y., Jamali, T., & Mofrad, M. R. (2013).
An agent based model of integrin clustering: Exploring the role of ligand clustering, integrin homo-oligomerization, integrin-ligand affinity, membrane crowdedness and ligand mobility.
Journal of Computational Physics, *244*, 264–278.
https://doi.org/10.1016/j.jcp.2012.09.010
Johnston, I. (2012). The chaos within: Exploring noise in cellular biology.
Significance, *9*(4), 17–21.
https://doi.org/10.1111/j.1740-9713.2012.00586.x
Karimi, F., O'Connor, A. J., Qiao, G. G., & Heath, D. E. (2018).
Integrin Clustering Matters: A Review of Biomaterials Functionalized with Multivalent Integrin-Binding Ligands to Improve Cell Adhesion, Migration, Differentiation, Angiogenesis, and Biomedical Device Integration.
Advanced Healthcare Materials, *7*(12), 1701324.
https://doi.org/10.1002/adhm.201701324
Kato, M., & Mrksich, M. (2004).
Using Model Substrates To Study the Dependence of Focal Adhesion Formation on the Affinity of IntegrinLigand Complexes.
Biochemistry, *43*(10), 2699–2707. https://doi.org/10.1021/bi0352670
Kim, J. K., Xu, Y., Xu, X., Keene, D. R., Gurusiddappa, S., Liang, X., Wary, K. K., & Höök, M. (2005). A novel binding site in collagen type III for integrins alpha 1 beta 1 and alpha 2 beta 1.
Journal of Biological Chemistry, *280*(37), 32512–32520.
https://doi.org/10.1074/jbc.M502431200
Klingbeil, G., Erban, R., Giles, M., & Maini, P. K. (2011).
STOCHSIMGPU: Parallel stochastic simulation for the Systems Biology Toolbox 2 for MATLAB. *Bioinformatics*, *27*(8), 1170–1171.
https://doi.org/10.1093/bioinformatics/btr068
Lavelin, I., Wolfenson, H., Patla, I., Henis, Y. I., Medalia, O., Volberg, T., Livne, A., Kam, Z., & Geiger, B. (2013).
Differential Effect of Actomyosin Relaxation on the Dynamic Properties of Focal Adhesion Proteins. *PLOS ONE*, *8*(9), e73549.
https://doi.org/10.1371/JOURNAL.PONE.0073549

Lee, C.-K., Wang, Y.-M., Huang, L.-S., & Lin, S. (2007). Atomic force microscopy: Determination of unbinding force, off rate and energy barrier for protein–ligand interaction. *Micron*, *38*(5), 446–461. https://doi.org/10.1016/j.micron.2006.06.014

Li, J., Su, Y., Xia, W., Qin, Y., Humphries, M. J., Vestweber, D., Cabañas, C., Lu, C., & Springer, T. A. (2017). Conformational equilibria and intrinsic affinities define integrin activation. *The EMBO Journal*, *36*(5), 629–645. https://doi.org/10.15252/embj.201695803

Macdonald, A., Horwitz, A. R., & Lauffenburger, D. A. (2008). Kinetic model for lamellipodal actin-integrin 'clutch' dynamics. *Cell adhesion & migration*, *2*(2), 95–105. https://doi.org/10.4161/CAM.2.2.6210

Mahabeleshwar, G. H., Feng, W., Reddy, K., Plow, E. F., & Byzova, T. V. (2007). Mechanisms of Integrin–Vascular Endothelial Growth Factor Receptor Cross-Activation in Angiogenesis. *Circulation Research*, *101*(6), 570–580. https://doi.org/10.1161/CIRCRESAHA.107.155655

Mardilovich, A., Craig, J. A., McCammon, M. Q., Garg, A., & Kokkoli, E. (2006). Design of a Novel Fibronectin-Mimetic PeptideAmphiphile for Functionalized Biomaterials. *Langmuir*, *22*(7), 3259–3264. https://doi.org/10.1021/la052756n

Margadant, C., & Sonnenberg, A. (2010). Integrin–TGF-β crosstalk in fibrosis, cancer and wound healing. *EMBO reports*, *11*(2), 97–105. https://doi.org/10.1038/embor.2009.276

Massey, V. L., Dolin, C. E., Poole, L. G., Hudson, S. V., Siow, D. L., Brock, G. N., Merchant, M. L., Wilkey, D. W., & Arteel, G. E. (2017). The hepatic "matrisome" responds dynamically to injury: Characterization of transitional changes to the extracellular matrix in mice. *Hepatology*, *65*(3), 969–982. https://doi.org/10.1002/hep.28918

Miller, A. E., Hu, P., & Barker, T. H. (2020). Feeling Things Out: Bidirectional Signaling of the Cell–ECM Interface, Implications in the Mechanobiology of Cell Spreading, Migration, Proliferation, and Differentiation. *Advanced Healthcare Materials*, *9*(8), 1901445. https://doi.org/10.1002/ADHM.201901445

Mollet, B. B., Comellas-Aragonès, M., Spiering, A. J. H., Söntjens, S. H. M., Meijer, E. W., & Dankers, P. Y. W. (2014). A modular approach to easily processable supramolecular bilayered

scaffolds with tailorable properties.
Journal of Materials Chemistry B, *2*(17), 2483–2493.
https://doi.org/10.1039/C3TB21516D

O'Brien, K. T., Golla, K., Kranjc, T., O'Donovan, D., Allen, S., Maguire, P., Simpson, J. C., O'Connell, D., Moran, N., & Shields, D. C. (2019). Computational and experimental analysis of bioactive peptide linear motifs in the integrin adhesome. *PLOS ONE*, *14*(1), e0210337. https://doi.org/10.1371/journal.pone.0210337

Oria, R., Wiegand, T., Escribano, J., Elosegui-Artola, A., Uriarte, J. J., Moreno-Pulido, C., Platzman, I., Delcanale, P., Albertazzi, L., Navajas, D., Trepat, X., García-Aznar, J. M., Cavalcanti-Adam, E. A., & Roca-Cusachs, P. (2017).
Force loading explains spatial sensing of ligands by cells.
Nature 2017 552:7684, *552*(7684), 219–224.
https://doi.org/10.1038/nature24662

Papin, J. A., Gabhann, F. M., Sauro, H. M., Nickerson, D., & Rampadarath, A. (2020).
Improving reproducibility in computational biology research.
PLOS Computational Biology, *16*(5), e1007881.
https://doi.org/10.1371/journal.pcbi.1007881

Poole, W., Pandey, A., Shur, A., Tuza, Z. A., & Murray, R. M. (2022).
BioCRNpyler: Compiling chemical reaction networks from biomolecular parts in diverse contexts.
PLOS Computational Biology, *18*(4), e1009987.
https://doi.org/10.1371/journal.pcbi.1009987

Popov, K., Komianos, J., & Papoian, G. A. (2016).
MEDYAN: Mechanochemical Simulations of Contraction and Polarity Alignment in Actomyosin Networks.
PLOS Computational Biology, *12*(4), e1004877.
https://doi.org/10.1371/journal.pcbi.1004877

Porter, J. C., & Hogg, N. (1998). Integrins take partners: Cross-talk between integrins and other membrane receptors. *Trends in Cell Biology*, *8*(10), 390–396. https://doi.org/10.1016/S0962-8924(98)01344-0

Scholma, J., Schivo, S., Urquidi Camacho, R. A., van de Pol, J., Karperien, M., & Post, J. N. (2014). Biological networks 101: Computational modeling for molecular biologists. *Gene*, *533*(1), 379–384.
https://doi.org/10.1016/j.gene.2013.10.010

Schwarz, U. S., & Gardel, M. L. (2012).
United we stand – integrating the actin cytoskeleton and cell–matrix adhesions in cellular mechanotransduction.

Journal of Cell Science, *125*(13), 3051–3060.
https://doi.org/10.1242/jcs.093716
Seeman, N. C. (2010). Nanomaterials Based on DNA.
Annual Review of Biochemistry, *79*(1), 65–87.
https://doi.org/10.1146/annurev-biochem-060308-102244
Shuaib, A., Motan, D., Bhattacharya, P., McNabb, A., Skerry, T. M., & Lacroix, D. (2019).
Heterogeneity in The Mechanical Properties of Integrins Determines Mechanotransduction Dynamics in Bone Osteoblasts.
Scientific Reports, *9*(1), 13113.
https://doi.org/10.1038/s41598-019-47958-z
Simoni, G., Reali, F., Priami, C., & Marchetti, L. (2019).
Stochastic simulation algorithms for computational systems biology: Exact, approximate, and hybrid methods.
WIREs Systems Biology and Medicine, *11*(6), e1459.
https://doi.org/10.1002/wsbm.1459
Smith, C. A., & Yates, C. A. (2018).
Spatially extended hybrid methods: A review.
Journal of The Royal Society Interface, *15*(139), 20170931.
https://doi.org/10.1098/rsif.2017.0931
Starruß, J., de Back, W., Brusch, L., & Deutsch, A. (2014).
Morpheus: A user-friendly modeling environment for multiscale and multicellular systems biology. *Bioinformatics*, *30*(9), 1331–1332.
https://doi.org/10.1093/bioinformatics/btt772
Sun, Z., Guo, S. S., & Fässler, R. (2016).
Integrin-mediated mechanotransduction.
Journal of Cell Biology, *215*(4), 445–456.
https://doi.org/10.1083/jcb.201609037
Székely, T., & Burrage, K. (2014). Stochastic simulation in systems biology.
Computational and Structural Biotechnology Journal, *12*(20), 14–25.
https://doi.org/10.1016/j.csbj.2014.10.003
Taubenberger, A., Cisneros, D. A., Friedrichs, J., Puech, P. H., Muller, D. J., & Franz, C. M. (2007).
Revealing early steps of alpha 2 beta 1 integrin-mediated adhesion to collagen type I by using single-cell force spectroscopy.
Molecular Biology of the Cell, *18*(5), 1634–1644.
https://doi.org/10.1091/mbc.E06-09-0777
van der Flier, A., & Sonnenberg, A. (2001).
Function and interactions of integrins.

Cell and Tissue Research, *305*(3), 285–298. https://doi.org/10.1007/s004410100417

van Gaal, R. C., Buskermolen, A. B. C., Ippel, B. D., Fransen, P.-P. K. H., Zaccaria, S., Bouten, C. V. C., & Dankers, P. Y. W. (2019). Functional peptide presentation on different hydrogen bonding biomaterials using supramolecular additives. *Biomaterials*, *224*, 119466. https://doi.org/10.1016/j.biomaterials.2019.119466

Vasilevich, A. S., Carlier, A., Boer, J. d., & Singh, S. (2017). How Not To Drown in Data: A Guide for Biomaterial Engineers. *Trends in Biotechnology*, *35*(8), 743–755. https://doi.org/10.1016/j.tibtech.2017.05.007

Voit, E. O., Qi, Z., & Miller, G. W. (2008). Steps of Modeling Complex Biological Systems. *Pharmacopsychiatry*, *41*(S 01), S78–S84. https://doi.org/10.1055/s-2008-1080911

Webber, M. J., Tongers, J., Renault, M.-A., Roncalli, J. G., Losordo, D. W., & Stupp, S. I. (2010). Development of bioactive peptide amphiphiles for therapeutic cell delivery. *Acta Biomaterialia*, *6*(1), 3–11. https://doi.org/10.1016/j.actbio.2009.07.031

Werner, M., Kurniawan, N. A., & Bouten, C. V. C. (2020). Cellular Geometry Sensing at Different Length Scales and its Implications for Scaffold Design. *Materials*, *13*(4), 963. https://doi.org/10.3390/ma13040963

Worthington, J. J., Klementowicz, J. E., & Travis, M. A. (2011). TGFβ: A sleeping giant awoken by integrins. *Trends in Biochemical Sciences*, *36*(1), 47–54. https://doi.org/10.1016/j.tibs.2010.08.002

Yan, B., Calderwood, D. A., Yaspan, B., & Ginsberg, M. H. (2001). Calpain Cleavage Promotes Talin Binding to the β3 Integrin Cytoplasmic Domain. *Journal of Biological Chemistry*, *276*(30), 28164–28170. https://doi.org/10.1074/jbc.M104161200

Ye, K., Wang, X., Cao, L., Li, S., Li, Z., Yu, L., & Ding, J. (2015). Matrix Stiffness and Nanoscale Spatial Organization of Cell-Adhesive Ligands Direct Stem Cell Fate. *Nano Letters*, *15*(7), 4720–4729. https://doi.org/10.1021/acs.nanolett.5b01619

Yu, J., Huang, J., Jansen, J. A., Xiong, C., & Walboomers, X. F. (2017). Mechanochemical mechanism of integrin clustering modulated by nanoscale ligand spacing and rigidity of extracellular substrates. *Journal of the Mechanical Behavior of Biomedical Materials*, *72*, 29–37. https://doi.org/10.1016/j.jmbbm.2017.04.018

Zaidel-Bar, R., Itzkovitz, S., Ma'ayan, A., Iyengar, R., & Geiger, B. (2007). Functional atlas of the integrin adhesome. *Nature Cell Biology*, *9*(8), 858–867. https://doi.org/10.1038/ncb0807-858

Zanetti, A., Lampugnani, M. G., Balconi, G., Breviario, F., Corada, M., Lanfrancone, L., & Dejana, E. (2002). Vascular Endothelial Growth Factor Induces Shc Association With Vascular Endothelial Cadherin. *Arteriosclerosis, Thrombosis, and Vascular Biology*, *22*(4), 617–622. https://doi.org/10.1161/01.ATV.0000012268.84961.AD

3

Win, Lose or Tie: Mathematical Modeling of Ligand Competition at the Cell–Extracellular Matrix Interface

This chapter has been **published** as: Karagöz, Z., Geuens, T., LaPointe, V. L. S., van Griensven, M., & Carlier, A. (2021). Win, Lose, or Tie: Mathematical Modeling of Ligand Competition at the Cell–Extracellular Matrix Interface. *Frontiers in Bioengineering and Biotechnology*, *9*. https://doi.org/10.3389/fbioe.2021.657244.

Abstract

Integrin transmembrane proteins conduct mechanotransduction at the cell–extracellular matrix interface. This process is central to cellular homeostasis and therefore is particularly important when designing instructive biomaterials and organoid culture systems. Previous studies suggest that fine-tuning the extracellular matrix composition and mechanical properties can improve organoid development. Towards the bigger goal of fully functional organoid development, we hypothesize that resolving the dynamics of extracellular matrix–integrin interactions will be highly instructive. To this end, we developed a mathematical model that enabled us to simulate three main interactions, namely integrin activation, ligand binding and integrin clustering. Different from previously published computational models, we account for the binding of more than one type of ligand to the integrin. This competition between ligands defines the fate of the system. We have demonstrated that an increase in the initial concentration of ligands does not ensure an increase in the steady state concentration of ligand-bound integrins. The ligand with higher binding rate occupies more integrins at the steady state than does the competing ligand. With cell type specific, quantitative input on integrin-ligand binding rates, this model can be used to develop instructive cell culture systems.

3.1 Introduction

The extracellular matrix (ECM) is a mesh of fibrous proteins that forms the basis of the tissue architecture and structurally supports the cells. The translation of biophysical cues provided by the ECM into biochemical signals by the cells is a process called mechanotransduction. For cells, mechanotransduction is central to maintaining homeostasis in many biological processes like proliferation, migration, differentiation and apoptosis (Miller *et al*., 2020). It is known, for example, that the composition and mechanical properties of the extracellular environment in which mesenchymal stem cells are grown influences whether they differentiate into adipocytes, osteoblasts or chondrocytes (Assis-Ribas *et al*., 2018). When mechanotransduction is disturbed, it results in aberrant cell behavior and thus impaired tissue function (Handorf *et al*., 2015).

Focal adhesions are multiprotein complexes where this mechanotransduction process is orchestrated. The main players in focal adhesions, responsible for physical interactions with the ECM, are integrins. Each integrin consists of non-covalently associated α and β subunits. To date, 24 unique integrins have been found in humans, which are combinations of 18 different α and eight different β subunits (Barczyk *et al*., 2010; Hynes, 2002). Each integrin heterodimer is able to recognize and bind to a defined set of ECM ligands via its ectodomain (Humphries *et al*., 2006; Hynes, 2002). Different ligand-bound integrins can further form clusters amongst each other via non-covalent links between α and β subunits. Approximately 50 integrins can cluster together (Changede *et al*., 2015). This way, integrins create physical anchor points between the extracellular space and the cytoskeleton and initiate the focal adhesion formation. Cytosolic ligands are recruited to cytoplasmic tails of integrin molecules, and mechanosensitive signaling is activated in the cell via the focal adhesions (Hynes, 2002).

Due to the broad range of cellular response activated via integrin-mediated signaling, integrins have been targets for tissue engineering applications. Recent developments in methods that make use of stem cells and targeted differentiation protocols, such as in organoid development, demonstrated the importance of a detailed understanding of mechanotransduction and particularly integrin–ECM interactions. So called “designer matrices” that are decorated with integrin-binding partners and that are adaptive in terms of their mechanical properties have been shown to enhance intestinal organoid culture survival and proliferation (Gjorevski *et al*., 2016). Similarly, by mimicking the physiological environment of early stages of embryonic development

in cell culture, the formation of human pluripotent stem cell–derived kidney organoids could be enhanced (Garreta *et al.*, 2019).

Maintaining the appropriate ECM composition is critical for kidney organoid development. For example, Geuens et al. reported an unwanted increase in specific ECM proteins when cell culture times were prolonged in an attempt to increase kidney organoid maturation (Geuens *et al.*, 2021). They performed a tandem mass spectrometry analysis to compare the ECM composition of kidney organoids that were cultured for 18 and 25 days. Older kidney organoid ECM was rich in collagens (specifically COL1A1, COL2A1 and COL6A1) and fibronectin, which are hallmarks of tissue fibrosis, compared to day 18 ECM. The analysis also showed an increase in αSMA — a myofibroblast marker — in older kidney organoids, that further indicated tissue fibrosis. Following this analysis, they encapsulated the kidney organoids in a soft hydrogel system, which prevented the unwanted ECM deposition, perhaps by better mimicking the natural environment in kidney development (Geuens *et al.*, 2021).

The effect of the abnormal accumulation of particular ECM proteins on cell phenotype is worth exploring for the future of organoid culture systems. The initial presence and the changes in the amounts of ECM proteins are sensed first by the integrins, the direct interaction partners of these proteins. Therefore, a detailed analysis and understanding of the effects of abnormal ligand deposition and ligand competition on integrin–ligand dynamics can help us understand the decision-making processes of the cells in response to the changes in ECM conditions (Garreta *et al.*, 2019; Geuens *et al.*, 2020; Miller *et al.*, 2020).

The high number of potential integrin–ligand pairs make it difficult to test and document the effects experimentally. Therefore, computational modeling provides a unique opportunity for exploring the integrin–ligand binding process and its subsequent effects. There exists a number of computational models that explain different processes in the integrin-related pathways. In particular, Hudson et al. studied the binding of fibronectin and von Willebrand Factor A (vWA) to integrin $\alpha v\beta 3$ as well as binding of collagen to $\alpha 1\beta 1$ using an ordinary differential equation (ODE) model; they reported an increase in ligand-bound integrin at the steady state when there is an increase in the concentration of ligands (Hudson *et al.*, 2017). However, they simulate the integrin–ligand binding exclusively for each ligand, which overlooks the fact that the ligands of the same integrin are in a competition to bind when

present at the same time.To fill this knowledge gap and identify potential patterns in integrin–ligand binding that occur due to the competition between multiple ligands for the same integrin, we developed an ODE model. Our model consists of three reaction levels: 1) integrin activation, 2) ligand binding and 3) ligand-bound integrin clustering (Figure 3.1). Using this model, we explore the changes in ligand-binding kinetics when the amount of ECM ligands changes over time, as in the case of kidney organoid cultures.

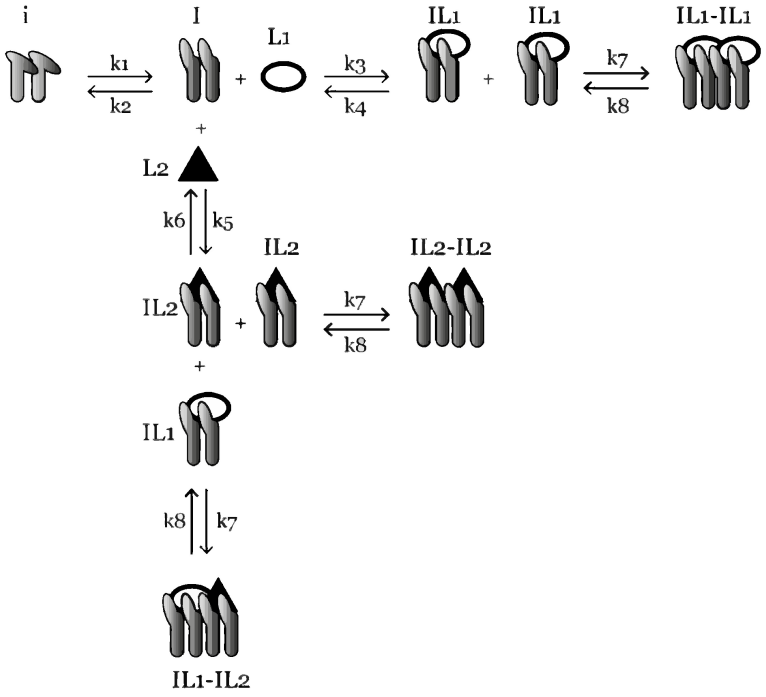

Figure 3.1: An overview of the ligand-competition model reactions. i is the inactive integrin, I is activated integrin, IL1 is L1-bound integrin, IL2 is L2-bound integrin, IL1-IL1 , IL2-IL2 and IL1-IL2 are three species of clustered integrins with different ligand compositions. k_1 – k_8 are reaction rate constants and their values are given in Table 3.1. Ordinary differential equations representing the reactions are given in the Methods section.

3.2 Methods

3.2.1 Ordinary Differential Equation Model

We used the Tellurium Python environment (Choi *et al.*, 2018) to generate and the libRoadRunner library (Somogyi *et al.*, 2015) to simulate the ligand competition model. The python code for the model and simulations as well as the SBML file for the model and the simulation results in csv format can be found in our GitHub repository (https://github.com/zeynepkaragoz/Ligand_competition_model) The mass-action kinetics scheme of the integrin–ligand competition model is given in Figure 3.1; here we present the differential equations for the model (Eqn. 3.1–3.9): where $[i]$ denotes the concentration of inactive integrins, $[I]$ is the concentration of active integrins, $[IL1]$ and $[IL2]$ are the concentrations of L1- and L2-bound integrins, respectively. $[C1]$, $[C2]$ and $[C3]$ are the concentrations of three distinct types of integrin clusters composed of IL1-IL1, IL2-IL2 and IL1-IL2, respectively. k_1-k_8 are the reaction rate constants of the reversible reactions in the model (Figure 3.1) and their values are given in Table 3.1.

$$\frac{d[i]}{dt} = -k_1[i] + k_2[I] \tag{3.1}$$

$$\frac{d[I]}{dt} = k_1[i] - k_2[I] - k_3[I][L1] + k_4[IL1] - k_5[I][L2] + k_6[IL2] \tag{3.2}$$

$$\frac{d[IL1]}{dt} = k_3[I][L1] - k_4[IL1] - 2(k_7[IL1]^2 - k_8[C1]) - k_7[IL1][IL2] + k_8[C3] \tag{3.3}$$

$$\frac{d[IL2]}{dt} = k_5[I][L2] - k_6[IL2] - 2(k_7[IL2]^2 - k_8[C2]) - k_7[IL1][IL2] + k_8[C3] \tag{3.4}$$

$$\frac{d[C1]}{dt} = k_7[IL1]^2 - k_8[C1] \tag{3.5}$$

$$\frac{d[C2]}{dt} = k_7[IL2]^2 - k_8[C2] \tag{3.6}$$

$$\frac{d[C3]}{dt} = k_7[IL1][IL2] - k_8[C3] \tag{3.7}$$

$$\frac{d[L1]}{dt} = -k_3[I][L1] + k_4[IL1] \tag{3.8}$$

$$\frac{d[L2]}{dt} = -k_5[I][L2] + k_6[IL2] \tag{3.9}$$

The inspiration for this model was a prior integrin–ligand binding model presented by Hudson *et al.*, 2017. However, their model included only one type of ligand available at a time for one integrin type. We have modified this model to account for the competition of multiple ligands binding to the same integrin. We have also added an integrin activation step, before the initiation of ligand binding. This was to accommodate the conformational change (from bent to extended) of the integrin ectodomain, required for the ligand binding site to become available (Li & Springer, 2017; Takagi & Springer, 2002; Zhu *et al.*, 2008). The rate of the activation step was calculated by (Yu *et al.*, 2017) using the energy required for the bent-to-extended conformation change (Huang *et al.*, 2012; Yu *et al.*, 2017). It should be noted that we do not make the distinction between the next two possible conformations (extended-closed and extended-open) after the ligand is bound to the integrin (Li & Springer, 2017; Zhu *et al.*, 2008), as the switch between these two states is highly related to the integrin cytoplasmic tails binding to cytoskeleton, which is out of the scope of this study. Since there are two types of ligand-bound integrins in our model (IL1 and IL2), we also make the distinction of three possible integrin clusters (C1, C2 and C3). However, we assumed the cluster association/dissociation rate constants (k_7 and k_8, respectively) for distinct cluster types are the same, simply because the molecules that are interacting, the integrins, are of the same type for each cluster.

We used the binding rate constants of fibronectin and vWA to integrin $\alpha\mathrm{v}\beta3$ as the L1 and L2 binding rate constants (Table 3.1). We chose to model integrin $\alpha\mathrm{v}\beta3$ because of its relevance in kidney fibrosis (Bülow & Boor, 2019; Conroy *et al.*, 2016; Henderson *et al.*, 2013). Similarly, we chose fibronectin as the first ligand (L1) as its expression is related to fibrosis (Eddy, 1996; Genovese *et al.*, 2014) and it is a relatively well characterized ligand of integrin $\alpha\mathrm{v}\beta3$ (Humphries *et al.*, 2006). We used vWA as the second $\alpha\mathrm{v}\beta3$-binding ligand (L2) of which we derived the binding rate constant from a previous

	Explanation	Value	Reference
k_1	Integrin αvβ3 activation	5×10^6 (nM×s)$^{-1}$	Yu *et al.*, 2017
k_2	Integrin αvβ3 inactivation	1.0×10^8 s^{-1}	Yu *et al.*, 2017
k_3	Fibronectin (L1) - αvβ3 binding	1.6×10^8 (nM×s)$^{-1}$	Hudson *et al.*, 2017
k_4	Fibronectin (L1) - αvβ3 unbinding	3.5×10^{-1} s^{-1}	Hudson *et al.*, 2017
k_5	vWA (L2) - αvβ3 binding	1.6×10^4 (nM×s)$^{-1}$	Hudson *et al.*, 2017
k_6	vWA (L2) - αvβ3 unbinding	2.3×10^{-2} s^{-1}	Hudson *et al.*, 2017
k_7	Integrin cluster formation	1.6×10^8 (nM×s)$^{-1}$	Yu *et al.*, 2017
k_8	Integrin cluster dissociation	0.5×10^7 s^{-1}	Yu *et al.*, 2017
i	Integrin αvβ3	0.05 nM	Hudson *et al.*, 2017

Table 3.1: Parameters used in the ODE model, their values and references.

model (Hudson *et al.*, 2017). Overall, we intended to demonstrate the simplest possible case of ligand competition where a low affinity and a high affinity ligand compete for binding to the integrin. L1 represents a high affinity ligand, whereas L2 represents a medium to low affinity ligand for integrin αvβ3 (Irvine *et al.*, 2002). This setup is relevant for natural cell-ECM interactions as well as for cells on synthetic substrates as one of the most widely used integrin-targeting peptide sequences RGD has varying affinities in different conformations (i.e. higher affinity when cyclic form versus lower affinity when in linear form) (Sankaran *et al.*, 2017; Verrier *et al.*, 2002; Xiao & Truskey, 1996). When provided with the necessary parameter set, our model can be used to simulate the interactions of other integrin–ligand pairs or even other receptor–ligand pairs which have similar activation-binding-clustering chemistry.

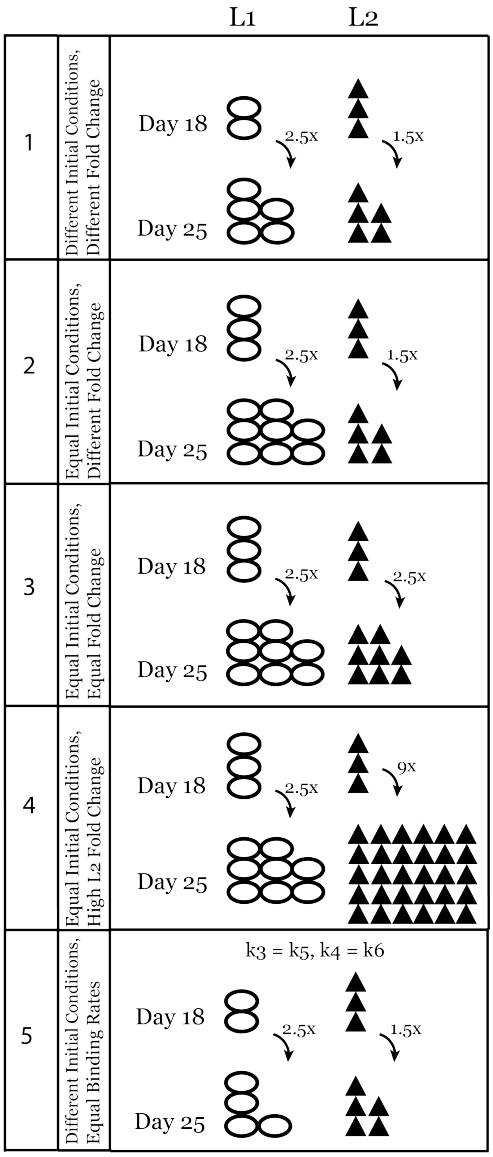

Figure 3.2: Schematic representation of experimental conditions that were tested using the ODE model of ligand competition. Conditions are numbered from 1 to 5 and this numbering is also used in the figures and results.

3.2.2 Design of *In silico* Experiments

Using the ODE system described above, we performed a set of *in silico* experiments, aimed at characterizing the effects of increased ECM ligand concentration on integrin binding in a cell culture system. Initial molar concentrations for fibronectin (0.18 nM) and vWA (0.33 nM) were taken from Hudson et al. while we used the fold changes reported by Geuens et al. between days 18 and 25 for these two ligands (2.5-fold and 1.5-fold for fibronectin and vWA) in kidney organoid culture (Geuens *et al.*, 2021). This way we obtained the test condition 1 "Different Initial Conditions, Different Fold Change" in Table 3.2 and Figure 3.2. In further *in silico* experiments, we set the initial concentrations of the two ligands equal (condition 2, Table 3.2 and Figure 3.2) and varied the fold change values (Equal, Different or High Fold Change for L2 only) between days 18 and 25 to test their effect on the system (conditions 3 and 4, Table 3.2 and Figure 3.2). Finally, we set the binding rates of the two ligands to be equal and used the initial concentration of test condition 1 once more to see the effect of binding rate constants independent of the effect of initial ligand concentrations and fold changes (condition 5, Table 3.2 and Figure 3.2). A schematic representation of all the tests is given in Figure 3.2.

	Test Condition	**Experiment Time**	**L1**	**L2**
1	Different Initial Conditions,	Day 18	0.18 nM	0.33 nM
	Different Fold Change	Day 25	0.46 nM	0.50 nM
2	Equal Initial Conditions,	Day 18	0.33 nM	0.33 nM
	Different Fold Change	Day 25	0.84 nM	0.50 nM
3	Equal Initial Conditions,	Day 18	0.33 nM	0.33 nM
	Equal Fold Change	Day 25	0.84 nM	0.84 nM
4	Equal Initial Conditions,	Day 18	0.33 nM	0.33 nM
	High Fold Change for L2	Day 25	0.84 nM	2.97 nM
5	Different Initial Conditions,	Day 18	0.18 nM	0.33 nM
	Equal Binding Rates	Day 25	0.46 nM	0.50 nM

Table 3.2: Conditions (1–5) with initial concentration values for competing ligands, for each experiment (different or equal initial conditions (IC); different, equal or high fold change (FC) between experiment days; different or equal binding rates (BR) for ligands) and for each time point (Day 18 and 25).

3.3 Results

Using our ODE-based model (Eqn. 3.1-3.9) and interactions described above (Figure 3.1), we performed simulations using reaction rate constants from the literature (Table3.11) and initial conditions changing according to Table 3.2 and Figure 3.2. The binding rate constant between integrin $\alpha v\beta 3$ and fibronectin is 104 times higher than that of integrin $\alpha v\beta 3$ and vWA (Hudson *et al.*, 2017). Therefore, in our model, L1 is the ligand with higher binding affinity while L2 has lower binding affinity for the same integrin. Although we use binding rate constants of fibronectin and vWA in this study, the computational model is generic and can be adapted for other integrin–ligand pairs by changing the corresponding parameter values.

The initial conditions for the integrin and both ligands at day 18 were set from Hudson *et al.*, 2017. The day 25 initial conditions for the two ligands were determined using the results of the kidney organoid ECM proteomics analysis (Table 3.2). It should be noted that in all *in silico* tests that are described in the following sections, the inactive integrin concentration ($[i]$) and active integrin concentration ($[I]$) reached a steady state value of almost zero. This means that all integrins in the system were found as either bound to a ligand and/or clustered with other ligand-bound integrins (Figure S.3.1).

3.3.1 The ligand with a higher binding rate dominates the integrin binding competition

First, we looked at how integrin–ligand binding dynamics change under conditions similar to the kidney organoid culture experiments. The proteomics analysis revealed that there was a 2.5– and 1.5–fold increase in the amount of fibronectin and vWA, respectively, between days 18 and 25 in the ECM. In our model, we simulated this scenario as condition 1, using the initial concentrations given in Tablee 3.2. The steady-state value was higher at day 25 than day 18 for L1-bound integrins (increase in the 10^{-6}th order, Figure 3.3A-1, Figure S.3.2A). The L2-bound integrin concentration, however, decreased at day 25 compared to day 18 (Figure 3.3B-1).

Second, to test the effect of the differences in initial conditions of the ligands (L1 = 0.18 nM and L2 = 0.33 nM) on our observations, we ran simulations with equal initial concentrations (0.33 nM) for L1 and L2 on day 18 and applied the same fold changes (Figure 3.2-2). Similar results were found for L1-bound integrin, whereas L2-bound integrin had an even lower steady-state

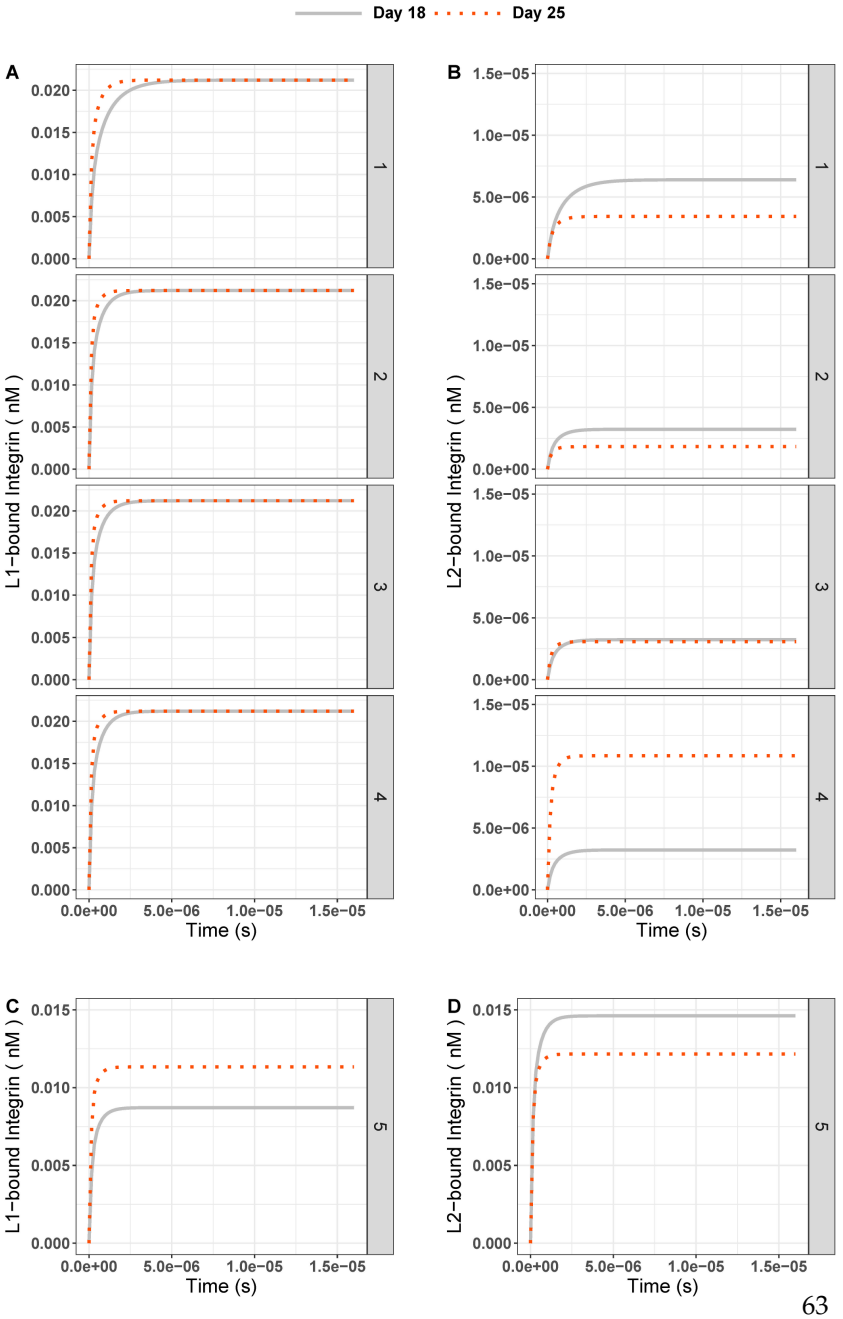

Figure 3.3: (Continued on the following page.)

Figure 3.3: (A) L1-bound and (B) L2-bound integrin concentrations over time in experiment days 18 (gray solid line) and 25 (red dotted line) for test conditions 1 to 5. The test conditions are as given in Table 3.2 and Figure 3.2: 1) Different IC are 0.18 nM for L1, 0.33 nM for L2; 2) Different FC are 2.5 for L1, 1.5 for L2; 3) Equal IC is 0.33 nM; Equal FC is 2.5; 3) High FC for L2 is 9. (C) L1-bound and (D) L2-bound integrin concentration over time for test condition 5 (Different IC and equal binding rate constants for ligands) (k_3 = k_5 = 1.6×10^8 (nM×s)$^{-1}$, k_4 = k_6 = 3.5×10^{-1} s^{-1}).

concentration (Day 18: 2.98×10^{-6} nM, Day 25: 1.77×10^{-6} nM, Figure 3.3B-2) compared to those from Different IC simulations (Day 18: 5.46×10^{-6} nM, Day 25: 3.24×10^{-6} nM, Figure 3.3B-1).

Third, we tested whether an equal fold change (2.5 for both L1 and L2, Figure 3.2-3) between days 18 and 25 affected the ligand competition. The steady state for L1-bound integrin did not change compared to previous test (Figure 3.3A-3, Figure S.3.2B-C). However, we observed an increase in the steady state of L2-bound integrins on day 25 (2.98×10^{-6} nM, Figure 3.3B-3) compared to that under Different FC conditions (1.77×10^{-6} nM, Figure 3.3B-2). This hinted that the fold change can affect the ligand competition in favor of L2.

Next, we simulated a 9-fold change (which was the maximum fold-change observed in kidney organoid ECM mass spectrometry experiments by Geuens *et al.*, 2021) between days 18 and 25 (Figure 3.2 condition 4) for L2. This simulation was done to reflect the effect of a higher fold of the ligand with the lower integrin binding rate on the system. We saw that with a 9-fold increase in the L2 amount on day 25, the steady-state concentration of L2-bound integrin was higher than on day 18 (Figure 3.3B-4) while the L1-bound integrin concentration pattern decreased, in the range of 10^{-6} nM, when compared to previous tests (Figure 3.3A-4, Figure S.3.2D). Mathematically, the decrease in L1-bound integrin compensated for the increase in the steady-state concentration of L2-bound integrin.

The main observation from simulating test conditions 1 to 4 was that the integrins bound to L1 have increased in number by increasing the ligand concentration at day 25 compared to day 18, but integrins bound to L2 have not always increased at day 25 with increasing ligand concentration. Only in test condition 4, with a 9-fold increase in the L2 amount on day 25, we saw that steady state concentration of L2-bound integrins on day 25 was higher than

that of day 18.

To further investigate the turning point for the fold change in L2, where the L2-bound integrin steady-state concentration at day 25 exceeds that of day 18, we ran a parameter scan of the model. For this, we varied the IC for L2 (keeping the IC for L1 at its day 25 concentration which is 0.84 nM) and compared the L2-bound integrin steady state at day 25 to that of day 18 (Figure 3.4). We ran simulations using 10 different initial concentrations for L2 that started from 0.5 nM (1.5-fold increase) and gradually increased to 2.97 nM (9-fold increase). Results showed that, under these parameter settings, the L2-bound integrin concentration at day 25 exceeded that at day 18 only when the L2 initial concentration was $>$0.77 nM (2.3–fold greater) (Figure 3.4).

In all tests so far, integrins were bound to L2, the ligand with a lower binding rate constant, at a lower concentration than the integrins were bound to L1, even when the ICs of the two ligands were equal. This observation implies that the binding rate constants of the two competing ligands, and not the initial concentrations, are of decisive importance for the binding competition.

Thus, we next tested the effect of changing the binding rate constants for L1 and L2 (Figure 3.2 and Table 3.2, condition 5). When we set the binding and unbinding rate constants of the two ligands equal ($k_3 = k_5 = 1.6 \times 10^8$ $(\text{nM}\times\text{s})^{-1}$ for binding and ($k_4 = k_6 = 3.5 \times 10^{-1}$ s^{-1} for unbinding) and used the same initial concentrations as in condition 1 (Table 3.2, L1 = 0.18 nM, L2 = 0.33 nM at day 18 and L1 = 0.46 nM, L2 = 0.50 nM at day 25), we observed L1- and L2-bound integrin concentrations to be similar at the steady state (Figure 3.3C and D). At day 18, the steady-state concentrations for L1 and L2 were 0.009 nM and 0.015 nM, respectively. With day 25 conditions, the steady-state concentrations of L1- and L2-bound integrins were 0.011 and 0.012 nM, respectively.

3.3.2 The ligand binding of integrin clusters reflects the results of the ligand competition

Next, we looked at the changes in integrin cluster (L1-L1, L1-L2, and L2-L2) concentrations over time. With different and equal initial conditions on day 18 and respective increases on day 25 (L1: 2.5-fold, L2: 1.5-, 2.5- and 9-fold), the composition of integrin clusters always reflected the effect of the ligand competition on integrin–ligand binding (Figure 3.5). In other words, there were always more L1-bound, integrin-containing clusters (Figure 3.5A)

at the steady state than L2-bound, integrin-containing clusters (Figure 3.4B) or mixed L1–L2-bound integrin clusters (Figure 3.5C). This showed that L1 with a higher binding rate is dominant over L2 in the clustering step.

When the two cluster species that contain L2-bound integrins were compared, we saw that the mixed L1–L2–bound integrin clusters were higher in concentration at the steady state than L2–L2–bound integrin clusters (Figure 3.5B and C) at all times. When day 25 results were compared to day 18, we saw the same pattern as for individual ligand-bound integrin species, namely:

1. L1-bound clusters had slightly higher steady state at day 25 than day 18;
2. The L2-bound, integrin-containing clusters had lower steady state concentrations at day 25 than day 18 unless the fold change of the ligand between two experiments exceeded 2.3-fold.

Similar to the results of ligand-bound integrins when the same binding-unbinding rates were used for both ligands, clusters with only L2-bound integrins were highest in concentration (0.007 nM), followed by L1–L2–bound mixed integrin clusters (0.004 nM) and L1–L1–bound integrin clusters (0.002 nM) (Figure 3.5D–F) on day 18. On day 25, with the same settings, the concentrations of the three different integrin clusters were similar: L1–L1 cluster = 0.004 nM, L2–L2 cluster = 0.005 nM, L1–L2 cluster = 0.004 nM (Figure 3.5D–F).

3.3.3 Local Sensitivity Analysis

Finally, we studied the sensitivity of each molecular species in the ligand competition model to changes in model parameters. We performed a local sensitivity analysis by increasing or decreasing by 20%, one of the model parameters at a time. We tested the individual effect of each of the eight binding rate constants (k_1–k_8), the initial concentrations of integrins (i) and the two competing ligands (L1, L2) on the steady state of each molecular species in the model. We used these steady-state values for each molecular species to calculate a parameter sensitivity value using the following formula:

$$Parameter\ Sensitivity\ =\ \frac{|SS\,(k+\Delta k)-SS(k)|}{SS(k)}\ /\ \frac{\Delta k}{k}$$

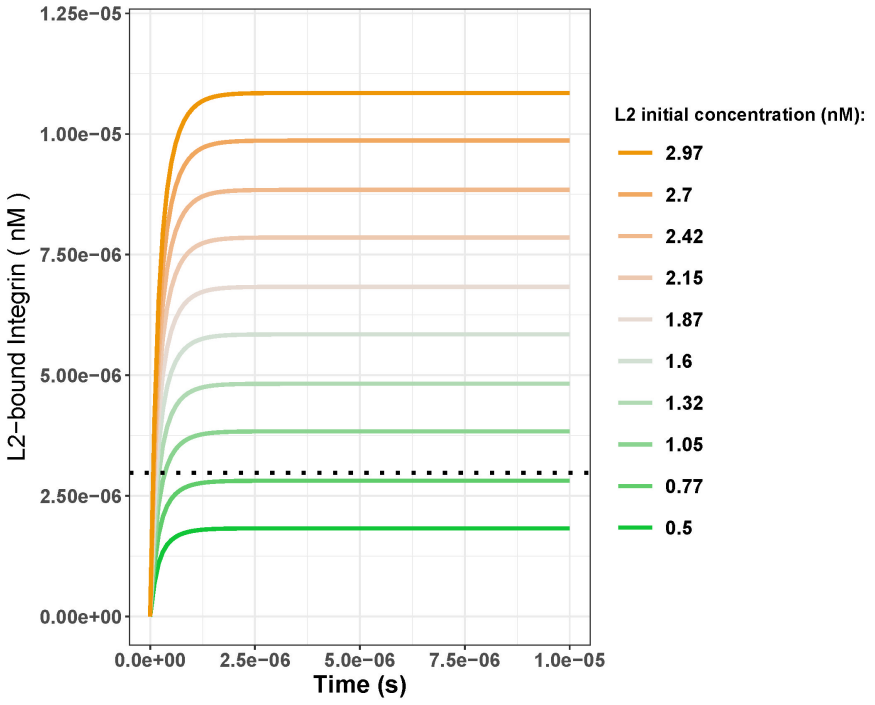

Figure 3.4: L2-bound integrin concentration over time with varying initial concentrations of L2 with the initial concentration of L1 kept constant at 0.84 nM. Black dotted line shows the day 18 steady-state concentration for L2-bound integrins when the initial L1 and L2 concentrations were both 0.33 nM. Comparing the steady-state concentrations from the line plots to the black dotted line, initial L2 concentrations greater than 0.77 nM result in the steady state of the L2-bound integrins exceeding that of day 18 (2.98 nM). This corresponds to a fold change of 2.3 between days 18 and 25.

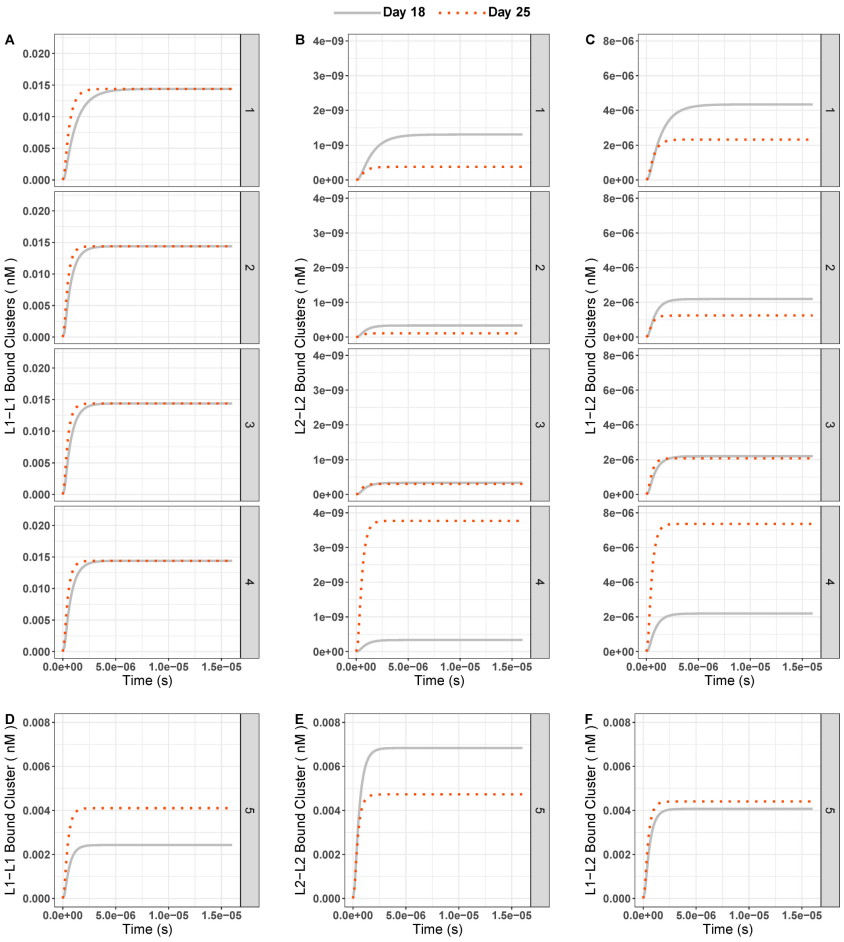

Figure 3.5: (A–C) Concentrations of ligand-bound integrin clusters L1–L1 (left column, A-1 to A-4), L2–L2 (middle column, B-1 to B-4), and L1–L2 (right column, C-1 to C-4) over time at days 18 (gray solid line) and 25 (red dotted line) for all test conditions (1–5). (D–F) Integrin cluster concentration over time for condition 5 (Different IC (L1 = 0.18 nM, L2 = 0.33 nM) and equal binding rate constants ($k_3 = k_5 = 1.6 \times 10^8$ (nM×s)$^{-1}$, $k_4 = k_6 = 3.5 \times 10^{-1}$ s^{-1}) for ligands).

$SS(k)$ represents the steady-state concentration when there is no change to the model parameter (i.e., the standard model outcome), $SS\,(k + \Delta k)$ represents the steady-state concentration when the parameter value was increased by 20% of the base value. Therefore, $\frac{\Delta k}{k}$ was 20% for our analysis. The effect of decreasing the parameter values by 20% was calculated in the same way, replacing $SS\,(k + \Delta k)$ with $SS\,(k - \Delta k)$. The results of this sensitivity analysis are given in Figure 3.6.

In general, the sensitivity pattern for a decrease in parameter values was the same as for an increase. Similar to the previous tests, L1-bound integrins and L1–L1–bound integrin clusters were the least affected by changes in model parameters. In contrast to the L1-bound integrin concentration, the steady-state, L2-bound integrin concentration was not only influenced by the L2 binding and unbinding rate constants (k_5 and k_6), but also by the L1 binding and unbinding rate constants (k_3 and k_4) as well as the initial L1 concentration. It is noteworthy that the L2-bound integrin concentration was affected by the changes in the initial amount of L1 and not by the L2 increase or decrease.

The L2–L2–bound integrin cluster was the most sensitive molecular species in the model (Figure 3.6). We observed that parameter changes that affected L2-bound integrins affected also the L2–L2–bound integrin clusters but in a more dramatic way: the steady state of L2–L2–bound integrin cluster was more than twice as sensitive to the 20% decrease in L1 initial concentration than that of the L2-bound integrin. A similar pattern was observed for the 20% increase in k_4 (L1 unbinding) and k_5 (L2 binding) as well as for the 20% decrease in k_3 (L1 binding) and k_6 (L2 unbinding). Interestingly, the mixed L1–L2–bound integrin clusters showed a very similar sensitivity pattern to L2-bound integrins, which is different from that of L2–L2-bound integrin clusters. These observations can be explained by the quadratic dependency of L2–L2-bound integrin clusters to L2-bound integrins (detailed in the discussion).

We should also note that both the steady state of inactive and active integrins did not show significant sensitivity to the changes in the initial concentration of inactive integrins (i) but were sensitive to the changes in L1 initial concentration (L1) (Figure 3.6). This is expected given that the amount of ligands in the system is in excess compared to integrin concentration (i = 0.05 nM, L1 = 0.18 nm, L2 = 0.33 nM) to mimic the biology of receptor–ligand binding (Hudson *et al*., 2017; Wanant & Quon, 2000). The excess ligand concentrations ensure that with the original reaction rate constants and in all the test scenarios, the unbound integrins in the system (both active and inactive) reach a

steady-state concentration close to zero and are found as ligand-bound (Figure S.3.1). The parameter sensitivity patterns of inactive and active integrins show that the imbalance between integrin–ligand amounts is maintained by L1, the ligand with higher binding affinity. It is the L1 initial concentration and its ligand binding-unbinding constants (k_3, k_4) that affect the steady-state concentrations of inactive and active integrins in the parameter sensitivity analysis, while the L2 initial concentration and its binding rates (k_5, k_6) are not determinants (Figure 3.6).

In line with this, when we set the initial integrin concentration to be higher (1 nM) than the total initial ligand concentration (0.51 nM), we observed a major shift in the parameter sensitivity patterns (Figure S.3.3). When the integrins were in excess compared to ligands, the steady states of the integrin molecules in the system were highly dependent on the initial integrin concentration (Figure S.3.3) instead of on the binding-unbinding constants when the ligands were in excess. This is expected as all ligands will be bound to the receptors in a system where there are more receptors than ligands. The amounts of ligand-bound receptors therefore correlate with the initial ligand concentrations.

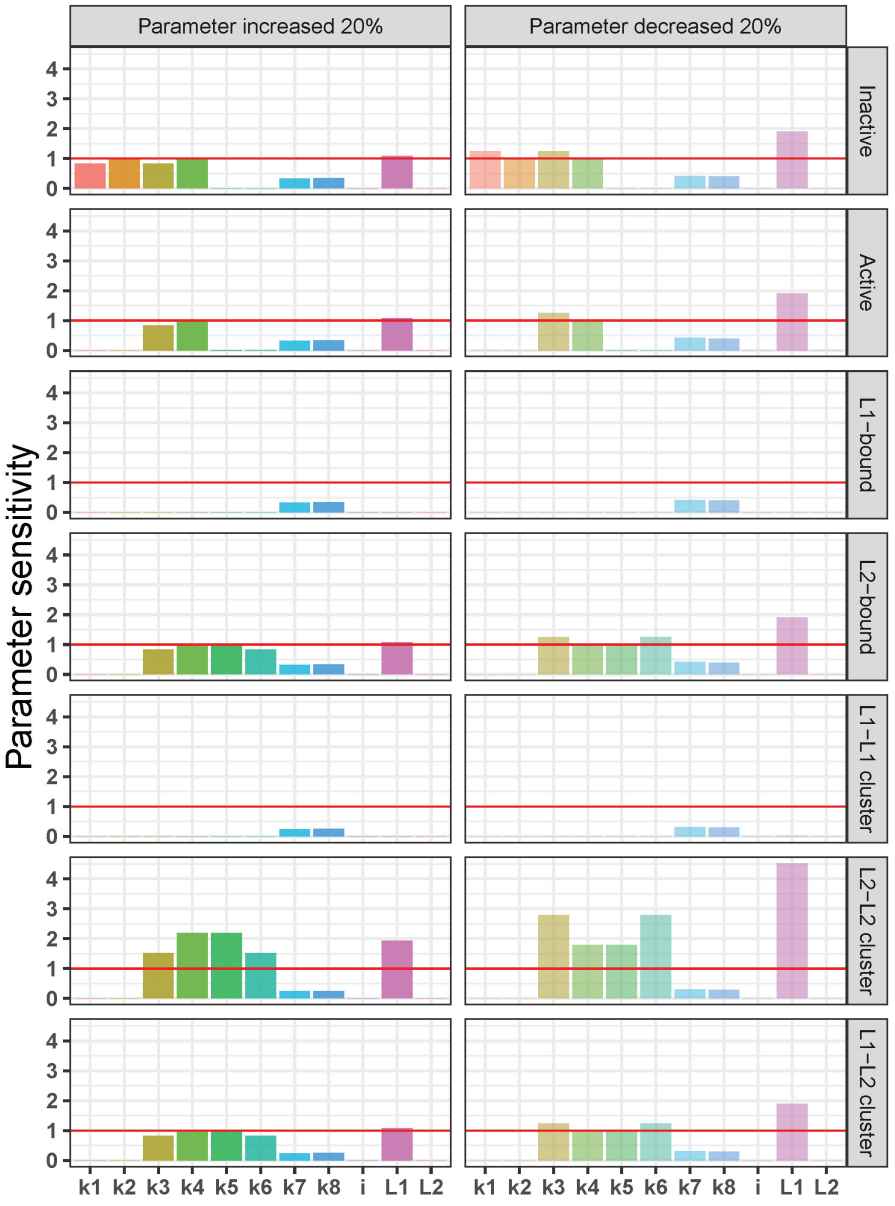

Figure 3.6: (Continued on the following page.)

Figure 3.6: Local sensitivity analysis of the integrin ligand competition model. Parameter sensitivity values on the y-axis indicate how a 20% increase (left) or decrease (right) in each parameter [rate constants for integrin activation-inactivation (k_1–k_2), L1 binding-unbinding (k_3–k_4), L2 binding unbinding (k_5–k_6), integrin cluster formation-dissociation (k_7–k_8), and initial concentrations of integrins (i) and the two ligands (L1 and L2)] affects the steady state of each molecular species in the model (from top to bottom: inactive and active integrins, L1-bound integrins, L2-bound integrins, L1-L1-, L2–L2-, and L1–L2-bound integrin clusters). Parameter sensitivity of > 1 (red horizontal lines) indicates that the steady state of a molecular species is highly dependent on changes in parameter values, and values < 1 indicates a lower sensitivity to changes in parameter values.

3.4 Discussion

Here we present an ODE model that can be used to explore the ligand-binding kinetics of integrins. The computational model involves three main biological reactions: 1) integrin activation, 2) integrin–ligand binding and 3) ligand-bound integrin clustering (Figure 3.1). At each step, the model allows us to track the concentration of each model species over time. Different from previously published models of integrin–ligand binding (Hudson *et al.*, 2017; Macdonald *et al.*, 2008; Yu *et al.*, 2017), we included two ligands that have the ability to bind to the same type of integrin, which allowed us to monitor the competition between these two ligands.

The first outcome of the different tests we performed using the ODE model was that all integrins were activated, bound to a ligand, and that a subset of these ligand-bound integrins were clustered (Figure S.3.1). Biologically, integrin activation happens in two ways: outside-in and inside-out. Outside–in activation is triggered by the interactions between integrins and ECM ligands while inside-out activation is triggered by the binding of talin to cytoplasmic tails of integrin molecule (Shams *et al.*, 2017). Talin is a protein that harbors multiple binding sites for other signaling molecules and the actin cytoskeleton (Miller *et al.*, 2020). Both these activation processes are not very well resolved but it is known that they influence one another (Shams *et al.*, 2017). The activation step in our model is not specific to either of the above activation mechanisms.

Our parameter sensitivity results indicated that the rates of integrin activation/inactivation did not have a significant impact on the steady-state con-

centrations of molecular species involved in reactions like ligand binding or integrin clustering (Figure 3.6). We can speculate that in a model that includes multiple interaction partners of integrins which affect the integrin activation or reactions of downstream signaling pathways which are dependent on the integrin activation, the integrin activation step would play a significant role in the model. It is known that for example, talin-mediated integrin activation is dynamically regulated by several potential mechanisms (Calderwood, 2004) such as talin proteolysis (Yan *et al.*, 2001) and competition between other proteins that bind to integrin from its cytosolic tails (Bouvard *et al.*, 2003). Yet the exact mechanisms of action and their relative significance are not resolved (Calderwood, 2004). Exploring these mechanisms and their effects on ligand binding and integrin clustering could be one potential extension to our model.

We used the results from a proteomics analysis of kidney organoid ECM when defining the ligand concentrations in our model simulations. Under these "experimental conditions", we observed that the steady-state concentration of L1-bound integrins was higher than the L2-bound integrins concentration (0.021 nM vs 6.393×10^{-6} nM, Figure 3.3A-1 and Figure 3.3B-1), even though the initial concentration of the L2 ligand is greater than L1 on day 25 (0.50 nM vs 0.46 nM,Table 3.2). We observed this pattern even when we systematically changed the initial concentrations of the two ligands and the concentration fold changes between days 18 and 25.

In their ODE model, Hudson *et al.*, 2017 also reported an increase in the ligand-bound integrin amount whenever there was in increase in the ligand concentration. However, their model included only one type of ligand binding to integrin at a time. When we account for ligand competition, we observed that an increase in ligand concentration did not ensure more ligand-bound integrins if the competing ligand has a higher binding rate (Figure 3.3). For the standard parameter settings, only fold changes greater than 2.3 led to an increase in L2-bound integrin amounts (for 0.84 nM L1 at day 25, Figure 3.4). However, even with high fold changes (9-fold compared to 2.5-fold), L1-bound integrins were always more abundant than L2-bound integrins at the steady state.

We can explain this observation, where an increase in (initial) ligand concentration results in a reduction of its integrin-bound, steady-state value, using the ODE system given in Eqn. 1–9. When at steady state, all ODE equations should be equal to zero because there is no time-dependent change in the concentrations of any of the molecular species. Using the steady state solutions

of Eqn. 8 and 9, we can get to the following dependencies between ligand-bound integrin concentrations at the steady state (IL1s and IL2s) and ligand concentrations at the steady state (L1s and L2s);

$$k_3[I_s][L1_s] = k_4[IL1_s] \tag{3.10}$$

$$[IL1_s] = \frac{k_3[I_s][L1_s]}{k_4} \tag{3.11}$$

$$k_5[I_s][L2_s] = k_6[IL2_s] \tag{3.12}$$

$$[IL2_s] = \frac{k_5[I_s][L2_s]}{k_6} \tag{3.13}$$

$$\frac{[IL1_s]}{IL2_s} = \frac{k_3 k_6[L1_s]}{k_4 k_5[L2_s]} \tag{3.14}$$

In our system, k_3 = 1.6 $\times$ 10^8 1/(nM $\times$ s) and k_4 = 3.5 $\times$ 10^{-1} 1/s while k_5 = 1.6 $\times$ 10^4 1/(nM $\times$ s) and k_6 = 2.3 $\times$ 10^{-2} 1/s. When plugged in to Eqn. 14, these rate constants provide $IL1s$ to be 660 times $IL2s$. The difference between the steady-state concentrations of the ligands, however, is not high enough to compensate for the big difference in rate constants, resulting in a big difference between steady-state concentrations of the two types of ligand-bound integrins. This also explains the differences in the sensitivity patterns of ligand-bound integrin species. The steady state of integrins bound to L1 with a higher binding rate constant (IL1) is less affected by the small perturbations in model parameters compared to L2-bound integrins (IL2) (Figure 3.6), because $\frac{k_3}{k_4}$ is big enough to compensate for a 20% change. From these results, we can conclude that in case of ligand competition for a receptor, the highest ratio — either the ratio of binding rate constants or the ratio of initial ligand concentrations — has the dominating effect on the steady-state concentrations of the ligand-bound receptors.

When the binding and unbinding rate constants of the two ligands are set to be equal (i.e. k_3 = k_4 and k_5 = k_6), we can see from Eqn. 3.11 and Eqn. 3.13 that the difference between steady-state concentrations of the ligand-bound integrins ($IL1_s$ and $IL2_s$) solely depend on the difference between the steady-state concentrations of the two competing ligands ($L1_s$ and $L2_s$). Since we assume mass conservation in the system, the following equations hold true for the total amount of ligands in the system at the steady state:

$$[L1] = [L1_s] + 2[C1_s] + [C3_s] + [IL1_s] \tag{3.15}$$

$$[L2] = [L2_s] + 2[C2_s] + [C3_s] + [IL2_s] \tag{3.16}$$

$L1$ and $L2$ represent the initial (and total) ligand concentrations in the system. As all the rate constants for forward and reverse reactions become equal for the scenario where the two ligands have equal binding rate constants, we can safely assume that the ligand concentrations at the steady state correlate with the initial ligand concentrations.

Using Eqn. 3.14, 3.15 and 3.16, we can explain what we observe in Figure 3.3C–D, i.e., for day 18 initial conditions of the two ligands with equal binding rates, the ratio of the steady-state concentration of L1-bound integrins (IL1) to that of L2-bound integrins (IL2) is 0.59 (0.009 nM /0.015 nM). This ratio is very similar to the ratio of initial L1 amount to initial L2 amount, which is 0.54 (0.18 nM /0.33 nM). When we look at the day 25 steady-state concentrations, we find the IL1/IL2 ratio to be 0.93 (0.011 nM /0.012 nM) and an initial ligand concentration ratio of 0.92. Therefore, the initial ligand concentrations, when the binding rate constants are equal, are informative for predicting the steady-state concentrations of ligand-bound integrins. In other words, with equal binding rates, the ligand with the highest initial condition will result in the highest integrin-bound, steady-state concentration and "win" the ligand competition. This observation is also in line with the literature. In another partial differential equation model of competitive receptor–ligand binding, the competing ligands both had binding affinities in the picomolar range and the steady-state concentrations of receptors bound to either of the ligand were directly correlated with the initial ligand concentrations (Mac Gabhann & Popel, 2004).

These explanations of the relationship between the binding affinities of competing ligands and the final amount of ligand-bound integrins can be the mathematical explanation of the experimental finding in which RGD peptides with different stereochemistry inhibit the binding of a subset of integrin ligands, while being ineffective for inhibiting other ligands. For example, one of the very early studies on cyclic versus linear RGD peptides reported that the peptides could inhibit vitronectin binding effectively while falling short on inhibiting fibronectin binding (Pierschbacher & Ruoslahti, 1987). This was because the peptide constructs had a larger affinity for the integrins compared to the affinity of vitronectin for the integrins while fibronectin still had the

highest affinity for the integrins therefore the peptide constructs failed to inhibit the adhesion to fibronectin. Ever since, many others developed integrin targeting peptides with various binding affinity and selectivity (Bernhagen *et al.*, 2017; Kimura *et al.*, 2009; Ma *et al.*, 2017; Mas-Moruno *et al.*, 2011; Piras *et al.*, 2012; Wang *et al.*, 2005). Although our computational results do not point out to a solution on how to improve the affinity of a ligand towards an integrin, we provide here a method for calculating the effect of having a higher affinity ligand on the binding of other competing ligands. This can be used to estimate the affinity that needs to be reached to prevent the binding of a specific competitive ligand, without having to run a series of experiments with a large set of ligands, different concentrations and/or timing.

As expected, due the same clustering rates k_7–k_8 for all cluster-types, the steady-state composition of ligand-bound integrin clusters (IL1–IL1, IL2-IL2 and IL1-IL2, Figure 3.1) was in correlation with the steady-state concentrations of single, ligand-bound integrins (Figure 3.3 and Figure 3.5). L1-bound, integrin-containing clusters were in abundance when compared to L2-bound, integrin-containing clusters, except when the binding rate constants were set to be equal for both ligands (Figure 3.5C–D). We can also explain this observation analytically by setting Eqn. 3.11–3.13 to zero to calculate the steady state of the three integrin cluster species. Then we obtain the following equations:

$$[C1_s] = \frac{k_7[IL1_s^2]}{k_8} \tag{3.17}$$

$$[C2_s] = \frac{k_7[IL3_s^2]}{k_8} \tag{3.18}$$

$$[C3_s] = \frac{k_7[IL1_s][IL2_s]}{k_8} \tag{3.19}$$

where $C1s$, $C2s$ and $C3s$ denote the steady-state concentrations of the three integrin cluster species composed of IL1–IL1, IL2–IL2 and IL1–IL2, respectively. Eqn. 3.17–3.19 reveal that the steady-state concentrations of all integrin clusters correlate with the steady-state concentrations of the ligand-bound integrin concentrations that they contain. Because of the quadratic term in Eqn. 3.18, the steady state of IL2–IL2 clusters (C2) is much more sensitive to small perturbations in model parameters than the steady state of L2-bound integrins (Figure 3.6). In contrast, the relatively high steady state value of L1-bound integrins balances the steady state of IL1-containing clusters (C1

and C3), therefore their sensitivity patterns are similar that of IL1 and IL2, respectively (Figure 3.6).

We should note that the integrin clusters in our model were composed only of two ligand-bound integrins, whereas in reality this number can be much higher. Previous models of integrin clustering suggest that as the ligand-binding rates increase, the size of integrin clusters decrease, possibly due to the decreased diffusion rate of ligand-bound integrins (Cheng *et al.*, 2020). Neither the exact number of possible integrins in a cluster nor the effect of the composition of integrin clusters is known. Since it is known that at focal adhesion points, more than one type of integrin can cluster together and they have different roles in the cluster (Roca-Cusachs *et al.*, 2009), it would be interesting to explore the downstream effects of having different ligand-bound integrins clustered together.

For the sake of simplicity and interpretability of the ligand competition, we assumed the spatial distribution of molecules to be homogenous in this model. Therefore, we used an ODE model and assumed the free ligands are always available to active integrins, independent of their spatial location. However, previous models with a focus on integrin clustering have suggested a limit to the distance between ECM ligands for the integrin clustering to occur (Jamali *et al.*, 2013; Yu *et al.*, 2017). Therefore, future models should focus on including the space dimension to integrin–ligand binding and clustering models, considering ligand spacing.

In natural tissues, there can be more than two ligands competing to bind to the same integrin. Therefore, our model is a simplified version of the real scenario. Nevertheless, we have shown that even with this simplified ligand-competition model, we can acquire more fundamental understanding of integrin–ligand binding. For example, we have shown that the vWA-bound integrins (IL2) are much lower in concentration than fibronectin-bound integrins (IL1) when the two ligands are allowed to bind simultaneously, in contrast to the model results of Hudson *et al.*, 2017.In addition, our model suggests that with an increasing number of ligands competing for the same integrin, the final distribution of ligand-bound integrins will correlate with the distribution of their binding affinities. When we added a third ligand to our system (L3), with a binding affinity even higher than L1, we observed that the number of L3-bound integrins were higher than both L1- and L2-bound integrins (Figure S.3.4). Whereas L1-bound integrins were still more abundant than L2-bound integrins (Figure S.3.4).

It would be interesting to expand the current model with different integrin types, to reflect the level of complexity of interactions at the cell–ECM interface. However, this would increase the number of parameters in the model and to date, binding rates for all integrin–ligand pairs are not known. Such future work should focus on obtaining binding rate constants specific to different integrin–ligand pairs. Surface plasmon resonance (Elosegui-Artola *et al.*, 2014; Kim *et al.*, 2005; Yan *et al.*, 2001) or single molecule dynamic force spectroscopy (Taubenberger *et al.*, 2007) are suitable techniques for this purpose. The current model focuses on the short-term behavior, neglecting ligand production and downstream signaling. As such, another interesting avenue to expand the ligand-competition model could be to include downstream cytosolic events from the ligand-bound integrins that alters the cell behavior. In the end, this would lead to the prediction of cell behavior using the information on the ECM composition.

In summary, with our model, we conclude that the control over the concentrations of ECM ligands would not be enough to have control over their integrin binding in case there is a significant difference between the binding rates of different ECM ligands. More specifically, our results show that, for the low-affinity ligand, not only its ligand binding-unbinding rates are important, but also the ligand binding-unbinding rates and initial concentration of the competing ligand with a faster binding rate (Figure 3.6). In light of this information, the increased production of ligands with higher binding affinity would disable lower-affinity ligands from binding to integrins. In cases where biochemical cues from slower binding ligands are needed for the healthy development of cells in culture, their development would be disrupted. This could be the root cause, for example, of persistent challenges in functional kidney organoid development field such as off-target cell populations, lack of vascularization and insufficient maturation introduced in prior sections (Geuens *et al.*, 2020; Nishinakamura, 2019).

To overcome such effect, either the binding of faster binding ligands needs to be impaired by blocking agents, or the cellular production of faster binding ligands needs to be prevented using molecular biology techniques. Alternatively, synthetic integrin ligands with controlled affinity could be used to selectively prevent binding of naturally produced ECM proteins. Of course, these preventive strategies require a thorough understanding of the integrin function, cellular signaling and decision-making affected by ligand-integrin interactions. Experimental biology going hand-in-hand with computational biology can answer many unknowns in the understanding of integrins (Karagöz, Rijns, *et al.*, 2021).

As such, this study shows that computational models can be informative to get a better understanding of the effects of ECM composition on the cell behavior and to develop cell culture conditions that would favor desired cell phenotypes. Moreover, since our model fundamentally explains a reaction system, in which there are two ligands available to bind to their receptor, the obtained relations and influential factors describing ligand competition are generic and applicable to other receptor–ligand interactions.

3.5 Supplementary Material

Figure S.3.1 (A) Inactive and (B) active integrin concentrations over time in experiment days 18 (gray solid line) and 25 (red dotted line) for test conditions 1 to 4. (C) Inactive and (D) active integrin concentrations over time for test condition 5. The experimental conditions 1 to 5 are as given in Table 3.2 in the main text.

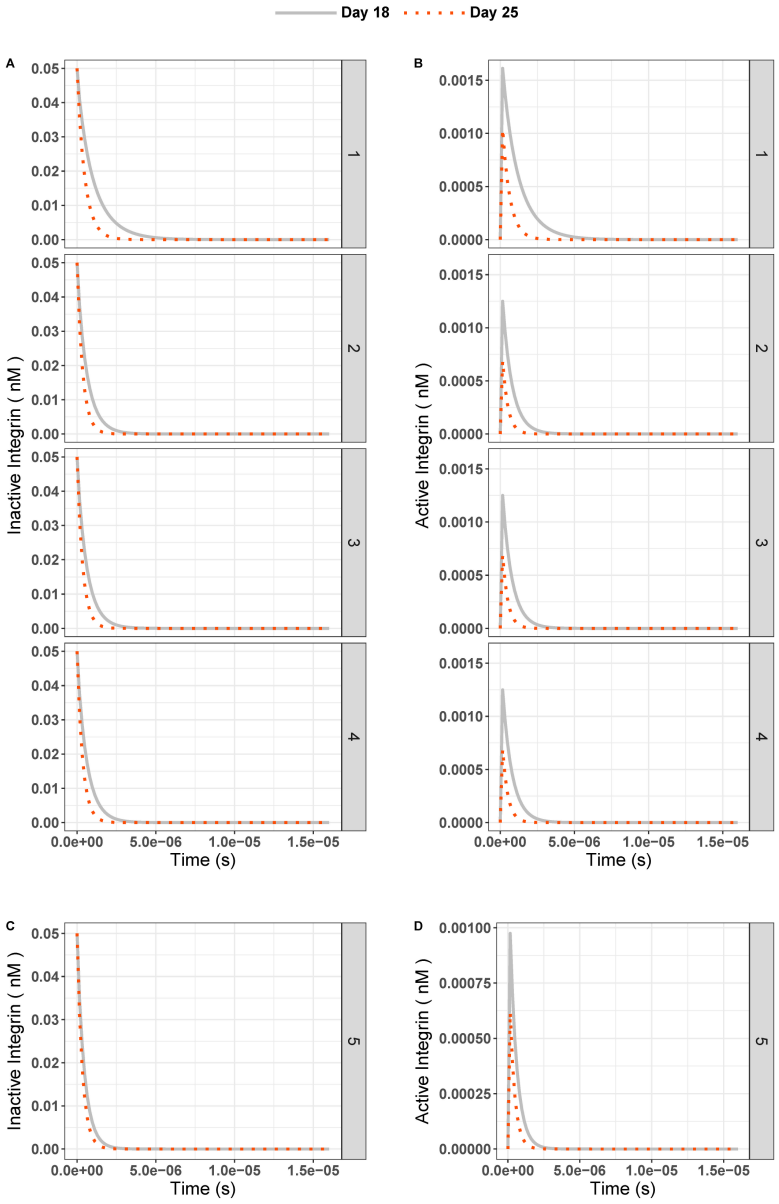

Figure S.3.2 Zoom into the Figure 3.3 in the main text. An increase was observed in L1-bound integrin steady state concentrations on day 25 compared to day 18 in test cases 1 (A), 2 (B) and 3 (C). (Continued on the following page)

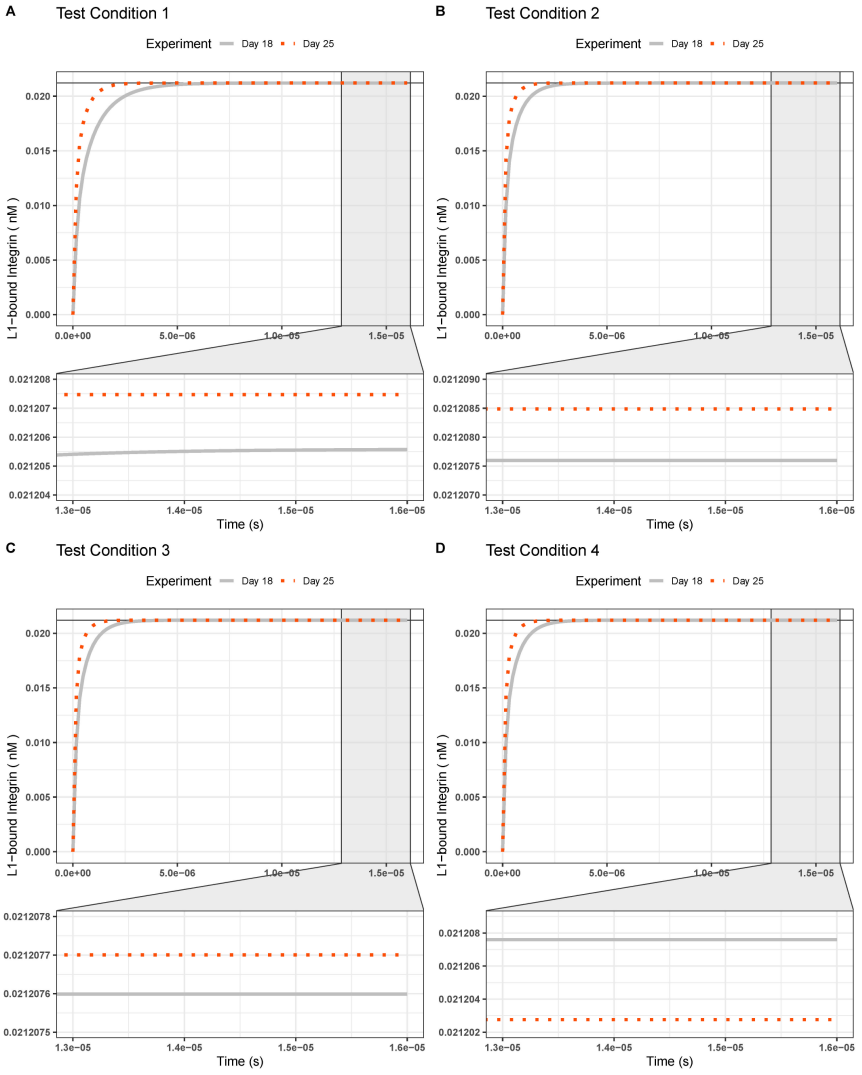

Figure S.3.2 In test condition 4 however, L2-bound integrin concentration increases on day 25 compared to day 18. This increase is compensated by a decrease in L1-bound integrin concentration (D). Note that in all four test conditions, the L1-bound integrin steady state concentration is higher than the L2-bound integrin steady state concentration.

Figure S.3.3 Parameter sensitivity analysis results for the model when the integrin initial concentration was set to be greater (1 nM) than the total initial concentration of the competing ligands (0.51 nM). Compared to the parameter sensitivity of model with original settings, the binding/unbinding rates are not as determinant. The inactive and active integrin steady state is highly dependent on the initial integrin concentration in this model, whereas in the original model, initial integrin concentration was not a determinant factor.

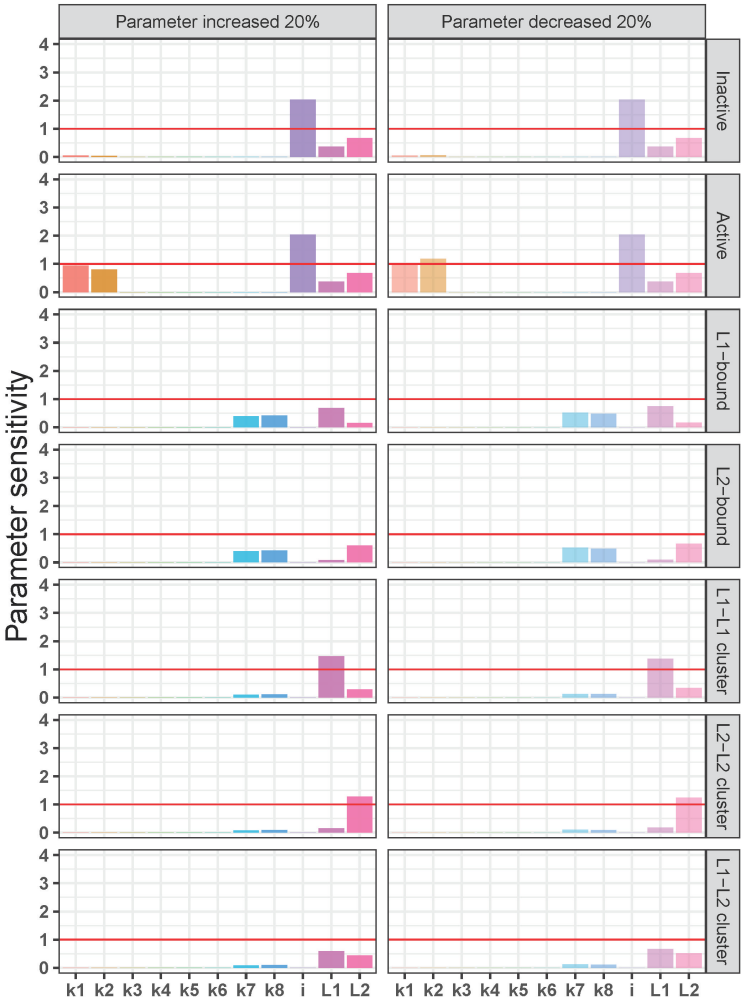

Figure S.3.4 Comparison of steady state concentrations of three ligand-bound integrin species in a theoretical 3-ligand model. We have created a ligand competition model with three ligands, L1 and L2 being the same ligands as in the ligand competition model explained in the main text. L3 was introduced as being the ligand with the highest affinity (k_on = 1.6×10^{10} (nM×s)$^{-1}$, k_off = 2.3×10^{-1} s^{-1}). We ran the simulations for equal initial ligand concentrations for all three ligands (L1 = L2 = L3 = 0.33 nM). The figure shows that the steady state concentrations of the ligand bound integrins depend on the affinity of each ligand towards the integrin. As such, L3-bound integrins were highest in concentration, followed by the L1-bound integrin concentration. The L2-bound integrins were lowest in concentration. Note that L3 in this model is not based on any actual ligand but was only added to the system to demonstrate the case of multiple high affinity ligands present in the binding competition.

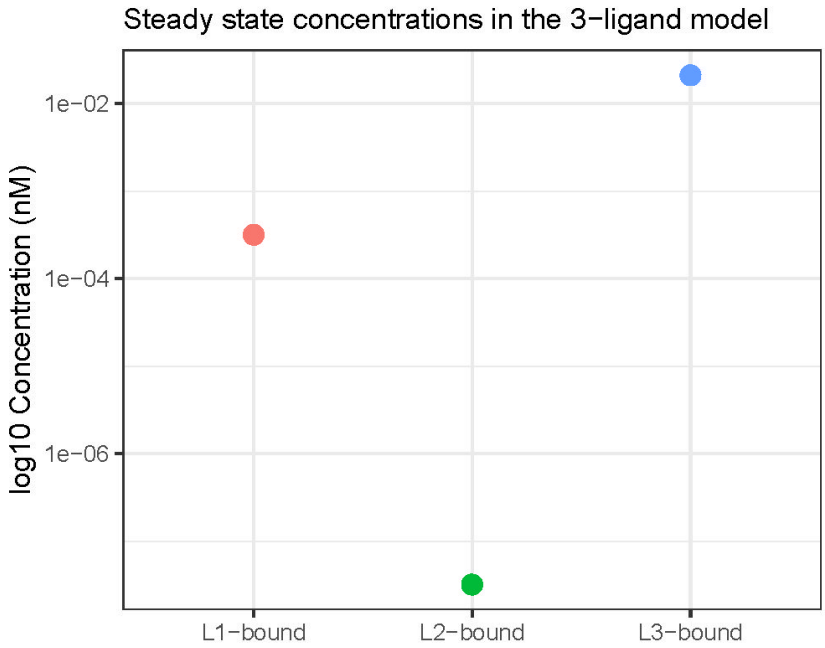

References

Assis-Ribas, T., Forni, M. F., Winnischofer, S. M. B., Sogayar, M. C., & Trombetta-Lima, M. (2018). Extracellular matrix dynamics during mesenchymal stem cells differentiation. *Developmental Biology*, *437*(2), 63–74. https://doi.org/10.1016/j.ydbio.2018.03.002

Barczyk, M., Carracedo, S., & Gullberg, D. (2010). Integrins. *Cell and Tissue Research*, *339*(1), 269–280. https://doi.org/10.1007/s00441-009-0834-6

Bernhagen, D., De Laporte, L., & Timmerman, P. (2017). High-Affinity RGD-Knottin Peptide as a New Tool for Rapid Evaluation of the Binding Strength of Unlabeled RGD-Peptides to alpha v beta 3, alpha v beta 5, and alpha 5 beta 1 Integrin Receptors. *Analytical Chemistry*, *89*(11), 5991–5997. https://doi.org/10.1021/acs.analchem.7b00554

Bouvard, D., Vignoud, L., Dupé-Manet, S., Abed, N., Fournier, H. N., Vincent-Monegat, C., Francesco Retta, S., Fässler, R., & Block, M. R. (2003). Disruption of focal adhesions by integrin cytoplasmic domain-associated protein-1 alpha. *Journal of Biological Chemistry*, *278*(8), 6567–6574. https://doi.org/10.1074/jbc.M211258200

Bülow, R. D., & Boor, P. (2019). Extracellular Matrix in Kidney Fibrosis: More Than Just a Scaffold. *Journal of Histochemistry and Cytochemistry*, *67*(9), 643–661. https://doi.org/10.1369/0022155419849388

Calderwood, D. A. (2004). Integrin activation. *Journal of Cell Science*, *117*(5), 657–666. https://doi.org/10.1242/JCS.01014

Changede, R., Xu, X., Margadant, F., & Sheetz, M. P. (2015). Nascent Integrin Adhesions Form on All Matrix Rigidities after Integrin Activation. *Developmental Cell*, *35*(5), 614–621. https://doi.org/10.1016/J.DEVCEL.2015.11.001

Cheng, B., Wan, W., Huang, G., Li, Y., Genin, G. M., Mofrad, M. R. K., Lu, T. J., Xu, F., & Lin, M. (2020). Nanoscale integrin cluster dynamics controls cellular mechanosensing via FAKY397 phosphorylation. *Science Advances*, *6*(10). https://doi.org/10.1126/SCIADV.AAX1909

Choi, K., Medley, J. K., König, M., Stocking, K., Smith, L., Gu, S., & Sauro, H. M. (2018). Tellurium: An extensible python-based modeling environment for systems and synthetic biology.

BioSystems, *171*, 74–79.
https://doi.org/10.1016/j.biosystems.2018.07.006
Conroy, K. P., Kitto, L. J., & Henderson, N. C. (2016).
v integrins: Key regulators of tissue fibrosis.
Cell and Tissue Research, *365*(3), 511–519.
https://doi.org/10.1007/s00441-016-2407-9
Eddy, A. A. (1996). Molecular insights into renal interstitial fibrosis.
Journal of the American Society of Nephrology, *7*(12).
Elosegui-Artola, A., Bazellières, E., Allen, M. D., Andreu, I., Oria, R., Sunyer, R., Gomm, J. J., Marshall, J. F., Jones, J. L., Trepat, X., & Roca-Cusachs, P. (2014). Rigidity sensing and adaptation through regulation of integrin types. *Nature materials*, *13*(6), 631.
https://doi.org/10.1038/NMAT3960
Garreta, E., Prado, P., Tarantino, C., Oria, R., Fanlo, L., Martí, E., Zalvidea, D., Trepat, X., Roca-Cusachs, P., Gavaldà-Navarro, A., Cozzuto, L., Campistol, J. M., Izpisúa Belmonte, J. C., Hurtado del Pozo, C., & Montserrat, N. (2019).
Fine tuning the extracellular environment accelerates the derivation of kidney organoids from human pluripotent stem cells.
Nature Materials, *18*(4), 397–405.
https://doi.org/10.1038/s41563-019-0287-6
Genovese, F., Manresa, A. A., Leeming, D. J., Karsdal, M. A., & Boor, P. (2014). The extracellular matrix in the kidney: A source of novel non-invasive biomarkers of kidney fibrosis?
Fibrogenesis and Tissue Repair, *7*(1), 4.
https://doi.org/10.1186/1755-1536-7-4
Geuens, T., Ruiter, F. A. A., Schumacher, A., Morgan, F. L. C., Rademakers, T., Wiersma, L. E., van den Berg, C. W., Rabelink, T. J., Baker, M. B., & LaPointe, V. L. S. (2021).
Thiol-ene cross-linked alginate hydrogel encapsulation modulates the extracellular matrix of kidney organoids by reducing abnormal type 1a1 collagen deposition. *Biomaterials*, *275*, 120976.
https://doi.org/10.1016/j.biomaterials.2021.120976
Geuens, T., van Blitterswijk, C. A., & LaPointe, V. L. (2020).
Overcoming kidney organoid challenges for regenerative medicine.
npj Regenerative Medicine, *5*(1), 1–6.
https://doi.org/10.1038/s41536-020-0093-4
Gjorevski, N., Sachs, N., Manfrin, A., Giger, S., Bragina, M. E., Ordóñez-Morán, P., Clevers, H., & Lutolf, M. P. (2016).

Designer matrices for intestinal stem cell and organoid culture. *Nature*, *539*(7630), 560–564. https://doi.org/10.1038/nature20168
Handorf, A. M., Zhou, Y., Halanski, M. A., & Li, W. J. (2015). Tissue stiffness dictates development, homeostasis, and disease progression. *Organogenesis*, *11*(1), 1–15. https://doi.org/10.1080/15476278.2015.1019687
Henderson, N. C., Arnold, T. D., Katamura, Y., Giacomini, M. M., Rodriguez, J. D., McCarty, J. H., Pellicoro, A., Raschperger, E., Betsholtz, C., Ruminski, P. G., Griggs, D. W., Prinsen, M. J., Maher, J. J., Iredale, J. P., Lacy-Hulbert, A., Adams, R. H., & Sheppard, D. (2013). Targeting of alpha v integrin identifies a core molecular pathway that regulates fibrosis in several organs. *Nature Medicine*, *19*(12), 1617–1624. https://doi.org/10.1038/nm.3282
Huang, J., Peng, X., Xiong, C., & Fang, J. (2012). Influence of substrate rigidity on primary nucleation of cell adhesion: A thermal fluctuation model. *Journal of Colloid and Interface Science*, *366*(1), 200–208. https://doi.org/10.1016/j.jcis.2011.09.046
Hudson, V. S., Dolin, C. E., Poole, L. G., Massey, V. L., Wilkey, D., Beier, J. I., Merchant, M. L., Frieboes, H. B., & Arteel, G. E. (2017). Modeling the Kinetics of Integrin Receptor Binding to Hepatic Extracellular Matrix Proteins. *Scientific Reports*, *7*(1), 1–13. https://doi.org/10.1038/s41598-017-12691-y
Humphries, J. D., Byron, A., & Humphries, M. J. (2006). Integrin ligands at a glance. *Journal of Cell Science*, *119*(19), 3901–3903. https://doi.org/10.1242/jcs.03098
Hynes, R. O. (2002). Integrins: Bidirectional, Allosteric Signaling Machines. *Cell*, *110*(6), 673–687. https://doi.org/10.1016/S0092-8674(02)00971-6
Irvine, D. J., Hue, K. A., Mayes, A. M., & Griffith, L. G. (2002). Simulations of cell-surface integrin binding to nanoscale-clustered adhesion ligands. *Biophysical Journal*, *82*(1), 120–132. https://doi.org/10.1016/S0006-3495(02)75379-4
Jamali, Y., Jamali, T., & Mofrad, M. R. (2013). An agent based model of integrin clustering: Exploring the role of ligand clustering, integrin homo-oligomerization, integrin-ligand affinity, membrane crowdedness and ligand mobility. *Journal of Computational Physics*, *244*, 264–278. https://doi.org/10.1016/j.jcp.2012.09.010

Karagöz, Z., Geuens, T., LaPointe, V. L. S., van Griensven, M., & Carlier, A. (2021). Win, Lose, or Tie: Mathematical Modeling of Ligand Competition at the Cell–Extracellular Matrix Interface. *Frontiers in Bioengineering and Biotechnology*, *9*. https://doi.org/10.3389/fbioe.2021.657244

Karagöz, Z., Rijns, L., Dankers, P. Y. W., van Griensven, M., & Carlier, A. (2021). Towards understanding the messengers of extracellular space: Computational models of outside-in integrin reaction networks. *Computational and Structural Biotechnology Journal*, *19*, 303–314. https://doi.org/10.1016/J.CSBJ.2020.12.025

Kim, J. K., Xu, Y., Xu, X., Keene, D. R., Gurusiddappa, S., Liang, X., Wary, K. K., & Höök, M. (2005). A novel binding site in collagen type III for integrins alpha 1 beta 1 and alpha 2 beta 1. *Journal of Biological Chemistry*, *280*(37), 32512–32520. https://doi.org/10.1074/jbc.M502431200

Kimura, R. H., Levin, A. M., Cochran, V. F., & Cochran, J. R. (2009). Engineered cystine knot peptides that bind alpha v beta 3, alpha v beta 5, and alpha 5 beta 1 integrins with low-nanomolar affinity. *Proteins: Structure, Function, and Bioinformatics*, *77*(2), 359–369. https://doi.org/10.1002/prot.22441

Li, J., & Springer, T. A. (2017). Integrin extension enables ultrasensitive regulation by cytoskeletal force. *Proceedings of the National Academy of Sciences of the United States of America*, *114*(18), 4685–4690. https://doi.org/10.1073/pnas.1704171114

Ma, Y., Ai, G., Zhang, C., Zhao, M., Dong, X., Han, Z., Wang, Z., Zhang, M., Liu, Y., Gao, W., Li, S., & Gu, Y. (2017). Novel linear peptides with high affinity to alpha v beta 3 integrin for precise tumor identification. *Theranostics*, *7*(6), 1511–1523. https://doi.org/10.7150/thno.18401

Mac Gabhann, F., & Popel, A. S. (2004). Model of competitive binding of vascular endothelial growth factor and placental growth factor to VEGF receptors on endothelial cells. *American Journal of Physiology - Heart and Circulatory Physiology*, *286*(1 55-1), 153–164. https://doi.org/10.1152/ajpheart.00254.2003

Macdonald, A., Horwitz, A. R., & Lauffenburger, D. A. (2008). Kinetic model for lamellipodal actin-integrin 'clutch' dynamics. *Cell adhesion & migration*, *2*(2), 95–105. https://doi.org/10.4161/CAM.2.2.6210

Mas-Moruno, C., Rechenmacher, F., & Kessler, H. (2011).
Cilengitide: The First Anti-Angiogenic Small Molecule Drug Candidate. Design, Synthesis and Clinical Evaluation.
Anti-Cancer Agents in Medicinal Chemistry, *10*(10), 753–768.
https://doi.org/10.2174/187152010794728639

Miller, A. E., Hu, P., & Barker, T. H. (2020).
Feeling Things Out: Bidirectional Signaling of the Cell–ECM Interface, Implications in the Mechanobiology of Cell Spreading, Migration, Proliferation, and Differentiation.
Advanced Healthcare Materials, *9*(8), 1901445.
https://doi.org/10.1002/ADHM.201901445

Nishinakamura, R. (2019).
Human kidney organoids: Progress and remaining challenges.
Nature Reviews Nephrology, *15*(10), 613–624.
https://doi.org/10.1038/s41581-019-0176-x

Pierschbacher, M. D., & Ruoslahti, E. (1987).
Influence of Stereochemistry of the Sequence Arg-Gly-Asp-Xaa on Binding Specificity in Cell Adhesion (tech. rep. No. 36).
https://doi.org/10.1016/S0021-9258(18)45376-8

Piras, M., Fleming, I. N., Harrison, W. T., & Zanda, M. (2012).
Linear trifluoroethylamine RGD peptidomimetics: Stereoselective synthesis and integrin αvβ3 affinity. *Synlett*, *23*(20), 2899–2902. https://doi.org/10.1055/s-0032-1317557

Roca-Cusachs, P., Gauthier, N. C., Del Rio, A., & Sheetz, M. P. (2009).
Clustering of alpha 5 beta 1 integrins determines adhesion strength whereas alpha v beta 3 and talin enable mechanotransduction.
Proceedings of the National Academy of Sciences of the United States of America, *106*(38), 16245–16250.
https://doi.org/10.1073/pnas.0902818106

Sankaran, S., Cavatorta, E., Huskens, J., & Jonkheijm, P. (2017).
Cell Adhesion on RGD-Displaying Knottins with Varying Numbers of Tryptophan Amino Acids to Tune the Affinity for Assembly on Cucurbituril Surfaces. *Langmuir*, *33*(35), 8813–8820.
https://doi.org/10.1021/acs.langmuir.7b00702

Shams, H., Soheilypour, M., Peyro, M., Moussavi-Baygi, R., & Mofrad, M. R. K. (2017). Looking "Under the Hood" of Cellular Mechanotransduction with Computational Tools: A Systems Biomechanics Approach across Multiple Scales.
ACS Biomaterials Science & Engineering, *3*(11), 2712–2726.
https://doi.org/10.1021/acsbiomaterials.7b00117

Somogyi, E. T., Bouteiller, J. M., Glazier, J. A., König, M., Medley, J. K., Swat, M. H., & Sauro, H. M. (2015). LibRoadRunner: A high performance SBML simulation and analysis library. *Bioinformatics*, *31*(20), 3315–3321. https://doi.org/10.1093/bioinformatics/btv363

Takagi, J., & Springer, T. A. (2002). Integrin activation and structural rearrangement. *Immunological Reviews*, *186*, 141–163. https://doi.org/10.1034/j.1600-065X.2002.18613.x

Taubenberger, A., Cisneros, D. A., Friedrichs, J., Puech, P. H., Muller, D. J., & Franz, C. M. (2007). Revealing early steps of alpha 2 beta 1 integrin-mediated adhesion to collagen type I by using single-cell force spectroscopy. *Molecular Biology of the Cell*, *18*(5), 1634–1644. https://doi.org/10.1091/mbc.E06-09-0777

Verrier, S., Pallu, S., Bareille, R., Jonczyk, A., Meyer, J., Dard, M., & Amédée, J. (2002). Function of linear and cyclic RGD-containing peptides in osteoprogenitor cells adhesion process. *Biomaterials*, *23*(2), 585–596. https://doi.org/10.1016/S0142-9612(01)00145-4

Wanant, S., & Quon, M. J. (2000). Insulin receptor binding kinetics: Modeling and simulation studies. *Journal of Theoretical Biology*, *205*(3), 355–364. https://doi.org/10.1006/jtbi.2000.2069

Wang, W., Wu, Q., Pasuelo, M., McMurray, J. S., & Li, C. (2005). Probing for integrin alpha v beta 3 binding of RGD peptides using fluorescence polarization. *Bioconjugate Chemistry*, *16*(3), 729–734. https://doi.org/10.1021/bc049763s

Xiao, Y., & Truskey, G. A. (1996). Effect of receptor-ligand affinity on the strength of endothelial cell adhesion. *Biophysical Journal*, *71*(5), 2869–2884. https://doi.org/10.1016/S0006-3495(96)79484-5

Yan, B., Calderwood, D. A., Yaspan, B., & Ginsberg, M. H. (2001). Calpain Cleavage Promotes Talin Binding to the β3 Integrin Cytoplasmic Domain. *Journal of Biological Chemistry*, *276*(30), 28164–28170. https://doi.org/10.1074/jbc.M104161200

Yu, J., Huang, J., Jansen, J. A., Xiong, C., & Walboomers, X. F. (2017). Mechanochemical mechanism of integrin clustering modulated by nanoscale ligand spacing and rigidity of extracellular substrates. *Journal of the Mechanical Behavior of Biomedical Materials*, *72*, 29–37. https://doi.org/10.1016/j.jmbbm.2017.04.018

Zhu, J., Luo, B. H., Xiao, T., Zhang, C., Nishida, N., & Springer, T. A. (2008). Structure of a Complete Integrin Ectodomain in a Physiologic Resting State and Activation and Deactivation by Applied Forces. *Molecular Cell*, *32*(6), 849–861. https://doi.org/10.1016/j.molcel.2008.11.018

4

Force-dependent focal adhesion assembly and disassembly: a computational study

This chapter has been **published** as: Honasoge, K. S., Karagöz, Z., Goult, B. T., Wolfenson, H., LaPointe, V. L. S., & Carlier, A. (2023). Force-dependent focal adhesion assembly and disassembly: A computational study. *PLOS Computational Biology*, *19*(10), e1011500. https://doi.org/10.1371/journal.pcbi.1011500.

Abstract

Cells interact with the extracellular matrix (ECM) via cell–ECM adhesions. These physical interactions are transduced into biochemical signals inside the cell and influence cell behavior. Although cell–ECM interactions have been studied extensively, it is not completely understood how immature (nascent) adhesions develop into mature (focal) adhesions and how this process is influenced by mechanical forces. Given the small size, dynamic nature and short lifetimes of nascent adhesions, studying them using conventional microscopic and experimental techniques is challenging. Computational modelling provides a valuable resource for simulating and exploring various "what if?" scenarios *in silico* and identifying key molecular components and mechanisms for further investigation. Here, we present a simplified mechanochemical model based on ordinary differential equations with three major proteins involved in adhesions: integrins, talin and vinculin. Additionally, we incorporate a hypothetical signal molecule that influences adhesion (dis)assembly rates. We find that assembly and disassembly rates need to vary dynamically to limit maturation of nascent adhesions. The model predicts biphasic variation of actin retrograde velocity and maturation fraction with substrate stiffness, with maturation fractions between 18–35%, optimal stiffness of $\sim$1 pN/nm, and a mechanosensitive range of 1-100 pN/nm, all corresponding to key experimental findings. Sensitivity analyses show robustness of outcomes to small changes in parameter values, allowing model tuning to reflect specific cell types and signaling cascades. The model proposes that signal-dependent disassembly rate variations play an underappreciated role in maturation fraction regulation, which should be investigated further. We also provide predictions on the changes in traction force generation under increased/decreased vinculin concentrations, complementing previous vinculin overexpression/knockout experiments in different cell types. In summary, this work proposes a model framework to robustly simulate the mechanochemical processes underlying adhesion maturation and maintenance, thereby enhancing our fundamental knowledge of cell–ECM interactions.

4.1 Introduction

Direct contact between cells and the extracellular matrix (ECM) through adhesions is a crucial component of multicellular organisms (Thomas *et al.*, 1999). Integrins are transmembrane ECM receptor proteins that assemble as non-covalently bonded heterodimers with α and β subunits (Hynes, 1987).

The integrin ectodomain binds ECM ligands while the cytoplasmic tail is indirectly linked to the actomyosin cytoskeleton of the cell forming a supramolecular assembly or 'clutch' (Berrier & Yamada, 2007; Campbell & Humphries, 2011; Chan & Odde, 2008; Jiang *et al*., 2003). This indirect link consists of a dynamic network of over 200 proteins, collectively termed the 'integrin adhesome' (Horton *et al*., 2015; Winograd-Katz *et al*., 2014). Central to integrin function are the dynamics and balance of extra- and intracellular forces (Fortunato & Sunyer, 2022) which drive the force-dependent evolution of the integrin adhesion complexes (IACs) (Horton *et al*., 2015) leading to changes in their size and composition. *In vitro* studies have shown that adhesion assembly is a multi-step process where integrins are first activated by binding to intracellular adaptor protein molecules such as talin (Cluzel *et al*., 2005; Humphries *et al*., 2007; Pinon *et al*., 2014) and/or to an ECM ligand (Hynes, 2002). Once activated, integrins cluster at the site of adhesion, independent of force and substrate rigidity, to form nascent adhesions (NAs) (Askari *et al*., 2010; Bachir *et al*., 2014; Changede *et al*., 2015). Then, NAs either undergo disassembly or force-dependent maturation by the recruitment of other adaptor proteins such as vinculin, to form focal adhesions (FA) (Figure 4.1A) (C. K. Choi *et al*., 2008; Han *et al*., 2021). These three major steps of adhesion assembly also overlap in time and are not strictly sequential. Understanding interactions between key proteins of the integrin adhesome and force generation will provide valuable insight about cell-ECM interactions with consequences for developmental biology as it can potentially highlight therapeutic targets, contributing to advancements in regenerative medicine.

In addition to questions pertaining to adhesion (dis)assembly, adhesion maturation is also a complex process influenced by the mechanical properties of the substrate (Pelham & Wang, 1997; Schoenwaelder & Burridge, 1999), force-dependent conformational changes (Goult *et al*., 2018; Rothenberg *et al*., 2018; Z. Sun *et al*., 2019; Yao *et al*., 2016; Zhou *et al*., 2021), different catch and slip bond strengths (Aratyn-Schaus & Gardel, 2010; Jiang *et al*., 2003; Novikova & Storm, 2013) and intracellular forces (Giannone *et al*., 2007; Goult *et al*., 2022; Schoenwaelder & Burridge, 1999). How changes in these mechanical factors affect the biochemical composition of adhesions, and which factors determine the decision to mature a particular NA remains unclear.

Given the constraints and challenges of experimental studies, computational modeling can be a valuable resource. Many computational models of cell–ECM interactions have been developed since the first molecular-clutch model by Chan and Odde (2008) (Chan & Odde, 2008) that explained filopodial traction dynamics on compliant substrates (Cheng *et al*., 2016; Cirit *et al*., 2010; Lai &

Chiam, 2011; Macdonald *et al*., 2008; Sonn-Segev *et al*., 2015). Elosegui-Artola and colleagues have extended the Chan and Odde model to include adhesion reinforcement through increases in integrin density (Elosegui-Artola *et al*., 2016) and multiple integrin types (Elosegui-Artola *et al*., 2014). Integrin-based Rho signaling (Cheng *et al*., 2016) and reversible cross-links in the actin filament network (Tan *et al*., 2020) have also been included in previous studies by other groups. More recently, Venturini and Sáez, 2023 have developed an extensive multi-scale model of molecular clutch-driven adhesion mechanics. All these models explore adhesion formation, growth, and the influence of substrate stiffness and actomyosin forces on traction forces, but they are discrete models that simulate a relatively small number of individual particles. They also do not account for the increase in clutch stiffness after recruitment of vinculin and do not consider the disassembly processes to be dynamic and active. In addition, these models give little information about the changes to the overall biochemical composition of adhesions in the cell during the process of maturation of NAs to FAs.

In this study, we developed a new model using ordinary differential equations (ODEs) to describe the biochemical composition of cell–ECM adhesions over time based on mechanical properties like substrate stiffness, adaptor protein stiffness, actomyosin-generated forces, and bond characteristics. Using our model, we studied the fraction of NAs that have the potential to become mature FAs under different mechanical circumstances. Overall, the results from this study shed light on the mechanotransduction mechanisms underlying adhesion maturation and disassembly. This model also provides a reliable starting point to model the larger focal adhesome with over 200 identified proteins (Horton *et al*., 2015).

4.2 Methods

4.2.1 Differential equation model

We developed an ODE-based model that captures changes in the biochemical composition of cell–ECM adhesions based on mechanical properties of the environment and of intracellular proteins. Below we shortly describe the particular phases of the adhesion maturation process and how they are modelled (Figure 4.1B provides an overview of all the species in the system and their interactions). The reactions and parameters are explained in detail in

supplementary methods and Table S.4.1. Table 4.1 provides an overview of the terminology used throughout the manuscript.

Table 4.1: Terminology used in this manuscript.

Term	**Description**
Integrin-Adaptor Protein Complex (IAPC)	Assembly of integrin, talin and vinculin. Three possible IAPCs with talin bound to one, two, or three vinculin molecules are considered.
Pcomp	A pre-complex - an individual IAPC with talin bound to a single vinculin molecule.
Seed (Sx)	A cluster of 25 IAPCs bound parallelly (Fig 4.1C). Seeds are denoted by Sx, where x is the number of vinculin molecules bound to talin in each IAPC that makes up the seed, ($x \in \{1, 2, 3\}$).
Clust (Cx)	A cluster of 50 IAPCs bound parallelly (cluster size taken from (Changede *et al.*, 2015)) (Fig 4.1C). Clusts are denoted by Cx, where $x \in \{1, 2, 3\}$) is the number of vinculin molecules bound to talin in each IAPC that makes up the clust.
Order ($x \in \{1, 2, 3\}$)	The order of a seed/clust is indicative of the number of vinculin molecules bound to talin in each IAPC that makes up the seed/clust – Low, mid and high order seeds/clusts refer to seeds/clusts that are made of IAPCs containing one, two or three vinculin molecules respectively.
Clutch	An umbrella term that refers to a supramolecular assembly of integrins and adaptor proteins that can function as a molecular-clutch between the substrate and the cell (Fig 4.1C). In this model both seeds and clusts are capable of this function.
Actin Bound (AB) (Sxa, Cxa)	Talin and vinculin have actin-binding sites allowing clutches to bind to actin, experience a force and, consequently, an extension. Seeds and clusts that are bound to actin are said to be actin bound (AB) and are denoted by Sxa and Cxa respectively ($x \in \{1, 2, 3\}$).
Actin Unbound (AUB)	The talin–actin and vinculin–actin bonds break at certain force thresholds resulting in the clutches being unbound from actin. These are said to be actin unbound (AUB) clutches and are denoted by Sx and Cx ($x \in \{1, 2, 3\}$). AUB clutches do not experience any force or extension.

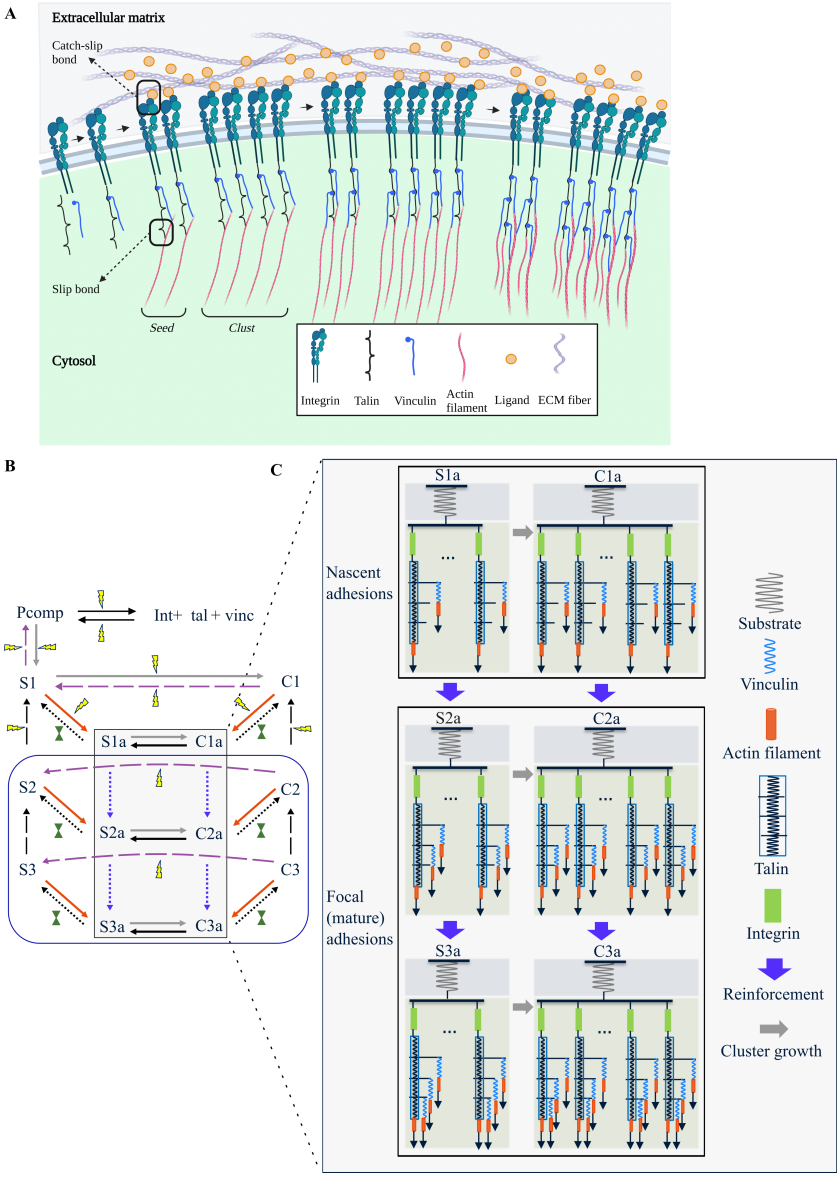

Figure 4.1: Overview of the processes modeled in this study. *Contd. on the following page.*

Figure 4.1: (A) - Integrins bind to talin and vinculin in a precomplexation step, then form a small cluster, termed 'seed'. Seeds can dimerise to form larger clusters, termed 'clusts'. Actin filaments pull on talin and vinculin causing cryptic vinculin-binding sites on talin to be exposed, promoting more vinculin recruitment. This chain can then break at the integrin–ligand catch-slip bond or the talin–actin slip bond (black boxes). See Table 4.1 for a detailed description of the terminology. (B) - Overview of reactions in the model. Int, tal, and vinc refer to concentrations of integrins, talin and vinculin respectively. Black rectangle encloses the reinforcement reactions (expanded further in Fig 1C). Grey arrows represent clust formation reactions. Red arrows represent actin binding reactions. Dotted arrows represent force-dependent reactions - blue dotted: reinforcement, black dotted: actin unbinding. Dashed arrows represent adhesion disassembly reactions, black dashed: talin refolding, purple dashed: cluster breakdown. Yellow lightning bolts indicate rates that undergo signal-dependent rate modification (SDRM), dark green solid hourglasses represent rates that undergo time-dependent rate modification (TDRM). The rate constants undergoing signal-dependent modifications are driven to zero after $\sim$158 s leaving active only the lower part of the model, enclosed in the blue box, representing adhesions that will undergo further maturation. (C) – Talin and vinculin are modelled as Hookean springs (also see Fig A in S1 Appendix). In this model, to capture the process of reinforcement, a maximum of three vinculin binding events occur sequentially (blue arrows) at different points along the talin rod, thereby increasing the stiffness of individual integrin–talin–vinculin spring systems. Clustering is modelled as an increase in the number of integrin–talin–vinculin spring systems in parallel (grey arrows).

Adhesion assembly starts with integrin activation. In this study, we model $\alpha_5\beta_1$ integrins and assume they are activated. We also assume that the ligand spacing on the substrate is sufficiently close for integrin clusters to form. Next, the activated integrins bind to talin and vinculin forming a single low-order integrin-adaptor protein complex (IAPC), also termed pre-complex (Pcomp) (Supplementary section **Integrin activation**), a necessary step for adhesion maturation (Han *et al.*, 2021). Up to 50 IAPCs cluster independent of substrate rigidity and tension to form NAs (Changede *et al.*, 2015). Here, as a simplification, the growth of clusters to the maximal size (50 IAPCs) occurs in two stages - first a small cluster of 25 IAPCs, termed 'seed' (denoted by 'Sx' (Figure 4.1C, Table 4.1) is formed, and a second stage where seeds dimerize, forming a large cluster with 50 IAPCs, termed 'clust' (denoted by 'Cx' (Figure 4.1C, Table 4.1, supplementary section **Integrin activation**)). Here, x $\in$ {1,2,3} denotes the number of vinculin molecules in the individual IAPCs.

Actin-unbound (AUB) seeds and clusts can bind to actin through the actin-binding sites on talin and vinculin, giving actin-bound (AB) seeds and clusts (denoted by 'Sxa' and 'Cxa' respectively, (supplementary section **Adhesion reinforcement**)) that can stretch to different extents (based on the value of x) and hence transmit varying magnitudes of force (Figure 4.1C). When a clutch is AUB, the stretched talin is likely to refold (Yao *et al.*, 2014; Yao *et al.*, 2016). In this model, we assume this makes it very unlikely for AUB seeds of mid- and high- order (S2, S3) to dimerize, and that AB seeds of all order (S1a, S2a, S3a) can dimerize to form AB clusts (C1a, C2a, and C3a) (Figure 4.1B). While the baseline actin-binding rate is k_{act} for all actin-binding reactions, signalling molecules such as focal adhesion kinase (FAK), Src and ERK kinases play a role in adhesion turnover, and their inhibition leads to more maturation (Webb *et al.*, 2004). To implement a similar mechanism to stop indefinite adhesion formation and maturation, we introduce in the model a signal dependent rate modification (SDRM) (see 'Signal dependent rate modification (SDRM)' for details).

Depending on the force on the integrin-ligand (catch-slip) bonds (Kong *et al.*, 2009) and the talin-actin (slip) bonds (Jiang *et al.*, 2003), the force-chain between the cell and the substrate can break at either of these bonds. We capture these phenomena through force-dependent (which in turn depends on substrate rigidity) actin unbinding rates (see supplementary section **Slip and catch bonds** for details). These bonds may also rupture due to random thermodynamic fluctuations before the clutches can reach their maximum force carrying capacity, resulting in a reduction of the total force exerted by the clutches. To account for the spontaneous clutch unbinding in a contin-

uous framework, we introduce a time dependent rate modification (TDRM) (see 'Force-dependent actin-unbinding and time-dependent rate modification (TDRM)' for details).

Up to eleven cryptic vinculin-binding sites (VBS) are uncovered when talin is stretched and unfolded (Gingras *et al*., 2005; Rio *et al*., 2009), leading to reinforcement by vinculin recruitment. In this simplified model, two vinculin-reinforcement events are considered (Supplementary section **Adhesion reinforcement**). Note that low order clutches (S1, C1) already contain one vinculin molecule per IAPC due to pre-complexation (Rxn 1.1 in Table S.4.2, Figure 4.1). Thus, in this model, the talin rod can be bound to at least 1 and at most 3 vinculin molecules. With this framework, we show that we can classify low order clutches (S1, S1a, C1, C1a (Figure 4.1C)) to represent NAs, and mid- and high-order clutches (S2, S2a, C2, C2a, S3, S3a, C3, C3a, (Figure 4.1C)) to represent more mature stages of adhesions, indicative of the fraction of NAs that mature into FAs (Section 'NA formation is rigidity- and force-independent').

The rate of talin unfolding and reinforcement occurring depends on the force experienced by the AB clutch, and increases with increasing force, similar to the Bell model (Bell, 1978; Wang *et al*., 2019; Yao *et al*., 2016) (for more details see section 'Adhesion reinforcement rates'). In the absence of sufficient force however, adhesions disassemble because of mechanical and chemical signals (Stumpf *et al*., 2020). Here, we model two parallel processes of disassembly, namely 1) talin refolding leading to removal of vinculin and weakening clutches, and 2) AUB clusters' breakdown into seeds leading to reduced force carrying capacity of the adhesions (supplementary section **Adhesion disassembly**).

The substrate–integrin–adaptor protein system was formulated as a system of Hookean springs. When clutches bind to the actin filaments, they provide resistance to the motion of actin filaments until bond rupture, caused either randomly or because the catch/slip bond force threshold is reached. We assume that the force exerted by myosin II motors on actin filaments is balanced by the drag force arising due to the viscosity of the cytoplasm. Thus, in the absence of integrin-mediated forces on actin filaments, they move with a constant retrograde velocity (see supplementary section **Actin retrograde velocity**). As a continuous ODE framework is used, we consider the same actin retrograde velocity for all clutches. The force on a clutch depends on its stiffness and extension. The stiffness of a clutch depends on the number of constituent IAPCs and the number of vinculin molecules in each IAPC

(see supplemenbtary sections **Reactions in the model** and **Force quantification**). The total force exerted on the actin filament network thus depends on the number of AB clutches of each type and their stiffnesses. Since we use a continuum approach to account for the abundance of each species, we discretize the concentrations to calculate the total force (see supplementary section **Force quantification**).

Together, the above described processes result in the following set of differential equations (See supplementary section **Reactions in the model** for more detailed descriptions):

$$\frac{d[int]}{dt} = -(\underbrace{k_{1f} \cdot [int] \cdot [tal] \cdot [vinc]}_{Pcomp\ formation} - \underbrace{k_{1r} \cdot [Pcomp]}_{Pcomp\ dissociation}) \tag{4.1}$$

$$\frac{d[tal]}{dt} = -(\underbrace{k_{1f} \cdot [int] \cdot [tal] \cdot [vinc]}_{Pcomp\ formation} - \underbrace{k_{1r} \cdot [Pcomp]}_{Pcomp\ dissociation}) \tag{4.2}$$

$$\begin{aligned}\frac{d[vinc]}{dt} = &-(\underbrace{k_{1f} \cdot [int] \cdot [tal] \cdot [vinc]}_{Pcomp\ formation} - \underbrace{k_{1r} \cdot [Pcomp]}_{Pcomp\ dissociation}) \\ &+ 25 \cdot \Bigg(-(\underbrace{k_{7f} \cdot [S1a] \cdot [vinc]^2 - k_{7r} \cdot [S2a]}_{S1a \underset{\longleftarrow}{reinforce} S2a}) \\ &- (\underbrace{k_{8f} \cdot [S2a] \cdot [vinc]^2 - k_{8r} \cdot [S3a]}_{S2a \underset{\longleftarrow}{reinforce} S3a}) + \underbrace{k_{17f} \cdot [S3]}_{S3 \xrightarrow{\text{refold}} S2} + \underbrace{k_{18f} \cdot [S2]}_{S2 \xrightarrow{\text{refold}} S1} \Bigg) \\ &+ 50 \cdot \Bigg(-(\underbrace{k_{12f} \cdot [C1a] \cdot [vinc]^2 - k_{12r} \cdot [C2a]}_{C1a \underset{\longleftarrow}{reinforce} C2a}) \\ &- (\underbrace{k_{13f} \cdot [C2a] \cdot [vinc]^2 - k_{13r} \cdot [C3a]}_{C2a \underset{\longleftarrow}{reinforce} C3a}) + \underbrace{k_{19f} \cdot [C3]}_{C3 \xrightarrow{\text{refold}} C2} + \underbrace{k_{20f} \cdot [C2]}_{C2 \xrightarrow{\text{refold}} C1} \Bigg)\end{aligned} \tag{4.3}$$

$$\frac{d[Pcomp]}{dt} = (\underbrace{k_{1f} \cdot [int] \cdot [tal] \cdot [vinc]}_{Pcomp\ formation} - \underbrace{k_{1r} \cdot [Pcomp]}_{Pcomp\ dissociation}) \tag{4.4}$$
$$- 25 \cdot \underbrace{(k_{2f} \cdot [Pcomp]^2 - k_{2r} \cdot [S1])}_{Seed\ formation}$$

$$\frac{d[S1]}{dt} = \underbrace{(k_{2f} \cdot [Pcomp]^2 - k_{2r} \cdot [S1])}_{Seed\ formation} - \underbrace{2 \cdot (k_{3f} \cdot [S1]^2 - k_{3r} \cdot [C1])}_{S1 \underleftrightarrow{dimerize} C1} \tag{4.5}$$
$$- \underbrace{(k_{4f} \cdot [S1] - k_{4r} \cdot [S1a])}_{Actin\ binding} + \underbrace{k_{18f} \cdot [S2]}_{S2 \xrightarrow{\text{refold}} S1}$$

$$\frac{d[S2]}{dt} = -\underbrace{(k_{5f} \cdot [S2] - k_{5r} \cdot [S2a])}_{Actin\ binding} + \underbrace{k_{17f} \cdot [S3]}_{S3 \xrightarrow{\text{refold}} S2} - \underbrace{k_{18f} \cdot [S2]}_{S2 \xrightarrow{\text{refold}} S1} + 2 \cdot \underbrace{k_{22f} \cdot [C2]}_{C2 \xrightarrow{\text{breakdown}} S2} \tag{4.6}$$

$$\frac{d[S3]}{dt} = -\underbrace{(k_{6f} \cdot [S3] - k_{6r} \cdot [S3a])}_{Actin\ binding} - \underbrace{k_{17f} \cdot [S3]}_{S3 \xrightarrow{\text{refold}} S2} + 2 \cdot \underbrace{k_{21f} \cdot [C2]}_{C3 \xrightarrow{\text{breakdown}} S3} \tag{4.7}$$

$$\frac{d[S1a]}{dt} = \underbrace{(k_{4f} \cdot [S1] - k_{4r} \cdot [S1a])}_{Actin\ binding} - \underbrace{(k_{7f} \cdot [S1a] \cdot [vinc]^2 - k_{7r} \cdot [S2a])}_{S1a \underleftrightarrow{reinforce} S2a} \tag{4.8}$$
$$- 2 \cdot \underbrace{(k_{14f} \cdot [S1a]^2 - k_{14r} \cdot [C1a])}_{S1a \underleftrightarrow{dimerize} C1a}$$

$$\frac{d[S2a]}{dt} = \underbrace{(k_{5f} \cdot [S2] - k_{5r} \cdot [S2a])}_{Actin\ binding} + \underbrace{(k_{7f} \cdot [S1a] \cdot [vinc]^2 - k_{7r} \cdot [S2a])}_{S1a \underleftrightarrow{reinforce} S2a} \tag{4.9}$$
$$- \underbrace{(k_{8f} \cdot [S2a] \cdot [vinc]^2 - k_{8r} \cdot [S3a])}_{S2a \underleftrightarrow{reinforce} S3a} - 2 \cdot \underbrace{(k_{15f} \cdot [S2a]^2 - k_{15r} \cdot [C2a])}_{S2a \underleftrightarrow{dimerize} C2a}$$

$$\frac{d[S3a]}{dt} = \underbrace{(k_{6f} \cdot [S3] - k_{6r} \cdot [S3a])}_{Actin\ binding} + \underbrace{(k_{8f} \cdot [S2a] \cdot [vinc]^2 - k_{8r} \cdot [S3a])}_{S2a \underleftrightarrow{reinforce} S3a}$$
$$- 2 \cdot \underbrace{(k_{16f} \cdot [S3a]^2 - k_{16r} \cdot [C3a])}_{S3a \underleftrightarrow{dimerize} C3a} \tag{4.10}$$

$$\frac{d[C1]}{dt} = \underbrace{(2 \cdot k_{3f} \cdot [S1]^2 - k_{3r} \cdot [C1])}_{S1 \underset{\longleftarrow}{dimerize} C1} - \underbrace{(k_{9f} \cdot [C1] - k_{9r} \cdot [C1a])}_{Actin\ binding} + \underbrace{k_{20f} \cdot [C2]}_{C2 \xrightarrow{refold} C1} \tag{4.11}$$

$$\frac{d[C2]}{dt} = -\underbrace{(k_{10f} \cdot [C2] - k_{10r} \cdot [C2a])}_{Actin\ binding} + \underbrace{k_{19f} \cdot [C3]}_{C3 \xrightarrow{\text{refold}} C2} - \underbrace{k_{20f} \cdot [C2]}_{C2 \xrightarrow{\text{refold}} C1} - \underbrace{k_{22f} \cdot [C2]}_{C2 \xrightarrow{\text{breakdown}} S2} \tag{4.12}$$

$$\frac{d[C3]}{dt} = -\underbrace{(k_{11f} \cdot [C3] - k_{11r} \cdot [C3a])}_{Actin\ binding} - \underbrace{k_{19f} \cdot [C3]}_{C3 \xrightarrow{\text{refold}} C2} - \underbrace{k_{21f} \cdot [C3]}_{C3 \xrightarrow{\text{breakdown}} S3} \tag{4.13}$$

$$\frac{d[C1a]}{dt} = \underbrace{(k_{9f} \cdot [C1] - k_{9r} \cdot [C1a])}_{Actin\ binding} - \underbrace{(k_{12f} \cdot [C1a] \cdot [vinc]^2 - k_{12r} \cdot [C2a])}_{C1a \underset{\longleftarrow}{reinforce} C2a} \tag{4.14}$$

$$+ \underbrace{(k_{14f} \cdot [S1a]^2 - k_{14r} \cdot [C1a])}_{S1a \underset{\longleftarrow}{dimerize} C1a}$$

$$\frac{d[C2a]}{dt} = \underbrace{(k_{10f} \cdot [C2] - k_{10r} \cdot [C2a])}_{Actin\ binding} + \underbrace{(k_{12f} \cdot [C1a] \cdot [vinc]^2 - k_{12r} \cdot [C2a])}_{C1a \underset{\longleftarrow}{reinforce} C2a} \tag{4.15}$$

$$- \underbrace{(k_{13f} \cdot [C2a] \cdot [vinc]^2 - k_{13r} \cdot [C3a])}_{C2a \underset{\longleftarrow}{reinforce} C3a} + \underbrace{(k_{15f} \cdot [S2a]^2 - k_{15r} \cdot [C2a])}_{S2a \underset{\longleftarrow}{dimerize} C2a}$$

$$\frac{d[C3a]}{dt} = \underbrace{(k_{11f} \cdot [C3] - k_{11r} \cdot [C3a])}_{Actin\ binding} + \underbrace{(k_{13f} \cdot [C2a] \cdot [vinc]^2 - k_{13r} \cdot [C3a])}_{C2a \underset{\longleftarrow}{reinforce} C3a} \tag{4.16}$$

$$+ \underbrace{(k_{16f} \cdot [S3a]^2 - k_{16r} \cdot [C3a])}_{S3a \underset{\longleftarrow}{dimerize} C3a}$$

$$\frac{d[signal]}{dt} = \frac{-k_{23_{vmax}} \cdot [signal]}{k_{23_{KM}} + [signal]} \tag{4.17}$$

Reactions in our model are, by default, considered to be reversible and follow mass-action kinetics, unless mentioned otherwise. Concentrations are written between square brackets (e.g., [int]) when mentioned in the text. Baseline parameter values and rate constants can be found in Table S.4.1. We refer the reader to supplementary section **Reactions in the model** for detailed descriptions of all reactions in the model and the underlying reasoning. Below, we highlight the novel methodological approaches (signal- and time-dependent rate modification (SDRM and TDRM)), and provide brief explanations of a few mathematical formulations and assumptions that are used in this model.

4.2.2 Signal dependent rate modification (SDRM)

Nascent adhesions (NAs) form in large numbers and most are disassembled within a time scale of a few minutes (Changede & Sheetz, 2017; C. K. Choi *et al*., 2008). As the cell protrudes, the distance between the cell membrane and the NAs increases, and actin depolymerization rates are higher away from the cell membrane (Oser & Condeelis, 2009). Thus, numerous NAs may be supported near the cell membrane but in the absence of this scaffold, many NAs disassemble. Various signal cascades also regulate adhesion disassembly. Signalling molecules such as focal adhesion kinase (FAK), Src and ERK kinases play a role in adhesion turnover, and their inhibition leads to more maturation (Webb *et al*., 2004). However, most studies have investigated the effects of signalling molecules on the turnover of FAs and not NAs (Hamadi *et al*., 2005; Vicente-Manzanares & Horwitz, 2011), and the exact mechanical or chemical triggers for NA disassembly remain elusive (Lin & Asaro, 2022). NA assembly at the cell front, maturation, and disassembly away from the leading edge occur constantly due to above mentioned mechanisms. In this study, we focus on one cycle of NA formation and investigated the differences in NA maturation on different substrate stiffnesses. To implement a mechanism to stop indefinite adhesion formation and maturation, it is hypothesized that there exists a signal molecule of which a minimum concentration, $\text{signal}_{\text{thresh}}$, is required for new NA formation and low-order AUB clutches (S1,C1) to bind actin (for maturation). The concentration [signal] of this molecule is initially high and decreases at an arbitrary rate following Michaelis-Menten kinetics given by Eq.4.17

Since we model the signal decay with Michaelis-Menten kinetics, initial estimates for values of the maximum velocity $k_{23_{\text{vmax}}}$ and the Michaelis constant

$k_{23_{KM}}$ were based on those reported in literature for FAK Tyr-397 phosphorylation in the presence of ATP (Rashmi *et al*., 2021) but were adjusted such that the concentration of [signal] reaches the $signal_{thresh}$ in 58 seconds, which is the approximate duration of the NA assembly phase as measured in experiments (Chan & Odde, 2008). When the [signal] falls below $signal_{thresh}$, it is analogous to a signalling pathway being activated, and some reactions rates are modified as detailed in section **Signal-dependent rate modification (SDRM)**. Thus, the rate of decay of [signal] determines the amount of time available before NA disassembly starts in which adhesion maturation can occur. Note that the model behaviour does not change if we assume the opposite i.e., [signal] increases over time and there is an upper limit for its concentration beyond which actin binding does not occur (Figure S.4.3B).

4.2.3 Force-dependent actin-unbinding and time-dependent rate modification (TDRM)

A cell–ECM force chain is broken if either the integrin–ligand (catch-slip) bond (Kong *et al*., 2009) or the talin–actin (slip) bond (Jiang *et al*., 2003) ruptures as a result of reaching the respective force thresolds or due to random thermodynamic fluctuations. This is described in detail under the supplementary methods sections **Slip and catch bonds** and **Time-dependent rate modification (TDRM)**. To capture the combined dynamics of the catch-slip and slip bonds, as well as the effect of random bond ruptures, the actin unbinding rates ($k_{4r}, k_{5r}, k_{6r}, k_{9r}, k_{10r}, k_{11r}$) are defined as follows:

$$k_{off_{CS}} = A \cdot e^{-b \cdot F_{clutch}} + C \cdot e^{d \cdot F_{clutch}} + k_{TDRM} \cdot k_{slip_{UL}} \cdot e^{\frac{F_{clutch}}{F_{th_i}}} \tag{4.18}$$

where F_{clutch} is the force on an individual IAPC in the clutch (see supplementary section **Force quantification** where F_{clutch} is described in detail). The first and second terms describe the integrin–ligand catch-slip bond, and the third term describes the talin-actin slip bond where F_{th_i} is bond rupture threshold for a given clutch type ($i \in \{1, 2, 3\}$, refer Table S.4.1) and $k_{slip_{UL}}$ is the unloaded dissociation rate. k_{TDRM} is the time-dependent rate modification (TDRM) factor that is required to qualitatively account for the reduction in the total force caused by spontaneous clutch unbinding events. k_{TDRM} is given by:

$$k_{TDRM} = 1 + k_{sens} \cdot t_{clutch} \cdot dt \tag{4.19}$$

where t_{clutch} is the number of simulated time-steps that a clutch remains actin-bound, *dt* is the time-step and k_{sens} is a parameter that determines the magnitude of the influence. In short, this definition captures the decreasing likelihood of an AB clutch remaining AB for long periods of time. It has been shown that integrin-ligand bonds undergo cyclic mechanical reinforcement (CMR) leading to longer lifetimes (Kong *et al*., 2013). This implies that on soft substrates where the force-loading rate is low, integrin-ligand bonds experience fewer force cycles in a given time period compared to stiff substrates and consequently are more likely to break on soft substrates. Previous studies model CMR with an increased bond-dissociation rate at low forces (Elosegui-Artola *et al*., 2016; Venturini & Sáez, 2023). Here, TDRM can also capture these effects as its effects are larger on softer substrates where clutches take longer to reach their force thresholds.

When an AB clutch experiences a force equal to its force threshold, it unbinds from actin and becomes an AUB clutch. Thus, the concentration of the AB clutch is set to 0, and the concentration of its AUB counterpart is increased by the same amount.

4.2.4 Adhesion reinforcement rates

The rate at which the talin rod unfolds increases with applied force and has been described in previous studies by the Bell model (Bell, 1978; Wang *et al*., 2019; Yao *et al*., 2016). Here, the Bell formulation was adapted such that the rate increases exponentially with force until the vinculin binding force threshold F_{vb} is reached, beyond which it remains constant. The rate is given by:

$$k_{unfold} = \begin{cases} k_{unfold_{UL}} \cdot e^{k_{UF} \cdot \frac{F_{clutch}}{F_{vb_i}}} & \text{if } F \leq F_{vb_i} \\ k_{unfold_{UL}} \cdot e^{k_{UF}} & \text{if } F > F_{vb_i} \end{cases} \tag{4.20}$$

where $k_{unfold_{UL}}$ is the rate of unloaded talin unfolding, k_{UF} is a parameter controlling force-dependence, F_{clutch} is the force experienced by an individual IAPC in the clutch, and F_{vb_i} is the vinculin binding force threshold, with $i \in \{1, 2\}$ corresponding to the first and second vinculin binding steps. Here, F_{vb_1} = 5 pN and F_{vb_1} = 12 pN (Rio *et al*., 2009; Yao *et al*., 2016). Vinculin binding is assumed to occur instantaneously once the VBS is uncovered (Wang *et al*., 2019; Wang *et al*., 2021), and hence the rates of reinforcement were determined based on the force-dependent unfolding kinetics of talin as observed in

single-molecule experiments using magnetic tweezers (Rio *et al.*, 2009). Detailed description of the method used for curve-fitting can be found in the supplementary section **Curve-fitting for parameter values**.

4.2.5 Local sensitivity analysis

As the model included many parameters whose values were either estimated or adapted to fit experimental data, a local sensitivity analysis was performed. The range of values tested for each parameter was the baseline value (Table S.4.1) $\pm 10\%$ and $\pm 20\%$. To quantify the influence, two different metrics were used as outcomes, namely 1) the concentration of integrins in mid- and high-order AB and AUB clutches ([S2]+[S2a]+[S3]+[S3a]+[C2]+[C2a]+[C3]+[C3a]) at equilibrium (the last time point), and 2) the optimal stiffness. Outcome 1 represents the total fraction of integrins in the system that made it beyond the initial force-independent stage of adhesion formation, indicative of the fraction of NAs that mature into FAs. Outcome 2 represents an overall influence on the system as it quantifies the mean force exerted during the length of the simulation for a variety of substrate stiffnesses. In addition, cells are known to be able to tune their mechanosensitive ranges to adapt to their environments, an aspect on which outcome 2 can shed light. As different parameters may have different levels of influence based on the substrate stiffness, the sensitivity of outcome 1 to each parameter was evaluated for four substrate stiffnesses (k_{sub} = 0.1, 1, 10, 100 pN/nm).

Parameter sensitivity analysis was performed on 22 parameters (supplementary section **Sensitivity analysis results**, Figure S.4.9 and Figure S.4.10), and the ones with the highest influence are presented in the main text. The parameter sensitivity for a parameter *p* for an outcome *i* was calculated as follows:

$$Sensitivity_{p,i} = \frac{|Outcome_i(p + \Delta p) - Outcome_i(p)|}{Outcome_i(p)} / \frac{\Delta p}{p} \tag{4.21}$$

where $Outcome_i(p + \Delta p)$ represents the value of the outcome metric with the changed parameter value, *Outcome$_i$(p)* is the value of the outcome metric with the baseline parameter value, and Δp and p are the change in the parameter and the baseline parameter value respectively.

4.2.6 Initial conditions

The initial concentrations of integrins, talin and vinculin were assumed to be equal and set to 1 μM, and that of all other species set at 0. Vinculin was assumed to be abundantly available within the cytoplasm and thus modelled at a constant concentration of 1 μM throughout the simulation.

4.2.7 Simulation Steps

All simulations were run for 600 seconds. Euler's forward integration method was used to solve the ODEs with a time step *dt* of 5 ms as used in previous computational studies (Chan & Odde, 2008; Elosegui-Artola *et al*., 2016). For mass conservation steps, see supplementary methods section "Signal-dependent rate modification (SDRM)". The steps of integration and the order of updates (Figure 4.2) of the different aspects of the model are as follows:

1. Force-dependent rate constants are calculated In particular, the following rates are evaluated at the current force:
    a) First reinforcement rates: (k_{7f},k_{12f}) using eq. 4.20
    b) Second reinforcement rates: (k_{8f}, k_{13f}) using eq. 4.20
    c) Signal-dependent rate modification: (k_{1r}, k_{2r}, k_{3r}, k_{4f}, k_{9f}, k_{18f}, k_{20f}, k_{21f}, k_{22f}) are updated by multiplying their baseline values by sig_{dep} (eq. S.56)
    d) Catch-slip bond rates with time-dependent rate modification: (k_{4r}, k_{5r}, k_{6r}, k_{9r}, k_{10r}, k_{11r}) using eq. 4.18 and eq. 4.19
2. Concentrations are updated based on current rate constants by solving the differential equations listed above
3. The slip bond threshold is checked for each clutch type
    a) If the slip bond threshold is reached, the force on the clutch is reset to 0
    b) The concentration of the actin-bound form of the clutch is converted to the actin-unbound form
4. The total force exerted by actin-bound clutches is calculated based on discretized concentrations using eq. S.54

5. Retrograde velocity is updated based on the current total force in the system using eq. S.50
6. All substrate-clutch spring systems are extended by an amount $v_{retro} \cdot dt$
7. Force on each clutch is updated using eq. S.52.

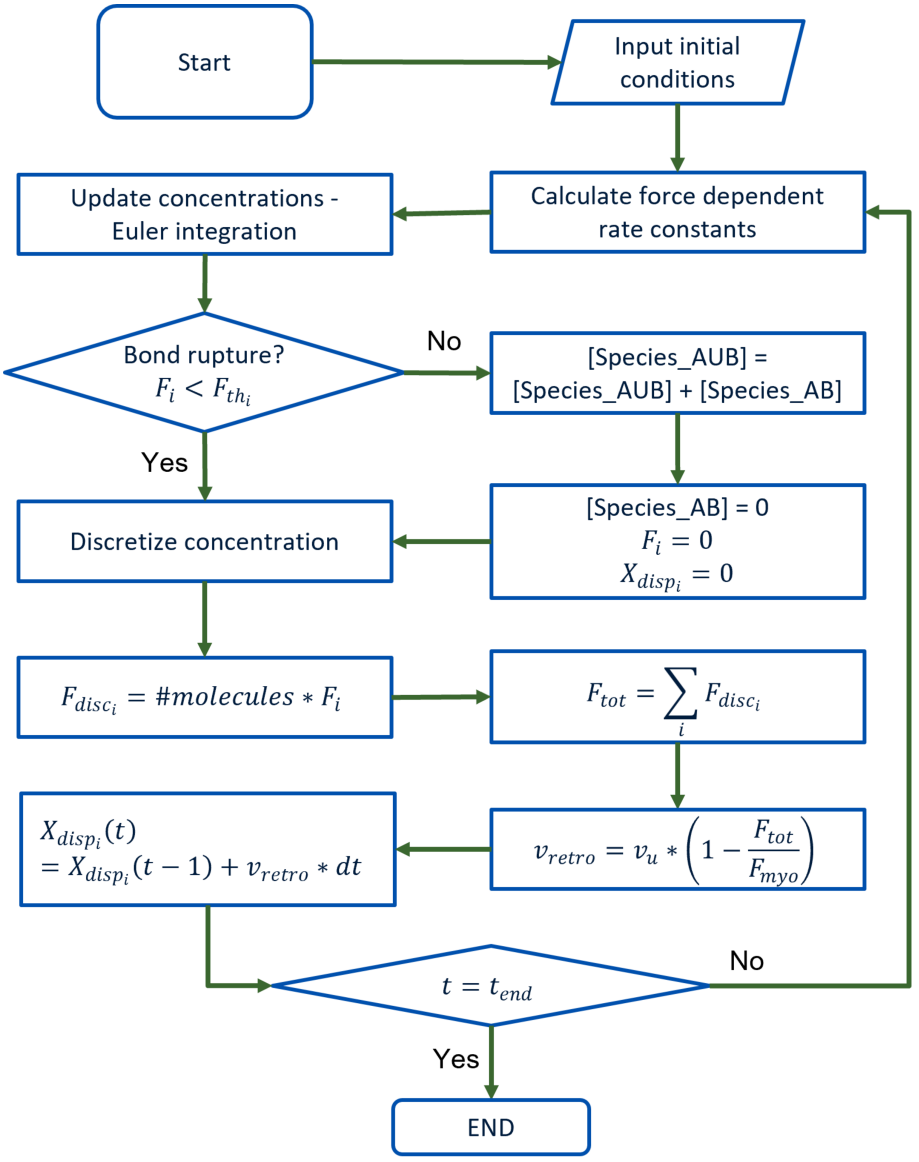

Figure 4.2: Schematic showing the flowchart for simulation and force quantification.

4.3 Results

To explore the influence of mechanical properties like substrate stiffness, adaptor protein stiffness, actomyosin-generated forces and bond characteristics on NA/FA maturation, we developed a computational model that captures the overall changes to the IAC compositions as adhesions form and mature. The model, based on ODEs, consists of a single compartment that represents a patch of the cell where adhesions form, and considers three core components: integrins, talin and vinculin, from which 14 other species are made. The dynamic NA/FA maturation is modelled by a total of 22 reactions (explained in Methods and supplementary section Reactions in the model, Table S.4.1 and Table S.4.2) that largely represent three distinct processes (Figure 4.1): (i) adhesion formation, (ii) reinforcement and growth, and (iii) adhesion disassembly.

Using our mechanochemical computational model, we find that dynamic rates of assembly and disassembly, which are likely regulated by biochemical signalling events, are essential to determine the subset of NAs that mature. The model was found to satisfy mass conservation (supplementary results section **The model satisfies mass conservation**, Figure S.4.2).

4.3.1 NA formation is rigidity- and force-independent

When only pre-complex, initial seed and clust formation reactions (Rx1, Rx2 and Rx3) were active (see supplementary section **Integrin activation**, Table S.4.2) the concentration of seeds and clusts for all substrate stiffnesses tested were equal, in line with previous experimental evidence showing that NA formation is substrate rigidity-independent (Changede *et al.*, 2015) (Figure 4.3A). This is the result of the rigidity- and force-independent rate constants (k_{1f}, k_{1r}, k_{2f}, k_{2r}, k_{3f}, k_{3r}) for reactions Rx1, Rx2 and Rx3. Thus, the concentration of seeds and clusts formed only depends on the initial concentrations of int, tal, and vinc, which were all set to 1 μM, with vinc being constant throughout the simulation (see Methods).

The baseline signal decay parameters (Table S.4.1) were set to match experimentally measured time periods for the assembly phase of NAs (C. K. Choi *et al.*, 2008), leading to the concentration of signal crossing the $signal_{thresh}$ at t_{sig} = 58.04 s (Figure 4.3A, Figure S.4.3 and supplementary section **Signal decay (or growth) rate matches nascent adhesion assembly phase**). Additionally,

when maturation (actin-binding) reactions were disabled, the predicted concentration of integrins in seeds and clusts was ≥ 0.1 μM (Figure 4.3A) for approximately 158 s, a duration indicative of the lifetime of nascent adhesions and is in line with experimentally measured average lifetimes of NAs of 135–180 s (Changede & Sheetz, 2017; Changede *et al.*, 2015; C. K. Choi *et al.*, 2008). Additionally, the concentrations of S1 and C1 also matched experimentally observed trends in abundance of early NAs (C. K. Choi *et al.*, 2008) (Figure 4.3A)

When actin-binding reactions were allowed however, the concentration of S1a and C1a reached a peak at 58 s (Figure 4.3B), followed by a sharp fall to 0. This decrease is because the signal-dependent reduction in actin-binding rates reduced the formation of these species, but the rate constants (k_{7f} and k_{12f}) of reinforcement reactions, Rx7 and Rx12, that transform S1a and C1a to S2a and C2a, respectively, remained unchanged. Thus, S1a and C1a were almost completely consumed after approximately 158 s. The model also predicts highest [S1a] and [S3a] to be on the 100 pN/nm and 1 pN/nm substrates respectively (Figure 4.3B), whereas [C1a] and [C3a] are always higher on 1 pN/nm. Given that in the absence of maturation reactions [S1] and [C1] are rigidity-independent, this highlights the difference in reinforcement rates between stiffnesses. The rate of consumption of S1a is lowest on the 100 pN/nm substrate as the clutches reach the talin-actin slip bond threshold rapidly, leaving little time for vinculin-binding reinforcement reactions, and hence clutches accumulate in this state. This explains the lower [S2a] and [S3a] on stiff substrates. Additionally, the maximum concentrations of AB clutches is limited only by the time taken for the clutch to reach its force threshold. For k_{sub} = 100 pN/nm the increase in mean periods of S1a to C1a is 0.02 seconds, which is negligible compared to 1.5-2 fold increases for other stiffnesses (Table 4.2). Thus clutches remain AB for a relatively much shorter time, leading to lower concentrations of [C1a] for k_{sub} = 100 pN/nm. As such, the model accounts for one cycle of NA assembly, followed by either maturation or disassembly. When maturation was enabled, the concentrations of S2a, C2a, S3a and C3a nearly reached an equilibrium after 600 s (Figure 4.3B). These results imply that in our model, low order species (S1, C1, S1a, C1a) represent NAs while mid- and high-order species (S2, C2, S2a, C2a S3, C3,S3a, C3a) represent the stable adhesions that may further mature to become FAs.

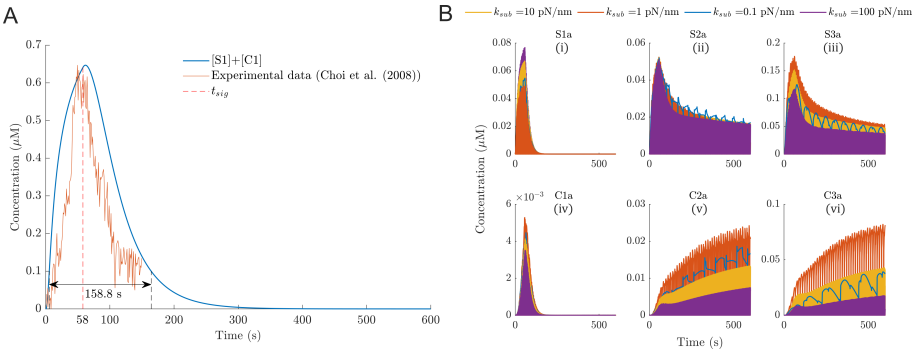

Figure 4.3: While NA formation is substrate stiffness independent, maturation is influenced considerably by stiffness. (A) – Concentration over time of species in the model that represent NAs (S1 and C1). The curves for all tested substrate rigidities overlap and hence appear as a single (blue) line. The vertical dotted line marks the time point when the signal threshold is crossed and hence new NA formation reduces. (B) – Concentrations over time of all the actin-bound species. Species representing NAs (S1a, C1a) increase initially before being driven to 0 after the signal concentration drops below the threshold. The highest levels of maturation occur on substrate of moderate stiffness (k_{sub} = 1 pN/nm).

4.3.2 Adhesion maturation is highest on moderate substrate stiffness

The concentrations of S3a, C2a and C3a are highest on a moderate substrate stiffness (1 pN/nm), and lower on stiffer or softer substrates (Figure 4.3B) in accordance with experimental findings (Bangasser *et al.*, 2017; Chan & Odde, 2008; Cheng *et al.*, 2016; Zhou *et al.*, 2017). In addition, in the early periods of the simulations (0 to 70 s, Figure S.4.4), the concentrations [C3a], [C2a] and [S3a] increase most rapidly on k_{sub}=1 pN/nm. While these results are for simulations with a constant vinculin concentration, similar results were obtained for limited vinculin conditions (supplementary results section **Limited vinculin results**, Figure S.4.5).

Although the concentration plots in Figure 4.3B are oscillatory due to the repeated bond-rupture events that transform AB clutches to AUB clutches, pushing the concentration of AB clutches to 0 and causing a spike in the concentration of AUB clutches, the peaks approach a steady state. We observed generally shorter periods of oscillations for AB clutches on stiffer substrates (Table 4.2), which is also reported by Venturini and Saez (2023) (Venturini & Sáez, 2023). The periods predicted in our simulations were in good agreement with previous studies (Table 4.2) (Bangasser *et al.*, 2013; Chan & Odde, 2008; Gong *et al.*, 2018; Venturini & Sáez, 2023). Note that the periods for C2a and C3a on k_{sub}=0.1 pN/nm, are of the order of the lifetime of NAs ($\sim$60 s) or higher. Thus, these results suggest that C2a and C3a can represent (partially) mature adhesions and not nascent adhesions, and that adhesions are likely to disassemble before sufficient reinforcement can occur on very soft substrates.

Table 4.2: Mean periods in seconds of different actin-bound clutches for different substrate stiffnesses.

Substrate stiffness (pN/nm)	**S1a**	**S2a**	**S3a**	**C1a**	**C2a**	**C3a**
0.1	15.37	32.72	55.74	30.43	64.83	110.48
1	2.01	4.22	7.15	3.67	7.76	13.18
10	0.47	0.94	1.58	0.62	1.26	2.13
100	0.31	0.61	1.02	0.33	0.64	1.07

4.3.3 Traction force is highest on substrates of moderate stiffness

An optimal substrate stiffness is one at which the highest traction force is generated at the adhesions (Bangasser *et al.*, 2013). At this stiffness, the time taken for the force on a clutch to reach the bond-rupture threshold is roughly equal to the lifetime of an unloaded AB-clutch that spontaneously dissociates from actin (or the substrate) due to thermodynamic fluctuations, maximizing the lifetime of a complete ECM-integrin-adaptor protein-actin chain (Bangasser & Odde, 2013; Chan & Odde, 2008). In our simulations, the highest traction force was reached at k_{sub} = 1 pN/nm, which also corresponded to the point where the lowest retrograde velocity was recorded (Figure 4.4A). The frequency of oscillations was higher for high stiffness substrates (Table 4.2) and the actin unbinding rate was higher for soft substrates (Figure S.4.6), suggesting that k_{sub} = 1 pN/nm gives rise to a 'load-and-fail' regime where clutches are loaded at a moderate rate, and 'frictional slippage' occurs on stiffer substrates where rapid loading causes clutches to disengage too quickly, resulting in lower average AB-clutch concentration (Bangasser *et al.*, 2013; Chan & Odde, 2008). Altogether, these observations show that the optimal stiffness for NA maturation in our model is at k_{sub} = 1 pN/nm.

Figure 4.4A shows the agreement between the mean retrograde velocity in our simulations and other computational (Elosegui-Artola *et al.*, 2014; Venturini & Sáez, 2023) and experimental (Chan & Odde, 2008) studies. A recent computational study also reports a similar biphasic behavior with an optimal stiffness around 10 pN/nm (Venturini & Sáez, 2023). However, this is only observed when the weakest link in the force chain in their model is simulated as a catch bond. Additionally, our model predicts a linear increase in the mean velocity between 10^0 pN/nm and 10^2 pN/nm (Figure 4.4B), which is the stiffness range where the cell is mechanosensitive – a change in stiffness translates linearly into a change in actin retrograde velocity. This is in good agreement with previous studies which report ranges of 10^0–10^1 to 10^0–10^2 pN/nm (Bangasser *et al.*, 2017; Chan & Odde, 2008; Selig *et al.*, 2020). The decrease in the predicted retrograde velocity for stiffnesses $> 10^1$ pN/nm in the computational study of Elosegui-Artola et al. (Elosegui-Artola *et al.*, 2014)(Figure 4.4A) arises because of reinforcement which they model as an increase in integrin density beyond a certain threshold force on a clutch. While the range of velocities reported varies, in our model, the lowest velocity depends on the concentration of myosin motors $conc_{myo}$, which is a free parameter that was adjusted such that the lowest velocity was within 10% of that

reported by Chan and Odde, 2008.

It is also important to note that the optimal stiffness of 1 pN/nm is reached only when the TDRM of actin-unbinding rates was applied (see subsection 'Force-dependent actin-unbinding and time-dependent rate modification (TDRM)' in Methods and supplementary section **Time-dependent rate modification (TDRM)**). In absence of TDRM, the equilibrium concentrations of mid- and high-order AB clutches ([S2a], [S3a], [C2a], [C3a]) are highest on k_{sub} = 0.1 pN/nm and decrease monotonically with increasing substrate stiffness (Figure S.4.7). Note that the decrease in equilibrium concentrations of mid- and high-order AB clutches caused by TDRM is the largest on k_{sub} = 0.1 pN/nm and least on k_{sub} = 100 pN/nm. In summary, these results show that TDRM of disassembly rates is essential for obtaining an optimal stiffness through mechanosensing. As adhesion assembly and disassembly are tightly regulated processes, altering factors that affect adhesion disassembly allows for more robustness and resilience in the mechanosensing and adhesion maturation processes.

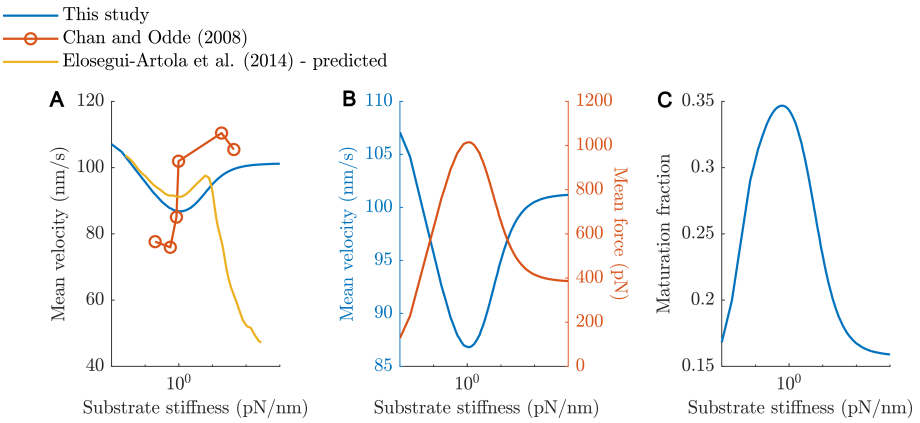

Figure 4.4: Model predictions of mean actin retrograde velocity and maturation fraction for the baseline model. (A) shows the predicted velocity vs substrate stiffness compared to previous studies, (B) shows the predicted velocity (blue) and mean force exerted by all adhesions (red) in this model, and (C) shows the NA maturation fraction vs substrate stiffness.

4.3.4 18% and 35% of NAs mature on soft and stiff substrates respectively

After identifying species in the model that represent NAs (S1, C1, S1a, C1a) and adhesions that mature to FAs (S2, C2, S2a, C2a, S3, C3, S3a, C3a) based on comparisons of their concentrations, bond formation and rupture times to values reported in literature, we used our model to predict the fraction of NAs that may mature into FAs on a range of substrate stiffnesses. Notably, our model also predicts a biphasic trend in maturation fraction (MF) (Figure 4.4C). More specifically, the MF ranges from approximately 18% on very soft substrates (10^{-2} pN/nm) to around 35% on substrates of moderate stiffnesses (10^{0} pN/nm), which lies within experimentally determined ranges of MFs under different conditions (Han *et al.*, 2021; Swaminathan *et al.*, 2016). The talin refolding factor $\text{tal}_{\text{rf}_{\text{factor}}}$ controls the rate of vinculin-dissociation and hence relative stability of higher order species in our model (see supplementary section **Adhesion disassembly**) and its baseline value is set to 0.5 in our simulations. As vinculin is known to 'lock' talin in the unfolded conformation (Yao *et al.*, 2014), reducing the value of $\text{tal}_{\text{rf}_{\text{factor}}}$ to 0.2 maintained the same trends but resulted in a slightly higher maturation fraction, ranging from 20% to 50% (Figure S.4.8).

4.3.5 Predicted NA maturation fraction is most sensitive to talin stiffness and vinculin availability

Our model predicted an optimal substrate stiffness of approximately 1 pN/nm at which 34.3% of NAs mature. To ensure both the optimal stiffness and MF predictions were not heavily influenced by the choice of parameter values, we performed a local sensitivity analysis on 22 parameters (supplementary section **Sensitivity analysis results**, Figure S.4.9, Figure S.4.10), and address the most important and representative ones here.

Increases in initial vinculin concentration $\text{Initial}_{\text{vinc}}$ leads to large increases in MF (Figure 4.5A) and small increases in the optimal stiffness (Figure 4.5B). A higher vinculin concentration increases the likelihood of maturation leading to increased force carrying capacity and consequently a shift of the optimal stiffness to stiffer regimes. In contrast, a lower vinculin availability leads to decreased maturation fractions and traction force and a higher mean retrograde velocity.

The optimal substrate stiffness, the stiffness at which the lowest mean retrograde velocity is observed (Figure 4.5B), was most sensitive to changes in k_{tal}, the stiffness of talin. Increasing k_{tal} shifts the optimum stiffness to softer substrates and reduces the MF (Figure 4.5B). Talin is the most abundant mechanosensitive component in the model and majorly contributes to determining the stiffness of clutches, which effectively determines the optimum substrate stiffness. Increasing the stiffness of talin results in stiffer clutches that reach the bond force-thresholds sooner, leaving less time for maturation reactions and consequently lower MF.

A higher (lower) initial integrin concentration $Initial_{int}$ only leads to a small decrease (increase) in the mean retrograde velocity, and has negligible effects on optimum stiffness (Figure 4.5 and Figure S.4.10). The increase (decrease) in the mean retrograde velocity is because there are more (fewer) clutches available to bind to actin and slow it down. However, the optimum stiffness is unaffected as this higher (lower) availability of integrins is true and of the same magnitude on all stiffnesses. Similarly, changes in the talin refolding rate, tal_{rf}, affect the mean retrograde velocities more than the optimum stiffness. This is explained with similar reasoning - changes in tal_{rf} affect the outcome on all substrate stiffnesses in the same way and do not cause any changes in the relative proportions of concentrations of different clutches or vinculin consumption.

An increase in v_u, the unloaded actin retrograde velocity, pushed the optimal substrate stiffness to softer substrates in line with previous computational studies (Bangasser *et al.*, 2013; Bangasser *et al.*, 2017) and leads to lower MF (Figure 4.5). A higher retrograde velocity causes faster force build-up resulting in frictional slippage on softer substrates. Similar to k_{tal}, it also results in lower MF. On the contrary, increases in k_{act} pushed the optimal substrate stiffness towards stiffer substrates and increases MF (Figure 4.5), which is due to the 'strengthening' of clutches as they are more likely to bind actin, get stretched and recruit vinculin, and on average there are more AB clutches resulting in higher forces on softer substrates (Bangasser *et al.*, 2013; Bangasser *et al.*, 2017).

Out of all the parameters, the stiffness of talin k_{tal}, initial vinculin concentration $initial_{vinc}$, talin refolding rate tal_{rf}, and the actin-binding rate k_{act} had the greatest influence on MF, similar for both an increase and decrease in the parameter values (Figure S.4.9). Importantly, the TDRM factor k_{sens}, and the cluster formation (k_{14f}, k_{15f}, k_{16f}) and disassembly (k_{21f}, k_{22f}) rates had negligible influences on the MF and optimal stiffness (Figure S.4.9, Figure S.4.10)

for the tested range of values ($\pm 20\%$).

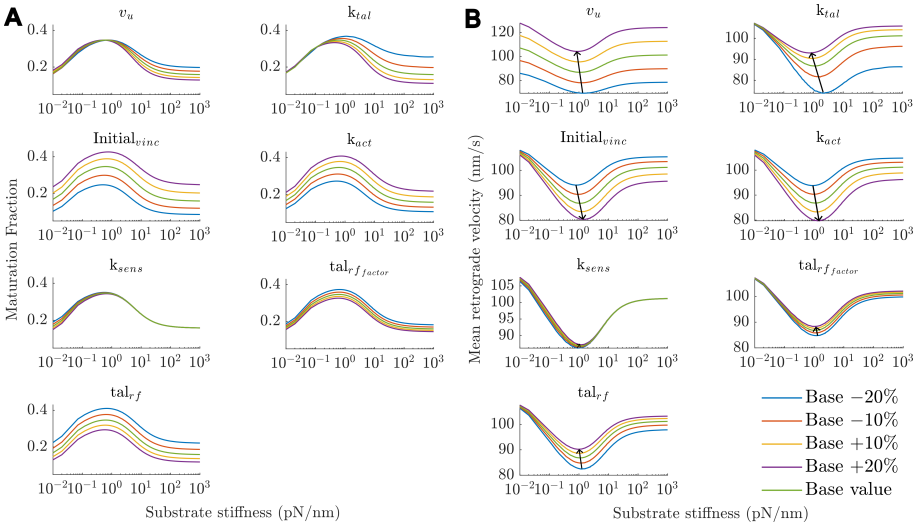

Figure 4.5: Sensitivity analysis results (A) – Maturation fraction vs stiffness and (B) – Mean retrograde velocity vs stiffness for a local variation in parameter values of different parameters. Black arrows in B point in the direction of increasing parameter value and track the optimal stiffness.

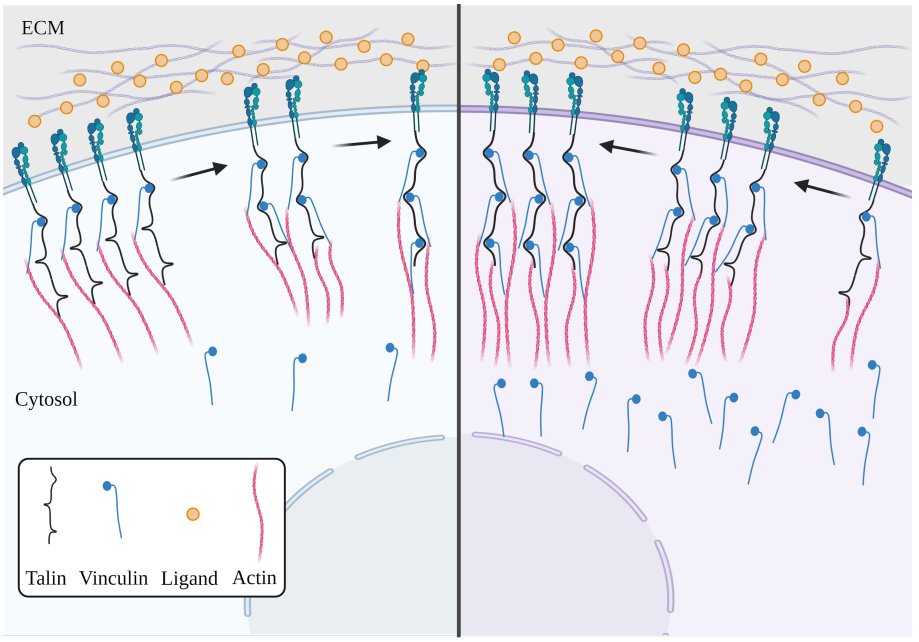

Figure 4.6: Vinculin concentration can influence maturation fraction. (A) and (B) are cell types or biological contexts where vinculin availability is low and high respectively. In A, the likelihood of vinculin binding to the exposed vinculin-binding sites on talin is low leading to a low maturation fraction. However, in B, due to a relatively higher vinculin availability, the integrin-actin link is highly likely to be reinforced by vinculin, increasing the maturation fraction.

4.4 Discussion

Although cell-ECM adhesions are extensively studied, the effects of mechanical properties of the ECM and intracellular proteins on the early processes of adhesion assembly, maturation and traction force generation remain unclear. Here, we present a computational model that innovatively bridges the discrete mechanical and continuous biochemical aspects of adhesion formation. Our model captures key trends in the maturation fraction (MF) of NAs, actin retrograde velocity, and the periods of bond formation-rupture cycles, all in agreement with experimental evidence (Chan & Odde, 2008; Gong *et al*., 2018; Han *et al*., 2021; Swaminathan *et al*., 2016). The predicted optimal substrate stiffness (Chan & Odde, 2008) and stiffness sensitivity range (Bangasser *et al*., 2017; Selig *et al*., 2020) also lie within experimentally determined ranges.

While the predicted mean actin retrograde velocity across the stiffness range tested is in agreement with an experimental study using embryonic chick forebrain neurons (Chan & Odde, 2008), the agreement with the study of Elosegui-Artola and colleagues (Elosegui-Artola *et al*., 2014) is limited to the softer regimes where the biphasic trend is also seen (compare yellow and blue line in Figure 4.4A). This discrepancy arises from the way reinforcement of adhesions is modelled. In particular, reinforcement in that study is modelled as an increase in the integrin density that occurs if a clutch experiences a force $\geq$87 pN, leading to an increase in integrin–ECM binding events and a larger number of bound clutches. In a recent computational study where reinforcement is also modelled similarly, a biphasic behavior is observed just as in our model but with the optimal stiffness being around 10 pN/nm (Venturini & Sáez, 2023). In our model, while there is an increase in the cluster size of clutches and additional vinculin recruitment leading to larger force carrying capacities, there is no change in the number of available integrins or the adhesion formation rates.

In this study, we assume relatively fast kinetics for the signal molecule to keep the NA assembly and disassembly phases in line with experimental data (C. K. Choi *et al*., 2008). It is important to note that there may be considerable differences in experimental results based on the cell types used, resulting in different time scales. However, since the model is relatively insensitive to changes in $\text{signal}_{\text{thresh}}$ (Figure S.4.9, Figure S.4.10), and consequently changes in t_{sig}, the overall behavior of the model is unlikely to change drastically when these parameters are tuned to represent specific cell types or, for instance, signal molecule kinetics. Thus, the generic signal molecule in the

model can potentially represent the level of unphosphorylated FAK or similar molecules whose change in (phosphorylation) state can set off signaling cascades leading to adhesion disassembly. Future work should aim to determine the underlying factors that induce and influence adhesion disassembly so that the generic signal molecule can be replaced with more accurate formulations and interactions. In particular, the identification of such concrete factors could help in determining the settings of $\text{signal}_{\text{thresh}}$.

Based on our results, the factors affecting the NA disassembly dynamics play a more important role than those affecting assembly dynamics. We applied TDRM, an innovative method to account for spontaneous bond-rupture events in NA formation in an ODE framework. TDRM was necessary to establish the optimal stiffness because in its absence, maturation is highest on soft substrates as forces on the clutches build up slowly, giving long durations for maturation reactions to occur. TDRM counters this by increasing the rate of clutch-actin bond-rupture and hence prevents maturation. With the baseline value of the TDRM factor k_{sens}, the effect of TDRM on bond-rupture rate is highest on soft substrates and negligible on stiffer substrates due to the short clutch lifetimes. Walcott *et al.*, 2011 predicted and experimentally verified that disassembly processes begin earlier for soft substrates, and this arises from force- and strain-dependent bond formation and rupture probabilities. In addition, cyclic mechanical reinforcement (CMR) of integrin-ligand bonds strengthens them, increasing the lifetimes, implying that on soft substrates where force-loading is relatively slow and force remains low for longer durations, these bonds are less reinforced and are more likely to break (Kong *et al.*, 2013). In previous studies, CMR has been modelled as an increase in bond-dissociation rates at low forces (Elosegui-Artola *et al.*, 2016; Venturini & Sáez, 2023). TDRM can be considered as a method to coarsely account for these processes. However, while the outcomes of TDRM are similar to the effects of CMR as modelled in (Elosegui-Artola *et al.*, 2016; Venturini & Sáez, 2023), the differences between the two methods need to be investigated further. Surprisingly, the optimal stiffness was insensitive to changes in the parameter that controls the magnitude of TDRM (k_{sens}, Figure 4.5B) . This was unexpected since TDRM was essential for establishing an optimal stiffness implying a major role of this parameter in determining model behavior (Figure S.4.6, Figure S.4.7). It is likely that the explored sensitivity range ($\pm 20\%$) was too narrow to considerably change the behavior of the model, which should be investigated more in depth in the future. Note as well that in this study we performed a local sensitivity analysis focusing on those parameters that can directly be traced to a biological phenomenon (for instance k_{act}, $\text{Initial}_{\text{vinc}}$) we

introduced as part of SDRM and TDRM (for instance k_{sens}, $signal_{thresh}$), or assumed (for instance, $tal_{rf_{factor}}$). Considering the non-linear nature of the model, it would be interesting to conduct a more rigorous, global sensitivity analysis (i.e. using Bayesian Optimization) in the future to further identify the most significant parameters of the model.

Another benefit of our model is that it allows the prediction of the maturation fraction of adhesions for a range of substrate stiffnesses. While there are no studies to the best of our knowledge that explicitly investigate the MFs for different substrate stiffnesses, the predicted range of MFs for the stiffness range tested in this study was within the range of experimentally determined fractions (Han *et al*., 2021; Swaminathan *et al*., 2016).

Our sensitivity analysis results show that the MF is highly influenced by the amount of integrins and vinculin available, actin-binding rate, and the talin-refolding rate (Figure 4.5A). These factors can possibly be experimentally controlled, through introducing mutations in the proteins, allowing the predictions to be tested. Additionally, the MF and optimal stiffness were found to be insensitive to variations in the TDRM factor k_{sens} and the cluster formation and disassembly rates, suggesting that the model is locally robust to these factors and the parameters can be tuned to be specific to experimental conditions or cell lines. This suggests that the model can be used to predict the MFs for a variety of conditions by varying molecular stiffnesses, initial concentrations of talin, integrin, and vinculin, different clustering, maturation, and disassembly rates among many other parameters. This can potentially shed light on how traction force exerted by the cell is affected by biochemical alterations within the cell.

For instance, vinculin plays an important role in both cell-ECM adhesions and cell-cell adhesions through cadherins. Numerous studies indicate interdependence and cooperativity of these two processes, mediated through signal cascades or proteins that are essential in both types of adhesions, to varying degrees in different cell types (Bays & DeMali, 2017; X. Chen & Gumbiner, 2006; McCain *et al*., 2012; Mertz *et al*., 2013; Rooij *et al*., 2005; Tsai & Kam, 2009). While vinculin knockout studies have shown that traction force generation is impaired, with some studies reporting a decrease of nearly 50% in the absence of vinculin, overexpression of vinculin results in extremely strong adhesions that suppresses cell motility (Dumbauld *et al*., 2013; Fernandez *et al*., 1993; Fernández *et al*., 1992; Mierke *et al*., 2008; Rahman *et al*., 2016; Thievessen *et al*., 2013). However, this leaves unanswered questions about

how relatively less drastic changes in vinculin availability arising from crosstalk between integrins and cadherins adhesion complexes affect traction force generation and adhesion maturation. Our model predicts that a 20% decrease in the vinculin concentration results in a $\sim 9\%$ increase in the actin retrograde velocity (or equivalently a 9% decrease in the traction force exerted due to lower MFs) at the optimal substrate stiffness (Figure 4.5). Thus, our model can be especially valuable to make predictions and generate hypotheses of how (local) adhesion protein concentrations influence the early processes of adhesion assembly, maturation and traction force generation.

Overall, our model improves on previous studies in several aspects. Firstly, the process of maturation is more accurately captured by accounting for multiple vinculin recruitment events that progressively increase the clutch stiffness in a continuous ODE framework. Previous studies either did not account for this or at most accounted for recruitment of one vinculin (Chan & Odde, 2008; Cheng *et al*., 2016; Cirit *et al*., 2010; Elosegui-Artola *et al*., 2016; Lai & Chiam, 2011; Macdonald *et al*., 2008; Sonn-Segev *et al*., 2015). Secondly, this model couples changes in discrete mechanical factors of adhesion maturation such as clutch stiffness with the continuous framework of biochemical reactions underlying adhesion maturation. This is particularly important because the continuous biochemical models do not explicitly account for force on the clutches, and discrete mechanical models of adhesion formation do not capture the resulting experimentally measurable biochemical changes that occur.

While it is clear from our results that the adhesion assembly and disassembly rates must be dynamic and dependent on a signal to achieve the maturation of only a fraction of the NAs that are initially formed, we acknowledge several limitations to this study. First, we do not model numerous proteins involved in the process of maturation or the continuous increase in the area of the adhesion (Geiger & Yamada, 2011). Second, we simplified vinculin recruitment and growth of cluster size to occur in two discrete steps, and no spatial effects (e.g. proximity to an actin fiber, distance of adhesion from the cell membrane) are accounted for. And third, we assume that integrins, talin and vinculin are available in roughly equal proportions near the adhesions (initial concentrations are the same), which may not necessarily be true. However, the sensitivity analysis clearly highlight the robustness and reliability of the model behaviour for a range of $\pm 20\%$ in these ratios (Figure 4.5). Despite these limitations, our model reproduced experimentally observed trends with respect to force, substrate stiffness, time periods of oscillation in concentrations of the different seeds and clusts (Bangasser *et al*., 2013; Chan & Odde,

2008; Gong *et al.*, 2018). Furthermore, our results are reasonably close to discrete, stochastic computational studies as mentioned earlier even though our model bridges discrete and continuous aspects. The model thus provides a reliable foundation for further investigations.

What remains to be explored, perhaps by building on our model, is the interaction between the various signal cascades that regulate NA maturation. The ubiquitous signaling molecule FAK is also force-activated adding a further layer of interactions and complexity (Domingos *et al.*, 2002; Tomar & Schlaepfer, 2009). In addition, the KANK family of proteins are known to impair the actin binding capacity of talin, thereby weakening the integrin-actin linkage, and affecting the catch and slip bond dynamics (L. Sun *et al.*, 2016). They also play a role in targeting microtubules to focal adhesions which aids in their disassembly through multiple signal cascades (Bouchet *et al.*, 2016). By expanding the current model framework to include these interactions, it has the potential to robustly simulate the mechanochemical processes underlying mechanotransduction and provide valuable insight into cell signaling, communication and organization, hence contributing to advances in developmental biology and regenerative medicine.

4.5 Supplementary Material

4.5.1 Implementation

The model and the simulations were implemented using MATLAB R2020a (Inc, 2022). All code and scripts used in this study are publicly available via GitHub at https://github.com/CarlierComputationalLab/force-dependent-adhesion-composition.git.

4.5.2 Supplementary methods

4.5.3 Hookean spring system

The substrate–integrin–adaptor protein system was formulated as a system of Hookean springs. As *seeds* and *clusts* contain 25 and 50 integrin–adaptor protein complexes connected in parallel (Figure 4.1C, main text), their stiffnesses are 25 and 50 times the stiffness of a single integrin–adaptor protein complex. This is derived in the following section.

4.5.4 Stiffness of a integrin-adaptor protein complex

Talin has multiple hidden vinculin binding sites that are uncovered as the talin rod unfolds due to the application of force in the process of reinforcing the link between the ECM and the actomyosin network of the cell. Talin was found to form a pre-complex with one vinculin molecule before entering adhesions (Han *et al.*, 2021). Thus, the fundamental building block of this model is an integrin–talin–vinculin complex as seen in Figure S.4.1. On application of force and experiencing a stretch, up to two more vinculin molecules are allowed to bind to represent two reinforcement steps. The vinculin binding sites are assumed to be evenly spaced on the talin rod. Thus, the stiffness of a complex containing one talin rod and n_{vinc} vinculin molecules is described in the following way.

Generally, the combined stiffness $k_{combined}$ of two springs with stiffnesses of $k_{spring1}$ and $k_{spring2}$ connected in series is given by

$$k_{combined} = \left(\frac{1}{k_{spring1}} + \frac{1}{k_{spring2}} \right)^{-1} \tag{S.1}$$

If connected in parallel, the combined stiffness is

$$k_{combined} = k_{spring1} + k_{spring2} \tag{S.2}$$

Let k_{tal} be the stiffness of talin, k_{vinc} be the stiffness of vinculin, and k_{sub} be the stiffness of the substrate (ECM). Figure S.4.1 shows a generalised integrin–adaptor protein complex bound to the substrate. The talin rod can be represented as four sub-springs of equal stiffness such that the stiffness when they are all connected in series is equal to k_{tal}. Namely springs A, B, C, and D represent the four sub-segments such that $k_{tal} = 4{\cdot}k_{4tal}$, where k_{4tal} is the stiffness of a sub-segment.

$$k_{tal} = \left(4{\cdot}\frac{1}{k_{4tal}} \right)^{-1} \rightarrow k_{4tal} = 4{\cdot}k_{tal} \tag{S.3}$$

Vinculin molecules are represented by springs E, F, and G. Using Eq. S.1 and Eq. S.2, the effective stiffness of the system of springs containing springs $\mathrm{A} - \mathrm{G}$ is given by:

$$k_{complex} = \left(\frac{1}{A} + \frac{1}{E + \left(\frac{1}{F + \left(\frac{1}{D+G} + \frac{1}{C} \right)^{-1}} + \frac{1}{B} \right)^{-1}} \right)^{-1} \tag{S.4}$$

The stiffness of springs A, B, C, and D is k_{4tal} (Eq. S.3). The stiffness of springs E, F, and G is k_{vinc} ($0.25\ pN/nm$ (Huang *et al.*, 2017)). Note that for complexes with one vinculin, G and F is 0, and similarly for complexes with two vinculins, G is set to 0.

4.5.5 Fractional extension of clutches

When talin binds to actin, the chain of links between the cell and the substrate is complete. Due to actin retrograde velocity of v_u, this system of springs containing the spring representing the substrate connected in series to a spring that represents the clutch ($seed$ or $clust$) experiences a total extension of $v_u \cdot dt$, where dt is the time step. This extension is thus shared between the substrate and the clutch based on their relative stiffnesses. The fraction of this extension that is experienced by the clutch is given by a_{clutch} is calculated in the following way.

Let k_{clutch} be the stiffness of the clutch ($25 \cdot k_{complex}$ for a *seed*, $50 \cdot k_{complex}$ for a *clust*) and k_{sub} be the stiffness of the substrate. The integrin is considered to be a massless rigid body that does not undergo any physical change on the application of force. Thus, the system of springs is then reduced to two springs of stiffnesses k_{clutch} and k_{sub} connected in series, which can be represented by a 'combined' spring $comb$ with an effective stiffness k_{comb} given by

$$k_{comb} = \left(\frac{1}{k_{clutch}} + \frac{1}{k_{sub}} \right)^{-1} = \frac{k_{clutch} \cdot k_{sub}}{k_{clutch} + k_{sub}} \tag{S.5}$$

Thus, this spring experiences an extension of $v_u \cdot dt$ in every time step. The force on this spring is then,

$$F_{comb} = k_{comb} \cdot (x_{comb}) \tag{S.6}$$

where $x_{comb} = v_u \cdot dt$.

Since the extension x_c is the sum of extensions of the springs representing the substrate and the clutch,

$$x_{comb} = x_{sub} + x_{clutch} \tag{S.7}$$

where x_{sub} and x_c are extensions of the substrate and clutch springs respectively.

Therefore,

$$x_{clutch} = x_{comb} - x_{sub} \tag{S.8}$$

Since springs in series experience the same force, the force on the substrate spring is equal to the force on the *comb* spring. Therefore

$$x_{clutch} = \ x_{comb} - \frac{F_{sub}}{k_{sub}} = x_{comb} - \frac{F_{comb}}{k_{sub}} = x_{comb} - \frac{k_{comb} \cdot x_{comb}}{k_{sub}} \tag{S.9}$$

This implies

$$x_{clutch} = x_{comb} \cdot \left(1 - \frac{k_{comb}}{k_{sub}}\right) = x_{comb} \cdot \left(1 - \frac{k_{clutch}}{k_{clutch} + k_{sub}}\right) \tag{S.10}$$

$$\rightarrow \ x_{clutch} = x_{comb} \cdot \left(1 - \frac{k_{clutch}}{k_{clutch} + k_{sub}}\right) = x_{comb} \cdot a_{clutch} \tag{S.11}$$

where $a_{clutch} = \left(1 - \frac{k_{clutch}}{k_{clutch} + k_{sub}}\right)$ is the fractional extension of a clutch of stiffness k_{clutch} is connected to a substrate of stiffness k_{sub}.

4.5.6 Force on the fourth talin sub-spring

The talin–actin bond is a 2 pN slip bond (Jiang *et al.*, 2003). However, integrins bound to talin that is further bound to multiple vinculins can carry a force much higher than 2 pN (Roca-Cusachs *et al.*, 2012). For both of these to be true, the different domains of the talin rod must experience different forces, and the talin–actin slip bond is likely dependent on the force experienced by the talin rod domain that binds actin. Here, the fourth talin sub-spring binds actin and hence the slip bond rupture occurs when this particular spring experiences a force of 2 pN.

The force experienced by spring D in Figure S.4.1 is given by $F_D = k_D \cdot x_D$ where $k_D = k_{4tal}$, and x_D is the extension of spring D. x_D in terms of the extension of the entire system x_{comb} (i.e. the extension of the $comb$ spring) is derived as follows. Note that x_{ijk} is the general representation of the extension of the spring system containing springs i, j, and k.

The total force on the system:

$$F_{comb} = k_{comb} \cdot x_{comb} \tag{S.12}$$

Since springs in series experience the same force,

$$F_{comb} = F_{sub} = F_{clutch} = F_A \tag{S.13}$$

Extension of clutch:

$$x_{clutch} = x_{comb} - x_{sub} \tag{S.14}$$

Extension of spring A:

$$x_A = \frac{F_A}{k_A} = \frac{F_{clutch}}{k_A} = \frac{k_{clutch} \cdot x_{clutch}}{k_A} \tag{S.15}$$

Extension of spring system containing springs B − C − D − F − G:

$$x_{BCDFG} = x_{clutch} - x_A \tag{S.16}$$

Since springs in series experience the same force, force on spring B:

$$F_B = F_{BCDGF} \tag{S.17}$$

Extension of spring B:

$$x_B = \frac{F_B}{k_B} = \frac{F_{BCDFG}}{k_B} = \frac{k_{BCDFG} \cdot x_{BCDFG}}{k_B} \tag{S.18}$$

Extension of spring system containing springs C − D − G:

$$x_{CDG} = x_{BCDFG} - x_B \tag{S.19}$$

Since springs in series experience the same force, force on spring C:

$$F_C = F_{CDG} \tag{S.20}$$

Extension of spring C:

$$x_C = \frac{F_C}{k_C} = \frac{F_{CDG}}{k_C} = \frac{(k_{CDG} \cdot x_{CDG})}{k_C} \tag{S.21}$$

Extension of spring D:

$$x_D = x_{CDG} - x_C \tag{S.22}$$

On simply resubstituting for x_c and x_{CDG} in Eq. S.22 using Eq. S.12 to S.21, we obtain:

$$x_D = (x_{clutch} - x_A) \cdot \left(1 - \frac{k_{BCDFG}}{k_B}\right) \cdot \left(1 - \frac{k_{CDG}}{k_C}\right) \tag{S.23}$$

Since $x_{clutch} = x_{comb} \cdot a_{clutch}$, we get

$$x_D = (x_{comb} \cdot a_{clutch} - x_A) \cdot \left(1 - \frac{k_{BCDFG}}{k_B}\right) \cdot \left(1 - \frac{k_{CDG}}{k_C}\right) \tag{S.24}$$

From Eq. S.13 we have $F_A = F_{clutch}$. Hence,

$$x_A = \frac{F_A}{k_A} = \frac{F_{clutch}}{k_A} = \frac{k_{clutch} \cdot x_{clutch}}{k_A} = \frac{k_{clutch} \cdot (x_{comb} \cdot a_{clutch})}{k_A} \tag{S.25}$$

Therefore, the extension of spring D is given by

$$x_D = (x_{comb} \cdot a_{clutch}) \cdot \left(1 - \frac{k_{clutch}}{k_A}\right) \cdot \left(1 - \frac{k_{BCDFG}}{k_B}\right) \cdot \left(1 - \frac{k_{CDG}}{k_C}\right) \tag{S.26}$$

4.5.7 Reactions in the model

4.5.8 Integrin activation

Integrins transition from a low-affinity to a high-affinity state when they bind to ECM ligands or cytosolic adaptor proteins such as talin (Calderwood, 2004; Li & Springer, 2018). Once ligand-bound, the integrin is anchored to the ECM, enabling bi-directional transmission of force. In this study, we model $\alpha_5\beta_1$ integrins and assume they are activated.

4.5.9 Pre-complexation of integrin, talin and vinculin

$$Rx1 = k_{1f} \cdot [int] \cdot [tal] \cdot [vinc] - k_{1r} \cdot [Pcomp] \tag{S.27}$$

Pre-complexation of talin and vinculin is necessary for NA maturation (Han *et al.*, 2021). The first reaction is the combined reaction involving talin (tal) and vinculin ($vinc$) binding to integrin (int) to form an integrin-adaptor protein complex termed $Pcomp$. This species does not bind to actin and hence does not experience force. The reaction is reversible and has a forward rate constant of k_{1f} and a reverse rate constant of k_{1r}.

4.5.10 Integrin clustering

Integrin clustering to form NAs is critical for cellular mechanosensitivity (Miller *et al.*, 2020). Clustering is initiated by integrin binding to talin (Ellis *et al.*, 2014), vinculin recruitment to the adhesion (Humphries *et al.*, 2007) and force application (Changede *et al.*, 2015; C. K. Choi *et al.*, 2008; Roca-Cusachs *et al.*, 2009). Ligand type and density on the ECM also influence clustering, with

an upper limit for ligand spacing of around 60 nm (Jiang *et al*., 2003; Roca-Cusachs *et al*., 2009; Schvartzman *et al*., 2011). Integrin clustering is a continuous process and clusters can grow to contain up to 50 integrins (Changede *et al*., 2015).

As a simplification, here the growth of clusters to the maximal considered size (50 integrin–adaptor protein complexes) is split into two stages with the initial clustering resulting in a small cluster of 25 integrin–adaptor protein complexes, termed '*seed*' and denoted by 'Sx', and a second clustering reaction where *seeds* dimerize to give a large cluster with 50 integrin-adaptor protein complexes, termed '*clust*' and denoted by 'Cx' (Figure 4.1C). Here, $x = (1, 2, 3)$ and denotes the number of vinculin molecules in the individual integrin-adaptor protein complexes. Actin-bound *seeds* and *clusts* are denoted by 'Sxa' and 'Cxa' respectively. We assume that the ligand spacing is sufficiently close for integrin clusters to form.

4.5.11 Seed formation

$$Rx2 = k_{2f} \cdot [Pcomp]^2 - k_{2r} \cdot [S1] \tag{S.28}$$

To form a *seed*, 25 $Pcomp$s come together at a constant rate of k_{2f} and are assumed to bind simultaneously and parallelly to form the lowest order AUB *seed*, $S1$. $S1$ *seeds* breakdown to give 25 $Pcomp$s at a constant rate of k_{2r}. The order of the reaction with respect to $Pcomp$ is set to two to account for any intermediate steps that might be present in the process of clustering (setting the order to one gives similar results, see Figure S.4.12.

4.5.12 Clust formation through seed dimerization

$$Rx3 = k_{3f} \cdot [S1]^2 - k_{3r} \cdot [C1] \tag{S.29}$$

$$Rx14 = k_{14f} \cdot [S1a]^2 - k_{14r} \cdot [C1a] \tag{S.30}$$

$$Rx15 = k_{15f} \cdot [S2a]^2 - k_{15r} \cdot [C2a] \tag{S.31}$$

$$Rx16 = k_{16f} \cdot [S3a]^2 - k_{16r} \cdot [C3a] \tag{S.32}$$

$S1$ *seeds* reversibly dimerize with constant forward and reverse rates (k_{3f} and k_{3r}), forming lowest order AUB *clusts*, $C1$, containing 50 $Pcomp$s. Higher-order AUB *seeds* ($S2,\ S3$) are not allowed to dimerize as they experience talin

refolding (Yao *et al*., 2014; Yao *et al*., 2016) and hence should be more likely to break down than to form *clusts*. However, AB *seeds* of all orders ($S1a,\ S2a$, and $S3a$) can dimerize to form AB *clusts* ($C1a$, $C2a$, and $C3a$).

4.5.13 Actin binding/unbinding

$$Rx4 = k_{4f} \cdot [S1] - k_{4r} \cdot [S1a] \tag{S.33}$$
$$Rx5 = k_{5f} \cdot [S2] - k_{5r} \cdot [S2a] \tag{S.34}$$
$$Rx6 = k_{6f} \cdot [S3] - k_{6r} \cdot [S3a] \tag{S.35}$$
$$Rx9 = k_{9f} \cdot [C1] - k_{9r} \cdot [C1a] \tag{S.36}$$
$$Rx10 = k_{10f} \cdot [C2] - k_{10r} \cdot [C2a] \tag{S.37}$$
$$Rx11 = k_{11f} \cdot [C3] - k_{11r} \cdot [C3a] \tag{S.38}$$

Actin-unbound (AUB) clutches $(S1,\ S2,\ S3,\ C1,\ C2,\ C3)$ can bind to actin filaments through the actin-binding sites on talin and vinculin. This results in actin-bound (AB) clutch $(S1a,\ S2a,\ S3a,\ C1a,\ C2a,\ C3a)$ (Figure 4.1C) that can experience and transmit force. The baseline actin-binding rate is k_{act} for all actin-binding reactions.

4.5.14 Force-dependent actin-unbinding and time-dependent rate modification (TDRM)

As explained in the main text (Section 'Force-dependent actin unbinding and time-dependent rate modification') and supplementary sections **Slip and catch bonds** and **Time-dependent rate modification (TDRM)**, the combined bond-rupture rate of the catch-slip and slip bonds depend on the force on the clutches and are given by :

$$k_{off_{CS}} = A \cdot e^{-b \cdot F_{clutch}} + C \cdot e^{d \cdot F_{clutch}} + k_{TDRM} \cdot k_{slip_{UL}} \cdot e^{\frac{F_{clutch}}{F_{th_i}}} \tag{S.39}$$

where F_{clutch} is the force on an individual complex in the clutch, F_{th_i} is the talin–actin slip bond rupture threshold $i \in \{1, 2, 3\}$, $k_{slip_{UL}}$ is the unloaded dissociation rate of talin from actin, and k_{TDRM} is the TDRM fac-

tor (explained in supplementary section **Time-dependent rate modification (TDRM)**).

4.5.15 Adhesion reinforcement

When talin is subject to extensions, a maximum of eleven vinculin-binding sites (VBS) that are otherwise cryptic are uncovered (Gingras *et al*., 2005; Rio *et al*., 2009). This allows for more vinculin to be recruited to reinforce the bond with the actin network. In this model, we consider two vinculin-reinforcement events.

Since we assume vinculin binds instantaneously once the vinculin binding site is uncovered, the rates of the reinforcement reactions are equal to the rate at which talin unfolds, which depends on the force experienced by the clutch as explained in the main text in section Force quantification.

4.5.16 First vinculin reinforcement

$$Rx7 = k_{7f} \cdot [S1a] \cdot [vinc]^2 - k_{7r} \cdot [S2a] \tag{S.40}$$

$$Rx12 = k_{12f} \cdot [C1a] \cdot [vinc]^2 - k_{12r} \cdot [C2a] \tag{S.41}$$

A low order AB clutch $(S1a,\ C1a)$ is stretched when it is pulled by actin. The first VBS is uncovered when each complex within the AB clutch experiences a force of 5 pN leading to additional vinculin binding (Yao *et al*., 2016). The forward rates $(k_{7f},\ k_{12f})$ of these reactions are dependent on the force experienced by the AB clutches undergoing reinforcement and are given by eq. 4.20 (main text).

4.5.17 Second vinculin reinforcement

$$Rx8 = k_{8f} \cdot [S2a] \cdot [vinc]^2 - k_{8r} \cdot [S3a] \tag{S.42}$$

$$Rx13 = k_{13f} \cdot [C2a] \cdot [vinc]^2 - k_{13r} \cdot [C3a] \tag{S.43}$$

A mid-order $(S2a,\ C2a)$ AB clutch is stretched further on application of force resulting in a second VBS being uncovered when the force reaches 12 pN(Rio

et al., 2009), allowing further vinculin binding. The forward rates of these reactions ($k_{8f},\ k_{13f}$) depend on the force experienced by the AB clutches undergoing second reinforcement and are given by eq. 4.20 (main text).

Reinforcement of *seeds*and *clusts*is modelled as a single-step reaction where simultaneous recruitment of 25 and 50 vinculin molecules respectively occurs. However, the orders of the reinforcement reactions ($Rx7$, $Rx8$, $Rx12$, $Rx13$, Table S.4.2) with respect to $vinc$ were chosen to be 2 to approximately account for the influence of possible intermediate stages in the reactions.

4.5.18 Adhesion disassembly

In the absence of sufficient force, adhesions disassemble because of mechanical and chemical signals (Stumpf *et al*., 2020). Here, we model two parallel processes of disassembly, namely talin refolding and cluster breakdown.

4.5.19 Talin refolding

$$Rx17 = k_{17f} \cdot [S3] \tag{S.44}$$
$$Rx18 = k_{18f} \cdot [S2] \tag{S.45}$$
$$Rx19 = k_{19f} \cdot [C3] \tag{S.46}$$
$$Rx20 = k_{20f} \cdot [C2] \tag{S.47}$$

Once a *seed* or a *clust* unbinds from actin due to bond rupture (Section **Actin binding/unbinding**), the clutch is no longer held under force. This increases the likelihood of stretched talin refolding and the recruited vinculin molecules dissociating. However, vinculin binding stabilizes stretched talin and reduces refolding rates(Yao *et al*., 2014). Additionally, the vinculin exchange rate is nearly 60% higher in NAs than in stable adhesions (Möhl *et al*., 2009). Therefore, the first talin-refolding event that results in a high to mid order transition ($S3\ to\ S2$ and $C3\ to\ C2$, rate constants $k_{17f},\ k_{19f}$) occurs at a slower rate than the second talin-refolding event that results in a mid to low order transition ($S2\ to\ S1$ and $C2\ to\ C1$, rate constants k_{18f}, k_{20f}). In particular, the rates of the first talin-refolding and second talin-refolding reactions are given by $k_{17f} = k_{19f} = tal_{rf_{factor}} \cdot tal_{rf}\ s^{-1}$ and $k_{18f} = k_{20f} = tal_{rf} \cdot sig_{dep}\ s^{-1}$ respectively, where $tal_{rf_{factor}}$ is the factor by which the first talin-refolding rate

is slower than the second, and tal_{rf} is the baseline talin refolding rate (Table S.4.1). The talin-refolding events are irreversible reactions ($Rx17$, $Rx18$, $Rx19$, $Rx20$, Table S.4.2) since the VBS on talin is assumed to be covered for AUB *seeds* and *clusts*.

4.5.20 Clust breakdown to seed

$$Rx21 = k_{21f} \cdot [C3] \tag{S.48}$$

$$Rx22 = k_{22f} \cdot [C2] \tag{S.49}$$

AUB *clusts* can break down to give two AUB *seeds* through an irreversible reaction (Figure 4.1B). Since a high order *clust* $(C3)$ is more robust to talin-refolding, we also assume it is more stable than a mid-order *clust* $(C2)$. Hence, the high-order AUB *clust* to high-order AUB *seed* ($C3$ *to* $S3$) transition was assumed to be slower than mid-order AUB *clust* to mid-order AUB *seed* ($C2$ *to* $S2$). The baseline rates for these breakdown reactions were set at $k_{21f} = 0.005\ s^{-1}$ and $k_{22f} = 0.008\ s^{-1}$, respectively. While these values were arbitrarily chosen, they were of the same order of magnitude as reverse rates of *seed* dimerization reactions ($Rx14$, $Rx15$, and $Rx16$, Table S.4.2).

4.5.21 Actin retrograde velocity

The cell membrane at the leading-edge pushes back on actin filaments undergoing actin-polymerization. Additionally, myosin II motors that are present away from the cell edge pull on the actin filaments with a force of 2 pN per motor (Cooper, 2000; Kee & Robinson, 2008; Molloy *et al*., 1995). These two forces cause an overall flow of actin filaments away from the cell membrane, known as the actin retrograde flow. Coupling the retrograde flow to the ECM through the adaptor protein–integrin–ligand chain effectively establishes a connection between the cell and its environment.

We assume that the force exerted by myosin II motors on actin filaments is balanced by the drag force arising due to the viscosity of the cytoplasm. Thus, in the absence of integrin-mediated forces on actin filaments, they move with a constant retrograde velocity. When clutches bind to the actin filaments, they provide resistance to the motion of actin filaments until they unbind, either spontaneously or because the catch/slip bond threshold is reached. This resistance decelerates the actin filaments. When the resistance provided by

clutches is equal to the force exerted by myosin II motors, the actin filaments stop moving and the retrograde velocity is reduced to 0. Since all forces act along a single axis in the model, applying force balance gives a linear relationship between force and velocity:

$$v_{retro} = v_u \cdot \left(1 - \frac{F_{total}}{F_{myo}}\right) \tag{S.50}$$

where v_u is the unloaded velocity of the actin filaments, F_{total} is the total force exerted by all AB clutches (see section **Force quantification**), and F_{myo} is the total force exerted by myosin II motors.

F_{myo} is given by:

$$F_{myo} = \ n \ \cdot \ conc_{myo} \cdot F_{myo_{single}} \tag{S.51}$$

where n is a conversion factor to convert concentrations to number of molecules (see Table S.4.1), $conc_{myo}$ is the concentration of active myosin II motors, and $F_{myo_{single}}$ is the force produced by a single myosin II motor. $conc_{myo}$ was adjusted such that the lowest value of velocity achieved for the baseline model was within 10% of that observed in experiments (Chan & Odde, 2008). As a continuous ODE framework is used, we consider the same actin retrograde velocity for all clutches.

4.5.22 Force quantification

The force on a clutch depends on its stiffness which depends on the number of constituent IAPCs and the number of vinculin molecules in each IAPC (see supplementary methods section 1.1). As clutches are connected in series to the substrate spring, when actin filaments pull the system of springs by unit distance, the extension is shared between the clutch and the substrate (Figure 4.1C). The fractional extension a_{clutch} (for calculation, see section **Fractional extension of clutches**) experienced by the clutch when the entire system experiences unit extension, depends on the ratio of the stiffness of the clutch to the stiffness of the entire substrate–clutch system.

The total force on the network of actin filaments depends on the number of AB clutches of each type and the extensions of the respective clutches. Since we use a continuum approach to account for the abundance of each species,

the concentrations need to be discretized. The need to discretize arises as the model treats the different clutches and force-exerting species as springs of certain stiffnesses. Thus, the force generated depends on the number of springs of a certain stiffness that experience an extension.

Concentrations are discretized by assuming a volume of 1 μm^3 which is approximately the volume of large focal adhesions and their immediate surroundings (Franz & Müller, 2005). The concentrations were multiplied by the volume and the Avogadro number, N_A, accounting for the different units to obtain a discrete number of clutches. As mentioned earlier, all members of a certain species experience the same extension and force. The force exerted by one clutch of a particular species is

$$F_{clutch} = k_{clutch} \cdot (a_{clutch} \cdot v_{retro} \cdot dt) \tag{S.52}$$

Where k_{clutch} is the stiffness of the clutch, a_{clutch} is the fractional extension of the clutch (derivation in section **Fractional extension of clutches**), v_{retro} is the retrograde velocity in the current time step and dt is the duration of the time step. Then, the total force exerted by all clutches of this type is

$$F_{total_{clutch}} = m_{clutch} \cdot F_{clutch} \tag{S.53}$$

where m is the number of clutches of a particular type i.e., the discretized concentration.

Therefore, the total force exerted by all AB clutches in the system is given by:

$$F_{total} = \sum_{clutch} m_{clutch} \cdot F_{clutch} \tag{S.54}$$

4.5.23 Substrate rigidity range

A range of substrate rigidities based on previous computational studies, between 0.1 pN/nm and 100 pN/nm, was used for simulations in this model (Chan & Odde, 2008). For all investigations except parameter sensitivity, analysis four stiffnesses, namely k_{sub} =[0.1,1,10,100] pN/nm were used. For parameter analysis and to plot figures 3, 4, S6, S7, 519 values of k_{sub} spaced

approximately logarithmically between 0.1 pN/nm and 1000 pN/nm were used to obtain a more continuous distribution of stiffnesses.

To compare our simulated results with experimental results, substrate stiffness when expressed in terms of a Young's modulus was converted to a Hookean spring constant according to

$$k_{substrate} = \frac{4\pi r}{E} \tag{S.55}$$

where E is the Young's modulus, and r is the radius of a circular adhesion site ($r = 550\,nm$) as described in Cheng *et al*., 2016 and Elosegui-Artola *et al*., 2014.

4.5.24 Signal-dependent rate modification (SDRM)

Numerous nascent adhesions (NAs) form at the moving edge but only a few remain after a few minutes (Changede & Sheetz, 2017; C. K. Choi *et al*., 2008). The assembly of NAs correlates with cell protrusion speed and actin polymerization is necessary for the nucleation of NAs (C. K. Choi *et al*., 2008; Vicente-Manzanares *et al*., 2007). Actin network branching reduces away from the cell edge (Okeyo *et al*., 2009; Oser & Condeelis, 2009). Since actin is depolymerized more rapidly away from the cell membrane (Oser & Condeelis, 2009) not all the NAs that were formed can be supported without an extensive actin filament network, and hence disassemble. Many signalling molecules such as focal adhesion kinase (FAK), Src and ERK kinases are known to influence adhesion disassembly. FAK phosphorylated at Tyr-397 was found to be positively correlated to adhesion disassembly rates (Webb *et al*., 2004). FAK is also inhibited closer to the leading edge of the cell due to its interactions with Arp2/3, a protein involved in actin branching (Swaminathan *et al*., 2016). Actin branching reduces away from the leading edge (Okeyo *et al*., 2009; Oser & Condeelis, 2009), implying that FAK is less inhibited in regions further from the leading edge. Since NA disassembly occurs as they move away from the leading edge, FAK may be implicated in NA disassembly. Additionally, calpain is known to be involved in regulating adhesion disassembly through proteolysis of talin(Franco *et al*., 2004), and its inhibition leads to disruption of adhesions containing zyxin (Bhatt *et al*., 2002).

Here, we model a hypothetical signal molecule which is essential for new NA formation ($Rx1,\ Rx2,\ Rx3$, Table S.4.2) and low-order AUB clutches ($S1,\ C1$)

to bind actin (for maturation) ($Rx4,\ Rx9$, Table S.4.2). We impose that a minimum concentration, $signal_{thresh}$, of the signal molecule is required for these reactions to occur. The concentration $[signal]$ of this molecule is initially high and decreases according to eq.4.17 (main text). Thus, the rate of decay of $[signal]$ determines the amount of time available before NA disassembly starts in which adhesion maturation can occur. The model behaviour does not change by assuming the opposite i.e., $[signal]$ increases over time and there is an upper limit for its concentration beyond which actin binding does not occur (Figure S.4.3B).

The modifications to the rates were made by multiplying the baseline rate constant by a signal-dependent rate modification (SDRM) factor given by the function:

$$sig_{dep} = \begin{cases} 1 & [signal] > [signal_{thresh}] \\ \left(\frac{1}{[signal_{thresh}]}\right) \cdot [signal] & [signal] \ \leq [signal_{thresh}] \end{cases} \tag{S.56}$$

This results in sig_{dep} having a value of 1 before $signal_{thresh}$ is crossed but would then decrease at the same rate as $[signal]$ (Figure S.4.3A).

Thus, if the $[signal]$ falls below $signal_{thresh}$, the rates of the following reactions were modified as described:

$$Pre-complexformation(Rx1) : k_{1f} = k_{1f_{base}} \cdot sig_{dep} \tag{S.57}$$
$$S1formationfromPcomp(Rx2) : k_{2f} = k_{2f_{base}} \cdot sig_{dep} \tag{S.58}$$
$$C1formationfromS1(Rx3) : k_{3f} = k_{3f_{base}} \cdot sig_{dep} \tag{S.59}$$
$$Actin-bindingrate(Rx4, Rx9) : k_{4f} = k_{9f} = k_{act} \cdot sig_{dep} \tag{S.60}$$

where k_{act} is the baseline actin-binding rate.

The breakdown rates of mid-order clutches $(S2, C2)$ to low-order clutches $(S1,\ C1)$ also decrease after $[signal]$ falls below the threshold to reflect the fact that the adhesions that are chosen to be matured are not broken down, and may progress to form FAs. As FAs are much larger in size compared to NAs, it implies that the large clusters $(C3,\ C2)$ are less likely to break down to smaller clusters $(S3,\ S2)$ if they are undergoing maturation to FAs. Thus, the rates of breakdown of high and mid-order *clusts* to *seeds* $(C3\ to\ S3,\ C2\ to\ S2)$

were also made $[signal]$-dependent. These rates were modified in the following way:

$$S2, C2toS1, C1breakdownrate(Rx18, Rx20) : k_{18f} = k_{20f} = tal_{rf} \cdot sig_{dep} \tag{S.61}$$

$$C3breakdowntoS3(Rx21) : k_{21f} = k_{21f_{base}} \cdot sig_{dep} \tag{S.62}$$

$$C2breakdowntoS2(Rx22) : k_{22f} = k_{22f_{base}} \cdot sig_{dep} \tag{S.63}$$

where tal_{rf} is the baseline talin-refolding rate.

Once the $signal$ concentration goes below $signal_{thresh}$, mechanisms to disassemble the initially formed clusters must become more active. Without an increase in activity, integrins will accumulate in low order AUB clutches $(S1,\ C1)$ since the rate of breakdown of $S1$ to $Pcomp$ is a very small value at baseline. To ensure these species are broken down once $signal_{thresh}$ is crossed, the reverse rates of $Pcomp$ formation ($Rx1$), $seed$ formation ($Rx2$), and $seed$ dimerization ($Rx3$) need to be increased. These rates are modified in the following way:

$$C1breakdown(Rx3) : k_{3r} = \begin{cases} 0.0001 & [signal] > [signal_{thresh}] \\ k_{dis} \cdot (1 - sig_{dep}) & [signal] \leq [signal_{thresh}] \end{cases} \tag{S.64}$$

$$S1breakdown(Rx2) : k_{2r} = \begin{cases} 0.0001 & [signal] > signal_{thresh} \\ k_{dis} \cdot (1 - sig_{dep}) & [signal] \leq [signal_{thresh}] \end{cases} \tag{S.65}$$

$$Pcompbreakdown(Rx1) : k_{1r} = \begin{cases} k_{1r_{base}} & [signal] > [signal_{thresh}] \\ 2 \cdot k_{1r_{base}} \cdot (1 - sig_{dep}) & [signal] \leq [signal_{thresh}] \end{cases} \tag{S.66}$$

The value of k_{dis} was obtained by multiplying the experimentally measured disassembly rate (C. K. Choi *et al.*, 2008) by a factor such that the simulations closely matched the experimentally determined NA assembly-disassembly curves (C. K. Choi *et al.*, 2008) (Figure 4.4, main text).

4.5.25 Slip and catch bonds

The talin–actin bond is a slip bond whose stability decreases with increasing force (Jiang *et al.*, 2003), implying a monotonically increasing unbinding rate with force. Here, we assume the unbinding rate increases exponentially with force according to the Bell model (Bell, 1978). The stability of catch bonds increases with the application of force (Dembo *et al.*, 1988). With integrins, both catch and slip bond characteristics were observed in different force regimes, leading to the concept of a catch-slip bond. Particularly, the catch-slip behaviour was observed for $\alpha_5\beta_1$, $\alpha_4\beta_1$ and $\alpha_L\beta_2$ integrins under different force regimes (W. Chen *et al.*, 2010; Y. I. Choi *et al.*, 2014; Kong *et al.*, 2009). In a catch-slip bond, the lifetime of the bond increases up to a force threshold beyond which the lifetime starts to decrease. A fully connected force chain (ligand–integrin–adaptor protein–actin filament) can be broken at two points, namely at the talin–actin slip bond or the integrin–ligand catch-slip bond. In this model, integrins are assumed to be ligand-bound when they are actin-bound. Thus, an actin-bound clutch is considered to become actin-unbound when either the integrin-ligand bond or the talin-actin bond is broken. The effective rate of actin-unbinding of a particular clutch depends on the force experienced by individual complexes in the clutch and is given by a sum of the catch-slip and slip bond rates:

$$k_{off_{CS}} = A \cdot e^{-b \cdot F_{clutch}} + C \cdot e^{d \cdot F_{clutch}} + k_{slip_{UL}} \cdot e^{\frac{F_{clutch}}{F_{th_x}}} \tag{S.67}$$

where F_{clutch} is the force on an individual complex in the clutch, F_{th_x} is the talin–actin slip bond rupture threshold ($x \in \{1, 2, 3\}$ (Table S.4.1), $k_{slip_{UL}}$ is the unloaded dissociation rate of talin from actin. The first and second terms define the integrin-ligand catch-slip bond - $A \cdot e^{-b \cdot F_{clutch}}$ captures the decrease in unbinding rate characteristic of a catch bond and $C \cdot e^{d \cdot F_{clutch}}$ captures the increase in unbinding rate characteristic of a slip bond , b and d are parameters that control the force-dependency of the unbinding rate.

Since vinculin also binds actin, reinforcement increases the force-carrying capacity of a clutch. The vinculin–actin bond is a catch-slip bond that is maximally stable at 8 pN of force (Huang *et al.*, 2017). The talin–actin slip bond is the weaker link of these two, with a rupture force of 2 pN (Jiang *et al.*, 2003). Therefore, for any increase in force up to 8 pN, the vinculin–actin unbinding rate reduces, effectively maintaining the actin-bound state of a clutch for longer. To maintain simplicity, instead of explicitly modelling the vinculin–actin catch bond, reinforcement was modelled as an increase in

the force thresholds for the talin-actin slip bond. The force thresholds were increased by 0.5 pN for each reinforcement event, effectively increasing the force thresholds for mid $(S2a,\ C2a)$ and high $(S3a,\ C3a)$ order AB clutches, F_{th2} and F_{th3}, to 2.5 and 3 pN respectively (Table S.4.1). Once the force on AB clutches reaches the corresponding force threshold, they are assumed to immediately unbind from actin to give their AUB counterparts, resulting in the concentration of AB clutches going to 0, and that of AUB clutches increasing by the same amount.

4.5.26 Time-dependent rate modification (TDRM)

Although integrins cluster on substrates of all stiffnesses, the traction force generated and consequently the maturation of adhesions depends on the substrate stiffness (Chan & Odde, 2008; Cheng *et al.*, 2016; Zhou *et al.*, 2017). Once unbound, the talin in the clutch returns to its folded state and the unfolding process needs to start again. While this can result in an equilibrium being established with a large number of simultaneously bound clutches, the force on each clutch remains low and only increases slowly. Therefore, even though the number of bound clutches (or concentration) is high, the average force per clutch (total force divided by the number of bound clutches) remains low as the clutches are likely to unbind spontaneously before reaching their maximum force carrying capacity.

The model in this study is a continuous model that aims to captures the overall 'average' behaviour of all clutches. As such, all clutches of a particular kind are said to experience the same force and this increases with every timestep until the respective thresholds are reached. Thus, the total force exerted by a certain clutch type is the product of the concentration and the force on one such clutch. This makes it challenging to account for the reduction in the total force that is caused by spontaneous clutch unbinding events as it is impossible to keep track of force on individual clutches. To account for this we introduce a method of time dependent rate modification (TDRM) to capture the (individual, discrete) spontaneous clutch unbinding events in a continuous framework. Since the total force exerted by a particular family of clutches is the product of the concentration of the clutch and the force on one such clutch, by introducing a time-dependent increase in the unbinding rate, it is possible to ensure that the total force does not monotonically increase.

More specifically, as derived and described by Novikova et al. (Novikova & Storm, 2013), the probability p_{closed} that a bond that is closed at time t remains

closed at time $t + \Delta t$ reduces exponentially and is approximately equal to:

$$p_{closed}\,(t+\Delta t)\ \sim e^{-k_{LT}\cdot\,\Delta t} \tag{S.68}$$

where $\frac{1}{k_{LT}}$ is the expectation value of the lifetime (Novikova & Storm, 2013) (this theoretical formulation is only used to support our formulation of TDRM, and we do not use the expectation value k_{LT} in our model). Thus, the probability of bond-rupture increases with time spent in the bonded state, Δt, asymptotically reaching the value of 1. Hypothetically, as the probability of bond-rupture p_{open} approaches 1 (p_{closed} approaches 0), the bond-rupture rate approaches infinity causing all bound clutches to unbind. Clearly, the bond-rupture rate grows exponentially with decreasing p_{closed}. In this model, the time step dt is fixed (Table S.4.1). Because we use Euler's forward integration method, the concentrations at time $t + \Delta t$ is given by $rate \cdot dt$. Thus allowing an unlimited, exponential growth in reaction rates can lead to numerical errors such as negative concentrations. As such, to limit the unbinding rates and prevent numerical integration errors, we approximate the first part of the exponential curve with a linear function. But consider a linear function of the type $f(x) = ax$ and an exponential function of the form $g(x) = e^{ax}$. It can be observed that $f\,(x) \leq\ g\,(x)\ \forall x$. Therefore, if the increase in unbinding rate is approximated by a linear function instead of an exponential one, the maximum value of $rate \cdot dt$ for the time-scales of this model will not be too large and will avoid numerical integration errors. With this approach, the model still captures the qualitative effects of an increasing unbinding rate, but the effect will not be as pronounced as it would be if an exponential function is used.

Thus, TDRM was incorporated by modifying the rate constants for actin-unbinding reactions ($k_{4r},\ k_{5r},\ k_{6r},\ k_{9r},\ k_{10r},\ k_{11r}$) by multiplying the unloaded dissociation rate of the slip bond, $k_{slip_{UL}}$ with a TDRM factor given by:

$$k_{TDRMFactor} = 1 + k_{sens} \cdot t_{clutch} \cdot dt \tag{S.69}$$

where k_{sens} determines the sensitivity to the time t_{clutch} that AB $seeds$ or AB $clusts$ spend in the force-loading phase. t_{clutch} increases by 1 in each time step until the force F_{clutch} on each complex in the clutch equals $F_{th_{clutch}}$, the threshold force, when it is reset to 0. The value of k_{sens} can be taken to represent the reciprocal of the lifetime of the bond just as k_{LT} in eq. S.68.

The lifetime of the talin-actin bond under physiological conditions is between 10–100 seconds (Owen *et al.*, 2022). Here, a baseline value of $k_{sens} = 0.05$ is used (implying a lifetime of 20 seconds), but it is important to note that the qualitative trends in the model outcomes remained the same for values of $k_{sens} \geq 0.02$ (lifetime ≤ 50 seconds).

Since the chain of links between the ECM and the actin cytoskeleton can break at the integrin–ECM or the talin–actin linkages, an increase in either the integrin–ECM catch-bond rupture or talin–actin slip bond rupture in essence has the same effect on the results of the model – both lead to an incomplete chain and subsequent loss of force transmission. As TDRM was devised to qualitatively capture bond-rupture dynamics, we limited the effect of TDRM to the unloaded slip bond dissociation rate $k_{slip_{UL}}$. However, increasing both the unloaded slip and catch-bond dissociation rates ($k_{slip_{UL}}$, A and B in Eq S.39) also results in the same trends but with a larger difference between concentrations of species on soft and stiff substrates, and consequently the maturation fraction (Figure S.4.13)

4.5.27 Curve-fitting for parameter values

The values of parameters of the integrin–ligand catch bond and the rate of talin unfolding due to force were determined by fitting double and single exponential equations respectively to experimental data (Kong *et al.*, 2009; Rio *et al.*, 2009) using the in-built MATLAB function 'fminsearch'. Specifically, for the catch bond, force-bond lifetime data of the Mn^{2+} activated $\alpha_5\beta_1$- Fn (fibronectin) from Kong *et al.*, 2009 was obtained by digitizing Figure 3C in the publication. For the rate of talin unfolding, data from experiments involving stretching of full-length talin by Rio et al. (2009) (Rio *et al.*, 2009) was used (Figure 4.4F in the main text).

The stiffness of talin used in this study (0.1 pN/nm) was obtained by calculating the gradient of force-extension curves in the linear regime at low extensions of full length talin rod as reported by Yao *et al.*, 2016.

4.5.28 Mass conservation

Mass conservation was checked by calculating the sum of concentrations of integrins and talin across all integrin and talin containing species in the model. The equations for mass conservation are below:

$$\text{Integrins} : [int] + [Pcomp] + 25 \cdot ([S1] + [S2] + [S3] + [S1a] + [S2a] + [S3a]) \tag{S.70}$$
$$+ 50 \cdot ([C1] + [C2] + [C3] + [C1a] + [C2a] + [C3a])$$
$$\text{Talin} : [tal] + [Pcomp] + 25 \cdot ([S1] + [S2] + [S3] + [S1a] + [S2a] + [S3a]) \tag{S.71}$$
$$+ 50 \cdot ([C1] + [C2] + [C3] + [C1a] + [C2a] + [C3a])$$
$$\text{Vinculin} : [vinc] + [Pcomp] + 25 \cdot ([S1] + [C1] + [S1a] + [C1a]) \tag{S.72}$$
$$+ 50 \cdot ([S2] + [S2a] + [C2] + [C2a])$$
$$+ 75 \cdot ([S3] + [S3a] + [C3] + [C3a])$$

4.5.29 Fitting a line through force peaks

For Figure S.4.11, to quantify the peak force exerted by each species and the total force exerted by all species over time, the peaks of the force-time data were identified using a built-in MATLAB function 'findpeaks'. A smoothing spline was then fit through the identified peaks using the 'fit' function in MATLAB.

4.5.30 Supplementary results

4.5.31 The model satisfies mass conservation

Testing for mass conservation showed that the total concentration of integrins and talin during the simulation remained at the initial concentrations of 1 µM (Figure S.4.2). This was also true for vinculin when the simulation was run with a limited amount of vinculin (not shown). This shows that there are no runaway variables or leaks in the system of differential equations used.

4.5.32 Signal decay (or growth) rate matches nascent adhesion assembly phase

Figure S.4.3A shows the concentration of $signal$ over time. The rate of decay of the signal molecule was adjusted such that it crosses the concentration threshold $signal_{thresh}$ (of 0.1 μM) after around 58 seconds. t_{sig} is the time at

which this threshold is crossed. NA formation reactions are allowed to undergo for this duration as it is the length of the experimentally determined NA assembly phase (C. K. Choi *et al.*, 2008).

The behaviour of the model does not change if the converse is assumed – i.e. the signal grows with time and above a certain concentration of $signal$ (here the threshold is set to 0.9 μM) the signal-dependent reactions start to slow down. The growth rates can be adjusted to result in the same time dynamics (Figure S.4.3B).

4.5.33 Limited vinculin results

As the simulations by default assume a constant concentration of vinculin, to investigate whether the optimal substrate stiffness is obtained even in limited vinculin environments, the initial concentration of vinculin was set to 1 uM, equal to that of integrin and talin, and was not replenished during the simulation. The rest of the parameters were maintained at baseline values. The general trends for concentrations of mid and high order clutches remained the same with limited vinculin concentration (Figure S.4.5). A key difference was that the concentration of high-order clutches was lower by almost an order of magnitude (Figure S.4.5(iii) vs Figure S.4.7A(iii)) and the concentration of low-order clutches was nearly twice as high compared to constant vinculin conditions (Figure S.4.5(i) vs Figure S.4.7A(i)). This coupled decrease and increase in concentrations show that the *seed* and *clust* ($S1,\ C1,\ S1a,\ C1a$) formation occurred to the same extent, but maturation was lower when vinculin was limited. While the maturation fraction varied biphasically with substrate stiffness when the vinculin concentration was kept constant (Figure S.4.7A(iv)), there was a monotonic decrease when the vinculin concentration was limited (Figure S.4.5(iv)). Increasing k_{sens} increased this difference (not shown).

4.5.34 Investigating the biphasic relation between traction force and substrate stiffness

To ensure that the biphasic relationship between force and substrate stiffness indeed arises from a combination of low force and low concentrations of clutches, we can look at the total force exerted by each clutch on substrates of different stiffnesses. The total force exerted by a species, which we term

'force-concentration' for simplicity, is the product of the discretized concentration of the species and the force on one clutch of the species (S.58). To capture the general trend, a curve can be fitted on the peaks of the force-concentration plots. Figure S.4.11 shows these fitted curves for each species on four substrate stiffnesses. Notably, the force-concentration of $C3a$ and $S3a$ are the highest on all stiffnesses as they are the most reinforced clutches and have the highest force-carrying capacities. The force-concentration of $S3a$ is higher than that of $C3a$ initially even though the force-capacity of $C3a$ is twice that of $S3a$ (as $C3a$ is a dimer of $S3a$). But there is a gradual reduction of this difference over time due to continued dimerization of $S3a$ into $C3a$.

4.5.35 Sensitivity analysis results

Figures Figure S.4.9 and Figure S.4.10 show the results of sensitivity analysis conducted on 22 different parameters on the two outcomes detailed in the main text. Of these, 7 parameters were chosen to be shown in Fig4.5 (main text), either because the outcomes were highly sensitive to these parameters or because they were of particular interest and had a relatively low influence.

4.5.36 Supplementary tables

Table S.4.1 Parameter values used for the baseline model

Parameter	Definition	Value	Ref.	Remark	Ref. type
$k_{1f_{base}}$	Pre-complex formation	0.12 s^{-1}	Bachir *et al.*, 2014; Lavelin *et al.*, 2013		*Experimental*
k_{1rbase}	Pre-complex dissociation	0.095 s^{-1}	Bachir *et al.*, 2014		*Experimental*
$k_{2f_{base}}$	S1 formation from Pcomp	0.021 s^{-1}	C. K. Choi *et al.*, 2008		*Experimental*
$k_{3f_{base}}$	C1 formation from S1	0.021 s^{-1}	C. K. Choi *et al.*, 2008		*Experimental*
k_{7r}	Vinculin dissociation from AB $seed$	0.0001 s^{-1}		*Estimate*	
k_{8r}	Vinculin dissociation from AB $seed$	0.0001 s^{-1}		*Estimate*	
k_{12r}	Vinculin dissociation from AB $clust$	0.0001 s^{-1}		*Estimate*	
k_{13r}	Vinculin dissociation from AB $clust$	0.0001 s^{-1}		*Estimate*	
k_{14f}	S1a dimerization	1 s^{-1}	Cheng *et al.*, 2020		*Computational*
k_{14r}	C1a dissociation to S1a	0.001 s^{-1}		*Estimate*	
k_{15f}	S2a dimerization	1 s^{-1}	Cheng *et al.*, 2020		*Computational*

k_{15r}	C2a dissociation to S2a	0.001 s^{-1}		*Estimate*	
k_{16f}	S3a dimerization	1 s^{-1}	Cheng *et al.*, 2020		*Computational*
k_{16r}	C3a dissociation to S3a	0.001 s^{-1}		*Estimate*	
$k_{21f_{base}}$	C3 dissociation to S3	0.005 s^{-1}		*Estimate*	
$k_{22f_{base}}$	C2 dissociation to S2	0.008 s^{-1}		*Estimate*	
$k_{23_{KM}}$	Michaelis-Menten constant for signal decay	2.13 μM		*Estimate*	
$k_{23_{vmax}}$	Maximum velocity for signal decay reaction	0.1 $\mu M s^{-1}$		*Estimate*	
$k_{unfold_{UL}}$	Rate of unloaded talin unfolding	1.54 s^{-1}	Rio *et al.*, 2009		*Experimental*
$k_{off_{UL}}$	Unloaded talin-actin unbinding rate	0.35 s^{-1}	Chan and Odde, 2008	*Estimate based on literature*	*Computational*
k_{uf}	Talin-unfolding exponent factor	0.05	Rio *et al.*, 2009		*Experimental*
A	Catch bond parameter	2.52 s^{-1}	Kong *et al.*, 2009		*Experimental*
b	Catch bond parameter	-0.107 s^{-1}	Kong *et al.*, 2009		*Experimental*
C	Catch bond parameter	0.000123 s^{-1}	Kong *et al.*, 2009		*Experimental*
d	Catch bond parameter	0.1897 s^{-1}	Kong *et al.*, 2009		*Experimental*

F_{th1}	Force threshold for talin-actin slip bond for low order clutch	2 pN	Jiang *et al.*, 2003		*Experimental*
F_{th2}	Force threshold for talin-actin slip bond for mid order clutch	2.5 pN	Jiang *et al.*, 2003	*The increase is estimated to account for vinculin-actin bond*	*Experimental*
F_{th3}	Force threshold for talin-actin slip bond for high order clutch	3 pN	Jiang *et al.*, 2003	*The increase is estimated to account for vinculin-actin bond*	*Experimental*
F_{vb1}	Force threshold for 1^{st} vinculin binding event	5 pN	Yao *et al.*, 2016		*Experimental*
F_{vb2}	Force threshold for 2^{nd} vinculin binding event	12 pN	Rio *et al.*, 2009		*Experimental*
n	Conversion factor from concentration to molecules	Local volume*N_A			
$conc_{myo}$	Concentration of active myosin motors	4 μM		*Adjusted*	

$F_{myo_{single}}$	Force exerted by a single myosin motor	2 pN	Molloy *et al.*, 1995		*Experimental*
v_u	Unloaded actin retrograde velocity	110 nm/s	Chan and Odde, 2008; Elosegui-Artola *et al.*, 2016		*Computational, Experimental*
dt	Time step	0.005 s		*Used in this study*	
Local volume	Volume of focal adhesions and their immediate surroundings	1 um^3	Franz and Müller, 2005	*Estimate*	*Experimental*
k_{tal}	Stiffness of talin molecule	0.1 pN/nm	Yao *et al.*, 2016	*Estimate from force-extension curves*	*Experimental*
k_{vinc}	Stiffness of vinculin molecule	0.25 pN/nm	Huang *et al.*, 2017		*Experimental*
k_{sub}	Substrate stiffness	0.1-100 pN/nm		*Tested*	
tal_{rf}	Talin refolding rate	1 s^{-1}	Yao *et al.*, 2016	*Estimate based on experimental data (Fig 4.5e)*	*Experimental*

$tal_{rf_{factor}}$	Talin refolding rate factor for 1^{st} refolding event	0.5		*Estimate*	
k_{sens}	Time-dependency factor	0.05		*Estimate*	
k_{dis}	Disassembly rate of nascent adhesions	0.02434 s^{-1}	C. K. Choi *et al.*, 2008	*Adjusted – experimental rate was multiplied by 2*	*Experimental*
$signal_{thresh}$	Threshold concentration of signal	0.1 μM		*Arbitrary*	
N_A	Avogadro's constant	$6.023 \cdot 10^{23}$			

Table S.4.2 Reactions in the model

Rx number	Reaction
Rx1	$k_{1f} \cdot [int] \cdot [tal] \cdot [vinc] - k_{1r} \cdot [Pcomp]$
Rx2	$k_{2f} \cdot [Pcomp]^2 - k_{2r} \cdot [S1]$
Rx3	$k_{3f} \cdot [S1]^2 - k_{3r} \cdot [C1]$
Rx4	$k_{4f} \cdot [S1] - k_{4r} \cdot [S1a]$
Rx5	$k_{5f} \cdot [S2] - k_{5r} \cdot [S2a]$
Rx6	$k_{6f} \cdot [S3] - k_{6r} \cdot [S3a]$
Rx7	$k_{7f} \cdot [S1a] \cdot [vinc]^2 - k_{7r} \cdot [S2a]$
Rx8	$k_{8f} \cdot [S2a] \cdot [vinc]^2 - k_{8r} \cdot [S3a]$
Rx9	$k_{9f} \cdot [C1] - k_{9r} \cdot [C1a]$
Rx10	$k_{10f} \cdot [C2] - k_{10r} \cdot [C2a]$
Rx11	$k_{11f} \cdot [C3] - k_{11r} \cdot [C3a]$
Rx12	$k_{12f} \cdot [C1a] \cdot [vinc]^2 - k_{12r} \cdot [C2a]$
Rx13	$k_{13f} \cdot [C2a] \cdot [vinc]^2 - k_{13r} \cdot [C3a]$
Rx14	$k_{14f} \cdot [S1a]^2 - k_{14r} \cdot [C1a]$
Rx15	$k_{15f} \cdot [S2a]^2 - k_{15r} \cdot [C2a]$
Rx16	$k_{16f} \cdot [S3a]^2 - k_{16r} \cdot [C3a]$
Rx17	$k_{17f} \cdot [S3]$
Rx18	$k_{18f} \cdot [S2]$
Rx19	$k_{19f} \cdot [C3]$
Rx20	$k_{20f} \cdot [C2]$
Rx21	$k_{21f} \cdot [C3]$
Rx22	$k_{22f} \cdot [C2]$
Rx23	$-\frac{k_{23_{vmax}} \cdot [signal]}{k_{23_{KM}} + [signal]}$

4.5.37 Supplementary figures

Figure S.4.1 The Hookean spring system of an individual complex used in this model. Complexes bind in groups of 25 and 50 to form seeds and clusts respectively. A, B, C, D together represent the talin rod, here modelled as having 4 sub-domains. Springs E,G, and F represent vinculin molecules.

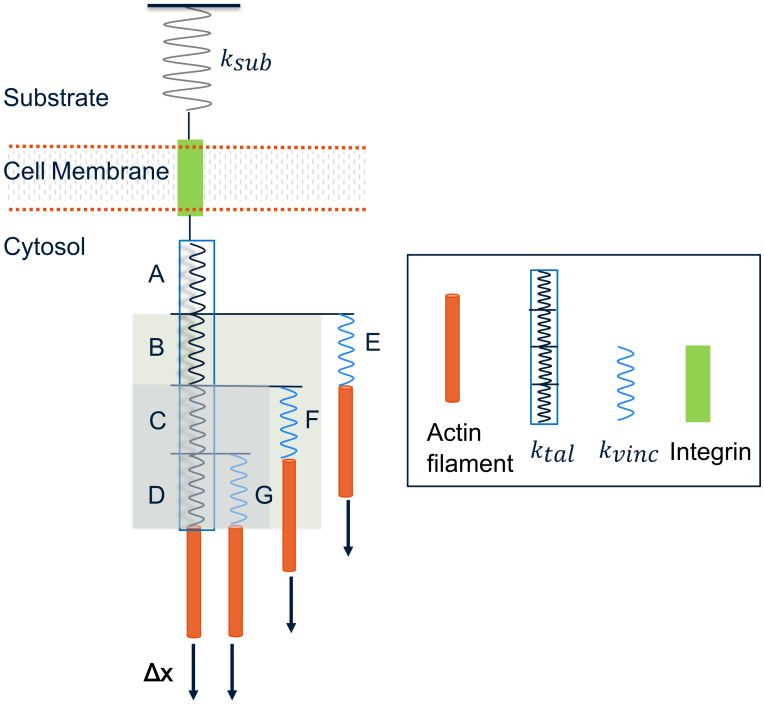

Figure S.4.2 Mass conservation of integrins (A) and talin (B) is satisfied. The concentration remains at 1 μM for the entire duration of the simulation.

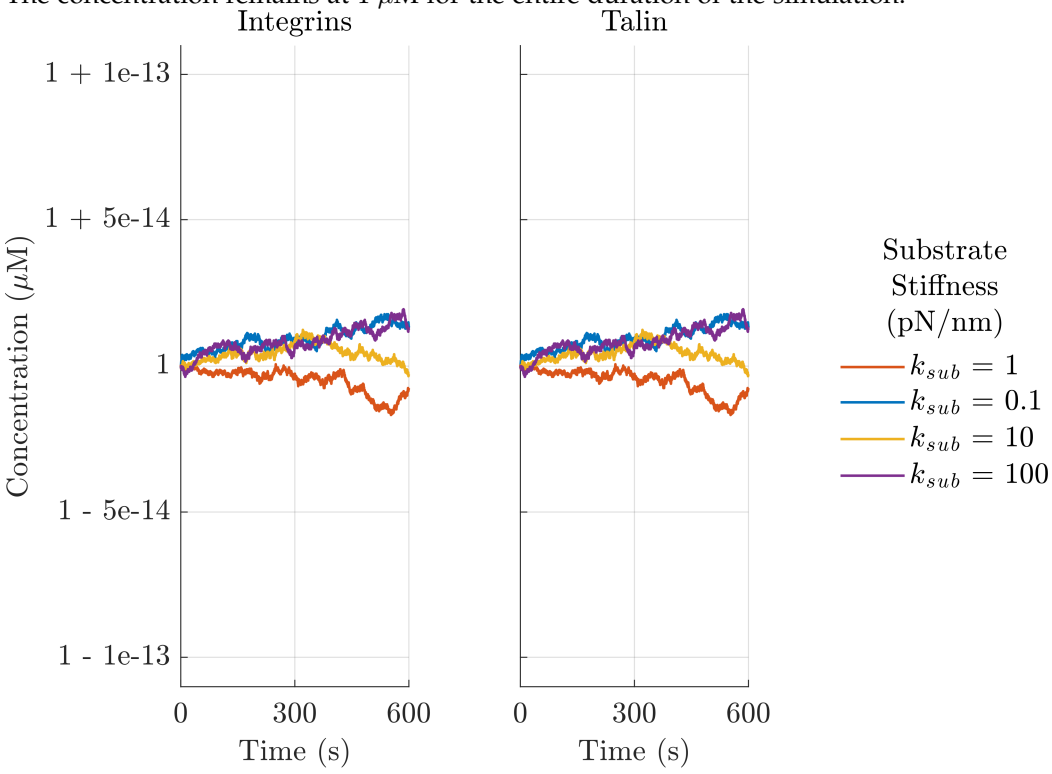

Figure S.4.3 Concentration of signal (blue) over time. The yellow line represents the value of the SDRM factor. The orange vertical line marks the time at which $[signal]$ goes (A) below (or above (B)) $signal_{thresh}$ which is shown by the orange dashed line. t_{sig} is the time when $[signal]$ crosses the threshold $signal_{thresh}$. A and B show signal decay and signal growth, respectively. The time t_{sig} and the SDRM factor are also identical in both.

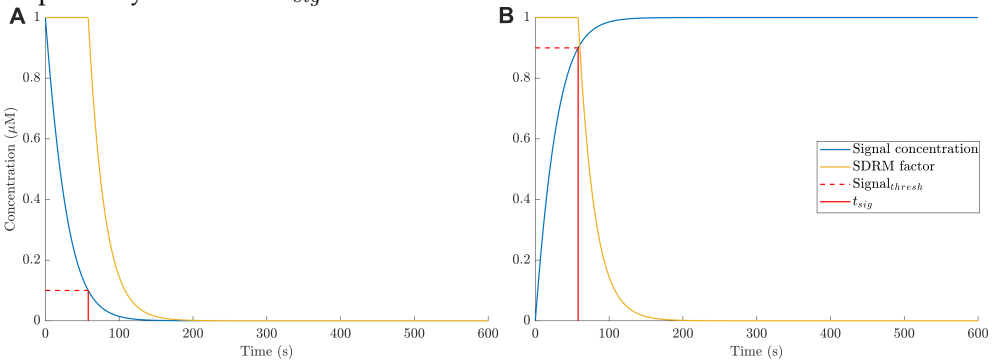

Figure S.4.4 Concentrations of actin-bound species (i-vi) in the first 70 seconds of the simulation. The growth of mid and higher order seeds and clusts is most rapid on a substrate of moderate stiffness (k_{sub} =1 pN/nm).

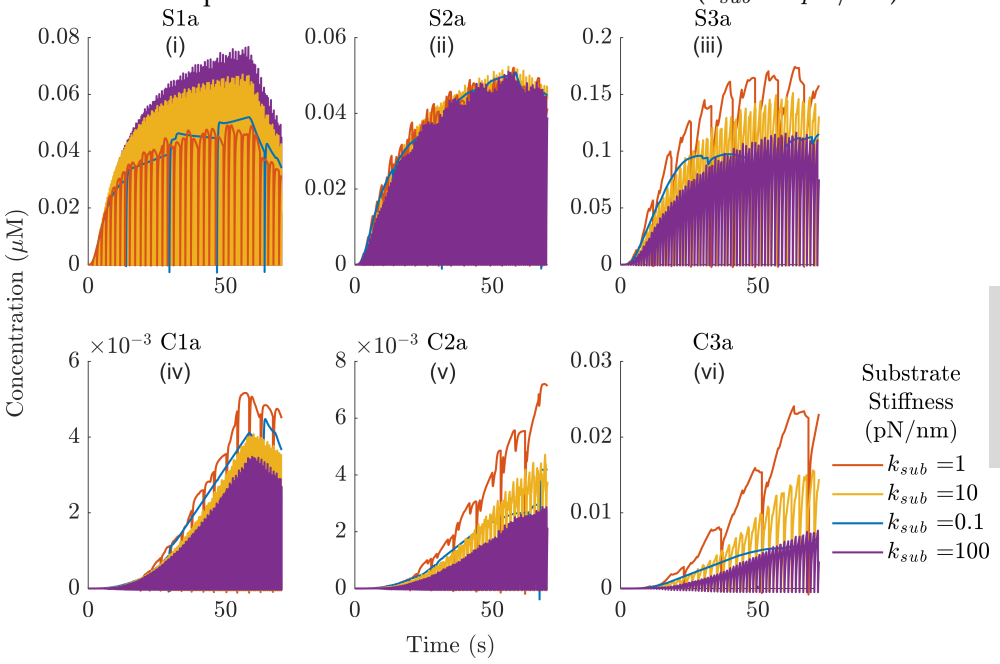

Figure S.4.5 Limited vinculin test. Concentrations of integrins in (i) low-, (ii) mid-, and (iii) high-order species when vinculin concentration is limited to 1 μM. (iv) shows the maturation fraction (or the concentration of integrins in mature adhesions) increases monotonically with increasing stiffness.

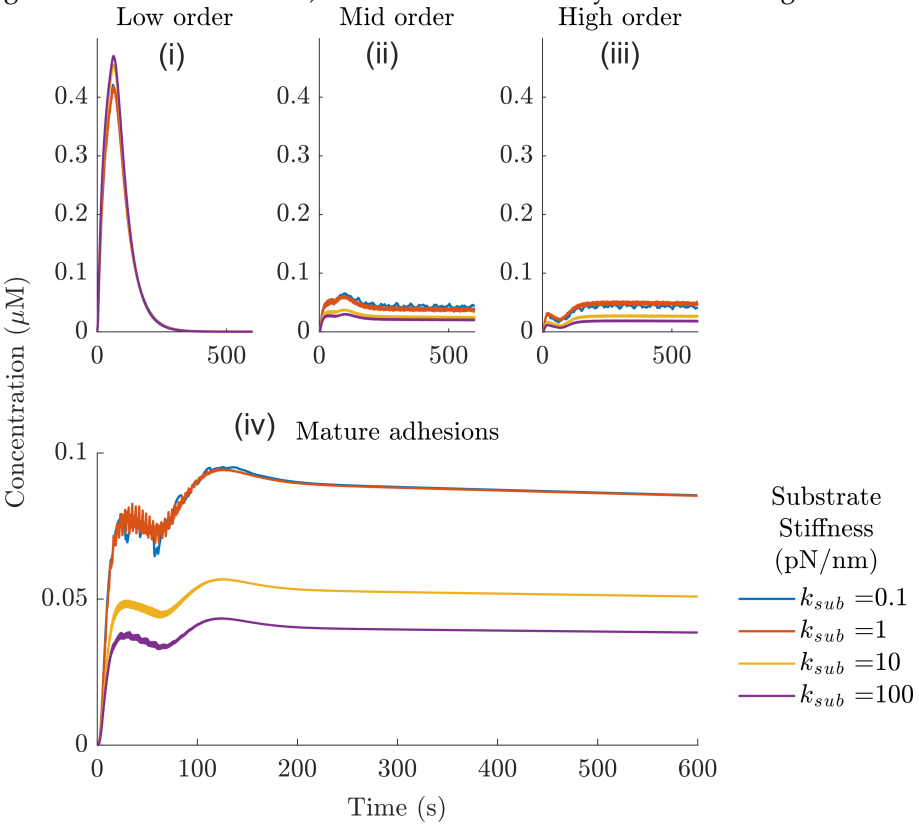

Figure S.4.6 The effect of TDRM. Value of the actin-unbinding rates for the largest clusts C3a, k_{11r} (bottom) and the smallest seeds S1a, k_{4r} (top) over time for soft (A, C, E, G) and stiff (B, D, F, H) substrates for simulations with (A-D) and without (E-H) TDRM. The effect of TDRM is highly pronounced for $k_{sub} = 0.1\ pN/nm$ seen as a jump in the maximum value from $\sim 2.7\ s^{-1}$ *to* $\sim 6.8\ s^{-1}$ but negligible for $k_{sub} = 100\ pN/nm$ as the time period in actin-binding phase is very short.

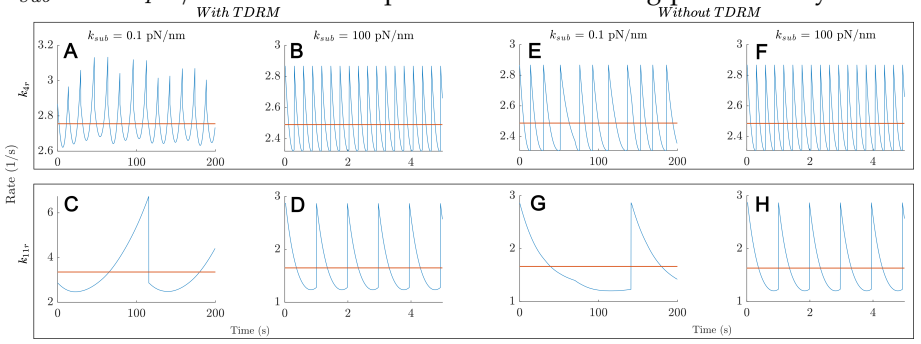

Figure S.4.7 Concentrations of integrins in (i) low-, (ii) mid-, and (iii) high-order species in simulations with (A) and without (B) TDRM. (iv) shows the maturation fraction (or the concentration of integrins in mature adhesions). In A(iv), a biphasic trend is seen – the highest maturation fraction is on an optimal substrate stiffness of $k_{sub} = 1\ pN/nm$ (orange curves) whereas in B(iv), a monotonic decrease in maturation fraction is seen.

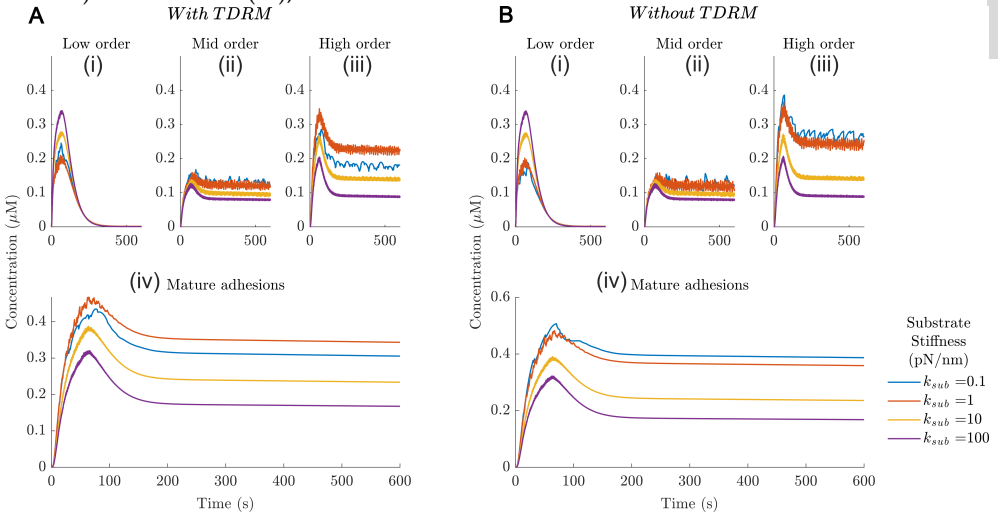

Figure S.4.8 Concentrations of integrins in A(i) low-, A(ii) mid-, and A(iii) high-order species when the talin refolding factor $tal_{rf_{factor}}$ was set to 0.2/s. A(i–v) shows the maturation fraction (or the concentration of integrins in mature adhesions). B(i – vi) show the concentrations of actin-bound species under the same conditions.

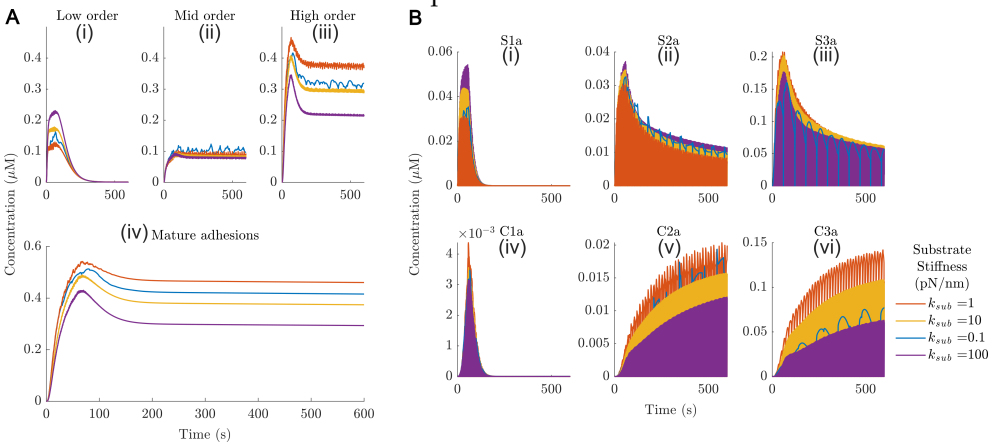

Figure S.4.9 Sensitivity analysis for outcome 1: Maturation fraction. Panels A, B, C, and D represent the sensitivities of the outcome for changes of +20%, +10%, -10%, and -20% to the parameter values respectively. Refer to Table S.4.1 for parameter descriptions.

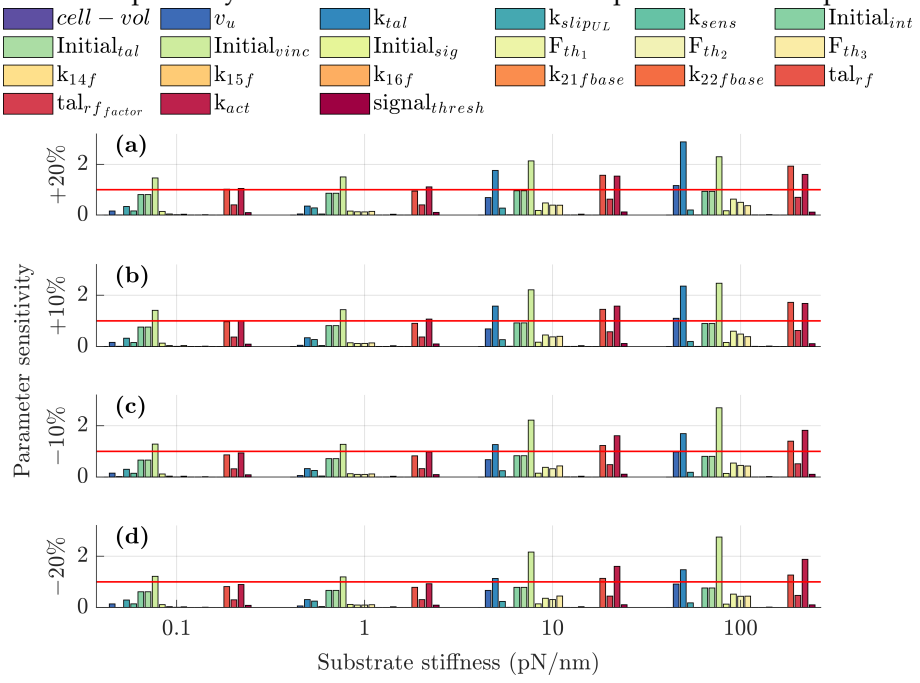

Figure S.4.10 Sensitivity analysis for outcome 2: Optimum stiffness. Panels A, B, C, and D represent the sensitivities of the outcome for changes of +20%, +10%, -10%, and -20% to the parameter values respectively. Refer to Table S.4.1 for parameter descriptions.

Figure S.4.11 Curve fitting. Plots of the curve fitted over peaks of the force exerted by each species on substrates of varying stiffness (A-D). The total force exerted by all clutches on a particular substrate is shown by the black dotted line.

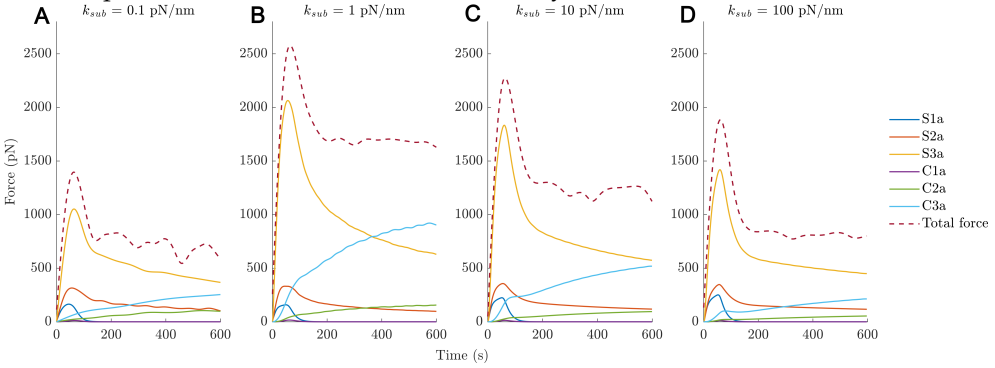

Figure S.4.12 Concentrations of integrins in A(i) low-, A(ii) mid-, and A(iii) high-order species when the order of reinforcement reactions were set to 1. A(iv) shows the maturation fraction (or the concentration of integrins in mature adhesions). B(i – vi) show the concentrations of actin-bound species under the same conditions.

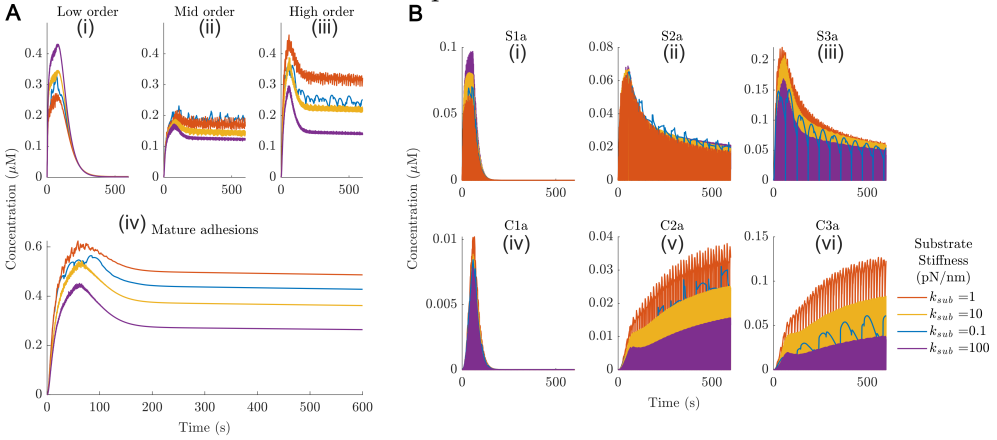

Figure S.4.13 Concentrations of integrins in A(i) low-, A(ii) mid-, and A(iii) high-order species when both slip and catch bond dissociation rates are modified with TDRM. A(iv) shows the maturation fraction (integrins in mature adhesions). B(i–vi) show the concentrations of actin-bound species under the same conditions in Table S.4.1.

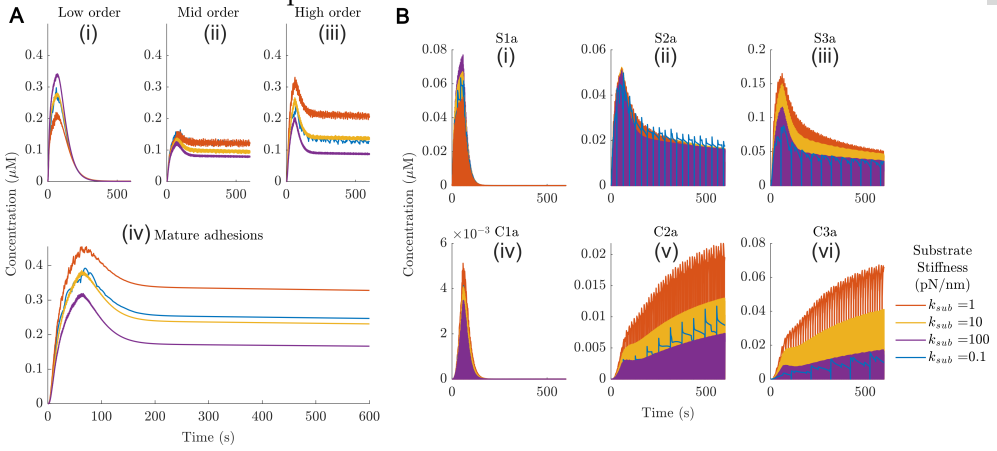

5

Computational Evidence for Multi-Layer Crosstalk Between the Cadherin-11 and PDGFR Pathways

This chapter has been **published** as: Karagöz, Z., Passanha, F. R., Robeerst, L., van Griensven, M., LaPointe, V. L. S., & Carlier, A. (2023). Computational evidence for multi-layer crosstalk between the cadherin-11 and PDGFR pathways. *Scientific Reports*, *13*(1), 15804. https://doi.org/10.1038/s41598-023-42624-x.

Abstract

Various cell surface receptors play an important role in the differentiation and self-renewal of human mesenchymal stem cells (hMSCs). One example of such receptors are the cadherins, which maintain cell–cell adhesion and mechanically couple cells together. Recently, cadherin-11, which is a member of the type II classical cadherin family, has been shown to be involved in the fate commitment of hMSCs. Interestingly, cadherin-11 has no known intrinsic signaling activity and is thought to affect cell behavior via interactions with other cell surface receptors. Members of the platelet-derived growth factor receptor (PDGFR) family are hypothesized to be one of the interaction partners of cadherin-11. Experiments confirmed that PDGFR-α binding to extracellular cadherin-11 regions increases the PDGFR-α activity, whereas the interaction between PDGFR-β and cadherin-11 suppresses the activity of the growth factor receptor. Cadherin-11 knockdown experiments also decreased cell proliferation. These interactions between cadherin-11 and PDGFRs indicate a crosstalk between these receptors and their downstream signaling activities but the nature of this crosstalk is not entirely known. In this study, we used a computational model to represent the experimentally proven interactions between cadherin-11 and the two PDGFRs and we inspected whether the crosstalk also exists downstream of the signaling initiated by the two receptor families. The computational framework allowed us to monitor the relative activity levels of each protein in the network. We performed model simulations to mimic the conditions of previous cadherin-11 knockdown experiments and to predict the effect of crosstalk on cell proliferation. Overall, our predictions suggest the existence of another layer of crosstalk, namely between β-catenin (downstream to cadherin-11) and an ERK inhibitor protein (e.g. DUSP1), different than the crosstalk at the receptor level between cadherin-11 and PDGFR-α and -β. By investigating the multi-level crosstalk between cadherin and PDGFRs computationally, this study contributes to an improved understanding of the effect of cell surface receptors on hMSCs proliferation.

5.1 Introduction

For decades we have known that signaling does not occur linearly, but through a complex network of interacting signals and pathways made up of signaling molecules (Barabási & Oltvai, 2004). Using wet laboratory experiments, a myriad of these signaling molecules have been identified and scientists have also tried to understand the crosstalk between them. However, these experiments have their limitations when it comes to studying the relationship between large networks of signaling pathways, as they can only isolate parts of the pathways and cannot look at the whole network. Computational models are better equipped to predict and analyze pathway crosstalk, as they offer a systematic way to conduct multivariate experiments that are impossible to perform *in vitro*, and they can also generate experimentally testable predictions. In our study, we have taken a wet laboratory experiment that studied the interaction between receptor tyrosine kinase, a cell surface receptor, and a specific cadherin, a cell adhesion protein (Takeichi, 2018) and we used computational modeling to add to the evidence and better understand the extent of the crosstalk.

There has been recent interest in the physical interaction between cadherin-11 and the two receptor tyrosine kinases (RTKs), PDGFR-α (Madarampalli *et al*., 2019) and PGDGFR-β (Liu *et al*., 2020; Passanha *et al*., 2022) in fibroblasts and human mesenchymal stem cells (hMSCs) respectively. Passanha et al., 2022 reported that by using gene knockdown to temporarily decrease the expression of cadherin-11, the cadherin-11 knockdown cells have a more prolonged expression of phosphorylated ERK in the nuclei and these cells also show decreased proliferation. Similarly, Liu et al., 2019 showed that knocking down cadherin-11 also results in a decrease in proliferation. ERK is known to be downstream of the various RTKs including PGDGFR-β and so the current hypothesis is that the physical interactions between PGDGFR-β and cadherin-11 point towards a crosstalk between these two pathways. Although the receptor level interactions between RTKs and cadherins have been confirmed by wet laboratory experiments, we still know very little about the extent of this crosstalk as we lack experimental tools to investigate it. Here we want to use computational modeling to explore potential downstream interactions on top of the known receptor level interactions and expand the knowledge of this interesting crosstalk.

The ERK pathway is central to the progression of the cell cycle, proliferation, and growth of eukaryotic cells. It is known to be regulated by many growth

factor receptors and thus part of many different signaling pathways, including the RTK and the cadherin pathways (Ramos, 2008). Using computational modeling, we isolated the RTK and cadherin-11 pathways and looked at how the crosstalk between these two pathways affects the ERK nuclear translocation leading to changes in cell proliferation. We observed that the downstream signaling in our model did not reflect the experimental evidence without a player between β-catenin (a subunit of the cadherin protein complex) and ERK that can influence proliferation. We, therefore, concluded that crosstalk at the receptor level between the RTK and cadherin-11 pathways alone is insufficient for cadherin-11 to influence hMSC proliferation through the ERK pathway, and that an additional level of crosstalk could be in place. By being able to study this interconnectedness between pathways, we have shown that our model can be used to describe the nature of the crosstalk between signaling molecules which is not always possible experimentally.

5.2 Methods

5.2.1 Model Development

We built the signaling network in Figure 5.1 to include the PDGFR-α and PDGFR-β–induced ERK pathway as well as the cell–cell contact signaling via cadherin-11. The network represents the interactions of two adjacent cells and focuses on the intracellular response of one of these cells in contact. The receptor level interactions capture the experimentally established activation of PDGFR-α by cadherin-11 of the neighboring cell and the inhibition of PDGFR-β by cadherin-11 on the cell membrane. PDGFR-α and -β are activated by their ligands PDGF-α (a in Figure 5.1) and PDGF-β (b in Figure 5.1). The ERK pathway is activated downstream to the growth factor receptors, and follows the classical RAS-RAF-MEK-ERK cascade. ERK then activates its own inhibitor, DUSP1, which activates the cell cycle protein cyclin-D1. Downstream to cadherin-11, we included β-catenin that is inhibited by cadherin-11. B-catenin has shown to inhibit DUSP family proteins (Zeller *et al.*, 2012), to interfere with the RAS-RAF-MEK-ERK cascade. Within this network, we also propose the inhibition of DUSP1 by β-catenin to be a key crosstalk mechanism, besides the experimentally established receptor-level interactions described earlier.

We developed an ordinary differential equation (ODE) model to represent the known and suggested crosstalk between PDGFR and cadherin-11 as well as

their downstream effectors. All the ODEs in the model (Table 5.1) have the form suggested by Mendoza and Xenarios, 2006, given in Eq.5.1, to capture the qualitative behavior of cadherin-11 and PDGFR and their effect downstream, observed in the experiments by both Madarampalli *et al*., 2019 and Passanha *et al*., 2022. We chose this type of equation as it allows a signaling network to be translated into a continuous dynamical system and study its stable steady state and qualitative behavior without the need for precise data on the signaling stoichiometry and kinetics.

$$\frac{dX_i}{dt} = \frac{-\ e^{0.5\ \times\ h}\ +\ e^{-h\ \times\ (\omega_i - 0.5)}}{(1 - e^{0.5\ \times\ h})\ \times\ (1 +\ e^{-h\ \times\ (\omega_i - 0.5)})}\ -\ (k_i\ \times\ X_i) \tag{5.1}$$

The model equations (Table 5.1) represent the rate of change in the activity level of each protein in the network. Here the "activity level" indicates the net effect of a protein in its active form (either in the phosphorylated form or otherwise functional). For example, when we mention "activity of ERK" in relation to this model, we mean "phosphorylated ERK in the nucleus, where it is active". The activity level of proteins varies between 0 and 1 (1 being maximum activity) and it is unitless, due to the nature of the ODEs described in Mendoza and Xenarios, 2006. It is important to note that, by using this type of ODEs, we were able to investigate the activation/inactivation of signalling proteins in the network, without explicitely modelling the biochemical reactions among the proteins or the molar concentrations of the proteins in the network. Therefore, if the activity of a protein is above zero, it indicates the presence and activity of that protein in the system, without implying any relation to its molar concentration.

Each ODE has an activation term and a decay term. The decay term mimics the autoinhibition or the inactivation of proteins in the cell over time. The general decay parameter, k_i, was set to 1 for all proteins for simplicity. Only for the β-catenin decay parameter, we used $k_{iB} = 2$ to compensate for its high initial activity and to account for the involvement of β-catenin in other intracellular pathways (Valenta *et al*., 2012). The activation term in the ODEs includes a parameter omega (ω) which is specific to each protein and the values of ω can be calculated using the generalized equation Eq.5.2 and the parameters in Table 5.2.

$$\omega_i = \left(\frac{1.0 \ + \ \sum a_n}{\sum a_n}\right) \times \left(\frac{\sum x_n^a \ \times a_n}{1.0 \ + \sum x_n^a \ \times a_n}\right) \times \left(1 - \left(\frac{1 + \ \sum \beta_n}{\sum \beta_n}\right) \times \ \left(\frac{\sum \beta_n \times x_n^i}{1 + \sum \beta_n \times x_n^i}\right)\right) \tag{5.2}$$

ω_i represents the total input to the activity of each protein at a particular time. x_n^a is a set of activators and x_n^i is a set of inhibitors of the protein X_i. The alpha (α_n) parameters represent activation and the beta (β_n) parameters represent inhibition between proteins. For example, PDGFR-β is activated by its own ligand PDGF-β while it is also inhibited by cadherin-11 therefore we use $\alpha_{pdgfrB_{by_b}}$ to represent the activation and $\beta_{pdgfrB_{by_{cdh11}}}$ to represent the inhibition in ω_{pdgfrB}. As such, using the parameters in Table 5.2, we mathematically built the network given in Figure 5.1.

The parameters a and b and the initial activity levels of PDGF-A and PDGF-B were adjusted to meet the quantitative measurements of PDGFR-α and PDGFR-β activity levels in cadherin-11 knockdown experiments by Madarampalli *et al.*, 2019 and Passanha *et al.*, 2022, respectively. The remaining parameters were set to a default value of 1, as suggested by Mendoza and Xenarios, 2006 in case of insufficient experimental data. It is important to note that by using this type of ODEs, we were able to capture the qualitative behavior of the whole network and the changes in the activity levels of each protein at the steady state, while the time, and consequently also the dynamics, were arbitrary, as described in detail in Mendoza and Xenarios, 2006.

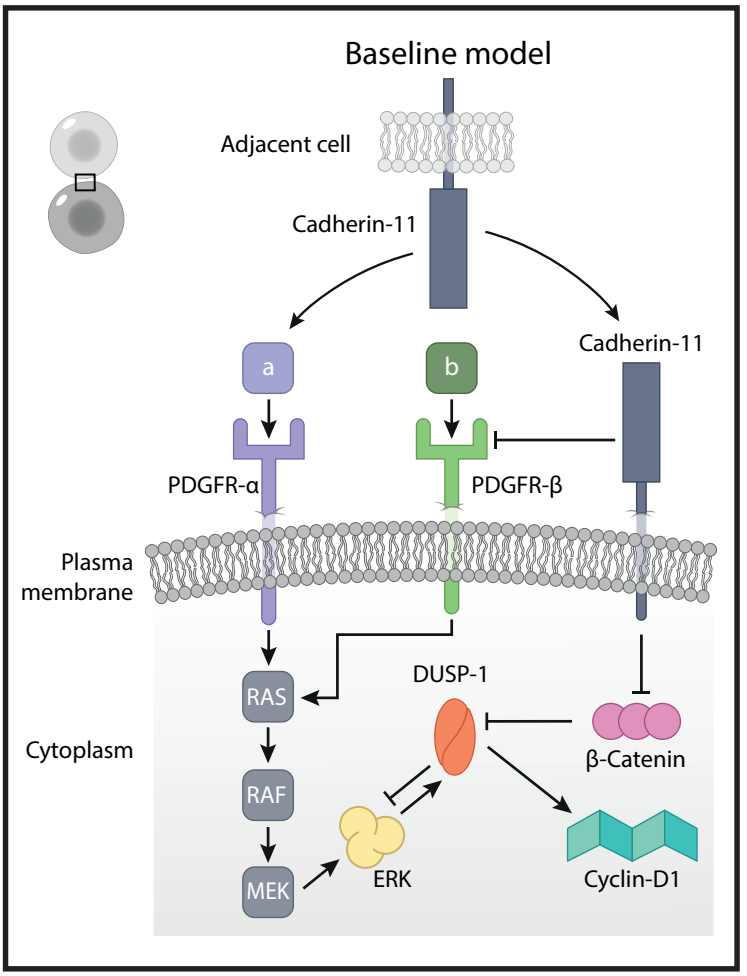

Figure 5.1: The schematic representation of receptor level crosstalk between growth factor receptors (PDGFR-α and PDGFR-β) and cadherin-11, and the proposed crosstalk between β-catenin and ERK via the ERK inhibitor DUSP1. Arrows represent activation and blunt arrows represent inhibition. The network represents the interactions of two adjacent cells (top left corner) and focuses on the intracellular response of one of these cells in contact.

Table 5.1: Ordinary differential equations governing the activity levels of each protein in the model network.

Nr.	Equation
3	$\frac{dcdh11}{dt} = \frac{-e^{0.5 \times h} + e^{-h \times (\omega_{cdh11}-0.5)}}{(1-e^{0.5 \times h}) \times (1+ e^{-h \times (\omega_{cdh11}-0.5)})} - (k_i \times cdh11))$
4	$\frac{dpdgfrA}{dt} = \frac{-e^{0.5 \times h} + e^{-h \times (\omega_{pdgfrA}-0.5)}}{(1-e^{0.5 \times h}) \times (1+ e^{-h \times (\omega_{pdgfrA}-0.5)})} - (k_i \times pdgfrA))$
5	$\frac{dpdgfrB}{dt} = \frac{-e^{0.5 \times h} + e^{-h \times (\omega_{pdgfrB}-0.5)}}{(1-e^{0.5 \times h}) \times (1+ e^{-h \times (\omega_{pdgfrB}-0.5)})} - (k_i \times pdgfrB))$
6	$\frac{dras}{dt} = \frac{-e^{0.5 \times h} + e^{-h \times (\omega_{ras}-0.5)}}{(1-e^{0.5 \times h}) \times (1+ e^{-h \times (\omega_{ras}-0.5)})} - (k_i \times ras))$
7	$\frac{draf}{dt} = \frac{-e^{0.5 \times h} + e^{-h \times (\omega_{raf}-0.5)}}{(1-e^{0.5 \times h}) \times (1+ e^{-h \times (\omega_{raf}-0.5)})} - (k_i \times raf))$
8	$\frac{dmek}{dt} = \frac{-e^{0.5 \times h} + e^{-h \times (\omega_{mek}-0.5)}}{(1-e^{0.5 \times h}) \times (1+ e^{-h \times (\omega_{mek}-0.5)})} - (k_i \times mek))$
9	$\frac{derk}{dt} = \frac{-e^{0.5 \times h} + e^{-h \times (\omega_{erk}-0.5)}}{(1-e^{0.5 \times h}) \times (1+ e^{-h \times (\omega_{erk}-0.5)})} - (k_i \times erk))$
10	$\frac{ddusp1}{dt} = \frac{-e^{0.5 \times h} + e^{-h \times \left(\omega_{dusp1}-0.5\right)}}{(1-e^{0.5 \times h}) \times \left(1+ e^{-h \times \left(\omega_{dusp1}-0.5\right)}\right)} - (k_i \times dusp1))$
11	$\frac{dBcat}{dt} = \frac{-e^{0.5 \times h} + e^{-h \times (\omega_{Bcat}-0.5)}}{(1-e^{0.5 \times h}) \times (1+ e^{-h \times (\omega_{Bcat}-0.5)})} - (k_{iB} \times Bcat))$
12	$\frac{dcyclinD1}{dt} = \frac{-e^{0.5 \times h} + e^{-h \times (\omega_{cyclinD1}-0.5)}}{(1-e^{0.5 \times h}) \times (1+ e^{-h \times (\omega_{cyclinD1}-0.5)})} - (k_i \times cyclinD1))$

Table 5.2: Parameter values used in the baseline simulation.

Parameter	Value	Explanation
c	0.1	Initial cell–cell adhesion via the cadherin-11 on the adjacent cell. Value adjusted using Madarampalli *et al.*, 2019
a	0.1	Initial PDGF-A ligand activity. Value adjusted using Madarampalli *et al.*, 2019 and Passanha *et al.*, 2022
b	0.4	Initial PDGF-B ligand activity. Value adjusted using Madarampalli *et al.*, 2019 and Passanha *et al.*, 2022
$Bcat$	1	Initial β-catenin activity
ω_{cdh11}	$\left(\frac{1.0 + \alpha_{cdh11_{by_c}}}{\alpha_{cdh11_{by_c}}}\right) \times \left(\frac{c \times \alpha_{cdh11_{by_c}}}{1.0 + (c \times \alpha_{cdh11_{by_c}})}\right)$	Total input to the activity of cadherin-11
ω_{pdgfrA}	$\left(\frac{1.0 + \alpha_{pdgfrA_{by_a}} + \alpha_{pdgfrA_{by_c}}}{\alpha_{pdgfrA_{by_a}} + \alpha_{pdgfrA_{by_c}}}\right) \times \left(\frac{a \times \alpha_{pdgfrA_{by_a}} + c \times \alpha_{pdgfrA_{by_c}}}{1.0 + \left(a \times \alpha_{pdgfrA_{by_a}} + c \times \alpha_{pdgfrA_{by_c}}\right)}\right)$	Total input to the activity of PDGFR-α

ω_{pdgfrB}	$\left(\frac{1.0 + \alpha_{pdgfrB_{by_b}}}{\alpha_{pdgfrB_{by_b}}}\right) \times \left(\frac{b \times \alpha_{pdgfrB_{by_b}}}{1.0 + b \times \alpha_{pdgfrB_{by_b}}}\right) \times \left(1 - \left(\frac{1 + \beta_{pdgfrB_{by_{cdh11}}}}{\beta_{pdgfrB_{by_{cdh11}}}}\right) \times \left(\frac{\beta_{pdgfrB_{by_{cdh11}}} \times cdh11}{1 + (\beta_{pdgfrB_{by_{cdh11}}} \times cdh11)}\right)\right)$	Total input to the activity of PDGFR-β
ω_{ras}	$\left(\frac{1.0 + \alpha_{ras_{by_{pdgfrA}}} + \alpha_{ras_{by_{pdgfrB}}}}{\alpha_{ras_{by_{pdgfr}}} + \alpha_{ras_{by_{pdgfrB}}}}\right) \times \left(\frac{pdgfrA \times \alpha_{ras_{by_{pdgfrA}}} + pdgfrB \times \alpha_{ras_{by_{pdgfrB}}}}{1.0 + \left(pdgfrA \times \alpha_{ras_{by_{pdgfrA}}}\right) + \left(pdgfrB \times \alpha_{ras_{by_{pdgfrB}}}\right)}\right)$	Total input to the activity of RAS
ω_{raf}	$\left(\frac{1.0 + \alpha_{raf_{by_{ras}}}}{\alpha_{raf_{by_{ras}}}}\right) \times \left(\frac{ras \times \alpha_{raf_{by_{ras}}}}{1.0 + (ras \times \alpha_{raf_{by_{ras}}})}\right)$	Total input to the activity of RAF
ω_{mek}	$\left(\frac{1.0 + \alpha_{mek_{by_{raf}}}}{\alpha_{mek_{by_{raf}}}}\right) \times \left(\frac{raf \times \alpha_{mek_{by_{raf}}}}{1.0 + (raf \times \alpha_{mek_{by_{raf}}})}\right)$	Total input to the activity of MEK
ω_{erk}	$\left(\frac{1.0 + \alpha_{erk_{by_{mek}}}}{\alpha_{erk_{by_{mek}}}}\right) \times \left(\frac{mek \times \alpha_{erk_{by_{mek}}}}{1.0 + (mek \times \alpha_{erk_{by_{mek}}})}\right) \times \left(1 - \left(\frac{1 + \beta_{erk_{by_{dusp1}}}}{\beta_{erk_{by_{cdusp1}}}}\right) \times \left(\frac{\beta_{erk_{by_{dusp1}}} \times dusp1}{1 + (\beta_{erk_{by_{dusp1}}} \times dusp1)}\right)\right)$	Total input to the activity of ERK

ω_{dusp1}	$\left(\frac{1.0 + \alpha_{dusp1_{by_{erk}}}}{\alpha_{dusp1_{by_{erk}}}}\right) \times \left(\frac{erk \times \alpha_{dusp1_{by_{erk}}}}{1.0 + \left(erk \times \alpha_{dusp1_{by_{erk}}}\right)}\right) \times \left(1 - \left(\frac{1 + \beta_{dusp1_{by_{Bcat}}}}{\beta_{dusp1_{by_{Bcat}}}}\right) \times \left(\frac{Bcat \times \beta_{dusp1_{by_{Bcat}}}}{1 + \left(Bcat \times \beta_{dusp1_{by_{Bcat}}}\right)}\right)\right)$	Total input to the activity of DUSP1
ω_{Bcat}	$1 - \left(\frac{1 + \beta_{Bcat_{by_{cdh11}}}}{\beta_{Bcat_{by_{cdh11}}}}\right) \times \left(\frac{cdh11 \times \beta_{Bcat_{by_{cdh11}}}}{1 + \left(cdh11 \times \beta_{Bcat_{by_{cdh11}}}\right)}\right)$	Total input to the activity of β-catenin
$\omega_{cyclinD1}$	$\left(\frac{1.0 + \alpha_{cyclinD1_{by_{dusp1}}}}{\alpha_{cyclinD1_{by_{dusp1}}}}\right) \times \left(\frac{dusp1 \times \alpha_{cyclinD1_{by_{dusp1}}}}{1.0 + (dusp1 \times \alpha_{cyclinD1_{by_{dusp1}}})}\right)$	Total input to the activity of Cyclin-D1
h	1	Gain value of all ω functions
k_i	1	General decay parameter
k_{iB}	2	Decay parameter for β-catenin activity
$\alpha_{cdh11_{by_c}}$	1	Activation of cadherin-11 by cell–cell adhesion (c)
$\alpha_{pdgfrA_{by_a}}$	0.5	Activation of PDGFR-α by PDGF-α ligand. Value adjusted using Madarampalli *et al.*, 2019 and Passanha *et al.*, 2022

$\alpha_{pdgfrA_{by_c}}$	0.5	Activation of PDGFR-α by extracellular cadherin-11 binding. Value adjusted using Madarampalli *et al.*, 2019 and Passanha *et al.*, 2022
$\alpha_{pdgfrB_{by_b}}$	0.5	Activation of PDGFR-β by PDGF-β ligand. Value adjusted using Madarampalli *et al.*, 2019 and Passanha *et al.*, 2022
$\beta_{pdgfrB_{by_{cdh11}}}$	1	Inhibition of PDGFR-β by same-cell cadherin-11
$\alpha_{ras_{by_{pdgfrA}}}$	1	Activation of RAS by PDGFR-α
$\alpha_{ras_{by_{pdgfrB}}}$	1	Activation of RAS by PDGFR-β
$\alpha_{raf_{by_{ras}}}$	1	Activation of RAF by RAS
$\alpha_{mek_{by_{raf}}}$	1	Activation of MEK by RAF
$\alpha_{erk_{by_{mek}}}$	1	Activation of ERK by MEK
$\beta_{erk_{by_{dusp1}}}$	1	Inhibition of ERK by DUSP1
$\alpha_{dusp1_{by_{erk}}}$	1	Activation of DUSP by ERK
$\beta_{dusp1_{by_{Bcat}}}$	1	Inhibition of DUSP by β-catenin

$\beta_{Bcat_{by_{cdh11}}}$	1	Inhibition of β-catenin by cadherin-11
$\alpha_{cyclinD1_{by_{dusp1}}}$	1	Activation of Cyclin-D1 by DUSP1

5.2.2 Simulations

We used the Virtual Cell software (VCell) version 7.4.0 (Cowan *et al.*, 2012; Schaff *et al.*, 1997) to simulate the network. The baseline model, all different simulation setups, and the results can be accessed within the VCell software (available at https://vcell.org, model name: "cdh11-pdgfr-erk-feedback-v2" by user "zeynepkaragoz").

We first performed a simulation of the baseline model (Table 5.3: Baseline model) using the parameters in Table 5.2. This simulation provided a baseline steady state activity for each protein in the network. In the next simulation (Table 5.3: Cadherin-11 knockdown) we set the initial cadherin-11 activity to zero on both the cell for which the intracellular signaling is modeled and on the adjacent cell, mimicking the experimental cadherin-11 knockdown. We then compared the steady state activity levels of the cadherin-11 knockdown simulation to the baseline activity levels. Other simulations have been performed to test the effect of different crosstalk modes in the network, namely the crosstalk only at the receptor level, crosstalk only downstream to the receptors or both at the same time. These simulations have been explained in the text where relevant, and the corresponding parameter changes are given in Table 5.3.

5.2.3 Parameter Scan

To ensure our choice of parameters around the proposed crosstalk between DUSP1 and β-catenin did not force the system to behave in a biased way, we performed a parameter scan in groups of two at a time. First, different values (0.1, 0.5, 1.0, 5.0, 7.0, 10.0) of the parameter determining the inhibition of DUSP1 in the network ($\beta_{dusp1_{by_{Bcat}}}$) were scanned against different values of $Bcat$ (0.1, 0.3, 0.5, 0.7, 1.0) and $\alpha_{dusp1_{by_{erk}}}$ (0.1, 0.5, 1.0, 5.0, 7.0, 10.0), which are the two parameters that contribute to the activation of DUSP1 in the network. Second, the parameter that contributes to the inhibition of ERK by DUSP1 ($\beta_{erk_{by_{dusp1}}}$) was scanned against the parameter that contributes to the activation of ERK ($\alpha_{erk_{by_{mek}}}$). Last, $\beta_{erk_{by_{dusp1}}}$ was scanned against the parameter that contributes to the activation of cyclin-D1 by DUSP1 ($\alpha_{cyclinD1_{by_{dusp1}}}$). For the last two scans, we used the same parameter space for all parameters (0.1, 0.5, 1.0, 5.0, 7.0, 10.0). For all four parameter scans, parameters were varied simultaneously to cover all 25 combinations of the parameter sets.

As the output of the parameter scan, we reported the difference in steady state activity levels of cyclin-D1 and ERK as a measure of the change in cell proliferation compared to the baseline. Simulation with the baseline model parameters (all equal to 1) resulted in equal activity levels for cyclin-D1 and ERK. If for a parameter set, the cyclin-D1 activity was higher than ERK activity we classified this as "increased proliferation" compared to the baseline. If the cyclin-D1 activity was lower than ERK activity, we classified this as "decreased proliferation" compared to the baseline. For the cyclin-D1 activity matching the ERK activity we classified this as no change in proliferation compared to the baseline model parameter set. The results of this analysis are summarized in Figure 5.3 and the numerical results are given in Table S.5.1-4.

5.3 Results

First, in order to ensure that the baseline model captured the experimentally established activation of PDGFR-α by cadherin-11 on an adjacent cell and the inhibition of PDGFR-β by cadherin-11 in the cell membrane, we ran the baseline model simulation as is (Table 5.3: Baseline model), the cadherin-11 knockdown simulation (Table 5.3: Cadherin-11 knockdown), a simulation where the receptor interaction was disrupted via blocking the cadherin-11 binding to PDGFR-α (Table 5.3: Cell–cell contact off and cadherin–PDGFR-α binding off), and a simulation where the receptor interaction was disrupted by blocking the cadherin-11 binding to PDGFR-β (Table 5.3: Cell–cell contact off and cadherin–PDGFR-β binding off). In line with Passanha et al., 2022, the cadherin-11 knockdown resulted in a 50% decrease in PDGFR-α and a 30% increase in PDGFR-β activity compared to the baseline simulation (Figure S.5.1, Cadherin-11 knockdown). Also in line with Madarampalli et al., 2019, the absence of cadherin-11 binding to PDGFR-α resulted in 50% lower PDGFR-α activity while PDGFR-β activity did not change compared to the baseline simulation (Figure S.5.1, Cell–cell contact off and cadherin–PDGFR-α binding off). Lastly, the absence of the cadherin-11 binding to PDGFR-β only increased the PDGFR-β activity by 30% but did not affect the PDGFR-α activity compared to the baseline simulation (Figure S.5.1, Cell–cell contact off and cadherin–PDGFR-β binding off). It is important to note that these simulations were done only to confirm that the parameters of the model had been adjusted correctly for the part of the model network for which we have experimental evidence. As such, these results are not providing proof for the

whole network, but they are important in linking the model to prior experiments.

Next, we explored the remaining parts of the model in a cadherin-11 knockdown simulation (Table 5.3: Cadherin-11 knockdown). Figure 5.2 summarizes the changes in activity levels of the proteins in the network in a cadherin-11 knockdown simulation compared to their baseline activity levels. The two proteins whose activities were inhibited by cadherin-11 in the model, namely β-catenin and PDGFR-β, showed an overall increase in activity, as expected (Figure 5.2A, Figure 5.2B Cadherin-11 knockdown). PDGFR-α, on the other hand, had lower activity in the cadherin-11 knockdown, as it is normally activated by cadherin-11, alongside its own ligand (Figure 5.2A, Figure 5.2B Cadherin-11 knockdown). The net effect of the cadherin-11 knockdown on ERK was an increase in activity, while both DUSP1 and cyclin-D1 showed decreased activities (Figure 5.2A, Figure 5.2B, Cadherin-11 knockdown). In the context of our computational model, we interpreted the decreased cyclin-D1 activity compared to the baseline in the cadherin-11 knockdown as a decrease in cell proliferation.

Table 5.3: Setups of the four main simulations referred to in the main figures.

Name	Explanation	Parameters changed
Baseline model	All interactions are active in the network. We use the parameters in Table 5.2 without alterations.	
Cadherin-11 knockdown	We mimic the cadherin-11 knockdown by setting the initial cell–cell contact to 0. This way cadherin-11 can never be present during the simulation, similar to an experimental knockdown of the protein (Passanha *et al.*, 2022).	$c = 0$
Cell–cell contact off and cadherin–PDGFR-α binding off	Mimicking the Madarampalli *et al.*, 2019 experiments, cadherin-11 is not able to bind to another cadherin-11 or PDGFR-α. Since it cannot dimerize with another cadherin-11, it cannot inhibit β-catenin, but it can bind to PDGFR-β via intermembrane domains and inhibit its activity, suggesting that this binding is not via an extracellular site but via intermembrane sites of the two receptors.	$c = 0$ $\beta_{Bcat_{by_{cdh11}}} = 0$ $cdh11 = 0.18$
Cell–cell contact off and cadherin–PDGFR-β binding off	Mimicking the Madarampalli *et al.*, 2019 experiments, interaction of cadherin-11 and PDGFR-β on the cell membrane is blocked, cadherin-11 binding to PDGFR-α is still possible.	$\alpha_{cdh11_{by_c}} = 0$
Crosstalk disabled	We disable the activation of PDGFR-α by cadherin-11, inhibition of PDGFR-β by cadherin-11, and inhibition of DUSP1 by β-catenin.	$\alpha_{pdgfrA_{by_c}} = 0$ $\beta_{pdgfrB_{by_{cdh11}}} = 0$ $\beta_{dusp1_{by_{Bcat}}} = 0$

Crosstalk disabled and cadherin-11 knockdown	In addition to the changes in the "crosstalk disabled" simulation, we set cell–cell contact to 0.	$\alpha_{pdgfrA_{by_c}} = 0$ $\beta_{pdgfrB_{by_{cdh11}}} = 0$ $\beta_{dusp1_{by_{Bcat}}} = 0$ $c = 0$
Receptor interaction disabled	Crosstalk disabled only at the receptor level by blocking the activation and inhibition of PDGFR-α and PDGFR-β by cadherin-11.	$\alpha_{pdgfrA_{by_c}} = 0$ $\beta_{pdgfrB_{by_{cdh11}}} = 0$
Receptor interaction disabled and cadherin-11 knockdown	In addition to the changes in the "receptor interaction disabled" simulation, we set the cell–cell contact to 0.	$\alpha_{pdgfrA_{by_c}} = 0$ $\beta_{pdgfrB_{by_{cdh11}}} = 0$ $c = 0$
Downstream interaction disabled	Crosstalk disabled only at the level of β-catenin inhibiting DUSP1, while receptor level crosstalk is active.	$\beta_{dusp1_{by_{Bcat}}} = 0$
Downstream interaction disabled and cadherin-11 knockdown	Crosstalk disabled at the level of β-catenin inhibiting DUSP1 and cell–cell contact set to 0.	$\beta_{dusp1_{by_{Bcat}}} = 0$ $c = 0$

Having observed that the cadherin-11 knockdown simulation of the baseline model setup reflected the experimental observations of increased ERK activity and decreased proliferation in hMSCs, we moved to testing the contribution of different modes of crosstalk to these results. When the crosstalk at the receptor level (i.e. activation of PDGFR-α by cadherin-11 on an adjacent cell membrane and inhibition of PDGFR-β by cadherin-11 on the cell's own membrane) was disabled and the cadherin-11 knockdown simulation was repeated (Table 5.3: Receptor interaction disabled and cadherin-11 knockdown), the same ERK and cyclin-D1 activities were reached as in the cadherin-11 knockdown simulation using the baseline model (Figure 5.2B, Receptor interaction disabled and cadherin-11 knockdown). In other words, the removal of receptor level interactions did not affect the cadherin-11 influence on proliferation. This implies the receptor level crosstalk is not the primary mode of crosstalk that maintains the cadherin-11–dependent cell proliferation.

In order to test the effect of the crosstalk at the level of β-catenin and DUSP1, we modified the model to remove both the inhibition of DUSP1 by β-catenin and the receptor crosstalk (Table 5.3: Crosstalk disabled). In this case, β-catenin activity remained the same as in the baseline simulation, while PDGFR-α had a lower activity due to the lack of activation by cadherin-11 (Figure 5.2B, Crosstalk disabled versus Baseline). On the contrary, PDGFR-β activity increased in the absence of crosstalk, as it was no longer inhibited by cadherin-11. The net effect of not having the proposed multi-layered crosstalk between the two pathways resulted in decreased ERK activity and increased DUSP1 and cyclin-D1 activity (i.e., proliferation) compared to the baseline simulation (Figure 5.2B, Crosstalk disabled versus Baseline). When we simulated a cadherin-11 knockdown case for this version of the model (Table 5.3: Crosstalk disabled and cadherin-11 knockdown), we observed that the cadherin-11–mediated cell proliferation was disrupted. Unlike in the cadherin-11 knockdown, where the inhibition of DUSP1 by β-catenin was still active (Figure 5.2A, Figure 5.2B Cadherin-11 knockdown versus Baseline), we did not observe any change in the activities of PDGFR-α, PDGFR-β, Cyclin-D1, DUSP1 and ERK (Figure 5.2B, Crosstalk disabled and cadherin-11 knockdown versus Crosstalk disabled, and Figure S.5.2). Only the activity of β-catenin was increased, which was due to the absence of inhibition by cadherin-11 (Figure 5.2B, Crosstalk disabled and cadherin-11 knockdown versus Crosstalk disabled, and Figure S.5.2).

Next, we explored whether the crosstalk at the level of DUSP1 and β-catenin could maintain the cadherin-11–mediated cell proliferation on its own. To

do this, we kept the receptor level crosstalk active (cadherin-11 activating PDGFR-α and inhibiting PDGFR-β), disabled the inhibition of DUSP1 by β-catenin (Table 5.3: Downstream interaction disabled), and performed a cadherin-11 knockdown simulation with this setup (Table 5.3: Downstream interaction disabled and cadherin-11 knockdown). We observed the same changes in protein activity levels with this setup as in the "crosstalk disabled" simulation (Figure 5.2B crosstalk disabled versus downstream interaction disabled). These results indicated that cadherin-11 could mediate cell proliferation via its downstream effector β-catenin by inhibiting DUSP1 which is an ERK inhibitor. According to our model predictions, receptor level interactions between cadherin-11 and PGDFR-α and PDGFR-β, on the other hand, were insufficient to orchestrate the cadherin-11–mediated cell proliferation.

We also explored the parameters related to the proposed crosstalk at the level of β-catenin and DUSP1 with a parameter scan (Figure 5.3). This enabled us to ensure our choice of parameters in the baseline model was not forcing the network to behave in a biased way and to decide which protein–protein interactions had more weight in controlling the proliferative state of the network.

When using the baseline model parameters, ERK and cyclin-D1 activities were equal at the steady state. In addition, for all parameter sets and in each parameter scan, there were multiple other parameter combinations that resulted in equal ERK and cyclin-D1 activity (Figure 5.3, green areas). This ensured the baseline model results were not unique and were therefore not resulting from any particular parameter settings.

The first scan investigated the parameters influencing the inhibition of DUSP1 by β-catenin. It revealed that the initial β-catenin activity level was not decisive on the proliferation status of the network when compared to the inhibition of DUSP1 by β-catenin ($\beta_{dusp1_{by_{Bcat}}}$) (Figure 5.3A). In other words, the activity of β-catenin itself did not affect the steady state of Cyclin-D1 and ERK, whereas they were affected by the strength at which β-catenin inhibited DUSP. For values of $\beta_{dusp1_{by_{Bcat}}}$ greater than 1, the ERK activity was higher than the cyclin-D1 activity (i.e., the proliferation was lower than in the baseline model). For values less than 1 of $\beta_{dusp1_{by_{Bcat}}}$, the Cyclin-D1 activity was higher than the ERK activity (Figure 5.3A).

The second scan was performed between $\beta_{dusp1_{by_{Bcat}}}$ and $\alpha_{dusp1_{by_{erk}}}$, which are parameters that affect the strength of inhibition and activation of DUSP1, respectively. The results suggested that for the strong inhibition of DUSP1 by

β-catenin ($\beta_{dusp1_{by_{Bcat}}}$ = (5.0, 10.0)), the network exhibited decreased proliferation (Figure 5.3B, Cyclin-D1 < ERK), irrespective of the value of DUSP1 activation by ERK ($\alpha_{dusp1_{by_{erk}}}$). For the weaker inhibition of DUSP1 ($\beta_{dusp1_{by_{Bcat}}}$ = (0.1, 0.5, 1.0)), on the other hand, the increased value of DUSP1 activation by ERK ($\alpha_{dusp1_{by_{erk}}} = (5.0,\ 10.0)$) resulted in increased proliferation (Figure 5.3B, Cyclin-D1 > ERK). There exists a trade-off for values lower than or equal to 1 for both parameters, when the inhibition of DUSP1 by β-catenin exceeded the value of the activation of DUSP1 by ERK, the network exhibited decreased proliferation (Figure 5.3B, Cyclin-D1 < ERK). Whereas when $\beta_{dusp1_{by_{Bcat}}}$ was smaller than $\alpha_{dusp1_{by_{erk}}}$, the proliferation increased (Figure 5.3B, Cyclin-D1 < ERK).

The third parameter set explored the activation and inhibition of ERK by the downstream effectors of the PDGFRs and DUSP1, respectively. The results suggested that, apart from the combination of the weakest possible inhibition of ERK by DUSP1 ($\beta_{erk_{by_{dusp1}}}$ = (0.1, 0,5)) and the strongest possible activation of ERK by MEK ($\alpha_{erk_{by_{mek}}}$ = (10.0, 5.0, 1.0)), the network exhibited normal or increased proliferation (Figure 5.3C). In general, the stronger inhibition of ERK by DUSP1 resulted in increased proliferation, suggesting the control over ERK inhibition to be an important mechanism in controlling the proliferative status of the network.

In the final parameter scan, we further explored the interplay between the inhibition of ERK by DUSP1 and the activation of cyclin-D1 by DUSP1. For the stronger activation of cyclin-D1 ($\alpha_{cyclinD1_{by_{dusp1}}}$ =(5.0, 10.0)), the proliferation was always higher than baseline, regardless of the strength of ERK inhibition by DUSP1 (Figure 5.3D). However, for weaker activation of cyclin-D1, the degree of ERK inhibition by DUSP1 could compensate and sustain the same level of proliferation or even increase it. For $\alpha_{cyclinD1_{by_{dusp1}}}$ between 0.1 and 1.0, increasing $\beta_{erk_{by_{dusp1}}}$ increased the proliferation (Figure 5.3D).

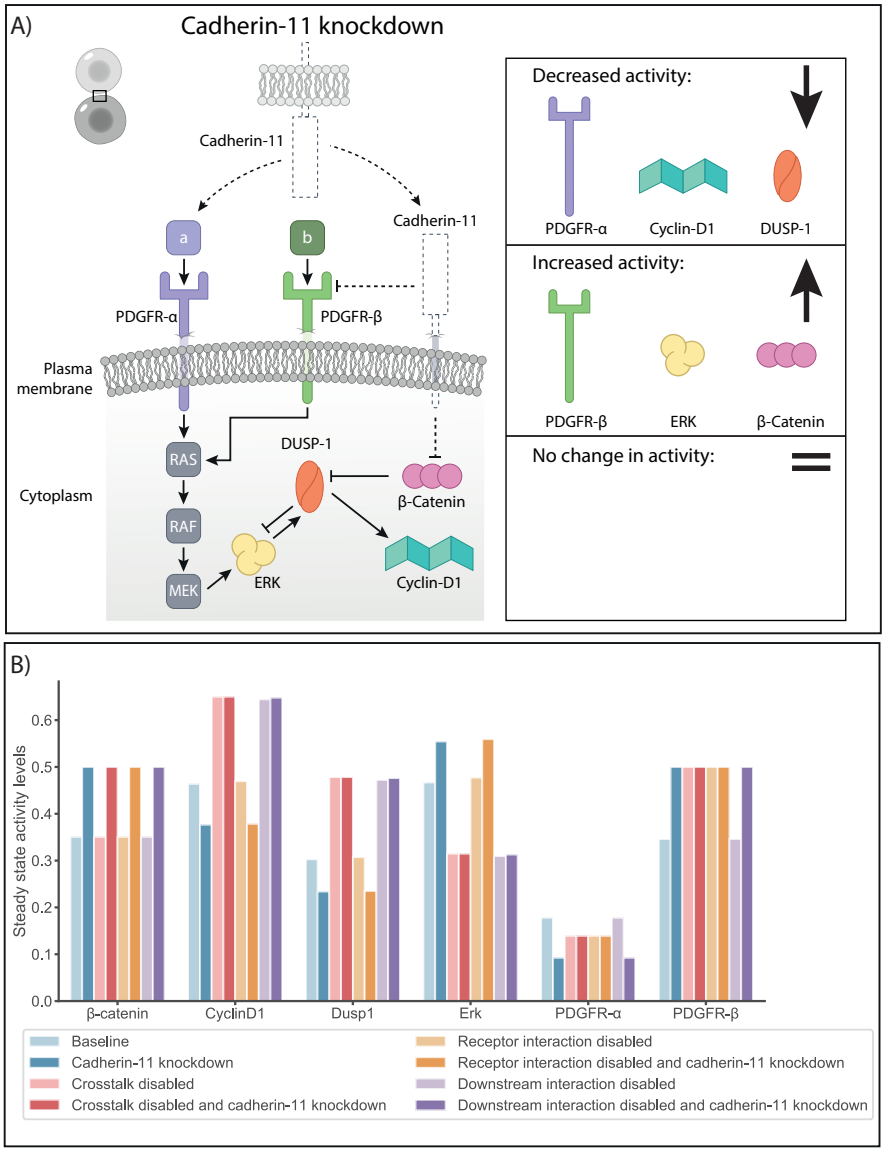

Figure 5.2: *(Continued on the following page.)*

Figure 5.2: A) Cadherin 11 knockdown simulation results compared to the baseline model simulation: The dashed lines indicate where the model components were modified in the simulation setup. The steady state activity levels of PDGFR-α, cyclin-D1 and DUSP1 decreased, while the activity levels of PDGFR-β, ERK and β-catenin increased in the cadherin-11 knockdown compared to the baseline simulation. The decrease in PDGFR-α activity and the increase in PDGFR-β activity agree with the experimental results (Madarampalli *et al.*, 2019; Passanha *et al.*, 2022). The proposed crosstalk protein, DUSP1, had decreased activity which resulted in increased ERK activity and decreased cyclin-D1 activity, which we interpreted as decreased proliferation. B) Summary of steady state activity levels of proteins in the network under different simulation setups. We compared the steady state activity levels in the cadherin-11 knockdown for each different setup (baseline, crosstalk disabled, receptor interaction disabled, and downstream interaction disabled).

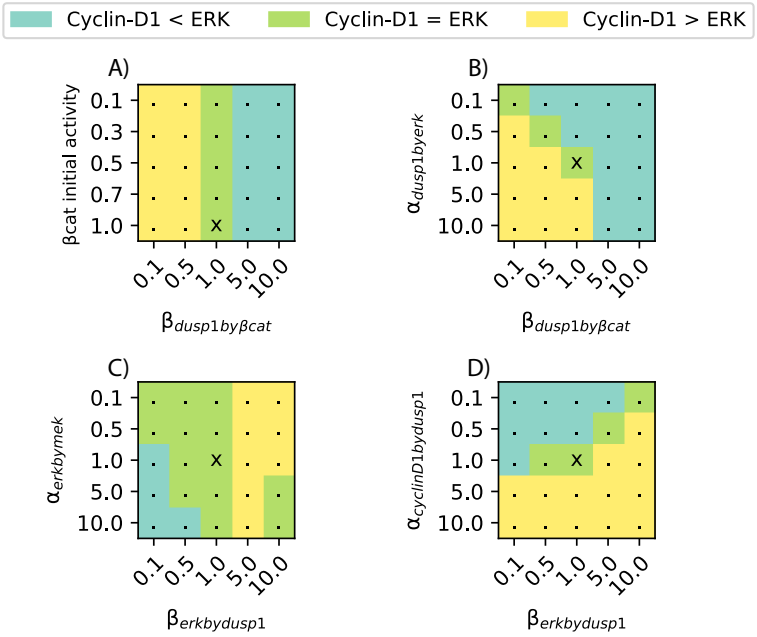

Figure 5.3: Change in proliferation status for varying parameters influencing the proposed crosstalk. The scan was performed using the numerical values on the axes for the respective parameters. Baseline parameter sets have been marked with an x in each plot. For each parameter set, the difference between the steady state activity level of cyclin D1 and ERK were compared. A) β-catenin initial activity and the inhibition of DUSP1 by β-catenin, B) activation of DUSP1 by ERK and inhibition of DUSP1 by β-catenin C) activation of ERK by MEK and inhibition of ERK by DUSP1 and D) activation of cyclin-D1 by DUSP1 and inhibition of ERK by DUSP1. Cyclin-D1 activity $>$ ERK activity indicates increased proliferation compared to the baseline parameter set, cyclin-D1 activity = ERK activity indicates sustained proliferation as in the baseline parameter set, cyclin-D1 activity $<$ ERK activity indicates decreased proliferation compared to the baseline parameter set.

5.4 Discussion

There has been a recent increase in exploring the different (signaling) roles cadherins play in various cell types other than establishing cell to cell contact (Halbleib & Nelson, 2006; Maître & Heisenberg, 2013; Niessen *et al*., 2011). One of the many ways in which cadherins participate in various signaling roles is through their crosstalk with RTKs (Chiasson-Mackenzie & McClatchey, 2018). For example, there is mounting evidence of the crosstalk between cadherin-2 and the fibroblast growth factor receptors, as well as cadherin-1 and epidermal growth factor receptor (Andl & Rustgi, 2004; Nguyen & Mège, 2016). Likewise, recent studies have shown that cadherin-11 specifically interacts with the RTKs PDGFR-α (Madarampalli *et al*., 2019) and PDGFR-β (Liu *et al*., 2020; Passanha *et al*., 2022). Passanha *et al*., 2022 also reported that cadherin-11–knockdown hMSCs have more phosphorylated ERK-positive nuclei and show decreased proliferation. Similarly, Liu *et al*., 2020 have shown that knocking down cadherin-11 also results in decreased proliferation. Although these experimental observations point to crosstalk between PDGFR-α, PDGFR-β and cadherin-11 at the receptor level in hMSCs, crosstalk between the signaling proteins that function downstream to these receptors remains to be explored. This knowledge could improve our understanding of hMSC proliferation and fate commitment, both of which are central to regenerative medicine research.

Downstream to the PDGFRs is the MAPK/ERK pathway which contains multifunctional proteins. Downstream to cadherin-11 is β-catenin which is known to be involved in other cellular activities. The complexity and multifunctionality of the downstream signaling make it experimentally challenging to study the possible ways by which PDGFRs and cadherin-11 engage in crosstalk, other than at the receptor level. To address this challenge, we created a computational model of the cadherin-11 and PDGFR signaling network that qualitatively matches the experimental observations at the level of receptor interactions. With our model, we were able to provide *in silico* evidence for an additional layer of crosstalk (i.e., at the downstream level between β-catenin and an ERK inhibitor DUSP1), beyond the known crosstalk happening at the receptor level between PDGFRs and cadherin-11.

Computational modeling enabled us to isolate the RTK and cadherin-11 pathways from other cellular signaling pathways they interact with (e.g., integrins, G-protein coupled receptors (GPCRs), TGFβ, *etc*.) and explore the role of each mode of crosstalk (receptor level, downstream signaling and a combination of both) in the network in a way that is not possible experimen-

tally. Disabling all possible crosstalk in the network, resulted in complete isolation of the ERK pathway from the cadherin-11, therefore the cadherin-11 knockdown did not affect cyclin-D1 or ERK activity (Figure 5.2B, crosstalk disabled and cadherin-11 knockdown compared to crosstalk disabled). Disabling the crosstalk only at the receptor level (i.e., between PDGFR-α and cadherin-11, and PDGFR-β and cadherin-11) and allowing the downstream interaction (i.e. β-catenin inhibiting DUSP1) rescued the activity level patterns and we observed that in case of a cadherin-11 knockdown while the receptor interaction was disabled, the ERK activity increased and cyclin-D1 activity decreased (Figure 5.2B, Receptor interaction disabled and cadherin-11 knockdown) matching the baseline simulation (Figure 5.2B, baseline and cadherin-11 knockdown). This suggests, the downstream interaction alone, can sustain the crosstalk between the cadherin-11 and PDGFR pathways and explain the observed decrease in proliferation in the cadherin-11 knockdown experiments. The observation that disabling the downstream crosstalk via β-catenin and the ERK inhibitor DUSP1 alone resulted in the same pattern as disabling all crosstalk (Figure 5.2B, Downstream interaction disabled versus crosstalk disabled) strengthens this hypothesis.

According to our simulations, the control over ERK inhibition in the network is very important. To ensure that our observations are not heavily influenced by our choice of parameters for the proposed crosstalk, we performed a sensitivity analysis. The results implied that for the strong inhibition of ERK (high $\beta_{erk_{by_{dusp1}}}$) by DUSP1, regardless of the degree of activation of ERK by MEK ($\alpha_{erk_{by_{mek}}}$), the system will have increased or at least sustained proliferation. Conversely, for strong ERK activation by MEK and weak inhibition of ERK by DUSP1, the proliferation was decreased (Figure 5.3).

Overall, the control over the inhibition of ERK seems to be critical in terms of changing the proliferative state of the system. This can be due to the fact that during cell proliferation, ERK is rapidly inactivated at the transition of the G1 to S phase (Mebratu & Tesfaigzi, 2009; Meloche, 1995). Prolonged ERK activation in the nucleus arrests the cell cycle at the G1 phase and therefore the cell does not undergo mitosis (Yamamoto *et al.*, 2006). Therefore, the tight regulation of ERK (inhibiting its activity) is necessary for cell proliferation. We suggest cadherin-11 and its downstream effector β-catenin play a part in the control over ERK inhibition, explaining why the cadherin-11 knockdown results in decreased hMSC proliferation (as shown experimentally by Passanha *et al.*, 2022).

In our model, we propose the ERK inhibitor in this network to be DUSP1 be-

cause the DUSP family of proteins dephosphorylate various members of the MAPK family including ERK (Chen *et al*., 2019; Huang & Tan, 2012). DUSP1 is a nuclear phosphatase that binds to ERK which leads to its dephosphorylation or inactivation, and reciprocally, ERK also promotes the activity of DUSP1 (Ferguson *et al*., 2016). This is not to say that other members of the DUSP family are not involved, but we chose to only highlight DUSP1 in our model for simplicity. We note that other signaling molecules can also regulate the activity of DUSPs, representing an additional signaling component that could be added to the model in the future. The DUSP family of proteins has also been shown to interact with β-catenin to interfere with the MAPK signaling cascade in murine liver cells (Zeller *et al*., 2012). Therefore, we suggest that in the scope of the RTK and cadherin-11 pathways, the receptor level crosstalk is insufficient for cadherin-11 to influence hMSC proliferation and an additional level of crosstalk is required between β-catenin and DUSP1. This has important implications for experiments concerning the control over hMSC proliferation.

Computational models are valid and useful in the range of biological systems they represent and for the biological data that is available to support them. In this study, we used an ODE model of the form described by Mendoza and Xenarios, 2006 to obtain a network that represents the qualitative characteristics of the RTK and cadherin-11 pathways and the crosstalk between them. This choice was made because we had a multitude of experimental data in the form of the relative abundance of active and inactive forms (i.e., phosphorylated and unphosphorylated forms) of proteins in the network and no kinetic information (i.e., binding–unbinding rates). Thus, a more classical mass action (or similar) type of model would have been difficult to construct and also to interpret, as the experiments were comparing relative protein abundances instead of absolute quantification. Nevertheless, with a network that focused on relative activities of proteins at the steady state, such as ours, we were able to conclude that a multi-level crosstalk between the two modeled pathways is needed to support the experimental observations. With the sensitivity analysis, we were able to show that the set of parameters we used was not unique to produce the results we obtained. This also indicated that more detailed information on the relative amounts of active/inactive proteins other than the RTKs, cadherin-11, and ERK could improve our choice of parameters and make the model more accurate in the future.

Similar to the cadherin-11–RTK interaction, other receptor couples are known to engage in crosstalk in other cell types (Andl & Rustgi, 2004; Chiasson-Mackenzie & McClatchey, 2018). For example, E-cadherin and epidermal

growth factor receptor (EGFR) have been shown to interact (Ramírez Moreno & Bulgakova, 2022). Similarly, N-cadherin interacts with fibroblast growth factor receptor (FGFR) (Kon *et al.*, 2019; Nguyen *et al.*, 2019; Nguyen & Mège, 2016). We suggest a computational reconstruction of the signaling pathways of these receptor pairs, using a similar approach as we presented here, will help to isolate the pathways from other cellular signaling and to discover new interactions between the receptor pairs, other than what could be tested experimentally.

In summary, we have shown that a crosstalk between β-catenin (downstream to cadherin-11) and an ERK inhibitor protein (e.g. DUSP1) is needed for the experimentally shown effect of cadherin-11 on hMSC proliferation. By investigating the multi-level crosstalk between cadherin and PDGFRs computationally, this study contributes to an improved understanding of the effect of cell surface receptors on hMSC proliferation. A detailed description of how hMSC proliferation is controlled by a multitude of cell surface receptors will provide new avenues for cell fate control and regenerative medicine therapies.

5.5 Supplementary Material

Table S.5.1 Parameter sensitivity analysis for β-catenin initial activity ($Bcat$) versus the inhibition of DUSP1 by β-catenin ($\beta_{dusp1_{by_{Bcat}}}$). Steady state activity levels of CyclinD1 and Erk are given for each parameter set in the search space.

Set A	Bcat	$\mathrm{fi}_{\mathrm{dusp1}_{\mathrm{byBcat}}}$	cyclinD1	erk
0	0.1	0.1	0.5	0.4
1	0.1	0.5	0.5	0.4
2	0.1	1	0.5	0.5
3	0.1	5	0.3	0.6
4	0.1	7	0.2	0.7
5	0.1	10	0.2	0.7
6	0.3	0.1	0.5	0.4
7	0.3	0.5	0.5	0.4
8	0.3	1	0.5	0.5
9	0.3	5	0.3	0.6
10	0.3	7	0.2	0.7

11	0.3	10	0.2	0.7
12	0.5	0.1	0.5	0.4
13	0.5	0.5	0.5	0.4
14	0.5	1	0.5	0.5
15	0.5	5	0.3	0.6
16	0.5	7	0.2	0.7
17	0.5	10	0.2	0.7
18	0.7	0.1	0.5	0.4
19	0.7	0.5	0.5	0.4
20	0.7	1	0.5	0.5
21	0.7	5	0.3	0.6
22	0.7	7	0.2	0.7
23	0.7	10	0.2	0.7
24	1	0.1	0.5	0.4
25	1	0.5	0.5	0.4
26	1	1	0.5	0.5
27	1	5	0.3	0.6
28	1	7	0.2	0.7
29	1	10	0.2	0.7

Table S.5.2 Parameter sensitivity analysis for activation of DUSP1 by ERK versus inhibition of DUSP1 by β-catenin ($a_{dusp1_{by_{erk}}}$ and $\beta_{dusp1_{by_{Bcat}}}$). Steady state activity levels of cyclinD1 and Erk are given for each parameter set in the search space.

Set	$\mathrm{a_{dusp1_{by_{erk}}}}$	$\mathrm{fi_{dusp1_{by_{Bcat}}}}$	cyclinD1	erk
0	0.1	0.1	0.5	0.5
1	0.1	0.5	0.4	0.5
2	0.1	1	0.4	0.5
3	0.1	5	0.3	0.6
4	0.1	10	0.2	0.7
5	0.5	0.1	0.5	0.4
6	0.5	0.5	0.5	0.5
7	0.5	1	0.4	0.5
8	0.5	5	0.3	0.6

9	0.5	10	0.2	0.7
10	1	0.1	0.5	0.4
11	1	0.5	0.5	0.4
12	1	1	0.5	0.5
13	1	5	0.3	0.6
14	1	10	0.2	0.7
15	5	0.1	0.6	0.3
16	5	0.5	0.6	0.4
17	5	1	0.6	0.4
18	5	5	0.3	0.6
19	5	10	0.2	0.7
20	10	0.1	0.7	0.3
21	10	0.5	0.6	0.3
22	10	1	0.6	0.4
23	10	5	0.4	0.6
24	10	10	0.2	0.7

Table S.5.3 Parameter sensitivity analysis for activation of ERK by MEK versus inhibition of ERK by DUSP1 ($a_{erk_{by_{mek}}}$ and $\beta_{erk_{by_{dusp1}}}$). Steady state activity levels of cyclinD1 and ERK are given for each parameter set in the search space.

Set	$\mathrm{a}_{\mathrm{erk}_{\mathrm{by}_{\mathrm{mek}}}}$	$\mathrm{fi}_{\mathrm{erk}_{\mathrm{by}_{\mathrm{dusp1}}}}$	cyclinD1	erk
0	0.1	0.1	0.5	0.5
1	0.1	0.5	0.5	0.5
2	0.1	1	0.4	0.4
3	0.1	5	0.4	0.3
4	0.1	10	0.3	0.2
5	0.5	0.1	0.5	0.5
6	0.5	0.5	0.5	0.5
7	0.5	1	0.5	0.5
8	0.5	5	0.4	0.3
9	0.5	10	0.3	0.2
10	1	0.1	0.5	0.6
11	1	0.5	0.5	0.5

12	1	1	0.5	0.5
13	1	5	0.4	0.3
14	1	10	0.3	0.2
15	5	0.1	0.5	0.6
16	5	0.5	0.5	0.5
17	5	1	0.5	0.5
18	5	5	0.4	0.3
19	5	10	0.3	0.3
20	10	0.1	0.5	0.6
21	10	0.5	0.5	0.6
22	10	1	0.5	0.5
23	10	5	0.4	0.3
24	10	10	0.3	0.3

Table S.5.4 Parameter sensitivity analysis for activation of cyclin-D1 by DUSP1 versus inhibition of ERK by DUSP1 ($a_{cyclind1_{by_{mek}}}$ and $\beta_{erk_{by_{dusp1}}}$). Steady state activity levels of cyclinD1 and ERK are given for each parameter set in the search space.

Set	$\mathrm{a}_{\mathrm{cyclinD1}_{\mathrm{by}_{\mathrm{dusp1}}}}$	$\mathrm{fi}_{\mathrm{erk}_{\mathrm{by}_{\mathrm{dusp1}}}}$	cyclinD1	erk
0	0.1	0.1	0.4	0.6
1	0.1	0.5	0.3	0.5
2	0.1	1	0.3	0.5
3	0.1	5	0.2	0.3
4	0.1	10	0.2	0.2
5	0.5	0.1	0.4	0.6
6	0.5	0.5	0.4	0.5
7	0.5	1	0.4	0.5
8	0.5	5	0.3	0.3
9	0.5	10	0.3	0.2
10	1	0.1	0.5	0.6
11	1	0.5	0.5	0.5
12	1	1	0.5	0.5
13	1	5	0.4	0.3
14	1	10	0.3	0.2

15	5	0.1	0.8	0.6
16	5	0.5	0.7	0.5
17	5	1	0.7	0.5
18	5	5	0.6	0.3
19	5	10	0.6	0.2
20	10	0.1	0.9	0.6
21	10	0.5	0.8	0.5
22	10	1	0.8	0.5
23	10	5	0.8	0.3
24	10	10	0.7	0.2

Figure S.5.1 Model parameters concerning the activity levels of PDGFR-α and PDGFR-β were adjusted to match the previous experimental studies Madarampalli *et al*., 2019 and Passanha *et al*., 2022. In the baseline model, PDGFR-β activity at the steady state is higher than PDGFR-α activity, in accordance with Passanha *et al*., 2022. Cadherin-11 knockdown simulation resulted in lower than normal PDGFR-α and greater than normal PDGFR-β activity, in accordance with Passanha *et al*., 2022. When cell–cell contact and cadherin-11 binding to PDGFR-α were disabled, lower than normal PDGFR-α activity but no change in the PDGFR-β activity were observed compared to the baseline model. When cell–cell contact and cadherin-11 binding to PDGFR-β were disabled, no change in the PDGFR-α activity level but an increase in PDGFR-β activity were observed compared to the baseline model.

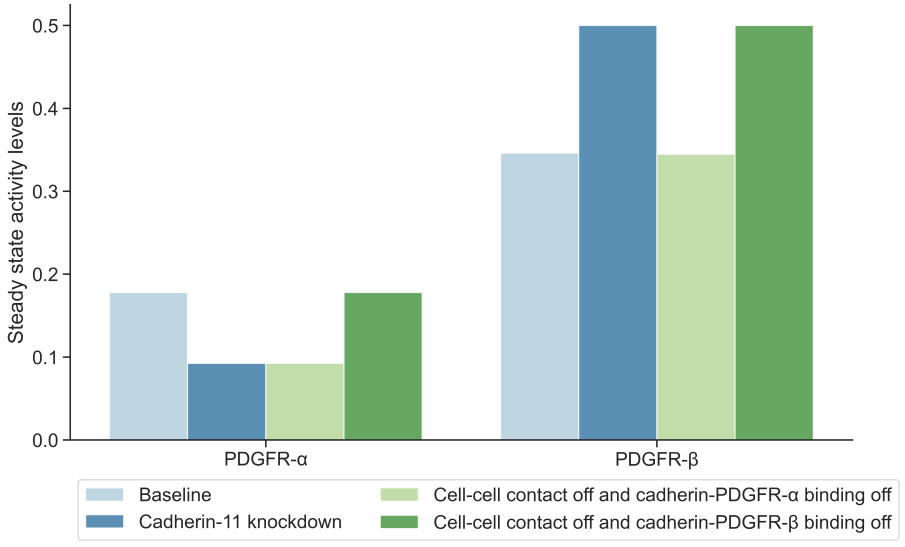

Figure S.5.2 Cadherin 11 knockdown simulation results when the proposed crosstalk is disabled: The dashed lines indicate where the model components were modified in the simulation setup. No change was observed in the activity levels of growth factor receptors and proliferation-related signaling molecules in case of a cadherin-11 knockdown when the proposed crosstalk mechanisms were disabled.

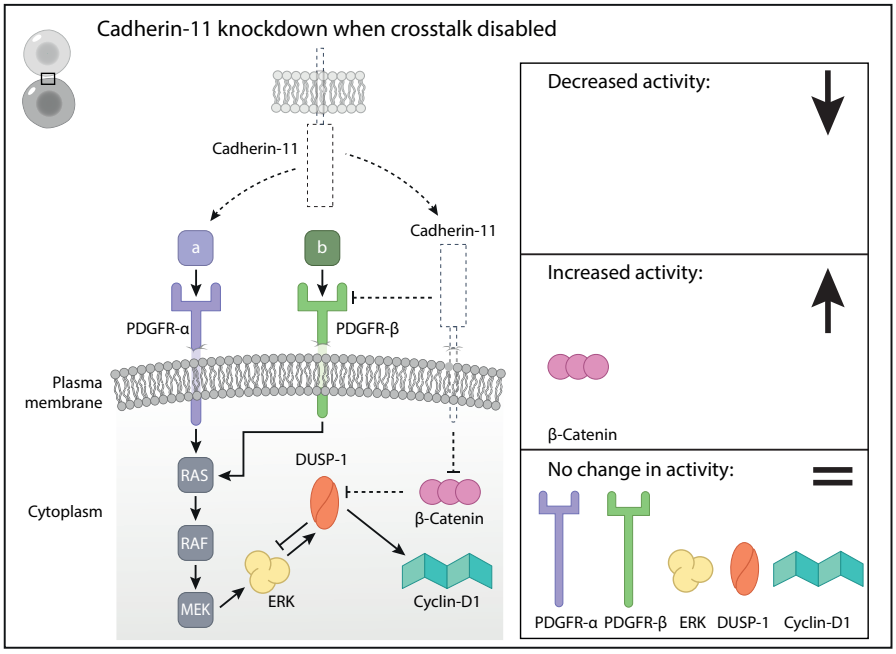

References

Andl, C. D., & Rustgi, A. K. (2004). No one-way street: Cross-talk between E-cadherin and receptor tyrosine kinase (RTK) signaling—A mechanism to regulate RTK activity. *http://dx.doi.org/10.4161/cbt.4.1.1431*, *4*(1), 35–38. https://doi.org/10.4161/CBT.4.1.1431

Barabási, A. L., & Oltvai, Z. N. (2004). Network biology: Understanding the cell's functional organization. *Nature Reviews Genetics 2004 5:2*, *5*(2), 101–113. https://doi.org/10.1038/nrg1272

Chen, H. F., Chuang, H. C., & Tan, T. H. (2019). Regulation of Dual-Specificity Phosphatase (DUSP) Ubiquitination and Protein Stability. *International Journal of Molecular Sciences 2019, Vol. 20, Page 2668*, *20*(11), 2668. https://doi.org/10.3390/IJMS20112668

Chiasson-Mackenzie, C., & McClatchey, A. I. (2018). Cell–Cell Contact and Receptor Tyrosine Kinase Signaling. *Cold Spring Harbor Perspectives in Biology*, *10*(6), a029215. https://doi.org/10.1101/CSHPERSPECT.A029215

Cowan, A. E., Moraru, I. I., Schaff, J. C., Slepchenko, B. M., & Loew, L. M. (2012). Spatial modeling of cell signaling networks. *Methods in cell biology*, *110*, 195–221. https://doi.org/10.1016/B978-0-12-388403-9.00008-4

Ferguson, B. S., Nam, H., Stephens, J. M., & Morrison, R. F. (2016). Mitogen-Dependent Regulation of DUSP1 Governs ERK and p38 Signaling During Early 3T3-L1 Adipocyte Differentiation. *Journal of Cellular Physiology*, *231*(7), 1562–1574. https://doi.org/10.1002/JCP.25248

Halbleib, J. M., & Nelson, W. J. (2006). Cadherins in development: Cell adhesion, sorting, and tissue morphogenesis. *Genes & development*, *20*(23), 3199–3214. https://doi.org/10.1101/GAD.1486806

Huang, C. Y., & Tan, T. H. (2012). DUSPs, to MAP kinases and beyond. *Cell and Bioscience*, *2*(1), 1–10. https://doi.org/10.1186/2045-3701-2-24/FIGURES/5

Karagöz, Z., Passanha, F. R., Robeerst, L., van Griensven, M., LaPointe, V. L. S., & Carlier, A. (2023). Computational evidence for multi-layer crosstalk between the

cadherin-11 and PDGFR pathways. *Scientific Reports*, *13*(1), 15804. https://doi.org/10.1038/s41598-023-42624-x

Kon, E., Calvo-Jiménez, E., Cossard, A., Na, Y., Cooper, J. A., & Jossin, Y. (2019). N-cadherin-regulated FGFR ubiquitination and degradation control mammalian neocortical projection neuron migration. *eLife*, *8*. https://doi.org/10.7554/ELIFE.47673

Liu, Y., Lei, P., Row, S., & Andreadis, S. T. (2020). Cadherin-11 binds to PDGFR Beta and enhances cell proliferation and tissue regeneration via the PDGFR-AKT signaling axis. *The FASEB Journal*, *34*(3), 3792–3804. https://doi.org/10.1096/FJ.201902613R

Madarampalli, B., Watts, G. F., Panipinto, P. M., Nguygen, H. N., Brenner, M. B., & Noss, E. H. (2019). Interactions between cadherin-11 and platelet-derived growth factor receptor-alpha signaling link cell adhesion and proliferation. *Biochimica et Biophysica Acta - Molecular Basis of Disease*, *1865*(6), 1516–1524. https://doi.org/10.1016/j.bbadis.2019.03.001

Maître, J. L., & Heisenberg, C. P. (2013). Three Functions of Cadherins in Cell Adhesion. *Current Biology*, *23*(14), R626–R633. https://doi.org/10.1016/J.CUB.2013.06.019

Mebratu, Y., & Tesfaigzi, Y. (2009). How ERK1/2 activation controls cell proliferation and cell death: Is subcellular localization the answer? *https://doi.org/10.4161/cc.8.8.8147*, *8*(8), 1168–1175. https://doi.org/10.4161/CC.8.8.8147

Meloche, S. (1995). Cell cycle reentry of mammalian fibroblasts is accompanied by the sustained activation of P44mapk and P42mapk isoforms in the G1 phase and their inactivation at the G1/s transition. *Journal of Cellular Physiology*, *163*(3), 577–588. https://doi.org/10.1002/JCP.1041630319

Mendoza, L., & Xenarios, I. (2006). A method for the generation of standardized qualitative dynamical systems of regulatory networks. *Theoretical Biology and Medical Modelling*, *3*(1), 1–18. https://doi.org/10.1186/1742-4682-3-13

Nguyen, T., Duchesne, L., Sankara Narayana, G. H. N., Boggetto, N., Fernig, D. D., Uttamrao Murade, C., Ladoux, B., & Mège, R. M. (2019). Enhanced cell–cell contact stability and decreased N-cadherin-mediated migration upon fibroblast growth factor

receptor-N-cadherin cross talk. *Oncogene 2019 38:35*, *38*(35), 6283–6300. https://doi.org/10.1038/s41388-019-0875-6

Nguyen, T., & Mège, R. M. (2016). N-Cadherin and Fibroblast Growth Factor Receptors crosstalk in the control of developmental and cancer cell migrations. *European journal of cell biology*, *95*(11), 415–426. https://doi.org/10.1016/J.EJCB.2016.05.002

Niessen, C. M., Leckband, D., & Yap, A. S. (2011). Tissue organization by cadherin adhesion molecules: Dynamic Molecular and Cellular Mechanisms of Morphogenetic Regulation. *Physiological Reviews*, *91*(2), 691–731. https://doi.org/10.1152/PHYSREV.00004.2010/ASSET/IMAGES/LARGE/Z9J0021125760017.JPEG

Passanha, F. R., Divinagracia, M. L., & LaPointe, V. L. S. (2022). Cadherin-11 Regulates Cell Proliferation via the PDGFR Beta-ERK1/2 Signaling Pathway in Human Mesenchymal Stem Cells. *Stem Cells*. https://doi.org/10.1093/STMCLS/SXAB019

Ramírez Moreno, M., & Bulgakova, N. A. (2022). The Cross-Talk Between EGFR and E-Cadherin. *Frontiers in Cell and Developmental Biology*, *9*, 3968. https://doi.org/10.3389/FCELL.2021.828673/BIBTEX

Ramos, J. W. (2008). The regulation of extracellular signal-regulated kinase (ERK) in mammalian cells. *The International Journal of Biochemistry & Cell Biology*, *40*(12), 2707–2719. https://doi.org/10.1016/J.BIOCEL.2008.04.009

Schaff, J., Fink, C. C., Slepchenko, B., Carson, J. H., & Loew, L. M. (1997). A general computational framework for modeling cellular structure and function. *Biophysical journal*, *73*(3), 1135–1146. https://doi.org/10.1016/S0006-3495(97)78146-3

Takeichi, M. (2018). Historical review of the discovery of cadherin, in memory of Tokindo Okada. *Development Growth and Differentiation*, *60*(1), 3–13. https://doi.org/10.1111/dgd.12416

Valenta, T., Hausmann, G., & Basler, K. (2012). The many faces and functions of Beta-catenin. *The EMBO Journal*, *31*(12), 2714. https://doi.org/10.1038/EMBOJ.2012.150

Yamamoto, T., Ebisuya, M., Ashida, F., Okamoto, K., Yonehara, S., & Nishida, E. (2006). Continuous ERK Activation Downregulates Antiproliferative Genes

throughout G1 Phase to Allow Cell-Cycle Progression. *Current Biology*, *16*(12), 1171–1182. https://doi.org/10.1016/J.CUB.2006.04.044

Zeller, E., Mock, K., Horn, M., Colnot, S., Schwarz, M., & Braeuning, A. (2012). Dual-specifi city phosphatases are targets of the Wnt/Beta-catenin pathway and candidate mediators of Beta-catenin/Ras signaling interactions. *Biological Chemistry*, *393*(10), 1183–1191. https://doi.org/10.1515/HSZ-2012-0130/DOWNLOADASSET/HSZ-2012-0130AD.PDF

6

A Mechanobiological Model of the Reversible Fibroblast to Myofibroblast Transition

This chapter is being **prepared for print** in collaboration with Karagöz, Z., Dazzi, C., Vogel, V., Checa, S. and Carlier, A..

Abstract

Fibroblasts are connective tissue cells responsible for producing and maintaining the extracellular matrix (ECM). During tissue growth, but also in response to injury or inflammation, fibroblasts undergo a phenotypic change known as fibroblast to myofibroblast transition (FMT), acquiring a more contractile phenotype. Myofibroblasts, characterized by the expression of alpha-smooth muscle actin (αSMA) filaments, thus play a crucial role in tissue development, remodeling, and wound healing. They produce ECM, generate mechanical forces for wound contraction, and contribute to tissue structure rebuilding. However, prolonged myofibroblast activation can lead to fibrosis, where excessive ECM accumulation causes scarring and loss of tissue function. Previous studies with *de novo* grown fibroblast microtissues demonstrated the complexity of the FMT and its reversal. These studies identified distinct zones within the microtissues, with the growth front containing predominantly myofibroblasts and the tissue core housing fibroblasts. The growth front exhibited higher myofibroblast activity and stretched fibronectin (FN) fibers. Researchers proposed the existence of reciprocal feedback loops between cellular pathways, ECM production, fiber tension, and cell decision-making during FMT. To gain more quantitative insights into the multifactorial dynamic interplay between ECM composition and mechanics and cell phenotype, we developed an *in silico* model comprising two modules: a biological module representing observed changes during the reversible FMT, and a mechanically-tuned ECM module which considers compositional and tensional changes into tissue mechanical properties and strains. The two modules were coupled to simulate the intricate feedback loops observed experimentally. Overall, simulation of the cellular events linked to the mechanical response of the *in silico* microtissue suggests that the local and gradual production of ECM proteins can instruct the tissue material properties in a way to constrain the myofibroblast activity to the growth front. The difference in timing of fibronectin and collagen fibrillogenesis eventually creates the difference between the mechanical and biological properties of the high strain growth front and low strain tissue core, with a sharp transition zone between them. Understanding the spatiotemporally controlled cell-ECM feedback further will help explain experimental observations and the role of ECM compositional changes in reverting FMT in mature tissue by altering mechanical properties, which is important for the development of strategies against scarring.

6.1 Introduction

Fibroblasts are cells of the connective tissue, which are, amongst others, responsible for producing and maintaining the extracellular matrix (ECM). Fibroblasts have a spindle-shaped morphology and they are normally quiescent under homeostatic conditions (Plikus *et al.*, 2021). Upon injury or inflammation, fibroblasts undergo phenotypic changes acquiring a more contractile phenotype which is called myofibroblast (Schuster *et al.*, 2023). This process is called fibroblast to myofibroblast transition (FMT) and is essential for tissue development, remodeling and wound healing (D'Urso & Kurniawan, 2020).

Myofibroblasts have enhanced ability of ECM production and they are characterized by the expression of alpha-smooth muscle actin (αSMA) filaments, which provide the contractile property to the cells. Myofibroblasts generate mechanical forces that aid in wound contraction, leading to the reduction in wound size (Schuster *et al.*, 2023). They also deposit and remodel ECM proteins, helping to rebuild the tissue structure. However, once the healing is complete, myofibroblast activity needs to diminish. Prolonged activation of myofibroblasts leads to fibrosis, which is a pathological condition characterized by excess accumulation of ECM, resulting in scarring and eventually loss of tissue or organ function (D'Urso & Kurniawan, 2020; Schuster *et al.*, 2023).

Previous experimental studies with fibroblast microtissues have demonstrated the intricate nature of FMT and its reversal. Initially, Kollmannsberger *et al.*, 2018 used microfabricated clefts to mimic wound architecture and grew fibroblast microtissues in these clefts. Results indicated a clear distinction between the growth front and the tissue core in terms of myofibroblast activity, suggesting the myofibroblasts revert back to fibroblast phenotype in the interior of the growing microtissue. The growth front contained mostly myofibroblasts which express αSMA and which have more YAP/TAZ (a transcriptional co-activator for mechanosensitive gene expression). In the growth front, the fibronectin (FN) fibers have also been found to be more stretched.

Later, in a follow-up study, Benn *et al.*, 2023 used a similar but narrower cleft architecture to investigate how spatiotemporal changes of ECM composition and ECM fiber tension correlate with reversible FMT. Their results confirmed the distinct mechanical and biological properties of the growth front compared to the tissue core. The growth front, rich in tensed FN fibers, spatially correlated with αSMA expressing myofibroblasts and contained high levels

of tenascin-C (TNC) and issue transglutaminase (TG2). The cells and the FN fibers were aligned parallel to the growth front. The tissue core on the other hand was rich in collagen fibers and lacked αSMA expressing myofibroblasts, but contained rather more circular fibroblasts. They also identified a narrow transition zone between the growth front and the tissue core, where the reversal of FMT happened quickly. This reversal was initiated by TNC inhibiting FN-binding integrin adhesions in myofibroblasts, eventually reducing FN fiber tension. Following a sharp decrease in FN and TNC content in the ECM, as well as the breakdown of αSMA, the reversal of FMT, or myofibroblast to fibroblast transition (MFT) was completed. From the growth front (rich in FN) to tissue core (rich in collagen), there was also a shift in high FN-binding integrin ($\alpha5\beta1$) activity to high collagen-binding integrin ($\alpha2\beta1$) activity, showing an altered cell-ECM communication. When just one of the biological processes that contribute to spatiotemporal control of ECM maturation was disrupted, including the fiber cross-linking via TG2, degradation of TNC by matrix metalloproteinase (MMP), $\alpha2\beta1$ integrin-collagen binding and TGF-β receptor signaling, the MFT could not be completed and the tissue core still contained some myofibroblasts. Taken together, their results proposed the existence of reciprocal feedback loops between cellular pathways of ECM production, ECM fiber tension and cell decision-making, which all together seem to play a critical role in the FMT.

The simplicity of this microtissue platform is ideal to mathematically model the processes involved in order to distill more quantitative relationships between the parameters that tune the reversible FMT and to address various questions. How does this sharp change in ECM composition along the microtissue influence the mechanical environment surrounding the cells? How does the cell respond to mechanical signals that influence ECM production and alignment, and finally closing the sequential reciprocal feedback loops? Answering these questions will help explain the mechanisms of action that underlie the experimental observations of overlapping high ECM fiber stretch and myofibroblast phenotype. They may also provide evidence that the compositional changes in ECM can indeed revert the FMT in more mature tissue via changing the mechanical properties. In order to complement the microtissue experiments and address these questions, which have both biological and mechanical aspects, occurring at various scales, we built a multiscale, coupled mechobiological *in silico* model based on the previous knowledge on the intricate details of the biological processes in the reversible FMT. This *in silico* model, which has two modules that interact with one another, could be later used to conduct *in silico* experiments, that will inform experimentalists

before they can build combined biological and mechanical mictotissue platforms. A biological module was built in our *in silico* model to represent the experimentally observed biological and compositional changes during the reversible FMT. A mechanical module was built to translate the ECM compositional changes into mechanical properties of the tissue and to calculate tissue response to these compositional changes in terms of strains. The two modules were coupled to inform one another iteratively, similar to the intricate feedback loops observed experimentally in FMT. By keeping the *in silico* model geometry similar to the *in vitro* experiments, we were able to compare our results to previous observations. Our results show the dynamic interplay between the tissue mechanics and biology, agreeing to the previous literature on the reversible FMT. The results of this study provide critical insights into the relative importance of parameter sets that tune the FMT and with this, the reciprocal feedback loops between tissue mechanical environment and the cell decision-making.

6.2 Methods

Experiments on the development of fibroblast microtissues have indicated that the reversible FMT requires a dynamic interplay between biology and mechanics to tightly and spatiotemporally control the ECM composition and alignment. In the microtissue growth experiments, it was shown that the regions of high FN fiber strain spatially overlap with the regions of high myofibroblast activity. In order to link these observations with their mechanisms of action, including the underlying mechanical and biological processes that govern the reversible FMT (FMT-MFT), we created a computational model with biological and mechanical modules (Figure 6.1). For computational efficiency, we modeled one quarter (upper left corner, 250 μm by 250 μm) of the microfabricated cleft in Kollmannsberger *et al.*, 2018 (500 μm by 500 μm). Our 2D model represents one Z stack of their 3D microtissue *in vitro* model. The computational model accounts for four main categories of biological events 1) mechanosensitive activation of cellular signaling, 2) contractility-induced YAP/TAZ nuclear translocation, 3) ECM protein production and assembly of ECM and 4) altering of the ECM mechanical properties through the transient expression of TNC and TG2. The numbers (1-4) corresponding to the arrows in Figure 6.1c, represent these different categories. The exact biological processes that are necessary for the FMT to proceed were explained in Benn *et al.*, 2023, here we lump some of these processes together in our mechanobiological computational model. The arrows, corresponding equations and biologi-

cal processes that are implicitly considered by each equation are explained in detail in the following sections and also summarized in Table S.6.1.

6.2.1 Biological Module

The biological module represents the dynamic changes in protein production and degradation in response to the mechanical changes in the tissue. We included the production of αSMA, nuclear YAP/TAZ ratio and the production of FN and collagen as ECM proteins in our biological module. For computational simplicity, we did not explicitly model all the biological players unraveled by Benn *et al.*, 2023, such as tenascin-C (TNC) and tissue transglutaminase (TG2) activity. However, these processes were implicitly represented via nonlinear relationships between the components of the biological module, as explained below. The abundances of each of these variables are calculated with discrete equations explained below. The values are always between 0 and 1, corresponding to a relative abundance, allowing us to compare the abundances of different proteins in the biological module with one another.

The biological module has the nature of an agent-based model, where agents represent micro-scale regions in the developing tissue. We used Python 3.9 and specifically the numpy package (Harris *et al.*, 2020) to build the biological module. The location of the tissue agents, the abundance of extracellular and intracellular proteins and the cell type dominant at each agent are recorded in separate 3D numpy arrays. An array in numpy is a grid of values. The main array ($agent\_array[t, y, x]$) records a value of 1 where there is a tissue agent and 0 where there is empty space. Each 3D array has 101 grid positions in x and y directions (Figure 6.1b)and the third dimension (t) records the current iteration (time) in simulation. Every iteration (one time step) corresponds to hours in real time.

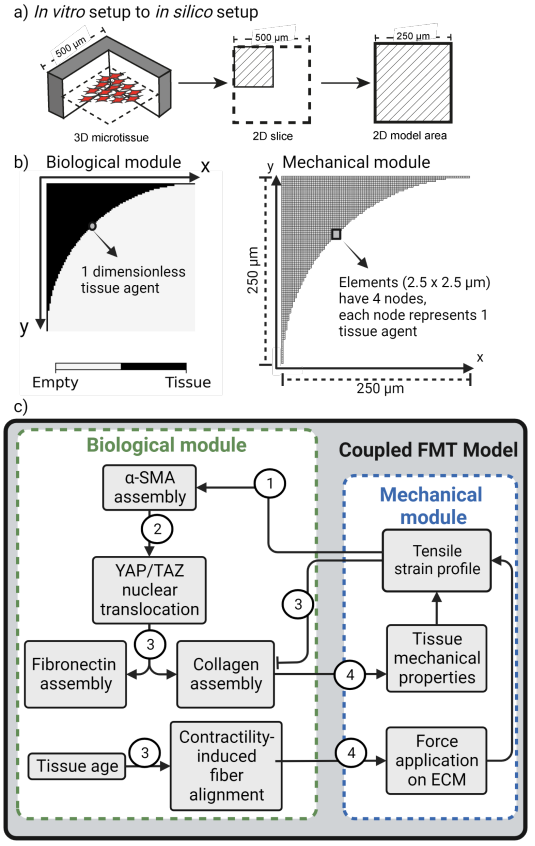

Figure 6.1: a) Using the *in vitro* setup (Benn *et al.*, 2023; Kollmannsberger *et al.*, 2018) to establish an *in silico* model used in this theoretical study. b) The dependencies of the biological and mechanical modules. Each tissue agent in the biological model corresponds to a node in the mechanical module. 4 nodes make up one finite element in the mechanical module mesh. c) The flow of information during one iteration of the simulation between the biological and mechanical modules of the integrated FMT model. Numbers 1-4 on the arrows between module components correspond to different biological processes that are necessary for the reversible FMT (FMT-MFT) to proceed (details in the method section or visit Figure 6.7 and Table S.6.1 for a summary). At each iteration the flow of information is repeated, iteratively updating both biological and mechanical module enabling various transient biological process that make the FMT-MFT possible.

All other variables of the biological module, namely αSMA, nuclear YAP/TAZ ratio, FN and collagen, are recorded in their own 3D arrays. The $agent\_array[t, y, x]$ informs other arrays iteratively where the new tissue is forming. The array that records the tissue tensile strains ($strain\_array[t, j, i]$) reads the tissue strains calculated by the Abaqus software (Abaqus 3DEXPERIENCE R2019x, see mechanical module below). The tissue level strains are then used to calculate the relative abundance of αSMA at each tissue agent following the equation below:

$$\alpha SMA[t,\ y,\ x]\ = \frac{strain\_array[t,\ y,\ x]^n}{K^n\ +\ strain\_array[t,\ y,\ x]^n} \tag{6.1}$$

The Hill type dependence of αSMA on tissue strains has been deduced from the experimental study of Kollmannsberger and colleagues (Kollmannsberger *et al.*, 2018) where they showed that higher FN strain in the ECM overlapped with high αSMA expression. Often used in systems biology, the Hill type equations are efficient for lumping multi-step biological processes (e.g., transcription, translation) into one step (Ang *et al.*, 2013). In our model the strain-dependent αSMA expression includes also the following mechanosensitive intermediate steps (Figure 6.1c, arrow 1): 1) Myofibroblasts assemble highly strained Fn fibers, which requires $\alpha5\beta1$ integrin activation and 2) via increased FAK and RhoA (downstream to $\alpha5\beta1$ integrin activation), cytoskeletal remodeling occurs via the build-up of a more contractile actomyosin cytoskeleton enriched with αSMA.

The cells that have αSMA assembled into their cytoskeleton are characterized as myofibroblasts experimentally. In our model, we also classify the dominant cell type in the tissue agents based on their αSMA content. Tissue agents which have αSMA $\geq$ 0.2 are classified as tissue regions with myofibroblast activity, tissue agents which have more than zero but less than 0.1 αSMA were classified as transition tissue regions where either FMT or MFT is happening. Tissue agents with zero αSMA were classified as regions with fibroblast activity.

Following the assembly of αSMA, the contractility of the cells increase and allow the opening of nuclear pores, resulting in the entry of more YAP/TAZ in the cell nucleus (Figure 6.1c, arrow 2) (Elosegui-Artola *et al.*, 2017; Heng *et al.*, 2021; Talele *et al.*, 2015). From the same experimental study (Kollmannsberger *et al.*, 2018), we obtained a dependency between the YAP/TAZ in the nucleus

and αSMA expression as a third degree polynomial. The nuclear YAP/TAZ at each tissue agent is calculated as below:

$$YAPnuc[t,\ y,\ x] = kyt0 \times \alpha SMA[t,\ y,\ x]^3 + kyt1 \times \alpha SMA[t,\ y,\ x]^2 + kyt2 \times \alpha SMA[t,\ y,\ x] + kyt3 \tag{6.2}$$

$kyt0$, $kyt1$ and $kyt2$ describe the mechanically regulated YAP/TAZ nuclear translocation while $kyt3$ describes the contractility-independent nuclear translocation of YAP/TAZ (Figure 6.1c, arrow 2, Table S.6.1).

Next, YAP/TAZ translocation to the nucleus is known to increase the production of ECM proteins indirectly (Cai *et al.*, 2021). In our biological model, the production, fibrillogenesis and degradation of the ECM proteins FN and collagen are maintained by the following equations:

$$FN[t,\ y,\ x] = \frac{YAPnuc[t,\ y,\ x]^3}{kfy + YAPnuc[t,\ y,\ x]^3} + k_{fibFN} \times FN[t-1,\ y,\ x] \tag{6.3}$$

$$Col[t,\ y,\ x] = \frac{kc}{1 + e^{(kcs \times strain\_array[t,\ y,\ x] - kcy \times YAPnuc[t,\ y,\ x])}} + k_{fibCol} \times Col[t-1,\ y,\ x] \tag{6.4}$$

The FN equation (Eq.6.3) has two parts, first is the Hill type dependence to nuclear YAP/TAZ which lumps together two intermediary processes 1) transcriptional regulation of FN gene expression and assembly and 2) YAP/TAZ-dependent profibrotic gene expression, including TNC. In the second part of the equation, k_{fibFN} describes both the fibrillogenesis, alignment and stretching of FN by highly contractile myofibroblasts and degradation of FN that accumulates from the previous time step of the simulation ($FN[t-1,\ y,\ x]$).

The collagen equation (Eq. 6.4) has a similar structure to the FN equation. In the first part, kc describes the total possible procollagen production per time step. The total amount changes based on the availability of relaxed FN fibers (low tissue strain in our model) and nuclear YAP/TAZ. kcs is the parameter that controls the strain dependency of collagen fibrillogenesis. Collagen

production has been shown to decrease with strain (Sun *et al.*, 2016) and collagen assembly into the ECM is instructed by the relaxed FN fibers (Benn *et al.*, 2023; Kubow *et al.*, 2015). Therefore, this equation also implies the transiently upregulated TNC binding to FN, causing the disassembly of integrin $\alpha5\beta1$ adhesions, resulting in FN relaxation and allowing collagen assembly. kcy, on the other hand, describes the nuclear YAP/TAZ assisted production of (pro)collagen. k_{fibCol} in the second part of the equation describes the fibrillogenesis and degradation of collagen that accumulates from the previous time point ($Col[t-1,\ y,\ x]$), similar to the FN equation. Note that k_{fibCol} is set to be larger than k_{fibFN} to reflect the fact that collagen fibrillogenesis occurs in more steps, thus takes longer time than that of FN, and that the FN degradation occurs faster (Kadler *et al.*, 2008).

The biological module also keeps track of the FN fiber angles (with respect to the x-axis, Figure 6.1b) at each tissue agent. FN fibers have been shown experimentally to be parallelly aligned at the growth front in the direction of the highly contractile myofibroblasts (Benn *et al.*, 2023). In our computational model, tissue age directly influences FN fiber alignment (Figure 1c, arrow 3) however biologically the process of ECM remodeling is more complicated. The ECM fibers get more enmeshed over time in the mature tissue, this happens gradually following the collagen assembly guided by the relaxation of FN fiber, as TNC blocks FN-Syndecan 4 binding thereby destabilizing the integrin $\alpha5\beta1$ adhesions (Benn *et al.*, 2023). The FN fiber angle (θ) for the tissue agents close to the growth front is calculated using the following equation:

$$\theta[t,\ y,\ x] \ = \ 90^\circ \ - \ arctan\left(\frac{(y_{max}-y)}{(x_{max}-x)}\right) \tag{6.5}$$

Where y_{max} and x_{max} are the y and x dimensions of the biological model array and y and x correspond to the coordinates of each tissue agent (e.g., in Figure 6.2a). The arctan function calculates the angle between x-axis and the straight line from the right bottom corner of the array to the position of the agent [x,y] (β in Figure 6.2a) . Right angle minus this value gives the fiber angle parallel to the growth front (θ in Figure 6.2a). The fiber angles of agents that are older than two days (8 iterations) were assigned randomly, corresponding to the mature tissue in Benn *et al.*, 2023.

At each iteration in the simulation, tissue agents in the biological module also search for available space to grow. The rule is, for each agent, the empty neighboring locations (out of eight possible neighbors) are collected in a list

and the agent is allowed to generate a copy of itself (divide) into one of the empty neighboring locations. If there is no empty neighboring location in the array, the agent is not allowed to divide. This rule implies the cell division only happens at the growth front, where there is available space. It is a simplification from the *in vitro*microtissue experiments, where cell proliferation was only observed at the growth front, which is occupied by highly proliferative myofibroblasts.

6.2.2 Mechanical Module

The mechanical module was used to calculate the tissue level strains in response to the contractile forces applied by the cells and the ECM material properties changing over time. Abaqus software was used to perform the finite element method (FEM) to obtain the resulting strains at each iteration. Essentially, each tissue agent in the biological module represents one node in the mechanical model geometry. Four nodes make up one square element for the FEM calculations. Each node was set to be 2.5 μm apart. Therefore, one edge of the mechanical model, which contained 101 nodes (corresponding to the 101 tissue agents in the biological module), represents 250 μm. Since we simulated the tissue growth, we updated the Abaqus input files with the new tissue geometry at every iteration.

We set different boundary conditions to every edge of the model. The nodes on the top edge of the cleft were constrained in displacement along the y-axis while the nodes on the left edge of the cleft were constrained along the x-axis. These boundary conditions ensured the tissue remains attached to the cleft external boundaries but can expand or contract over them. Our model focused on the upper left corner of the 500 μm by 500 μm cleft in the *in vitro*experiments. This suggests that the tissue at the bottom and left edges of our 250 μm by 250 μm model continues for another 250 μm in the *in vitro*setup. Therefore, we set symmetry boundary conditions along the x-axis and y-axis for the nodes on the right and bottom edges of the growing tissue respectively. The tissue growth (via the division of tissue agents at the growth front as described in the biological module) suggests the addition of new nodes and elements to the mechanical module at each iteration. This required us to iteratively update the model geometry at each iteration in the input file for the Abaqus software.

We assumed linear elasticity for the ECM in the mechanical model due to the small strains ($< 10\%$). Material properties (Young's modulus and Pois-

son's ratio) were assigned to the elements based on their collagen abundance. To calculate the collagen abundance per element, we averaged the collagen abundance in the four nodes (tissue agents) that make up an element. Elements with a collagen abundance between 0 and 0.1 were classified as "provisional matrix" and assigned a Young's modulus of 4×10^{-4} MPa (Achterberg *et al.*, 2014; Schuster *et al.*, 2023) and a Poisson's ratio of 0.3 (Szymanski *et al.*, 2017). Provisional matrix represents the newly produced FN rich ECM prior to collagen getting assembled (Schuster *et al.*, 2023). The collagen assembly into the ECM requires relaxed FN templating and once the collagen assembled into the ECM, it partially shields FN from being stretched by the cells (Kubow *et al.*, 2015). To reflect this effect of increased collagen content decreasing the FN fiber stretching in the ECM, elements with more collagen than 0.1 units have been assigned increasing Young's moduli with increasing collagen content (Roeder *et al.*, 2002). ECM materials were named "provisional matrix", "soft", "medium stiff", "stiff"and "maximum stiff" to reflect the decreasing stretchability of FN with increasing collagen content. All ECM material properties used in the model and their references can be found in Table 6.1 below.

ECM material name	**Collagen content**	**Young's modulus, Poisson's ratio**
Provisional ECM	Col < 0.1	4×10^{-4} MPa (Achterberg *et al.*, 2014), 0.3 (Szymanski *et al.*, 2017)
Soft ECM	$0.1 \leq$ Col < 0.4	1.54×10^{-3} MPa (Roeder *et al.*, 2002), 0.167 (Checa *et al.*, 2011)
Medium stiff ECM	$0.4 \leq$ Col < 0.7	10.7×10^{-3} MPa (Roeder *et al.*, 2002), 0.167 (Checa *et al.*, 2011)
Stiff ECM	$0.7 \leq$ Col < 1	16.6×10^{-3} MPa (Roeder *et al.*, 2002), 0.167 (Checa *et al.*, 2011)
Maximum stiff ECM	Col = 1	24.3×10^{-3} MPa (Roeder *et al.*, 2002), 0.167 (Checa *et al.*, 2011))

Table 6.1: Different materials used in the mechanical model based on the element-wise collagen abundance calculated in the biological model.

At each iteration, we randomly picked the force-applying nodes among all the nodes in the mechanical model to represent the traction force-applying cells embedded in the microtissue. Specifically, the force-applying cells were modeled as active force dipoles. For each force dipole, one core node (in

the middle, Figure 6.2b yellow node) and two force-applying nodes (15 μm apart, Figure 6.2b green nodes) were selected randomly from the agent array to represent approximately the size of a fibroblast (Freitas Jr., 1999). Each force-applying cell exerts a pulling force of 0.2×10^{-6} N in total magnitude (Rosowski *et al.*, 2018). Therefore, two concentrated forces (each being half of the total magnitude) pointing towards the core node were applied from the two force-applying nodes (Figure 6.2b). The direction of the forces were determined at each iteration by retrieving the FN fiber angle (θ) of the agent at the same location in the biological model that corresponded to the core node in the mechanical model. Fiber angles below 22.5° were assigned as force vectors along the x-axis, angles between 22.5° and 67.5° were assigned as force vectors diagonal to the x-axis, and angles above 67.5° up to 90° were assigned as force vectors perpendicular to the x-axis. The random selection of the force applying nodes allowed us to consider the small displacement of cells within the tissue and introduced some stochasticity to the model. Biologically this represents the dynamic nature of the tissue. Cells are not static and actively pull, changing their exact location. So the cell core that pulls can slightly shift. To represent this, we assigned the pulling locations randomly at each iteration.

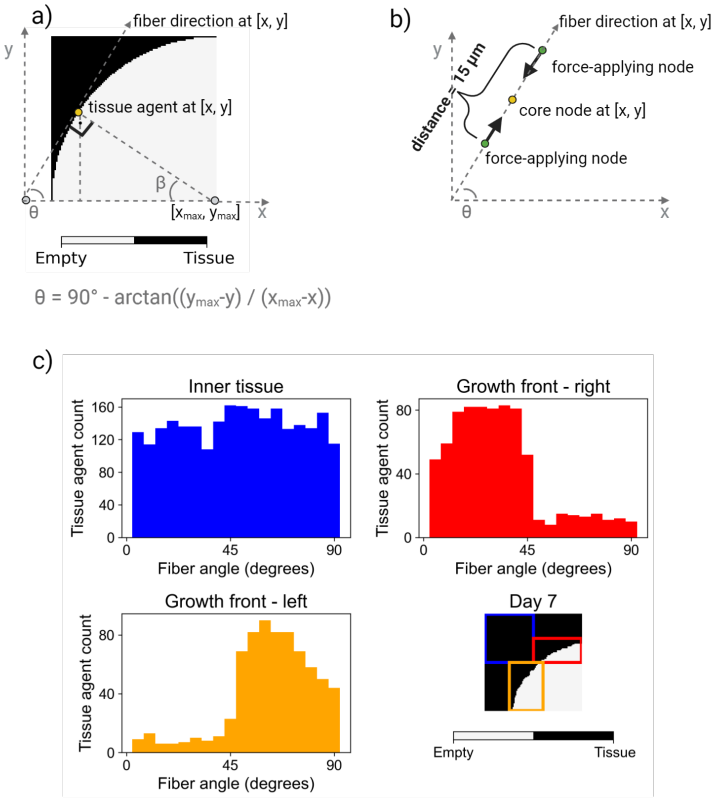

Figure 6.2: a) Geometrical explanation on fiber angle calculations for the tissue agents younger than 2 days at the growth front in the biological module. b) The schematic explanation of how fiber angles define the force vector direction in the mechanical module. The force applying node (yellow) and the nodes where the pulling forces are applied (green) are not true to size. The nodes and the distance between them are drawn larger for visualization purposes. c) Fiber angles of the younger tissue agents (yellow, red) versus older tissue agents (blue) at day 7 of the simulation. Fiber angle is measured with respect to the x-axis (bottom edge of the model space) and reported in degrees.

6.2.3 Coupling the two modules

In order to see the effects of the sharp change in ECM composition along the microtissue on the mechanical environment surrounding the cells and read out the cellular response to mechanical signals we coupled the two modules explained above. Arrows marked with number 4 in Figure 6.1c correspond to the points where biological module feeds into the mechanical module. These points of contacts have different biological meaning at different microtissue locations as described by Benn *et al*., 2023. Namely, in the growth front, where there are highly contractile cells and highly stretched FN, the mechanical model gets this input and reports back "high strains". Entering the transition zone, the relaxation of FN starts (due to the increase in TNC) leading to FN fibers-templating the nucleation of collagen fibrillogenesis. This is associated with a transient reduction of strain considered by the mechanical module. In the tissue core, the shift to collagen binding integrins occurs, resulting in reduced FAK, RhoA activity and contractility. The result is lowered strains which allow the assembly of ECM rich in collagen. In our computational model, these biological processes are implicit in the intermediary steps explained below.

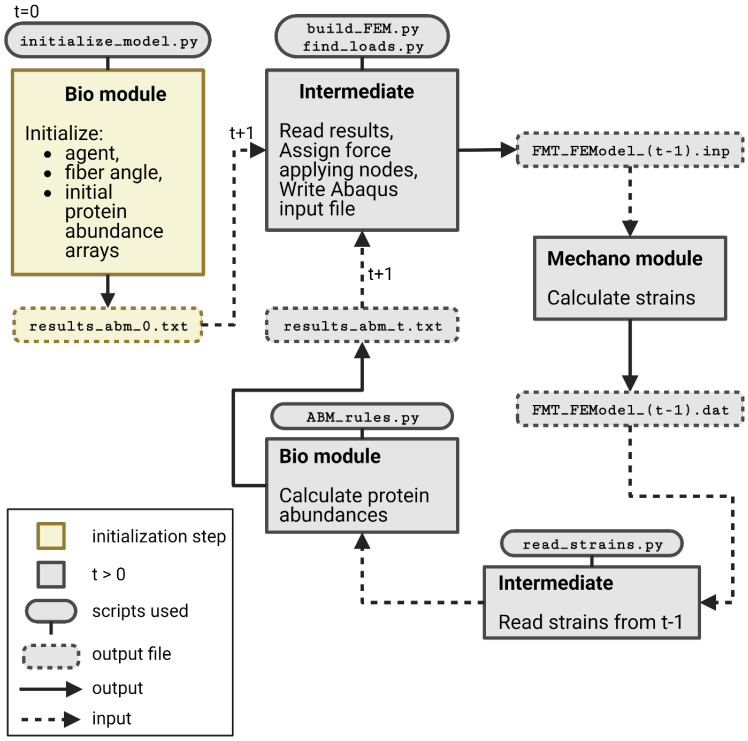

Figure 6.3: Coupled mechanobiological model steps, scripts used in the simulation process and input/output files. All the scripts and data are available on the project GitHub repository (https://github.com/carliercomputationallab/rFMT-Coupled-Mechanobiological-Model).

In order to bring the biological and mechanical modules of the model together we wrote intermediary scripts in Python 3.9 (Figure 6.3). The intermediate steps ensured the correct flow of information between the two modules. The model initiation (t = 0, Figure 6.3) step creates the initial tissue agent placement on the biological module grid and writes in the initial conditions of the model (fiber angles and protein abundances). These initial settings are written in a text file, which is read by the intermediary scripts "$build\_FEM.py$" and "$find\_loads.py$" to initiate the input file for the

mechanical model. Using the location of active agents, abundance of collagen and the fiber angles, the elements, material properties of elements and force directions are determined respectively. These are written in the input file for Abaqus "$FMT\_FEmodel\_(t-1).py$". Once the FEM calculations are done, results are saved in a text file ("$FMT\_FEmodel\_(t-1).dat$"), which is read by another intermediate script ("$calculate\_strains.py$"). Strain values per node are extracted from the Abaqus results file and used as input for each tissue agent in the biological module in the next iteration ("$ABM\_rules.py$"). This cycle is repeated until the end of simulation time and all the results files are stored with appropriate naming per iteration ("$results\_abm\_t.txt$"). All the scripts (main and intermediary), Abaqus input files and results files are stored in this project's GitHub repository and can be accessed openly (https://github.com/carliercomputationallab/rFMT-Coupled-Mechano biological-Model). The baseline model parameters are given in Table 6.2.

Table 6.2: Parameter values used in the baseline simulation. Values marked with an asterisk were estimated using the experimental data of Kollmannsberger *et al.*, 2018

Parameter	**Value (unitless unless it is specified)**	**Explanation of the processes that are considered in the equations where the parameters are used**
K	0.03*	Myofibroblasts assemble highly strained Fn fibers, which requires $\alpha5\beta1$ integrin activation and signaling. Via increased FAK and RhoA, cytoskeletal remodeling a more contractile actomyosin cytoskeleton enriched with αSMA is built.
n	4*	
kyt_0	0.65*	Contractility-dependent nuclear transport of YAP/TAZ
kyt_1	-1.2*	
kyt_2	0.85*	
kyt_3	0.3*	Contractility-independent nuclear transport of YAP/TAZ
kfy	0.1	YAP/TAZ-dependent FN secretion also implies: YAP-dependent profibrotic gene expression, including TNC.
$kfibFN$	0.1	FN fibrillogenesis, alignment and stretching.
kc	0.050	Total possible procollagen secreted

kc'	0.025 (Cui *et al.*, 2020)	Total possible procollagen secreted in the case of collagen inhibitor simulation
kcy	5	YAP/TAZ-dependent procollagen secretion
kcs	4	Collagen assembly that is dependent on relaxed FN fiber availability (implying transiently upregulated TNC binding to FN, causing the disassembly of integrin $\alpha5\beta1$ adhesions, relaxing FN fibers)
$kfibCol$	0.95	Collagen fibrillogenesis
Initial FN abundance	0.1*	Initially ECM only has low FN levels
Initial nuclear YAP/TAZ	0.2*	Initially there is only contractility-independent (background) nuclear YAP/TAZ
Initial αSMA	0	Initially αSMA is not incorporated into the cytoskeleton
Initial collagen abundance	0	Initially tissue does not contain collagen in the ECM
Force applied by one node	0.2×10^{-6} N (Rosowski *et al.*, 2018)	Force applied by one cell
Modified force applied by one node for blebbistatin simulation	0.1×10^{-6} N (Doss *et al.*, 2020)	Modified force applied by one cell for blebbistatin simulation

6.2.4 Biological and mechanical perturbations to the model

In order to test the mechanobiological model under different conditions and compare its validity with respect to the experimental conditions, we performed two perturbations. First one is the biological inhibitor, which reduces the total procollagen secretion per iteration by half, done here by introducing the modified parameter kc', instead of the original parameter kc (Table 6.2). kc' was set to 0.025, the half of the original parameter kc. This biological

in silico perturbation is similar to the effect of 1 mg/mL pirfernidone, which has been shown to reduce the collagen type 1 production by half in primary human intestinal fibroblasts (Cui *et al.*, 2020).

Second perturbation was a mechanical inhibitor, mimicking the effect of 10 μM blebbistatin addition to the culture medium, which reduces the total traction force applied by cells by half (Doss *et al.*, 2020). Thus, for the mechanical inhibitor, we reduced the total applied force by a node to 0.1×10^{-6} N (Table 6.2). All other parameters were kept the same as the baseline set up and the simulations were run for 19 days. The results were compared to the *in vitro* microtissue experiments of Benn *et al.*, 2023 and Kollmannsberger *et al.*, 2018.

6.3 Results

In order to investigate the integrated mechanical and biological processes that govern the reversible FMT, we performed a 19 day simulation using the parameters in Table 6.2 and compared our simulation results to the experimental results where available. At the end of 19 days (or 74 iterations in simulation time), the tissue size reaches 340 μm when measured diagonally from the growth front until the top left corner of the cleft.

Throughout the simulation, the fiber angle per tissue agent changes as the tissue agent matures. The FN fibers of tissue agents younger than three days are aligned with the growth front, while the fibers become more randomly aligned as tissue ages past three days. A comparison of fiber angles of the young tissue agents versus that of older tissue agents is shown in Figure 6.2c for day 7 of the simulation. We chose day 7 to illustrate this aspect simply for visualization purposes. The three histograms in Figure 6.2c show the number of tissue agents with the respective fiber angles. Inner tissue agents (blue) have a more balanced distribution of fiber angles (Figure 6.2c). Tissue agents localized towards the right hand side of the growth front (Figure 6.2c red box) have more fibers aligned between 0° to 45° to the x-axis of the cleft, representing a parallel alignment with the circular growth front. Tissue agents that are on the left hand side of the growth front (Figure 6.2c yellow box) on the other hand, have more fibers between 45° to 90° to the x-axis of the cleft, which again represents a parallel alignment with the growth front. In other words, at the growth front, the majority of fibers are parallel to the growth front, which corresponds to the experimental findings of Benn *et al.*, 2023.

Initially, at day 0, the *in silico* microtissue consists of fibroblasts and FN fibers (and no collagen). This corresponds to the softest ECM material in our simulations, with an elastic modulus of 4×10^{-4} MPa. At this point there is not yet αSMA produced and a baseline level of nuclear YAP/TAZ (0.2) is homogeneously present in all tissue agents. When cell traction forces are applied and tissue strains are calculated by the mechanical module of the model, the resulting strains are high ($\sim$10%) throughout the microtissue, except in the top left corner where the tissue is the most constrained by the solid cleft (Figure 6.5, Day 0). We let the simulation run for 4 iterations and calibrate. By the end of this period, which corresponds to 1 day in real time, the biological and mechanical environment in the *in silico* microtissue gains properties similar to the *in vitro*microtissues described in Benn *et al*., 2023 and Kollmannsberger *et al*., 2018. At the growth front, there are high tensile strains, high αSMA and nuclear YAP/TAZ, high FN and no collagen (Figure 6.5, Day 1). This spatial distinction with particular mechanical and biological properties at the growth front in comparison to the tissue center, holds true for the rest of the simulation time.

6.3.1 ECM with little collagen overlaps with regions of high strain and myofibroblast activity

The progression of tissue growth, ECM protein composition, tensile strains in the microtissue and cellular proteins αSMA and nuclear YAP/TAZ are reported over time in Figure 6.4. Overall, at the growth front, which corresponds to the provisional matrix regions, the strains are higher than in the tissue core. This high strain region of the *in silico* microtissue also overlaps with high αSMA abundance and high nuclear YAP/TAZ ratio in the tissue agents. This results in the higher abundance of FN in the younger tissue agents and the accumulation of collagen in the older tissue agents (Figure 6.4, ECM proteins).

We observe the myofibroblast phenotype constrained to the high strain region mainly at the growth front until the end of simulation (Figure 6.4). Note that we did not model cell migration, thus the tissue agents that were once at the growth front become embedded in the tissue core as new tissue forms. As such, the tissue agents that have a myofibroblast phenotype when they are at the growth front return back to fibroblast phenotype once they fall in the tissue core region. This shows that spatiotemporal change in tissue mechanics allows for the reversal of the FMT.

At day 19, there are four different tissue materials present in the *in silico* microtissue, namely the provisional, soft, medium stiff, and stiff matrices (Figure 6.5). These materials are defined in the mechanical module by the amount of collagen they contain and the elastic modulus of the material increases as the collagen abundance increases (Table 6.1). Taken together, simulation of the cellular events linked to the mechanical response of the *in silico* microtissue suggests that the local and gradual assembly of ECM proteins can instruct the tissue material properties in a way to constrain the myofibroblast activity to the growth front. The interplay between the biological and mechanical processes, tightly controlled in space and time, results in a transition zone in which the strains decrease, reversing the myofibroblast phenotype back to a fibroblast phenotype. As such, in the interior of the *in silico* microtissue only a fibroblast phenotype is found. It should be noted that, the sharp decrease in tissue strains, which we capture in the transition zone in our *in silico* model, is only possible naturally via the transient upregulation of ECM modulators that reduce the stability of cell-ECM contacts, i.e., TNC, as detailed more in discussion and modeled here implicitly.

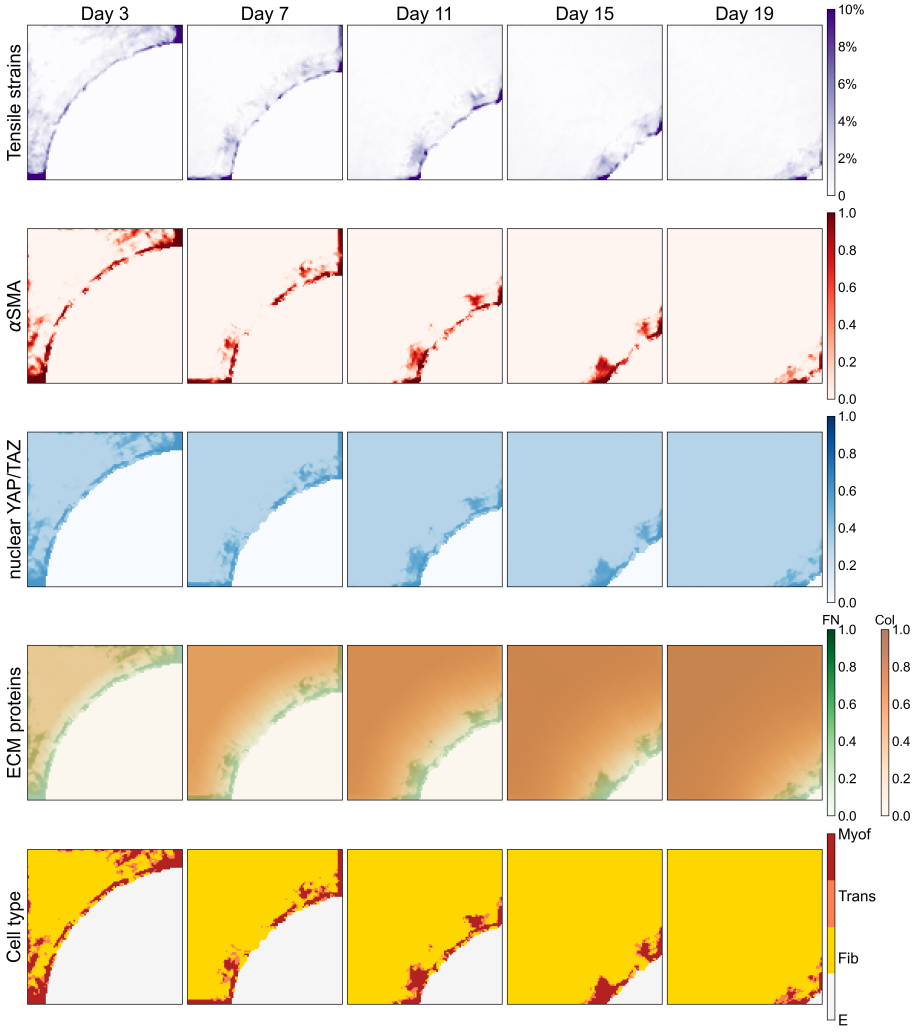

Figure 6.4: *in silico* microtissue growth monitored over time. Each row demonstrates one of the following tissue characteristics: tissue strains, abundances of αSMA, nuclear YAP/TAZ, ECM proteins collagen and FN, and the dominant cell type (fibroblast, transition or myofibroblast) at each tissue agent. Columns represent different timepoints in the simulation (days 3, 7, 11, 15, 19).

6.3.2 Spatiotemporal control over ECM production creates the biological and mechanical differences observed between the growth front, transition zone and the tissue core at day 19 in the *in silico* microtissue

Next, we look at a snapshot of the *in silico* microtissue at day 19 (Figure 6.5). We plot the mechanical and biological variables of the microtissue with respect to the distance to the growth front (direction shown in Figure 6.5a) and compare our simulation results to the experimental data where available.

At day 19, according to our simulation, we observe three distinct regions in the microtissue similar to the *in vitro*microtissue experiments (Benn *et al.*, 2023). First the growth front, where the tissue level strains are highest and vary between 1 to 4% in the initial 10 μm (Figure 6.5b). In this region, the αSMA abundance is also higher, changing between 0.12 and 0.75. Similarly, nuclear YAP/TAZ and FN abundance are highest in the growth front, reaching their peak at 0.55 and 0.65 respectively (Figure 6.5c). Collagen abundance in the growth front is low, ranging between 0 and 0.16, and should be carefully interpreted (Figure 6.5c). As collagen abundances lower than 0.1 in the biological module are considered to be too low to make a difference in the material definition in the mechanical module (Table 6.1), the collagen in the growth front region effectively represents procollagen, which is only secreted by the cells and not yet assembled into mature ECM.

Second region is the transition zone, where the tissue tensile strains decrease from 2% to almost zero, between 10 μm and 30 μm (Figure 6.5b). In the transition zone, αSMA sharply decreases close to zero, nuclear YAP/TAZ and FN gradually decrease from 0.38 to 0.30 and from 0.42 to 0.23 respectively (Figure 6.5c). In this region we also observe the collagen content in the ECM increasing from 0.16 to 0.31 (Figure 6.5c). The end of this transition zone is marked by the collagen abundance exceeding the FN abundance.

Third, the tissue core, which we plot only to 60 μm from the growth front, is the region where the collagen abundance continues to increase and reaches a maximum of 0.80. In this region, the tensile strains (Figure 6.5b) and αSMA abundance are zero, and nuclear YAP/TAZ and FN are present only at their background levels of 0.3 and 0.2 respectively (Figure 6.5c).

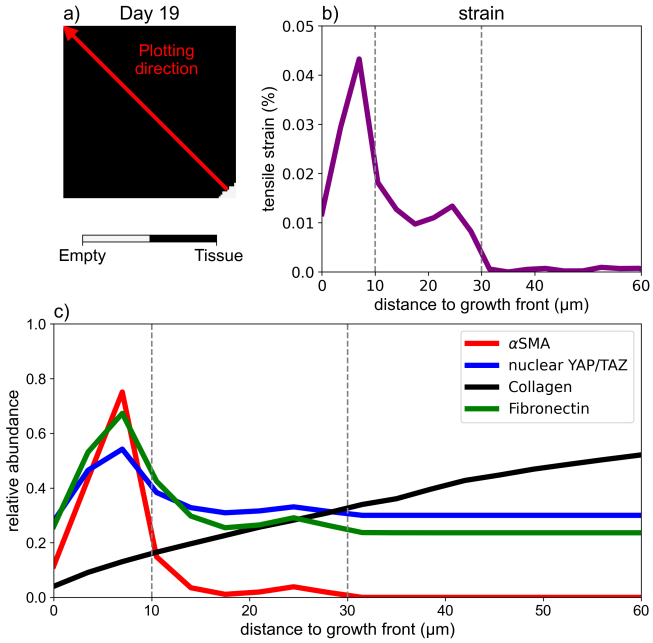

Figure 6.5: a) Snapshot of the *in silico* cleft at day 19, almost full with tissue. The red arrow indicates the direction along which b) the tissue tensile strains and c) αSMA abundance, nuclear YAP/TAZ ratio and ECM protein abundances are plotted at day 19 of the simulation.

Taken together, the peak in αSMA and FN and the low abundance of collagen in the growth front region qualitatively match the growth front definition in Benn *et al.*, 2023. Since the geometry is different in their experiments, and the geometry of the cleft is likely to change the contractile properties of the tissue, we cannot numerically compare our *in silico* results to the *in vitro*results by Benn *et al.*, 2023. However, simulated αSMA and nuclear YAP/TAZ abundances can be compared to the experimental measurements from Kollmannsberger *et al.*, 2018, as the cleft geometry is the same (Figure S.6.3). In order

to compare the fluorescence intensity measures from the experiments to our results, we scaled the αSMA fluorescence intensity measures to vary between 0 and 1, by matching the highest αSMA fluorescence intensity in the experiments to 1. This way the highest αSMA fluorescence intensity measured at the growth front in the experiments corresponds to 0.4 in our scale. Although our simulation overestimates the maximum αSMA abundance, the simulation and experimental results both indicate that the highest αSMA abundance occurs within the initial 10 μm of the microtissue (growth front), after which the αSMA abundance sharply decreases within the transition zone to reach zero in the tissue core (Figure S.6.3). The nuclear YAP/TAZ abundance in our simulation matches the experimental observations of Kollmannsberger *et al.*, 2018 (Figure S.6.3), with a peak in the transition zone and a constant baseline level in the tissue interior.

What is the underlying mechanism in the *in silico* model that drives the above described behavior of distinct zones with biologically distinct properties? Our simulation allowed us to clearly demonstrate that the fast assembly of highly stretchable FN fibers at the growth front, their relaxation in the transition zone, leading to a gradual accumulation of collagen in the tissue core, creates the mechanical environment needed for a high strain region at the growth front (of the *in silico* microtissue). It is important here to highlight that the (local) ECM composition in the biological module of our model instructs the (local) material properties of the tissue in the mechanical module. Therefore the ECM protein assembly into the ECM is both the response to the mechanical environment (in the form of tensile strains that lead to integrin activation, downstream YAP/TAZ translocation and protein production) and the factor that creates the mechanical environment of the *in silico* microtissue.

6.3.3 Biological and mechanical perturbations

After we established that the interplay between biological and mechanical properties of the microtissue is the key controller of the reversible FMT process, we applied perturbations to both biological and mechanical modules of our *in silico* model, to explore their interconnected nature. As biological inhibitor, we chose to mimic the addition of collagen production inhibitors to the culture medium, which are used for antifibrotic agents in the clinic (Knüppel *et al.*, 2017). For the mechanical inhibition, we mimicked the addition of blebbistatin to the culture medium, which inhibits cell contractility.

The biological inhibition of collagen production resulted in an overall increase in tissue strains calculated by the mechanical module (day 19 shown in Figure 6.6a). The higher strains (via biological processes explained in the previous section) result in less collagen and more FN abundance in the ECM compared to the baseline (Figure 6.6b). The overall effect of the collagen inhibitor was an increased myofibroblast activity (Figure 6.6c). In other words, the reversal of the FMT process was hampered with the biological inhibitor, whereas the reversal of the FMT was clearly observed in the baseline simulation behind the growth front (Figure 6.6c).

In the case of blebbistatin, the mechanical inhibitor of cell contractility, the tensile strains were zero throughout the tissue, except at the growth front. The strains in the growth front were lower than in the baseline simulation (day 19 shown in Figure 6.6a). Different from the biological inhibitor, with blebbistatin, the cell contractility was reduced by half. Hence in this case, the change in strains are not due to a change in the composition of the ECM (Figure 6.6b) but due to the reduced total force applied by contractile cells on the ECM. The overall myofibroblast activity (including at the growth front) was reduced with blebbistatin, compared to the baseline (Figure 6.6c). Note that the myofibroblast phenotype is directly linked to the abundance of αSMA in our model.

Both our simulation results from the biological and mechanical perturbations are in line with the observations from the *in vitro* microtissue experiments by Benn *et al*., 2023 and Kollmannsberger *et al*., 2018 respectively. With the addition of blebbistatin to the culture medium, Kollmannsberger *et al*., 2018 reported a decrease in the αSMA expression at the growth front compared to the control, similar to what we observed in our perturbation simulation (Figure 6.6d). With a biological inhibitor, Benn *et al*., 2023, described a less defined growth front with αSMA being expressed even further away from the growth front, in contrast to the control experiments without the addition of a biological inhibitor. This disturbance to the growth front can also be seen in our *in silico* microtissue experiment with biological inhibitor (Figure 6.6c).

Interestingly, the mechanical inhibitor blebbistatin, caused a decrease in the amount of FN at the growth front compared to the baseline (Figure 6.6f). The biological inhibitor on the other hand caused the growth front characteristics with high FN to expand, similar to its effect on αSMA (Figure 6.6f) and to the experimental observations (Benn *et al*., 2023). Unlike in the experiments, we observe that there is a constant FN abundance, leveling off around

0.2 throughout the tissue. This is due to the background YAP/TAZ nuclear translocation, irrespective of the amount of αSMA in the microtissue.

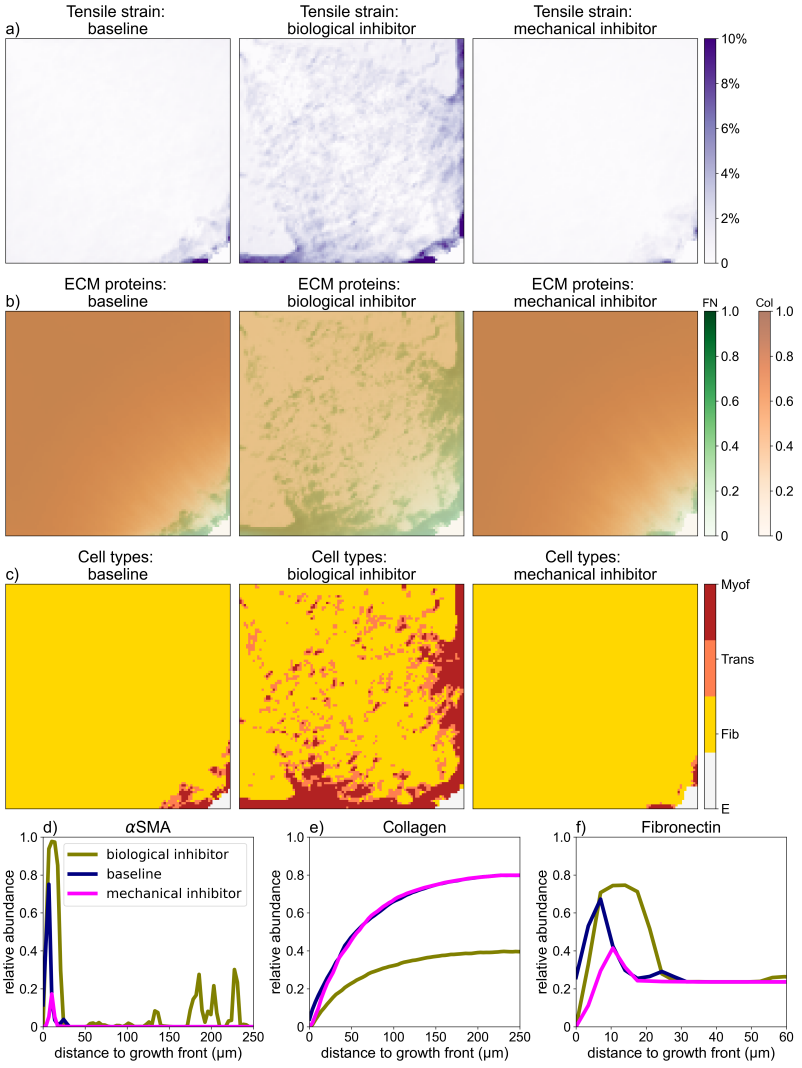

Figure 6.6: *Continued on the following page*

Figure 6.6: The effects of biological and mechanical perturbations on a) tissue principal tensile strains, b) ECM composition and c) cell phenotypes observed at day 19 of the simulation. The abundances of d) αSMA, e) collagen and f) FN at day 19, reported with respect to the distance to growth front under perturbation compared to the baseline.

6.4 Discussion

By coupling biological and mechanical processes in an integrated *in silico* model, we have shown that the spatiotemporal control over the ECM is guiding the tissue mechanical properties for a successful reversible FMT. This spatiotemporally controlled production of *de novo* ECM includes many tightly controlled biological processes. Among many, we modeled the strain-dependent αSMA expression, YAP/TAZ nuclear translocation and the FN and collagen production and degradation as ECM proteins in our biological module. Although we did not explicitly model some biological processes identified by *in vitro* microtissue experiments to be drivers of the reversible FMT, such as the integrin-mediated FAK and RhoA activity, TNC and TG2 expression and degradation, MMP activity (Benn *et al*., 2023), we still could capture similar features at the growth front, transition zone and tissue core as in *in vitro* experiments. As such, selected biologically relevant processes lumped together in a reduced set of parameters were captured by our mathematical equations governing the biological module.

In the growth front, where the tensile strains are predicted to be high by the mechanical module, our biological module resulted in the preesence of high levels of αSMA. Normally, activation of integrin $\alpha 5 \beta 1$ and the resulting FAK and RhoA activity helps the assembly of αSMA into the cytoskeleton, thus increasing the cellular contractility (Figure 6.7). In our model, this is captured by the Hill type equation between αSMA and tensile strains (Eq.6.1). Similarly, YAP/TAZ nuclear translocation increases in highly contractile cells due to the cells becoming flatter and nuclear pores opening more (Figure 6.7). This process we implicitly captured by Eq.6.2, as a third degree polynomial fit between α SMA and YAP/TAZ nuclear translocation. Finally, the fast production of tensed FN fibers at the growth front, which we could capture mathematically in the model by the Eq.6.3 implies the physical (via TNC tethering) and chemical (via TG2 crosslinking) stabilization of the provisional matrix (Figure 6.7). Since the mathematical relationship between strain and collagen works in a way to inhibit collagen assembly when strain is high, we

observed very low collagen assembly into the ECM in the growth front (Figure 6.7), corresponding to the experimental observations (Benn *et al.*, 2023). Note that the high strains at the tissue level also imply high fibronectin fiber strain in our model, since we do not explicitly model individual fibronectin fibers.

The transition zone is where the transition from highly contractile myofibroblast phenotype to quiescent fibroblast phenotype starts (Figure 6.7). Biologically, it was hypothesized that the FN relaxation (due to the TNC-mediated disassembly of integrin $\alpha5\beta1$ adhesions) initiates this transition (Benn *et al.*, 2023). FAK and RhoA signaling decreases as integrin $\alpha5\beta1$ adhesion is destabilized because TNC competes with Syndecan 4 (which normally stabilizes integrin $\alpha5\beta1$ adhesions) for binding the FN fibers (Benn *et al.*, 2023; Morgan *et al.*, 2013). Relaxed FN can then template the collagen assembly, thus collagen content also start increasing in the transition zone (Figure 6.7). In our computational model, this behavior of FN relaxation was captured by the reduced tissue strain, which directly increases collagen assembly. The lowered cell contractility is represented by αSMA disassembly, resulting in less nuclear YAP/TAZ (Figure 6.7). In the tissue core, all above described processes in the growth front are reversed (Figure 6.7). For the reversal of these mechanobiological processes, the cells need to establish the right mechanical environment through tightly controlled ECM production and degradation. With our 2-module model, we have shown that, indeed, as the microtissue grows and more collagen is assembled into the ECM towards the tissue core, the tensile strains get lower, so as to reverse the myofibroblast-related activities.

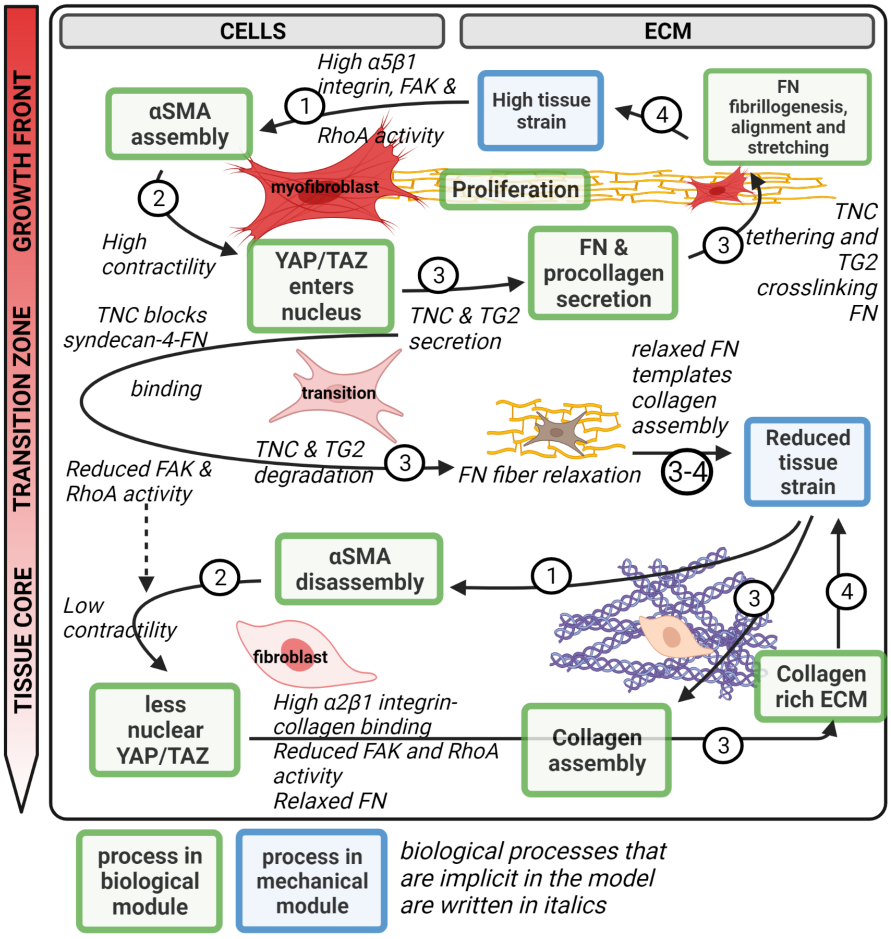

Figure 6.7: Summary of biological processes that are dominant in the a) growth front and b) tissue core. The processes that are captured explicitly in the coupled mechanobiological FMT model are in solid boxes (green for biological module, blue for mechanical module). The processes written in italics represent the biological processes that we implicitly represent in the model equations (explained in the Methods section in detail). *Continued on the following page.*

Figure 6.7: The numbers on the arrows indicate to which category the process belongs to 1) mechanosensitive activation of cellular signaling, 2) contractility-induced YAP/TAZ nuclear transport, 3) ECM protein production, assembly and ECM remodeling via tethering/crosslinking and 4) altering of the ECM mechanical properties. See Table S.6.1 for a textual summary of all the biological processes explained here, as well as the equations in the model that correspond to the processes.

The perturbations we performed both on the biological and also mechanical sides, showed that disturbing the tightly controlled ECM assembly dynamics results in disturbances to the FMT. In case the collagen production was inhibited, the tissue core was richer in highly strained FN fibers and low in collagen which resulted in more active myofibroblasts in the tissue core, meaning the reversibility of the FMT was disrupted. This implies, by inhibiting collagen production, the shift from FN-binding integrins to collagen-binding integrins does not occur, leaving FAK and RhoA activity high, resulting in higher contractility deeper in the tissue. In the case of cell contractility inhibition, the tissue level strains are lowered and the FN production is decreased. In turn, the myofibroblast activity is much less than in the baseline. This implies, with reduced cell contractility, YAP/TAZ entry to the nucleus is reduced, resulting in less FN production. Without the tensed FN FAK and RhoA activation is less than in the baseline, resulting in an overall decrease in myofibroblast activity. In both biological and mechanical inhibition, the growth front dynamics changed (Figure 6.6). This shows, once again, that the production of *de novo* ECM links the biological and mechanical processes enabling the reversal of FMT. In our simplified *in silico* model, one observation we could not capture is the major reduction in growth rate in case of contractility inhibition with blebbistatin, as observed by Kollmannsberger et al 2018. In our *in silico* model, microtissue is allowed to grow as long as there is available space in the model grid. Therefore inhibiting cell contractility did not affect the tissue growth, although it affected the other biological processes that are linked to contractility (e.g., YAP/TAZ nuclear translocation, FN production). In the future, the tissue growth mechanism in our model needs to be updated to accommodate this discrepancy with the biology.

Note that the mechanical module of our model was iteratively updated for the model geometry which was growing as tissue grows, and for the amount of collagen present in each tissue agent. In our *in silico* model, as the tissue grew and the collagen content in the ECM increased from the growth front

to the tissue core, the stiffness of the tissue material definition of the mechanical module increased (Figure S.6.2). The tensile strains were the response of the tissue to the cell contractile forces, under the continuously changing mechanical properties (geometry and collagen content). Since we were modeling the biological processes observed in a 3D microtissue, the stiffness definition should not be interpreted as the "substrate stiffness" concept in 2D tissue growth experiments. Here the definition of a stiffer ECM with increasing collagen content refers to the increased "stress-bearability" of the tissue (Castro *et al*., 2018; Roeder *et al*., 2002) and the decreased stretching of the FN fibers with increasing collagen fiber content (Kubow *et al*., 2015), as shown by experiments before.

We have made two main assumptions while building the mechanical module. First, we assumed a linearly elastic material description for the whole microtissue while individual collagen (Gachon & Mesquida, 2020) and FN fibers (Klotzsch *et al*., 2009; Peleg *et al*., 2012) are known to be not linear elastic. However, it is safe to assume linear elasticity in case the strains are low, at least for the collagenous tissues (Marqueti *et al*., 2019; Roeder *et al*., 2002) Throughout the simulation, the mean strains were lower than 2.5% for collagen containing tissue materials (Figure S.6.4a) and only for the provisional matrix, which did not contain collagen, the strains were higher (mean $< 10\%$, Figure S.6.4a). Note that we did not explicitly model individual FN fibers. From this and our test with an orthotropic elastic material definition giving similar results in terms of tissue strains (Figure S.6.4b), we assumed that linear elasticity was acceptable for our application. In the future, if material properties of early fibroblast tissue are explored more in detail experimentally, a more refined material description could be used instead of linear elasticity. Although there are no experimental material tests available, to our knowledge, for the early fibroblast tissue we modeled, the closest biological tissue, skin, has been tested for its mechanical properties before. In vivo tests of the forearm skin tissue has shown hyperelastic properties (Flynn *et al*., 2011) and also has found to behave anisotropically (Gahagnon *et al*., 2012). To account for these observations, the fibroblast microtissue could be represented by a hyperelastic anisotropic material, by modifying the parameters of the model described by Gasser *et al*., 2005. This model was initially developed for arterial walls, which have very different mechanical properties compared to the early fibroblast microtissue we have in our model. Therefore the adaptation of a hyperelastic anisotropic material requires detailed mechanical testing of the fibroblast microtissue for the required material parameters. Valero *et al*., 2015, for example, in their skin wound healing model,

used an anisotropic material model. Parameters of this model were previously defined by the experimental tests done by Ní Annaidh *et al*., 2012 on the anisotropic behavior of human skin. We believe it will be valuable to also do mechanical tests with the early fibroblast microtissues, in order to parametrize our *in silico* model, to further advance the knowledge on the reversible FMT.

Second, the magnitude of traction force was kept constant for every force-applying node although there is evidence that αSMA-positive myofibroblasts exert higher traction forces than fibroblasts (Hinz *et al*., 2001; Shinde *et al*., 2017) and that cells exert higher traction forces on stiff versus soft substrates (Provenzano & Keely, 2011). The main reason we kept the magnitude of traction force constant is the fact that myofibroblasts with αSMA are found in the mechanically most stretchable part of the tissue (growth front). Thus the soft environment in the growth front, requiring the cell not to exert as much force as in a stiffer environment, balances the increased force exertion due to αSMA. So, we assumed, the decreased force exertion due to softer ECM is evened out by the increase in force exertion due to high αSMA in the model, and the applied force is equal throughout the tissue. Similarly, in the high collagen (stiffer ECM) regions of the model, αSMA expression is low, which decreases the force exertion. For finer scale applications where individual cells or even sub-cellular components like actin cytoskeleton are explicitly modeled, the applied traction forces by individual cells could change. However, this requires single cell level experimental measurement of applied forces under matching experimental conditions.

Finally, in order to gain more insights into the effect of different parameters in the observed results, a parameter sensitivity analysis needs to be conducted. Such an analysis will also indicate which parameters are more influential on the control over the *in silico* FMT-MFT process. These potentially more influential parameters will then need to be experimentally determined before we can further develop this *in silico* platform.

In conclusion, with our coupled mechanobiological model of the reversible FMT, we have identified novel ECM production and degradation as key processes in the interplay between the biology and mechanics of microtissue growth. The difference in timing of FN and collagen fibrillogenesis eventually creates the difference between the mechanical and biological properties of the high strain growth front and low strain tissue core, with a sharp transition zone between them. The development of the integrated framework, which lumped together various processes, enabled us to identify the

key players in the dynamic interplay between the mechanics and the biology of the reversible FMT, important for controlling the process. Moreover, the integrated *in silico* platform represents an important building block to model other fibrotic processes, in addition to the FMT-MFT, and conduct preliminary *in silico* experiments to understand the influence of ECM (dis)assembly and mechanosensation thereon, preceding the establishment of more complicated experimental setups. Considering that FMT-MFT is a central process in wound healing and aberrations to it result in fibrosis, it is crucial to know for example, when and how to interrupt the process to prevent fibrosis. We believe our model provides fundamental knowledge for applications like active implants, where microtissues are combined with implants to improve tissue regeneration.

6.5 Supplementary Material

Table S.6.1 Summary of *in silico* model equations and the biological processes they represent, accompanying the Figures 6.1C and 6.7

Arrow number in Figure 6.1c and Figure 6.7	**Equation corresponding to the arrow**	**Explanation of the processes that are considered in the equations**
1	Eq.6.1	The Hill type dependence of αSMA on tissue strains has been deduced from Kollmannsberger et al., 2018. We lump in this equation the following processes described in Benn et al. 2023: Myofibroblasts assemble highly strained Fn fibers, which requires $\alpha5\beta1$ integrin activation and signaling, via increased FAK and RhoA, cytoskeletal remodeling and build-up of a more contractile actomyosin cytoskeleton enriched with αSMA.

2	Eq.6.2	The 3^{rd} degree polynomial dependence of nuclear YAP/TAZ on assembled αSMA has been deduced from Kollmannsberger et al., 2018. We lump in this equation the following processes described in Benn et al. 2023: High cell contractility promotes the translocation of YAP/TAZ from the cytoplasm to the nucleus, $kyt0$, $kyt1$, $kyt2$ represent contractility-dependent nuclear transport of YAP/TAZ $kyt3$ represents baseline (contractility-independent) nuclear transport of YAP/TAZ
3-FN	Eq. 6.3	This equation describes the FN secretion (first term) and FN fibrillogenesis (second term). The first term (YAP-dependent FN secretion) also implies: YAP-dependent profibrotic gene expression, including TNC. The second term with the parameter kfibFN describes the FN fibrillogenesis, alignment and stretching. FN fibers are crosslinked by TG2, which enhances their mechanical stability.

3-collagen	Eq.6.4	This equation describes the procollagen secretion and collagen fibrillogenesis. The parameter kcy in the first term describes YAP-dependent procollagen secretion Collagen assembly depends on the structural relaxation of FN fibers, this is described by the parameter kcs in this equation. (lower strain higher collagen assembly), therefore this equation also implies: Transiently upregulated TNC binding to FN, causing the disassembly of integrin $\alpha5\beta1$ adhesions. This results in FN relaxation TNC inhibiting its own expression and sharp decrease in TNC described in Benn et al. 2023. The second term with the parameter kfibCol describes the collagen fibrillogenesis which takes longer time than FN fibrillogenesis.

4	biological module to mechanical module transition	This step links the biological module and the mechanical module through the transient secretion of ECM associated molecules. These mechano-regulated processes described above and in the figure responds and tunes mechanical properties of the tissue material model. In the growth front, where there are highly contractile cells and highly stretched FN, the mechanical model gets this input and reports back ”high strains”. Entering the transition zone, the relaxation of FN starts (due to the increase in TNC) leading to Fn-templating the nucleation of collagen fibrillogenesis. This is associated with a transient reduction of strain considered by the mechanical module. In the tissue core, the shift to collagen binding integrins occurrs, resulting in reduced FAK, RhoA activity and contractility the result is the ECM rich in collagen.

Figure S.6.1 Distribution of the abundances of biological model variables throughout the microtissue at model initialization (Day 0) and after calibration of four iterations, or one day of simulation (Day1).

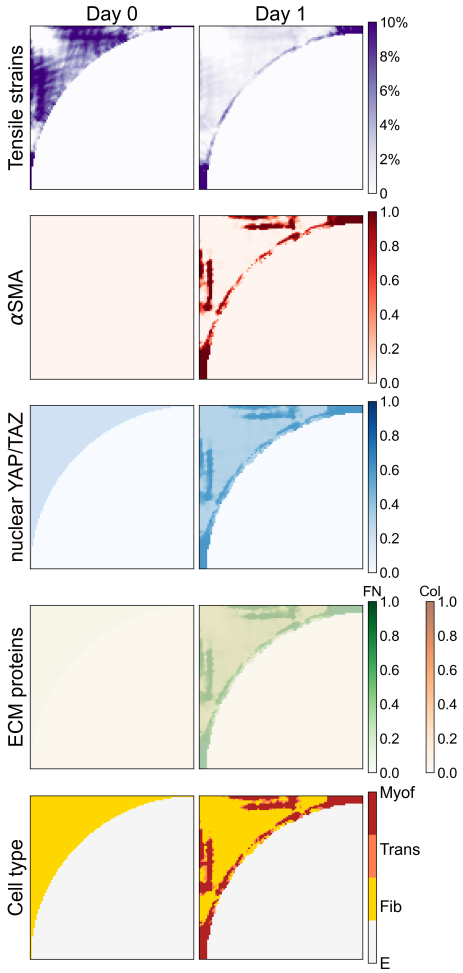

Figure S.6.2 Material stiffness properties of the microtissue over time. Defined material stiffness in the mechanical module is based on the collagen content of the tissue at each tissue agent location in the biological module. See Table 6.1 for collagen to material property conversion.

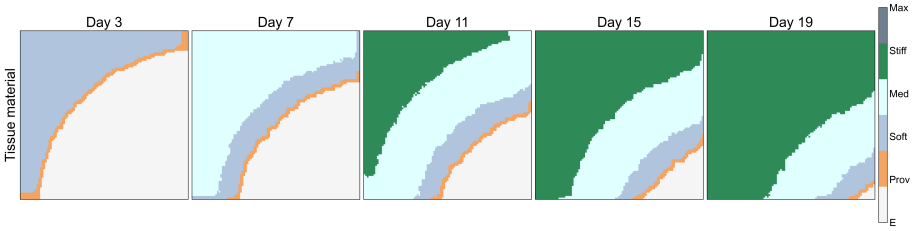

Figure S.6.3 Comparison of simulation results (solid lines) for a) αSMA abundance and b) nuclear YAP/TAZ ratio to experiments by Kollmannsberger *et al.*, 2018 (gray data points).

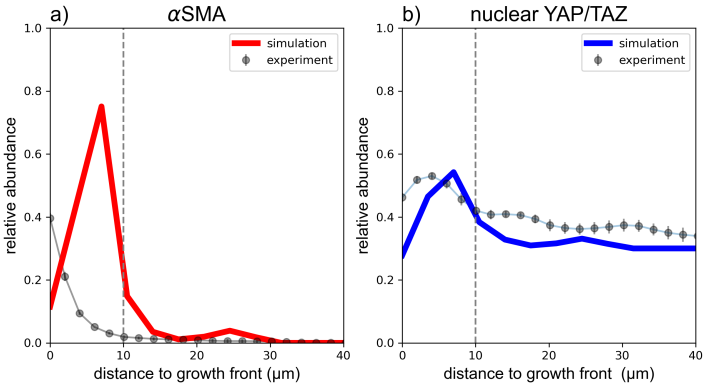

Figure S.6.4 Tissue strains calculated per different material properties (provisional, soft, medium stiff and stiff) with a) linear elastic material assumption and b) orthotropic elastic material assumption. Orthotropic materials have a different elastic modulus in each principal direction (E1 and E2). The principal material direction at each node is assumed to follow the fiber angle at each tissue agent, as calculated by Eq.6.5 in the main text. The elastic modulus in the direction of the fiber (E1) is assumed to be the same as in the linear elastic definition (depending on the collagen content of the tissue) and the elastic modulus on the direction orthogonal to the fiber direction (E2) is assumed to be 1/5 of the elastic modulus along the fiber.

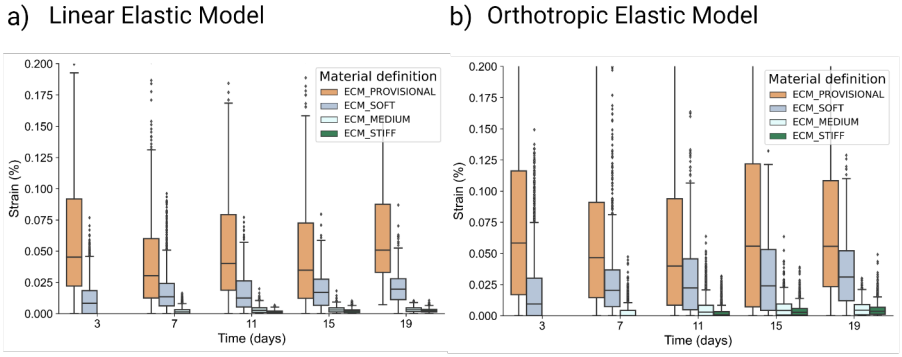

References

Achterberg, V. F., Buscemi, L., Diekmann, H., Smith-Clerc, J., Schwengler, H., Meister, J.-J., Wenck, H., Gallinat, S., & Hinz, B. (2014). The Nano-Scale Mechanical Properties of the Extracellular Matrix Regulate Dermal Fibroblast Function. *Journal of Investigative Dermatology*, *134*(7), 1862–1872. https://doi.org/10.1038/jid.2014.90

Ang, J., Harris, E., Hussey, B. J., Kil, R., & McMillen, D. R. (2013). Tuning Response Curves for Synthetic Biology. *ACS Synthetic Biology*, *2*(10), 547–567. https://doi.org/10.1021/sb4000564

Benn, M. C., Pot, S. A., Moeller, J., Yamashita, T., Fonta, C. M., Orend, G., Kollmannsberger, P., & Vogel, V. (2023). How the mechanobiology orchestrates the iterative and reciprocal ECM-cell cross-talk that drives microtissue growth. *Science Advances*, *9*(13), eadd9275. https://doi.org/10.1126/sciadv.add9275

Cai, X., Wang, K.-C., & Meng, Z. (2021). Mechanoregulation of YAP and TAZ in Cellular Homeostasis and Disease Progression. *Frontiers in Cell and Developmental Biology*, *9*.

Castro, A. P. G., Yao, J., Battisti, T., & Lacroix, D. (2018). Poroelastic Modeling of Highly Hydrated Collagen Hydrogels: Experimental Results vs. Numerical Simulation With Custom and Commercial Finite Element Solvers. *Frontiers in Bioengineering and Biotechnology*, *6*.

Checa, S., Prendergast, P. J., & Duda, G. N. (2011). Inter-species investigation of the mechano-regulation of bone healing: Comparison of secondary bone healing in sheep and rat. *Journal of Biomechanics*, *44*(7), 1237–1245. https://doi.org/10.1016/j.jbiomech.2011.02.074

Cui, Y., Zhang, M., Leng, C., Blokzijl, T., Jansen, B. H., Dijkstra, G., & Faber, K. N. (2020). Pirfenidone Inhibits Cell Proliferation and Collagen I Production of Primary Human Intestinal Fibroblasts. *Cells*, *9*(3), 775. https://doi.org/10.3390/cells9030775

Doss, B. L., Pan, M., Gupta, M., Grenci, G., Mège, R.-M., Lim, C. T., Sheetz, M. P., Voituriez, R., & Ladoux, B. (2020). Cell response to substrate rigidity is regulated by active and passive cytoskeletal stress. *Proceedings of the National Academy of Sciences*, *117*(23), 12817–12825. https://doi.org/10.1073/pnas.1917555117

D'Urso, M., & Kurniawan, N. A. (2020). Mechanical and Physical Regulation of Fibroblast–Myofibroblast Transition: From Cellular Mechanoresponse to Tissue Pathology. *Frontiers in Bioengineering and Biotechnology*, *8*.

Elosegui-Artola, A., Andreu, I., Beedle, A. E. M., Lezamiz, A., Uroz, M., Kosmalska, A. J., Oria, R., Kechagia, J. Z., Rico-Lastres, P., Le Roux, A.-L., Shanahan, C. M., Trepat, X., Navajas, D., Garcia-Manyes, S., & Roca-Cusachs, P. (2017). Force Triggers YAP Nuclear Entry by Regulating Transport across Nuclear Pores. *Cell*, *171*(6), 1397–1410.e14. https://doi.org/10.1016/j.cell.2017.10.008

Flynn, C., Taberner, A., & Nielsen, P. (2011). Modeling the Mechanical Response of In Vivo Human Skin Under a Rich Set of Deformations. *Annals of Biomedical Engineering*, *39*(7), 1935–1946. https://doi.org/10.1007/s10439-011-0292-7

Freitas Jr., R. A. (1999). Cytometrics. In *Nanomedicine*. Landes Bioscience.

Gachon, E., & Mesquida, P. (2020). Stretching Single Collagen Fibrils Reveals Nonlinear Mechanical Behavior. *Biophysical Journal*, *118*(6), 1401–1408. https://doi.org/10.1016/j.bpj.2020.01.038

Gahagnon, S., Mofid, Y., Josse, G., & Ossant, F. (2012). Skin anisotropy in vivo and initial natural stress effect: A quantitative study using high-frequency static elastography. *Journal of Biomechanics*, *45*(16), 2860–2865. https://doi.org/10.1016/j.jbiomech.2012.08.032

Gasser, T. C., Ogden, R. W., & Holzapfel, G. A. (2005). Hyperelastic modelling of arterial layers with distributed collagen fibre orientations. *Journal of The Royal Society Interface*, *3*(6), 15–35. https://doi.org/10.1098/rsif.2005.0073

Harris, C. R., Millman, K. J., van der Walt, S. J., Gommers, R., Virtanen, P., Cournapeau, D., Wieser, E., Taylor, J., Berg, S., Smith, N. J., Kern, R., Picus, M., Hoyer, S., van Kerkwijk, M. H., Brett, M., Haldane, A., del Río, J. F., Wiebe, M., Peterson, P., … Oliphant, T. E. (2020). Array programming with NumPy. *Nature*, *585*(7825), 357–362. https://doi.org/10.1038/s41586-020-2649-2

Heng, B. C., Zhang, X., Aubel, D., Bai, Y., Li, X., Wei, Y., Fussenegger, M., & Deng, X. (2021). An overview of signaling pathways regulating YAP/TAZ activity. *Cellular and Molecular Life Sciences*, *78*(2), 497–512. https://doi.org/10.1007/s00018-020-03579-8

Hinz, B., Celetta, G., Tomasek, J. J., Gabbiani, G., & Chaponnier, C. (2001). Alpha-Smooth Muscle Actin Expression Upregulates Fibroblast Contractile Activity. *Molecular Biology of the Cell*, *12*(9), 2730–2741.

Kadler, K. E., Hill, A., & Canty-Laird, E. G. (2008). Collagen fibrillogenesis: Fibronectin, integrins, and minor collagens as organizers and nucleators. *Current Opinion in Cell Biology*, *20*(5-24), 495–501. https://doi.org/10.1016/j.ceb.2008.06.008

Klotzsch, E., Smith, M. L., Kubow, K. E., Muntwyler, S., Little, W. C., Beyeler, F., Gourdon, D., Nelson, B. J., & Vogel, V. (2009). Fibronectin forms the most extensible biological fibers displaying switchable force-exposed cryptic binding sites.

Proceedings of the National Academy of Sciences, *106*(43), 18267–18272. https://doi.org/10.1073/pnas.0907518106

Knüppel, L., Ishikawa, Y., Aichler, M., Heinzelmann, K., Hatz, R., Behr, J., Walch, A., Bächinger, H. P., Eickelberg, O., & Staab-Weijnitz, C. A. (2017). A Novel Antifibrotic Mechanism of Nintedanib and Pirfenidone. Inhibition of Collagen Fibril Assembly. *American Journal of Respiratory Cell and Molecular Biology*, *57*(1), 77–90. https://doi.org/10.1165/rcmb.2016-0217OC

Kollmannsberger, P., Bidan, C. M., Dunlop, J. W. C., Fratzl, P., & Vogel, V. (2018). Tensile forces drive a reversible fibroblast-to-myofibroblast transition during tissue growth in engineered clefts. *Science Advances*, *4*(1), eaao4881. https://doi.org/10.1126/sciadv.aao4881

Kubow, K. E., Vukmirovic, R., Zhe, L., Klotzsch, E., Smith, M. L., Gourdon, D., Luna, S., & Vogel, V. (2015). Mechanical forces regulate the interactions of fibronectin and collagen I in extracellular matrix. *Nature Communications*, *6*(1), 8026. https://doi.org/10.1038/ncomms9026

Marqueti, R. d. C., Neto, I. V. d. S., Barin, F. R., & Ramos, G. V. (2019). Exercise and Tendon Remodeling Mechanism. In *Tendons*. IntechOpen. https://doi.org/10.5772/intechopen.79729

Morgan, M. R., Hamidi, H., Bass, M. D., Warwood, S., Ballestrem, C., & Humphries, M. J. (2013). Syndecan-4 Phosphorylation Is a Control Point for Integrin Recycling. *Developmental Cell*, *24*(5), 472–485. https://doi.org/10.1016/j.devcel.2013.01.027

Ní Annaidh, A., Bruyère, K., Destrade, M., Gilchrist, M. D., Maurini, C., Otténio, M., & Saccomandi, G. (2012). Automated Estimation of Collagen Fibre Dispersion in the Dermis and its Contribution to the Anisotropic Behaviour of Skin. *Annals of Biomedical Engineering*, *40*(8), 1666–1678. https://doi.org/10.1007/s10439-012-0542-3

Peleg, O., Savin, T., Kolmakov, G. V., Salib, I. G., Balazs, A. C., Kröger, M., & Vogel, V. (2012). Fibers with Integrated Mechanochemical Switches: Minimalistic Design Principles Derived from Fibronectin. *Biophysical Journal*, *103*(9), 1909–1918. https://doi.org/10.1016/j.bpj.2012.09.028

Plikus, M. V., Wang, X., Sinha, S., Forte, E., Thompson, S. M., Herzog, E. L., Driskell, R. R., Rosenthal, N., Biernaskie, J., & Horsley, V. (2021). Fibroblasts: Origins, definitions, and functions in health and disease. *Cell*, *184*(15), 3852–3872. https://doi.org/10.1016/j.cell.2021.06.024

Provenzano, P. P., & Keely, P. J. (2011). Mechanical signaling through the cytoskeleton regulates cell proliferation by coordinated focal adhesion and Rho GTPase signaling. *Journal of Cell Science*, *124*(8), 1195–1205. https://doi.org/10.1242/jcs.067009

Roeder, B. A., Kokini, K., Sturgis, J. E., Robinson, J. P., & Voytik-Harbin, S. L. (2002). Tensile Mechanical Properties of Three-Dimensional Type I Collagen Extracellular Matrices With Varied Microstructure. *Journal of Biomechanical Engineering*, *124*(2), 214–222. https://doi.org/10.1115/1.1449904

Rosowski, K. A., Boltyanskiy, R., Xiang, Y., Van den Dries, K., Schwartz, M. A., & Dufresne, E. R. (2018). Vinculin and the mechanical response of adherent fibroblasts to matrix deformation. *Scientific Reports*, *8*(1), 17967. https://doi.org/10.1038/s41598-018-36272-9

Schuster, R., Younesi, F., Ezzo, M., & Hinz, B. (2023). The Role of Myofibroblasts in Physiological and Pathological Tissue Repair. *Cold Spring Harbor Perspectives in Biology*, *15*(1), a041231. https://doi.org/10.1101/cshperspect.a041231

Shinde, A. V., Humeres, C., & Frangogiannis, N. G. (2017). The role of -smooth muscle actin in fibroblast-mediated matrix contraction and remodeling. *Biochimica et Biophysica Acta (BBA) - Molecular Basis of Disease*, *1863*(1), 298–309. https://doi.org/10.1016/j.bbadis.2016.11.006

Sun, L., Qu, L., Zhu, R., Li, H., Xue, Y., Liu, X., Fan, J., & Fan, H. (2016). Effects of Mechanical Stretch on Cell Proliferation and Matrix Formation of Mesenchymal Stem Cell and Anterior Cruciate Ligament Fibroblast. *Stem Cells International*, *2016*, e9842075. https://doi.org/10.1155/2016/9842075

Szymanski, J. M., Zhang, K., & Feinberg, A. W. (2017). Measuring the Poisson's Ratio of Fibronectin Using Engineered Nanofibers. *Scientific Reports*, *7*(1), 13413. https://doi.org/10.1038/s41598-017-13866-3

Talele, N. P., Fradette, J., Davies, J. E., Kapus, A., & Hinz, B. (2015). Expression of alpha-Smooth Muscle Actin Determines the Fate of Mesenchymal Stromal Cells. *Stem Cell Reports*, *4*(6), 1016–1030. https://doi.org/10.1016/j.stemcr.2015.05.004

Valero, C., Javierre, E., García-Aznar, J. M., Gómez-Benito, M. J., & Menzel, A. (2015). Modeling of anisotropic wound healing. *Journal of the Mechanics and Physics of Solids*, *79*, 80–91. https://doi.org/10.1016/j.jmps.2015.03.009

7

General Discussion

Regenerative medicine strives to restore damaged tissues and organs. Over time, both regenerative medicine and the discipline of tissue engineering have progressed, aiming to create cell culture and biomaterial systems and combinations thereof that closely resemble natural tissues. In order for tissue engineering to be successful, it is essential that the cells used to create the tissue are able to communicate and interact with each other and with the (bio)materials in a way that mimics the natural functioning of the tissue. This requires a deep understanding of the mechanisms of cell-cell and cell-ECM communication, as well as the ability to manipulate these processes in the lab. Computational modeling is a powerful tool for investigating the cell-cell and cell-ECM interactions. It allows us to study the complex processes in a more controlled and systematic way. By using computational models, we can study the effects of different variables, such as changes in the concentration of different proteins in the system, or the mechanical forces that cells experience. Having a thorough understanding of these fundamental processes will help us then to identify potential therapeutic targets for diseases that involve abnormal cell-cell or cell-ECM interactions such as fibrosis.

7.0.1 Contribution to research

Throughout this thesis, we introduced different dynamic computational models, all tackling various aspects of cell-cell and cell-ECM interactions with a focus on improving the tissue engineering and regenerative medicine field. In **Chapter 2** we reviewed the existing computational models of integrin signaling in the context of cell-ECM interactions, and identified the open questions in the area. We highlighted different modeling approaches that are suitable for different research questions. The remaining parts of this thesis were also inspired by this concept: there is no single true method when it comes to computational modeling of cell-cell and cell-ECM interactions and the validity of the computational models are defined within the scope of the research question. For example, in **Chapter 4** we explicitly modeled the concentration of proteins in the integrin adhesome to predict the fraction of nascent adhesion that has the potential to mature. On the other hand, in **Chapter 5**, we only modeled the activity levels of proteins, not absolute concentrations, to predict the cell proliferation status as a result of the (in)activity of proteins in the signaling cascades, as a multitude of experimental data in the form of the relative abundance of active and inactive forms (i.e., phosphorylated and unphosphorylated forms) of proteins in the network were available. Both models in these chapters use ordinary differential equations (ODEs) but the

mathematical expressions are adjusted to represent different aspects of the biological systems, because they tackle different challenges.

We focused on the previously uncharted competition between ECM proteins when binding to the same integrin sub-type in **Chapter 3**. We used an ODE model, building on a previously published model (Hudson *et al.*, 2017) and extending the knowledge by allowing the binding of two different integrin ligands to the same integrin. The ODE model enabled us to track the concentrations of free and integrin-bound ligands over time. The results showed that the ligands with high integrin binding affinity occupy more integrins than their low affinity competitors because the ratio of binding rates of ligands was much higher than the ratio of initial ligand concentrations. We showed mathematically, that when two ligands compete to bind to the same receptor, the highest ratio — either the ratio of binding rate constants or the ratio of initial ligand concentrations — has the dominating effect on the steady-state concentrations of the ligand-bound receptors. This conclusion implies that when designing (bio)materials with integrin targeting peptides for instance, the affinity between the peptides and the collection of integrin sub-types expressed by the cells should be carefully assessed alongside the concentrations of peptides used to functionalize the material.

The computational model described in **Chapter 4** expanded the knowledge on the integrin-ligand level to the integrin adhesome level. In this study we explored the biochemical reactions that take place at the cell-ECM interface at the adhesome scale using an ODE system similar to the previous chapter but explored the effect of cellular forces on the binding and unbinding reactions as well. By including the cellular forces in the equation, we showed that the focal adhesion maturation was dependent on the substrate stiffness in a biphasic manner. We have also shown the indispensable contribution of cell signaling to the adhesome assembly/disassembly dynamics. Time dependent rate modification (TDRM) of the nascent adhesion (dis)assembly rates, which biologically represented the spontaneous bond-rupture events in the nascent adhesion proved to be necessary to establish the experimentally observed ”optimal stiffness” concept for adhesion maturation. This model was an extension to the molecular clutch model of Chan and Odde, 2008 and provided a potential explanation for the different optimal stiffness preference of different cell types.

In addition to cell-ECM interactions, cell-cell interactions are also critical determinants of cell decision-making. In **Chapter 5** we explored the combinatorial effect of cadherin-11, a cell-cell adhesion protein, and PDGFRs, growth

factor receptors, on cell proliferation in hMSCs. This model was different than the previous models in nature, as the ODEs modelled here the standardized activity level of proteins in the network, rather than the exact concentrations of proteins. This allowed us to use the protein activity quantification data provided by our collaborators for calibrating and validating the model. In the end, with this model we were able to provide computational evidence for the existence of a new level of interaction between the growth factor and cadherin pathways. This model helped in the interpretation of the experimental observations and provided a possible mechanism of action for cadherin-mediated cell proliferation control in hMSCs.

Then in **Chapter 6**, we incorporated both cell-ECM and cell-cell interactions in a multiscale model of the reversible fibroblast to myofibroblast transition (FMT). Although integrins and cadherins were not explicitly modeled in this study, we represented the cell-ECM interactions as the effect of ECM protein composition and alignment on the activation of mechanotransductive cellular processes while the cell-cell interactions were represented via the traction forces that were applied by neighboring cells to the ECM. Using a coupled biological and mechanical model we showed that the mechanical properties of the ECM can direct the subcellular processes such as αSMA production, YAP/TAZ nuclear translocation and ECM protein production thus changing the cell behavior via myofibroblast activation. We also showed that the reversal of phenotyope, from myofibroblast to fibroblast, is possible with the maturation of collagen-rich ECM. These conclusions have important implications for wound healing models that are used in tissue engineering. First, we suggest that the reversibility of the FMT is an emerging property of the mechanosensitive de novo ECM protein production by the fibroblasts and myofibroblasts. Second, we provide mechanistic explanations to the results of biological and mechanical perturbations to the system. Any biological inhibitor that acts via slowing down the collagen production will disturb the reversibility of the FMT and any mechanical inhibitor that decreases cell contractility will disturb the activation of FMT.

All together, the research presented in this thesis highlights the importance of cell-cell and cell-ECM interactions in cell decision-making at different scales. We have shown that from single protein level to tissue level, all steps of cell-cell and cell-ECM interactions can influence the outcome of cell behavior (adhesion, proliferation, differentiation). Computational modeling allowed us to demonstrate the delicate control needed over not only biological, but also chemical and physical/mechanical aspects of the cell-cell and cell-ECM interactions for the normal functioning of cells and tissues. For example, the

integrin ligand competition is highly influenced by the physical affinity of proteins for one another. The adhesion (dis)assembly dynamics depend on the presence of other signaling proteins, on more stochastic bond rupture events and also on the mechanical reinforcement through force-dependent unfolding of proteins. Cadherin-11 and PDGFR signaling pathways crosstalk at different levels and each level of crosstalk has a different effect on the cell proliferation. The production of new ECM proteins influence cellular biology via changing the ECM mechanical properties as well as composition and relative abundance of integrin ligands. All of the biological, chemical, physical/mechanical control mechanisms (e.g., feedback loops, crosstalks, thresholds) are equally important. Yet they act on the different levels of cell-cell and cell-ECM interactions, therefore they need to be acknowledged while addressing complex biological challenges like mimicking the natural tissue environments using biomaterials.

7.0.2 Outstanding questions and future work

Regenerative medicine

In different chapters of this thesis, we addressed challenges of a different biological scale (i.e., protein, cell, tissue scales) of cell-cell and cell-ECM interactions. As often repeated throughout this thesis, biological systems are complex and multiscale. For example, the FMT process is influenced by both protein scale changes (e.g., YAP/TAZ nuclear translocation) and tissue scale changes (e.g., ECM straining), as highlighted in the multiscale model of **Chapter 6**. Therefore when developing (bio)material systems targeting cells (of the desired tissue) this multiscale effect of cell-cell and cell-ECM interactions should be carefully considered. In **Chapter 6**, we lay the building blocks of the FMT process which is key in healthy wound healing and fibrosis. However, to address challenges like fibrosis prevention in regenerative medicine, a more thorough approach in modeling is needed. Fibrosis is a highly multiscale problem, involving multiple cell types and physiological systems and difficult to tackle from a single point of view. That is why fibrosis is still an unresolved issue in regenerative medicine (Fernández-Colino *et al.*, 2019).

Along this line, a possible further extension to this thesis, could be to bring all the knowledge obtained from the four research projects at different scales together in a multiscale model of fibrosis, to test the effect of known and developing anti-fibrosis drugs (Figure 7.1). Such a novel multiscale model could

account for the three main receptors; integrins, cadherins and growth factor receptors on fibroblast cells which are represented in an agent based model setup. To accurately represent the cellular environment in fibrosis, this model could also include cells of the immune system (i.e., macrophages and lymphocytes) which are activated in fibrosis development. At the subcellular scale, we could use the information from **Chapters 3**, **4** and **5** to form an ODE network of integrin adhesome, cadherin and growth factor receptor pathways, including known crosstalks between the three (Barcelona-Estaje *et al*., 2021; Margadant & Sonnenberg, 2010). This would result in an agent based model, in which the subcellular processes are tracked with ODEs. When this is coupled to a FEM, similar to the one in **Chapter 6**, we could also see how the mechanical properties of the ECM and the tension generating capacity of the cells can change the adhesome formation (as implied in **Chapter 4**) and further mechanosensitive and mechanotransductive processes. Finally, using our knowledge from the **Chapter 2**, we could test the effect, dose dependency and interdependence of different anti-fibrosis drugs that are known to target integrins, cadherins and growth factors or their receptors (Blaschuk, 2022; Slack *et al*., 2022; Zhao *et al*., 2022). This model would also enable the discovery of new anti-fibrotic drugs or drug combinations by complementing *in vitro* fibrosis models (Alsharabasy & Pandit, 2021; Doryab *et al*., 2022; van Grunsven, 2017; Vazquez-Armendariz *et al*., 2022), allowing *in silico* testing of many different configurations otherwise too costly to do experimentally.

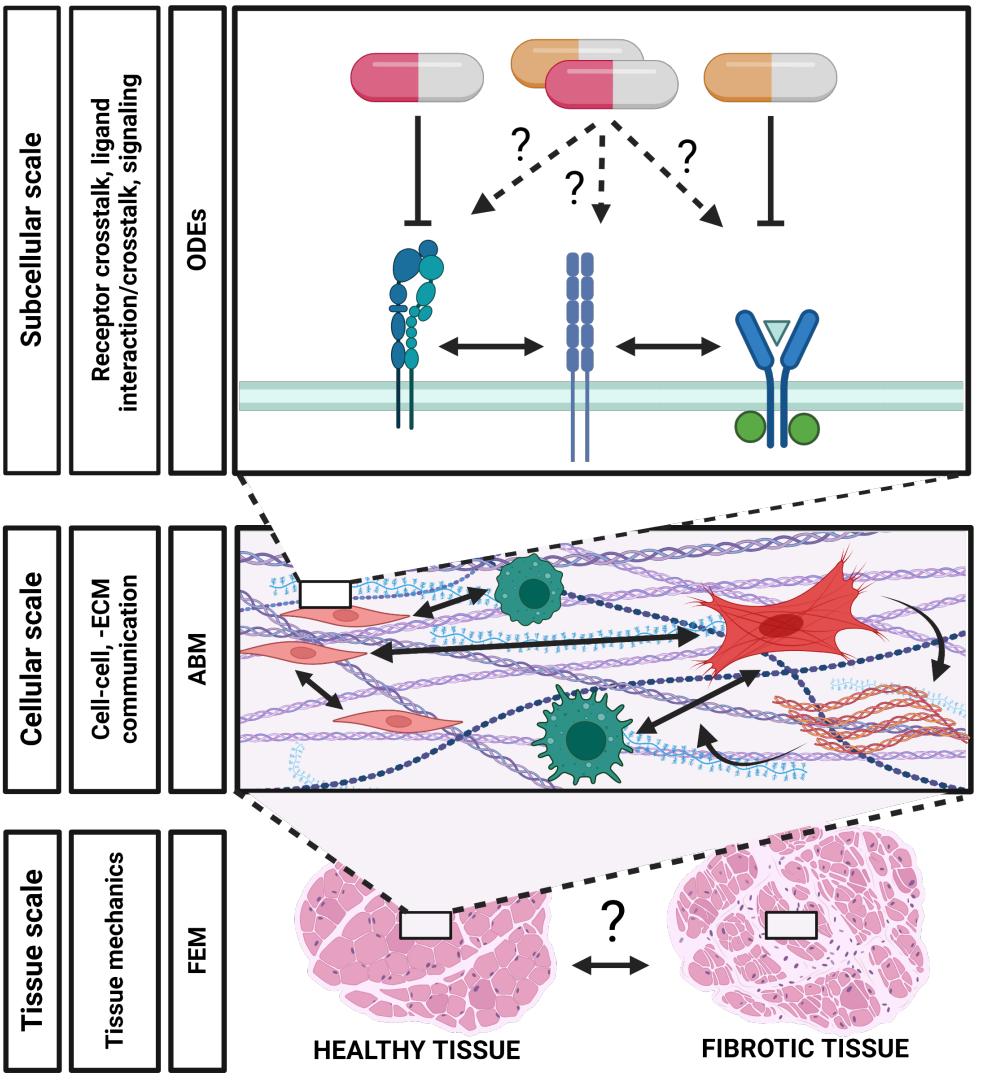

Figure 7.1: A summary of the proposed multiscale model of fibrosis, using information from all the research presented in different chapters of this thesis.

Computational biology

Multiscale computational models have the power to represent complex biological systems from the molecular level up to the level of whole tissues or organs. As understanding the effect of cell-cell and cell-ECM interactions on cell decision-making requires us to understand changes at the (macro)molecular level (e.g., interactions between proteins), at the cellular level (e.g., cell survival/death) and at the tissue/organ level (e.g., fibrosis/healthy tissue formation), multiscale models have a great potential to advance the tissue engineering and regenerative medicine field. Therefore the future of computational modeling efforts need to focus on building multiscale models to help improve tissue engineering and regenerative medicine. This also implies biological data produced at multiple scales will be needed. More and more quantitative methods are being developed and used at the molecule, cell and tissue/organ level in the regenerative medicine field. Multiscale models will also enable the incorporation of data from different sources and thus has the potential to unravel new relationships between different parts of the biological systems (Fletcher & Osborne, 2022).

A current challenge in the production, storage and sharing of the biological data, which is highly valuable for computational biology, is ensuring its quality. There are four principles, called the FAIR principles, to ensure the good quality of data in scientific research. The FAIR principles are a set of guidelines for making data Findable, Accessible, Interoperable, and Reusable (FAIR) (Wilkinson *et al.*, 2016). These principles were developed to promote the use of open data and to improve the interoperability and reuse of data in scientific research. The FAIR principles are particularly relevant for computational modeling of biological systems, as they can help to ensure that the data used to build models is of high quality and is easily accessible to other researchers. I believe the improvements in the field of (biological) data management will aid both the computational biology and the fields of biology that benefit from computational methods immensely in the years to come.

Besides the management of biological data that needs to improve and fit to standards, the resulting computational models that make use of the biological data need to be stored in properly managed databases and openly shared with the scientific community. It is important to share computational models openly as most of the time (also as mentioned in different chapters of this thesis) computational models build on one another. Therefore having access to past attempts in modeling a particular system is extremely valuable. There

are different ways to share published computational models with the scientific community. One is publishing the code used to generate the model and the simulations in an open-source software development platform such as GitHub (https://github.com/), which also allows version control for the modeller. Second is using a database offered by the modeling software to store all the code to the model and simulations. The VCell model database (https://vcell.org/) is an example to this option. It allows the user to view, load, run simulations and extract results from the open access models in the database. The third option is to use a more general database like BioModels (https://www.ebi.ac.uk/biomodels/), which allows the modeler to store their computational models in standardized formats that are globally accepted. As a strong advocate of open source coding and open science, I have shared all the computational models in this thesis with the scientific community, using at least one of the methods described here. The individual chapters can be visited to read about access options for each of the models. With this, I hope to have set a good example for the future generation of computational modelers.

Certainly, there is still a considerable amount of work to do, in order to achieve the goal of full, functional regeneration of damaged organs. However, regenerative medicine is improving with the help of tissue engineering. With this thesis, I believe I have also shown some examples regarding how computational modeling can be a great companion to regenerative medicine. Addressing the above-mentioned outstanding questions in regenerative medicine and computational biology will ultimately assist the development of novel treatment strategies.

References

Alsharabasy, A. M., & Pandit, A. (2021). Protocol for in vitro skin fibrosis model to screen the biological effects of antifibrotic compounds. *STAR Protocols*, *2*(1), 100387. https://doi.org/10.1016/j.xpro.2021.100387

Barcelona-Estaje, E., Dalby, M. J., Cantini, M., & Salmeron-Sanchez, M. (2021). You Talking to Me? Cadherin and Integrin Crosstalk in Biomaterial Design. *Advanced Healthcare Materials*, *10*(6), 2002048. https://doi.org/10.1002/adhm.202002048

Blaschuk, O. W. (2022). Potential Therapeutic Applications of N-Cadherin Antagonists and Agonists. *Frontiers in Cell and Developmental Biology*, *10*.

Chan, C. E., & Odde, D. J. (2008). Traction dynamics of filopodia on compliant substrates. *Science (New York, N.Y.)*, *322*(5908), 1687–1691. https://doi.org/10.1126/SCIENCE.1163595

Doryab, A., Taskin, M. B., Stahlhut, P., Groll, J., & Schmid, O. (2022). Real-Time Measurement of Cell Mechanics as a Clinically Relevant Readout of an In Vitro Lung Fibrosis Model Established on a Bioinspired Basement Membrane. *Advanced Materials*, *34*(41), 2205083. https://doi.org/10.1002/adma.202205083

Fernández-Colino, A., Iop, L., Ventura Ferreira, M. S., & Mela, P. (2019). Fibrosis in tissue engineering and regenerative medicine: Treat or trigger? *Advanced Drug Delivery Reviews*, *146*, 17–36. https://doi.org/10.1016/j.addr.2019.07.007

Fletcher, A. G., & Osborne, J. M. (2022). Seven challenges in the multiscale modeling of multicellular tissues. *WIREs Mechanisms of Disease*, *14*(1), e1527. https://doi.org/10.1002/wsbm.1527

Hudson, V. S., Dolin, C. E., Poole, L. G., Massey, V. L., Wilkey, D., Beier, J. I., Merchant, M. L., Frieboes, H. B., & Arteel, G. E. (2017). Modeling the Kinetics of Integrin Receptor Binding to Hepatic Extracellular Matrix Proteins. *Scientific Reports*, *7*(1), 1–13. https://doi.org/10.1038/s41598-017-12691-y

Margadant, C., & Sonnenberg, A. (2010). Integrin–TGF-β crosstalk in fibrosis, cancer and wound healing. *EMBO reports*, *11*(2), 97–105. https://doi.org/10.1038/embor.2009.276

Slack, R. J., Macdonald, S. J. F., Roper, J. A., Jenkins, R. G., & Hatley, R. J. D. (2022). Emerging therapeutic opportunities for integrin inhibitors. *Nature Reviews Drug Discovery*, *21*(1), 60–78. https://doi.org/10.1038/s41573-021-00284-4

van Grunsven, L. A. (2017). 3D in vitro models of liver fibrosis. *Advanced Drug Delivery Reviews*, *121*, 133–146. https://doi.org/10.1016/j.addr.2017.07.004

Vazquez-Armendariz, A. I., Barroso, M. M., El Agha, E., & Herold, S. (2022). 3D In Vitro Models: Novel Insights into Idiopathic Pulmonary Fibrosis Pathophysiology and Drug Screening. *Cells*, *11*(9), 1526. https://doi.org/10.3390/cells11091526

Wilkinson, M. D., Dumontier, M., Aalbersberg, I. J., Appleton, G., Axton, M., Baak, A., Blomberg, N., Boiten, J.-W., da Silva Santos, L. B., Bourne, P. E., Bouwman, J., Brookes, A. J., Clark, T., Crosas, M., Dillo, I., Dumon, O., Edmunds, S., Evelo, C. T., Finkers, R., … Mons, B. (2016). The FAIR Guiding Principles for scientific data management and stewardship. *Scientific Data*, *3*(1), 160018. https://doi.org/10.1038/sdata.2016.18

Zhao, M., Wang, L., Wang, M., Zhou, S., Lu, Y., Cui, H., Racanelli, A. C., Zhang, L., Ye, T., Ding, B., Zhang, B., Yang, J., & Yao, Y. (2022). Targeting fibrosis: Mechanisms and clinical trials. *Signal Transduction and Targeted Therapy*, *7*(1), 1–21. https://doi.org/10.1038/s41392-022-01070-3

Valorisation

The shift towards functionalized materials in tissue engineering began to gain prominence since the beginning of this century. Researchers realized that mimicking the dynamic and interactive nature of the native tissue microenvironment was crucial for successful tissue regeneration. This involved considering the biochemical, mechanical, and topographical cues that cells experience in their native environments. The goal was to create materials that could recapitulate the complex cell-matrix and cell-cell interactions observed in natural tissues, thus improving the regenerative capacity of cells, tissues and organs.

The ambitious aim of mimicking native tissue environment requires thorough understanding of cellular biology with all the reciprocal feedback between cells and their environment. Computational biology has been a crucial tool for tissue engineering and regenerative medicine by providing valuable insights, predictions, and guidance throughout the process. The computational models presented in this thesis contribute towards understanding the fundamental biological processes and predicting cell behavior. They can simulate and analyze the interactions between cells and between cells and their surrounding extracellular matrix (ECM). By integrating experimental data and existing knowledge, these models provide a deeper understanding of cellular adhesion (**Chapters 3, 4**), signaling pathways (**Chapter 5, 6**), and tissue development (**Chapter 6**). This information will help tissue engineering and regenerative medicine fields in designing optimized scaffold materials culture conditions with optimum stiffness, ECM mechanical properties and integrin/growth factor receptor targeting peptides predicted using the models in this thesis. Eventually, the aim to guide cell behavior towards desired outcomes will be one step closer.

The area that encompasses the utilization of personalized physiological computer simulations in every aspect of disease prevention, diagnosis, prognostic evaluation, treatment, and biomedical product development is termed "*in silico* medicine". In the future, the computational models in this thesis could be incorporated into bigger frameworks of *in silico* medicine as they have the capacity to be used for virtual testing and optimization of tissue engineering methods. *in silico* medicine is gaining more and more attention as global healthcare systems face the challenge of increasing de-

mand and costs. The need for scaling up the personalized treatment options as well as making them more accessible is also increasing (Lesage *et al.*, 2023). Computational biology and experts in this field are highly valuable in making *in silico* medicine applicable in the clinic. A report by the Virtual Physiological Human Institute (VPHi, http://www.vph-institute.org/) demonstrated the increasing confidence of clinicians on *in silico* tools for medical planning and prediction. Yet they have also indicated the difficulties in accessing up-to-date computational applications and proper technical expertise in the field of *in silico* medicine (Lesage *et al.*, 2023). These difficulties can be overcome by initiatives like VPHi with the support of national and global support. Recently, European Medicines Agency (EMA, https://www.ema.europa.eu/en) announced a work plan for increasing the utility of big data in regulation, to empower data-driven medicines regulation in the European Union. Similarly, The United States Food and Drug Administration (FDA, https://www.fda.gov/) agency has formed a Modeling and Simulation Working Group to focus on improving the use of computational models in addition to traditional methods for *in vitro* testing and *in vivo* studies. In summary, in the future, computational models like in this thesis will be used (with modifications) in predicting cell behavior, scaffold design and optimization and virtual testing and optimization of *in silico* medicine tools.

References

Lesage, R., Van Oudheusden, M., Schievano, S., Van Hoyweghen, I., Geris, L., & Capelli, C. (2023). Mapping the use of computational modelling and simulation in clinics: A survey. *Frontiers in Medical Technology*, *5*.

Summary

This thesis explores cell-cell and cell-extracellular matrix (ECM) interactions in regenerative medicine. Tissue engineering and regenerative medicine field aims to develop cell culture systems and biomaterials that mimic native tissues. The extracellular matrix facilitates communication between cells and is vital for organismal well-being. As such, imbalances in cell-ECM and cell-cell interactions can lead to impaired regeneration, such as fibrosis, resulting in reduced tissue function.

The thesis utilizes a computational approach to understand cell decision-making affected by these interactions and comprises a review and four original research articles, each focusing on a different aspect of cell-cell or cell-ECM communication.

Chapter 2 provides an overview of integrins' role in cell-ECM interactions and existing computational models thereof. Challenges in studying integrins are discussed, emphasizing the need for more specific experimental data. Chapter 3 presents a computational model of integrin activity, considering ligand binding competition. The model results suggest that both the binding affinity as well as relative ligand abundance need to be considered for successful biomaterial design.

Chapter 4 combines the biochemical and mechanical interactions occurring during the formation of integrin clusters and adhesions. The model predicts the fraction of nascent adhesions that can become mature focal adhesions under different substrate stiffnesses. Chapter 5 explores the crosstalk between cadherin-11 and platelet-derived growth factor receptors (PDGFRs) using a computational model. The model reveals the need for additional crosstalk between signaling pathways for cadherin-11 to influence cell proliferation, as was shown experimentally.

Chapter 6 models the reversible fibroblast to myofibroblast transition (FMT) initiated by ECM tension at the tissue level. The model highlights the dynamic interactions between cells and the ECM, proposing that the tightly regulated production of new ECM can reverse the FMT process.

Overall, this thesis emphasizes the significance of understanding the exquisite regulation of cell-cell and cell-ECM interactions for regenerative medicine,

using computational modeling. By unraveling these complexities, the research presented in this thesis has established important building blocks to improve regenerative medicine strategies with computational modeling approaches.

Samenvatting

Dit proefschrift onderzoekt cel-cel en cel-extracellulaire matrix (ECM) interacties in de regeneratieve geneeskunde. Binnen de regeneratieve geneeskunde tracht men geavanceerde celkweeksystemen en biomaterialen te ontwikkelen die natuurlijke weefsels nabootsen en het regeneratieve proces kunnen stimuleren. Belangrijk hiervoor is de extracellulaire omgeving. De extracellulaire matrix faciliteert namelijk de communicatie tussen cellen en is van vitaal belang voor het welzijn en correct functioneren van het weefsel. Onevenwichtigheden in cel-ECM of cel-cel interacties kunnen bijgevolg leiden tot verstoorde weefselregeneratie, de vorming van littekenweefsel (fibrose) en beperkte weefselfunctie.

Dit proefschrift gebruikt een computationele benadering om de besluitvorming van cellen te begrijpen en hoe die beïnvloed wordt door deze cel-cel en cel-ECM interacties. Het proefschrift bestaat uit een overzicht en vier originele onderzoeksartikelen, elk gericht op een ander aspect van cel-cel of cel-ECM communicatie.

Hoofdstuk 2 geeft een overzicht van de bestaande computationele modellen die de rol van integrines in cel-ECM interacties capteren en simuleren. Uitdagingen in het bestuderen van integrines worden besproken, waarbij de behoefte aan meer specifieke experimentele data wordt benadrukt. Hoofdstuk 3 presenteert een computationeel model van integrine activiteit, waarbij meerdere liganden kunnen binden aan dezelfde integrines en dus met elkaar in competitie gaan. Het model laat zien dat zowel de affiniteit als de relatieve ligand concentratie belangrijk is voor het ontwerp en de ontwikkeling van nieuwe biomaterialen.

Hoofdstuk 4 combineert de biochemische en mechanische interacties, die plaatsvinden tijdens de vorming van integrine clusters en adhesies. Het model voorspelt welke fractie van adhesies in wording uitgroeien tot volgroeide, focale adhesies, en dit voor verschillende substraatstijfheden. Hoofdstuk 5 onderzoekt de wisselwerking tussen cadherin-11 en platelet-derived growth factor receptors (PDGFRs) met behulp van een computationeel model. Het model onthult de noodzaak voor extra wisselwerking tussen cadherin-11 and PDGFR signaalwegen om celgroei te beïnvloeden, zoals ook experimenteel aangetoond

Hoofdstuk 6 modelleert de omkeerbare overgang van fibroblast naar myofibroblast (FMT) geïnitieerd door de mechanische spanning op weefselniveau. Het model benadrukt de dynamische interacties tussen cellen en de ECM en stelt voor dat de gecontroleerde productie van nieuwe extracellulaire matrix het FMT-proces kan omkeren.

Samenvattend benadrukt dit proefschrift het belang van cel-cel en cel-ECM interacties voor regeneratieve geneeskunde, welke door computationele modellering verkregen is. Door de ontwikkeling van belangrijke computationele bouwstenen alsook biologisch inzicht in de complexiteit van deze interacties draagt het onderzoek in dit proefschrift bij tot de verbetering van regeneratieve strategieën.

Acknowledgments

Here we are at the acknowledgements section, ironically placed at the end of this book although it is by far the most important. Pursuing this PhD was extremely lonely at times but I was lucky to have the right people around, supporting me along the way. These pages are reserved for those who made it possible for me to succeed and stay sane.

First and foremost, **Aurélie Carlier**, you have been much more than a supervisor to me in the past four years. I feel the luckiest to have you by my side. Throughout this thesis project you have always understood exactly what I needed to continue when I was struggling, and cheered for me the loudest when I achieved even the smallest thing. I admire your resilience, which gave me strength at times of defeat, and your kind heart, which amplified the happy moments (of which there were a lot!). Thank you a million times for always making time for me and being open. I am proud of you, as much as I know you are proud of me!

Martijn van Griensven, I am grateful to have had your guidance and support throughout these four years. You have been a perfect example of a real scientist who embraces change and is willing to always learn more and grow. Without your perspective I would have missed out on an integral part in this journey.

Big thank yous to the members of the assessment and defense committee; **Tim Welting**, **Sandra Loerakker**, **Liesbet Geris**, **Marian Breuer**, for taking time to read, evaluate and give feedback on this thesis.

Thanks to all of my colleagues in MERLN, for making this institute a great place to work. **Fiona Passanha**, **Vanessa LaPointe**, **Thomas Geuens**, **Sabine van Rijt**, **Xingzhen Zhang**, it has been a pleasure to collaborate with you. I will always be proud to have worked with you and learned from you! **Kailas Honasoge**, you have been the best master student-turned-into-co-author I could wish for! I am truly inspired by your curiosity and way of working. **Sangita Swapnasrita**, I cannot thank you enough for coming to my rescue every time I hit a roadblock. The day you told me "It will be very difficult, but you will make it!" when I was crying my eyes out in the dry lab has been a turning point in my project and look where we are! And **Hamidreza Jafarinia**, dankjewel -as you say in Dutch- for always keeping your calm and

reminding me things will eventually be okay. I am grateful to have observed the Carlier computational lab grow over the years. Thanks to all members, past and present, for making it a supportive and safe work group.

Thanks to the European Society of Biomechanics, I had the chance to work at the Julius Wolff Institute in Berlin as a part of my PhD project. I would like to extend my heartfelt gratitude to **Sara Checa** for welcoming me to her Computational Mechanobiology group. This research stay and the collaboration with your group was a breath of fresh air and I will always remember it happily.

Of course, without the help of **Chiara Dazzi**, I would not be writing these words because this project wouldn't have been completed! I feel grateful to have met you and discover this unspoken understanding between us. Remember that I will always be there to listen to you without judgment.

Many thanks to **Giorgio Biesso**, **Özgür Cebeci**, **Vahid Badali Gharatekan**, **Mahdi Jaber**, **Vincenzo Orassi**, **Siddarth Ananth-Swaminathan** and **Britt Waasdorp**, for making me feel so welcome and always being up for some fun! It was a pleasure to join this group of brilliant people even for just a short time.

Through the Materials Driven Regeneration Consortium, I had the pleasure to meet and discuss science with many bright scientists. Thanks especially to **Laura Rijns** and **Patricia Dankers** with whom I had the chance to form a collaboration very early in my PhD trajectory. Watching our projects grow alongside each other over the years has been a constant source of inspiration. Many thanks to **Viola Vogel** for her guidance and extensive feedback on the Chapter 6.

Without two people, my mom and dad, **Yasemin and Nazmi Karagöz**, this whole thing would be meaningless. I will always appreciate how hard you have worked for me to have this life. Thank you for always trusting me in every decision and wholly supporting me with everything you have.

I'd like to thank **Coşku Özdemirci** and **Ozan Pekmezci** for their unwavering presence during both celebrations and farewells.

Thank you **Arda Çiltepe**, **Julia Tielke**, and **Kaya Tielke** for allowing me a different way to experience the meaning of family.

Zeynep Dişbudak, your constant support during both the highs and lows of life means the world to me.

Yunus Şeker, you have been the most reliable friend and my biggest supporter in my running journey during the past four years. Thank you for always showing up.

Tezcan Gönüllü, **Duygu Özçelik**, **Sercan Sofracı**, **Kubilay Temurhan** and **Arca Yılmaz**, thank you all for the constant support in long runs, longer evenings, and on the dance floor.

Emre Ilgaz, thank you for allowing us to always pick up where we have left off and giving me the comfort of unconditionally trusting someone without the need to explain.

Gözde Tanrısevdir, your friendship made me remember how much I have to learn about myself and how much I enjoy the simple act of sharing. Although sometimes difficult, sharing the good and the bad with you allows me to always return to a state of calm and content. Thank you a million times for always being up for an emergency coffee date and trying out a new type of exercise with me!

Mert Akriş, **Ayyüce Aksakal**, **Ayça Arat**, **Bastiaan van Balen**, **Ezgi Çakmak**, **Oğuz Demet**, **Emrecan Demir**, **Melih Demirören**, **Utku Halıcı**, **Elias Herfurt**, **Loes Huijnen**, **Cem Karabulut**, **Beril Kazankıran**, **Alp Koçak**, **Hanife Martin**, **Attila Oğuz**, **Işıl Orhan**, **Nuray Özdemir**, **Oğulcan Ulu**, **Hilde Roeleveld**, **Mark Wolfert**, **Engincan Yerebasmaz** and **Veda Zeren**, thank you all for making the Netherlands home to me. Life is easier and so enjoyable with your presence.

Ellie Zwick, I often think about how much being your friend has taught me about friendship. A lot has changed since we were sitting next to each other and finding (good) excuses for having a beer with fries instead of working on our master theses. And don't get me wrong, I am grateful for all that change, but I am also grateful to still have that exact same feeling of sitting next to you every single day although we are often far away. It is truly precious to be in this -sometimes unexpected- journey of life as your friend and be as happy, sad, excited, exhausted and always hungry as one another.

Murat Sarıhan, words cannot express the warmth and comfort I get from being at home with you. We have seen each other's worst and best, we have changed so much and will continue to change, yet my feeling of being at home with you only grows stronger. You believe in me on days where I cannot stand being me. You make me stand up for myself when I am ready to give up. It is your voice I hear saying "I am proud of you" when I think I am

not enough. I am glad to have the premium subscription to your ever changing set of jokes and fictional personas via which we always find a way to get through the day. I love you for being you and I am excited to see what is next for us. LET IT RIP.

And I know this is unconventional but I would also like to thank myself. I once heard someone say "run a marathon to get to know yourself", and as much as I agree with that, I dare to suggest doing a PhD to get to know yourself. I thank myself for not quitting and for finding ways to heal when I am hurt. This thesis journey ended the way it did because I showed up for myself when I needed it, through the good and the painful. I am grateful for the joy I found in discovering what I am capable of mentally and physically.

Zeynep Karagöz
Maastricht
January 9, 2024

Published work

- Honasoge, K. S., Karagöz, Z., Goult, B. T., Wolfenson, H., LaPointe, V. L. S., & Carlier, A. (2023). Force-dependent focal adhesion assembly and disassembly: A computational study. *PLOS Computational Biology*, *19*(10), e1011500. https://doi.org/10.1371/journal.pcbi.1011500
- Karagöz, Z., Passanha, F. R., Robeerst, L., van Griensven, M., LaPointe, V. L. S., & Carlier, A. (2023). Computational evidence for multi-layer crosstalk between the cadherin-11 and PDGFR pathways. *Scientific Reports*, *13*(1), 15804. https://doi.org/10.1038/s41598-023-42624-x
- Zhang, X., Karagöz, Z., Swapnasrita, S., Habibovic, P., Carlier, A., & Rijt, S. (2023). Development of Mesoporous Silica Nanoparticle-Based Films with Tunable Arginine-Glycine-Aspartate Peptide Global Density and Clustering Levels to Study Stem Cell Adhesion and Differentiation. *ACS applied materials & interfaces*, *15*. https://doi.org/10.1021/acsami.3c04249
- Karagöz, Z., Geuens, T., LaPointe, V. L. S., van Griensven, M., & Carlier, A. (2021). Win, Lose, or Tie: Mathematical Modeling of Ligand Competition at the Cell–Extracellular Matrix Interface. *Frontiers in Bioengineering and Biotechnology*, *9*. https://doi.org/10.3389/fbioe.2021.657244
- Karagöz, Z., Rijns, L., Dankers, P. Y. W., van Griensven, M., & Carlier, A. (2021). Towards understanding the messengers of extracellular space: Computational models of outside-in integrin reaction networks. *Computational and Structural Biotechnology Journal*, *19*, 303–314. https://doi.org/10.1016/J.CSBJ.2020.12.025
- Akkose, U., Kaya, V. O., Lindsey-Boltz, L., Karagöz, Z., Brown, A. D., Larsen, P. A., Yoder, A. D., Sancar, A., & Adebali, O. (2021). Comparative analyses of two primate species diverged by more than 60 million years show different rates but similar distribution of genome-wide UV repair events. *BMC Genomics*, *22*(1), 600. https://doi.org/10.1186/s12864-021-07898-3

About the author

Zeynep Karagöz was born on October 2, 1992 in Izmir, Turkey. She earned her BSc degree in Molecular Biology and Genetics from Bogazici University, Istanbul in 2016. Same year she moved to Munich, Germany for her MSc studies at Ludwig-Maximilian University (LMU) where her focus was Computational Biology and Bioinformatics. During her MSc thesis work, she gained experience in RNA sequencing and statistical data analysis methods as well as transcriptome assembly methods. Following her MSc title, obtained in 2018, she continued working on comparative transcriptomics in Wolfgang Enard and Ines Hellmann's research group at LMU, Munich as a research assistant. In 2019, she briefly joined Ogün Adebali's research group at Sabanci University, Istanbul where she contributed towards a publication using her past experience in comparative omics analyses. In 2019, she joined MERLN Institute of Technology-Inspired Regenerative Medicine in Maastricht University for her PhD work under the supervision of Aurélie Carlier and Martijn van Griensven. She worked on computational modeling of cell – extracellular matrix (ECM) interactions to understand how cell decision-making is affected by changes in the ECM using various computational modeling techniques, including differential equations, agent-based modeling and finite element method. In 2022, she received the European Society of Biomechanics Mobility Award for Early Career Researchers to join Sara Checa's research group at Julius Wolff Institute, Charité University Hospital in Berlin, Germany for a short research visit. In 2023 she completed her PhD work, which resulted in this thesis.